Optimization of Graphene dispersion and functionalization processes for the development of different composites

by

Bruno Iraola Sáenz

A thesis submitted in partial fulfilment of the requirements of the University of the Basque Country for the degree of Doctor of Philosophy

Thesis Advisors
Dr. Izaskun Bustero (Tecnalia)
Dr. Antxon Santamaria (UPV-EHU)

Donostia - San Sebastián
June 2017

Dedicatoria

REDACTAR EXTENDIDO Especial agradecimiento a:
Fundacion Inaki Goenaga
Tecnalia
Departamento
Reologia universidad
Companeros
Familiares y amigos

Contents

Chapter 1

Introduction

1.1 Introduction

1.1.1 Introduction to Graphene and its Derivatives

Graphene is a monolayer allotrope of the carbon that consists on a honeycomb lattice with the carbon atoms bonded in a sp^2 hybridization (three carbon electrons in four hybridized bonding electrons $2s^1 2p_x{}^1 2p_y{}^1 2p_z{}^1$ and a fourth electron that spreads out over the top or bottom of the layer as a π electron) [91]. This two dimensional material stands as a basic building block for carbon allotropes of other dimensionalities: 0D fullerenes, 1D nanotubes and 3D graphite (Figure 1.1). It has been a subject of theoretical studies for more than sixty years and was presumed not to exist in the free state, until 2004, when graphene in a quasi-free state was isolated by a simple micro-mechanical cleavage method [6]. This discovery was awarded with the Nobel Prize in Physics in 2010.

Graphene is the thinnest compound known to human being at one atom thick (a million times thinner than human hair) and is also the lightest material known (one square meter coming in at around 0.77 mg).

The main reason for graphene to become such an interesting research subject is its outstanding and unique properties, which are directly related to the two-dimensionally spread C=C resonance structure and the hybridized electrons confined in it. It presents a thermal conductivity above 3000W/mK, which is dominated by the acoustic phonons. The physics of the two dimensional phonon transport raised up interest due to its exoticism, which led to research in many fields related with the thermal conductivity. It stands out the use of graphene as filler in polymers, what will be discussed in this thesis.

Additionally, graphene presents a room-temperature electron mobility of 2.5×10^5 $cm^2V^{-1}s^{-1}$with the ability to sustain extremely high densities of electric current (a million times higher than copper). Its intrinsic strength was determined experimentally to be up to 130 GPa and its Young modulus was measured in 1 TPa. A single graphene sheet, monoatomic, absorbs 2.3% of visible light, being its absorption virtually independent of the wavelength, what makes it optically active and observable by simple optical methods. Even different numbers of atomic layers can be determined for graphene in a transmission optical microscope [267]. It also presents a complete impermeability to any gases [157].

All this superlative properties of graphene make it suitable for its application on a wide variety of fields. It has already been successfully used in su-

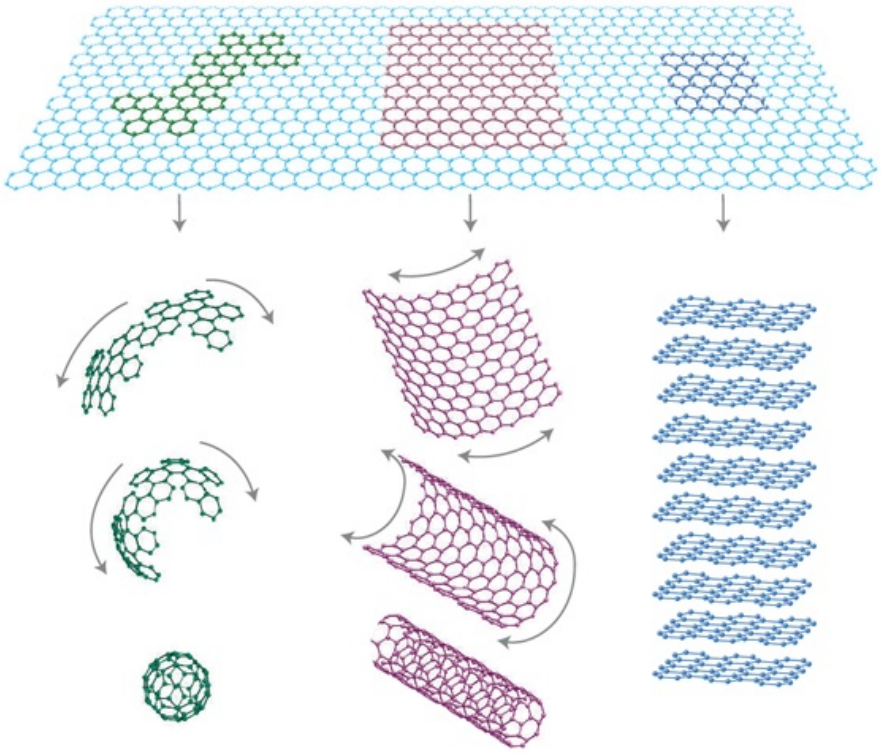

Figure 1.1: Graphene's two dimensional monolayer as a building material for 0D fullerenes, 1D nanotubes and 3D graphite [6]

percapacitors [261], in chemical sensors [118] and in corrosion inhibitors [177]. It also present great performance in photovoltaic cells [115], both as a conductive film [8] and as a counter electrode [42]. Graphene has been incorporated to nanocomposites [259] aiming not only the improvement on mechanical properties but also on thermal and electrical conductivity. Many energy storage devices based on graphene are being studied, including Li-Air batteries [270], Na-Air batteries [165] and fuel cells [240]. In the biomedicine field [56], graphene can be used in biodetection, drug distribution, regenerative medicine and implant surgery, and has been recently pointed as key piece for cancer diagnosis [48]. Furthermore, the combination of elasticity, transparency and electric-conductivity has a promising role in flexible electronics.

1.1.2 Why Graphene?

On the one hand, the importance and promising future of graphene make it stand out as a subject for research. The interest in graphene has arisen world-

wide in the recent years. The amount of publications related to this material grew drastically in the last decade and so did the industry around it, both for production of graphene and for the elaboration of graphene based materials and devices. Focusing on the magnitude of its impact in Europe, in 2013, the European Union Programme for Research and Innovation launched the Graphene Flagship [1], a visionary, science-driven, large-scale research initiative that aims to take graphene from the realm of fundamental science to industrial and societal applications. Up to 75 academic and industrial research groups involved in the project, with the participation of four Nobel Laureates and the funding of 1 billion euros [2], endorse the suitability of this extraordinary material.

On other hand, Tecnalia Research & Innovation has a great experience in studying graphene related nanoparticles, such as CNTs, for multiple fields and applications. Graphene shares many similarities in properties and structure with carbon nanotubes (CNT). They are even a precursor for the obtaining of graphene. CNTs were discovered by Iijima in 1991 [93] and have been widely studied since [51]. Their nanosize along with their mechanical, chemical, thermal and electrical properties attracted the interest of the scientific community for almost three decades. Tecnalia worked extensively on the research of CNTs, resulting on several PhD Thesis defended on this topic [10],[34],[70], the publication of dozens of articles and the participation in over 20 European Projects . Their similarities in structure and properties, makes it very interesting to take all the experience on CNTs and adjust it for its use on graphene.

The application of the mentioned knowledge and developments on CNTs to graphene in the fields of characterization, dispersion, functionalization and introduction into metal and polymer matrixes, would become the driver for this thesis.

1.2 Graphene synthesis

The market for graphene enhanced devices has great potential to take off, but until now, has been stymied by the cost of graphene synthesis (remains uneconomical for certain commercial applications), by the scaling and by the reproducibility. The industrial use of graphene will require large scale and cost-effective production methods, while providing a balance between ease of fabrication and final material quality. The synthesis methods are improving rapidly in effectiveness [250] and focus both on the decrease of the production costs and on the obtaining of defect-free high quality graphene. To date, many approaches for its production have being developed that can be classified in

two groups: The "Top-down" approximation, consisting in the obtaining of graphene from a bulk material, and the "Bottom-up" approximation, that consists on the growth of the carbon lattice atom by atom [157]. Ahead, the main methods are described:

"Top-down approximation"

Mechanical exfoliation: The first approximation consists in the mechanical cleavage and exfoliation of the graphene sheets from the bulk graphite. Liquid-phase mechanical exfoliation and micromechanical cleavage have been widely studied (this last one being worthy of a Nobel Prize in Physics in 2010). The mechanical cleavage allows obtaining large-area single-crystalline domains, with lengths on the order of micrometers [250]. However, these methods do not allow a true control of the number of layers, what has great impact on the final properties.

To overcome these limitations, the Hummers method [92] is employed, where the cleavage and the exfoliation come into action chemically instead of mechanically. Here, foregrounds the exfoliation of graphite oxide. It consists in the oxidation of graphite into graphite oxide using sulphuric acid in combination with $NaNO_3$ and $KMnO_4$. The oxidation breaks the two-dimensional π-conjugation of the graphene layers into nanoscale graphitic sp^2 domains surrounded by disordered, highly oxidised sp^3 domains and defects of carbon vacancies. The presence of the groups and the vacancies has a direct repercussion in the graphene properties, with great impact in the electrical conductivity. This graphite oxide can be then cleavage into one layered platelets by sonicating it in water or heating it rapidly so as solvent molecules and CO_2 in the interstitial spaces between the graphite oxide layers exert pressure to separate them. The obtained one layered platelets are known as graphene oxide (GO). It contains saturated sp^3 carbon atoms bounded to oxygenated functional groups, that cover epoxy, carboxyl and hydroxyl groups with a fewer presence of anhydrates, lactones, phenols, lactols, pyrones and ketones [14].This method is the most cost effective way to exfoliate bulk graphite but it requires an extra step of reduction to get to the graphene. The reduction process of the GO is usually made by thermal treatments (over 1000°C) or by chemical attacks.

Chemical reduction of GO: The complete reduction of GO to restore the graphene's sp^2 structure is, as already pointed, another way to obtain graphene. Many reduction agents have been studied in order to achieve an environmentally friendly, inexpensive method that allows the complete elimination of the functional groups present in GO. Hydrazine is used in N,N-dimethylformamide

[242] with great results. $NaBH_4$ has also been studied successfully [241] as well as hydroquinone on vigorous stirring at 80-100°C. However, these reduction agents, produce toxic waste, for what other alternatives such as vitamin C [275], [62], amino acid [41] and reducing sugar [282] have been developed. Wang and its coworkers presented a singular method were GO was reduced by making use of the reducing capability and the aromatic rings of tea polyphenol, present in green tea solution [247].

Liquid phase exfoliation: Is a cheap and easily scalable method that does not require expensive growth substrates. Graphite can be exfoliated in liquid environments exploiting ultrasounds to extract individual layers, in a process that requires: Dispersion, exfoliation and purification. Ideal solvents are those that minimize the interfacial tension between the liquid and the graphene flakes. Water has been used by itself [110] and with the assistance of surfactants such as SDBS [139], sodium cholate (SC) [82], sodium deoxycholate SDC [47], [89] and polymeric ones like pluronic [192] to stabilize the exfoliated graphene flakes against re-aggregation. N-methyl-pyrrolidone (NMP) was used by Hernandez et al to produce graphene [90] but the toxicity of the solvent hinders its use. The same problem appeared with N,N-Dimethylformamide (DMF) [103]. The exfoliation in ionic liquids have also been investigated, with the use o 1-butyl-3-methylimidazolium bis(trifluoro-methane-sulfonyl)imide ([Bmim]-[[TF2N]) [245] or 1-hexyl-3-methylimidazolium hexafluorophosphate (HMIH) [159]. Wang et al, reported concentrations over 5mg/mL for their process. The limitation of the phase exfoliation of graphite is the platelet size, since the exfoliation procedure induces in-plane fractures. To date, surface areas below $1\mu m^2$ [104], [232], [161] have been mostly reported [27].

Graphene from CNTs: The close relation between graphene and CNT allows it to be produced by the transformation of the nanotubes by several ways. The CNTs can be unzipped by using a chemical reaction to produce graphene [54]. They can be also coated by PMMA and unzip them using plasma processing [98]. Even the mechanical rubbing of multi-walled carbon nanotubes on micro-blades of glass has demonstrated to produce graphene sheets [39]. All these methods deepen on the similarities between both nanomaterials

"Bottom-up approximation"

Epitaxial growth on SiC substrates: The epitaxial growth is able to produce very high quality graphene up to ten microns, very suitable for electronics applications [250]. It grows over terraces of SiC, what limits the size of crystal size but can even overstep edges. Few layer graphene can be produced at

1200°C in few minutes [173]. Other substrates such as Pt, Co, Ru and Ir have been also studied [251], [52]. However, the high cost of the substrates and the requirement of highly specialized equipment and personnel still remain as the most remarkable limitations.

Chemical vapor deposition (CVD) and Plasma enhanced chemical vapor deposition (PECVD): The first successfully reported graphene films using CVD dates back to 2006 [208]. Several issues have been overcome and nowadays the CVD technique allows the growth of very large sheets of single layered graphene (75cm) and single crystals up to 1cm in diameter [250]. Despite not been able to satisfy the amounts of graphene required by the upcoming industry, is currently one of the best options for electronics and optical applications. A previous experience on CNT growing by CVD was used in the tunning of the conditions for graphene growth. The main difference is the catalysts, as the tubular shape of the CNTs makes it appropriate the use of nanoparticles where as the flat sheet of graphene requires the shape of a piece of foil [135]. PECVD offers two advantages compared to CVD: Lower growth temperature and lower deposition time. Graphene growth was claimed at 700°C on Fe_2O_3/Si substrate by Nang et al [237] by this method.

1.3 Present limitations on Graphene nomenclature

The isolation of graphene was reported just a few years ago, in 2004. The novelty of this material entails some difficulties with the standardization that have already been experienced in other nanomaterials.

Nanotechnology as a whole requires great efforts in order to standardize the processes, materials, characterizations and synthesis around it. The International Organization for Standarization (ISO) has only published 48 standards related to the nanotechnology topic[5]. In the case of CNTs, for example, several years were needed until the ISO presented the first standards for them and nowadays there are still many standards under development. Graphene, of course, is not an exception.

The standardization of graphene is a main topic in international conferences [4]. The Graphene Flagship announced in 2015 the creation of a standardization committee that will deliver a publication regarding standard methods and characterizing graphene, in 2016. In the words of Graphenea, one of the graphene producing companies of the standardization committee: <<The end goal of the standardization effort is to produce a database of the various forms

of graphene with all their properties and ways of measuring those properties, so that graphene sellers can properly categorize their products and buyers can know exactly what they are about to buy>>.

The remarkable variety of graphene-like materials also triggers difficulties. Different sheet-like, flake-like or two-dimensional carbon forms have gathered great interest in the recent years. Despite its similarities, these materials present important differences in layer number, lateral dimension, rotational faulting and chemical modification, being of great importance the proper definition of the material when presenting results. To date, the term "graphene" has been widely used for this sheet-like and flake-like carbon structures, including multilayer structures and structures with functional groups and non-carbon atoms.

To this regard, in 2013, the international editorial team for Carbon magazine published a nomenclature proposal for two-dimensional carbon materials [22]. The nomenclature used in this thesis is based on this proposal. The main definitions given by this team are as follows:

Graphene :<<A single-atom-thick sheet of hexagonally arranged, sp^2-bonded carbon atoms that is not an integral part of a carbon material, but is freely suspended or adhered on a foreign substrate. The lateral dimensions of graphene can vary from several nanometers to the macroscale. Note with this definition, other members of graphene family of 2D materials cannot be simply called "graphene" but must be named using a unique multi-word term that distinguishes them from the isolated monolayer>>.

Graphene layer : <<A single-atom-thick sheet of hexagonally arranged, sp^2-bonded carbon atoms occurring within a carbon material structure, regardless of whether that material structure has 3D order (graphitic) or not (turbostratic or rotationally faulted). The "graphene layer" is a conceptual structural unit that has been used for many years to describe the structure and texture of 3D carbon materials with primary sp^2-hybridized bonding.>>

Multi-layer graphene (MLG): << A 2D (sheet-like) material, either as a free-standing flake or substrate-bound coating, consisting of a small number (between 2 and about 10) of well-defined, countable, stacked graphene layers of extended lateral dimension. If the stacking registry is known it can be specified separately, such as "ABA-stacked multi-layer graphene", "Bernal-stacked multi-layer graphene" or "rotationally faulted multi-layer graphene">>.

Graphite Nanoplatelets (GNP): <<2D graphite materials with ABA or ABCA stacking, and having a thickness and/or lateral dimension less than 100 nm. The use of nanoscale terminology here can be used to help distinguish these new ultrathin forms from conventional finely milled graphite powders, whose thickness is typically >100 nm. An acceptable alternative term is "ultrathin graphite", though "ultra" is less specific than "nano" in describing the maximum thickness.>>

Graphene Oxide (GO): <<chemically modified graphene prepared by oxidation and exfoliation that is accompanied by extensive oxidative modification of the basal plane. Graphene oxide is a monolayer material with a high oxygen content, typically characterized by C/O atomic ratios less than 3.0 and typically closer to 2.0>>.

Reduced Graphene Oxide (rGO): <<graphene oxide (as above) that has been reductively processed by chemical, thermal, microwave, photo-chemical, photo-thermal or microbial/bacterial methods to reduce its oxygen content>>

Despite all the current efforts towards the standardization of graphene and graphene-derived materials, their exhaustive characterization is an unavoidable step when researching in related topics, whether they have been purchased as if they have been lab-made. Accordingly, **the second chapter of this thesis will focus on the characterization of the graphene-like materials that will be used later.**

1.4 Graphene Dispersion

Graphene presents outstanding properties that have already been mentioned. These properties are closely related to the 2D structure of a monolayer and vary with the stacking of additional graphene layers. For example, the surface area, a key factor for the use of graphene as a catalyst support, is measured in $2630 m^2/g$ [238] for a single sheet but rapidly decreases as more layers are stacked. Its electronic properties also undergo changes. The monolayer is considered an intrinsic semiconductor with a linear Dirac-like spectrum around Fermi energy, the bilayer can also be considered a semiconductor with one type of electron and one type of hole but for three and more graphene layers, the band structures become increasingly complicated along with the appearance of several charge carriers and large overlaps of conduction and valance bands [263]. Regarding the optoelectronic properties, the transmittance linearly decreases with the number of layers [210]. Finally, the thermal conductivity also decreases

with the number of layers, as described by S. Gosh et al [78]. Obviously, the impact of these variations on the performance of graphene-based applications can be dramatic.

As a single sheet of carbon atoms with a π-electron cloud over it, graphene has a strong tendency to agglomerate with other graphene sheets. The structure of the sp^2 hybridized orbitals generates important π-π interactions between different graphene layers. These interactions, added to the Van der Waals forces, set a forming tendency towards aggregations of hundreds of sheets which no longer present a nano-sized dimension, very similar to the well-known graphite structure.

This drawback is usually overcome by the dispersion of graphene in liquid medium, where it remains stable and un-stacked. Stabilized graphene dispersions in an appropriate solvent do not only avoid the reaggregation of the separated graphene monolayers but will also prevent inhalation related hazards, a big concern in mass production of nanomaterials. Many approximations have been developed in this area, attaining interesting results with a great variety of techniques. All these approaches could be summarized in three main groups of direct dispersion of the graphene: Solvent dispersion without stabilizers, Chemical functionalization of the graphene and Surfactant-stabilized graphene exfoliation [223].

Solvent dispersion without stabilizers: Graphene is exfoliated in a particular solvent in the absence of any surface modifying agent, surfactant or polymer. Generally, the graphene is added into the solvent and some kind of sonication is applied (bath or tip). The sonication provides high energy activation, which is needed to overcome the interlayer adhesion. The extent of exfoliation is known to increase with the sonication time [223]. Then, the dispersion is centrifugated in order to separate the well dispersed fraction from the non-stable one, what usually leads to the loss of an important amount of the graphene. The use of solvents that present affinity with the graphene surface will lower the surface tension and will be more suitable from a wetting perspective. Some solvent molecules can adsorb on the graphene surface whereas other will stand around the graphene sheet and solvate it. Both effects help to overcome the binding energy between graphene surfaces that make them tend to aggregate. Coleman and its group presented a method were this whole process is repeated with lower centrifugation speeds each time in order to obtain graphene sheets of larger dimensions [105]. Aida and Fukushima et all. used ionic liquids (1-hexyl-3-methylimidazolim hezafluorophosphate) to exfoliate graphene at a weight concentration of 0.53% [69],[191]. Other groups experimented with various water/DMF ratios and water/alcohol mixtures reaching about 0.1% by

weight and 10-20μg/mL respectively [283], [265].A single-atom-thick sheet of hexagonally arranged, sp^2-bonded carbon atoms that is not an integral part of a carbon material, but is freely suspended or adhered on a foreign substrate. The lateral dimensions of graphene can vary from several nanometers to the macroscale. Note with this definition, other members of graphene family of 2D materials cannot be simply called "graphene" but must be named using a unique multi-word term that distinguishes them from the isolated monolayer.

Chemical functionalization of graphene: Chemical functionality is produced on the graphene surface promoting solvation and exfoliation. The wide field of graphene functionalization has offered many possibilities to overcome graphene's limitations. Focusing on the dispersion field, covalent modifications, non-covalent modifications and atom substitutions have been studied as beneficial for a correct dispersion. The addition of certain functional groups or atoms can facilitate the correct incorporation of the hydrophobic graphene monolayers to multiple matrixes, increasing its affinity for that medium. The most common approximation consists in the oxidation of graphene to graphene oxide. The presence of a great variety of functional groups containing oxygen facilitates the solvation in some solvents. Furthermore, the product of the reduction of the graphene oxide, the reduced graphene oxide, restores the structure of the graphene but preserves some of the functional groups. For stable dispersions in water oxygen contents of 13-16% by weight were found to be needed, whereas 5-10% were required in nonaqueous ones like isopropanol [223]. Successful rGO concentrations up to 1.5% (w/w) have been reported [231].

Surfactant-stabilized graphene exfoliation: Based on the utilization of surfactants, polymers and other agents that physically adsorb onto graphene surfaces and stabilize them in given solvent against flocculation. Its most significant aspect is a strong interaction of the surfactant with the graphene surface [223]. The graphene sheets, once dispersed by an energy input, tend to reaggregate due to the attractive van der Waals forces from their surfaces when this energy ceases. The surfactants, when adsorbed on the graphene, provide steric hindrance and obstruct the reagglomeration of individual sheets. When ionic surfactants are used, not only influence the steric factors but also the electrostatic repulsion between graphene sheets with adsorbed surfactant. Sodium cholate and sodium deoxycholate both have been widely used, with the last one presenting five times more effectiveness (2.6g/mL) [183]. For docecyltrimethylammonium bromide, tetradecyltrimethyl ammonium bromide, hexadecytrimethylammonium bromide, sodium dodecylsulfate and pluronics F127 and F108 graphene concentrations of 0.5% to 1.0% w/w have been reported [156]. The stability of the graphene-surfactant dispersions will be influenced

by the amount, charge and morphology of the adsorbed surfactant, being still a topic of controversy the determination of which surfactant leads to better results [223].

Graphene dispersion is still a research topic, in particular figuring out the most cost efficient way to achieve scalable dispersion procedures [225].

Notwithstanding dispersions are one of the most extended ways to work with graphene and other nanomaterials, also present their own disadvantages that must be solved. The main problem when handling graphene dispersions comes from the instability of the suspended graphene. It tends to precipitate over time, what leads to notorious differences in graphene concentration for aliquots taken from the same dispersion. In addition to the dispersion techniques just explained, there are two other factors that have great impact on the stability of the dispersions: The solvent and the eventually employed surfactant.

The solvent choice opens a wide range of possibilities. Different applications require graphene to be dispersed in different solvents, for what many authors have worked towards this field. Shih C-J et al presented the results from molecular dynamics simulations for various polar solvents and the thermodynamic effect when stabilizing graphene [198]. Water, dimethylformamide (DMF), N-methyl pyrrolidone (NMP), γ-butyrolactone (GBL) and dimethyl sulfoxide (DMSO) were studied to estimate the relative resistance to aggregation that these solvents provide to graphene. Water proved to be the less effective stabilizer, followed by GBL and DMF. DMSO and NMP yield the best results. Khan U et al reported high concentration graphite dispersions in NMP up to 6% by weight, but displayed pronounced lack of stability [107]. However, they stated that the instability of the dispersions could be beneficial to certain applications. Different solvent mixtures have also been tried with various results. 2-amino-2-methyl-1-propanol (AMP) in combination with water reached a 0.03% graphene in weight according to Zhang H et al [273]. Zhu L et al reported graphene dispersions up to 0.1% in weight for certain DMF:water ratios [284]. Water/alcohol mixtures were studied by Yi M et all. yielding concentrations between 10-20μg/mL when using ethanol and isopropanol [266]. Jiantong Li et al even reported concentrations up to 0.39mg/mL for graphene dispersions in terpineol using a simple distillation process from a previous DMF graphene dispersion [126]. Nevertheless, despite these promising results towards organic solvents, water is catching great attention for stabilizing graphene dispersions, mostly for the interest in minimizing the use of volatile organic components in industrial processes, in order to avoid environmental hazards from its atmospheric emissions.

Regarding the surfactant, its choice would also depend on the application, as they present different chemical nature. Surfactants can enclose the graphene surface and provide steric or electrostatic repulsions to avoid the close contact between different layers. Most surfactants consist of a hydrophobic tail group and a hydrophilic head group. The mentioned repulsions will depend on the nature of the head group: Non-ionic surfactants have a polar head group (electrostatic repulsions) and ionic surfactants have an ionic head group (various repulsion sources) [206]. A great variety of studies have been carried out for the surfactant-stabilized graphene exfoliation [223] due to the availability of the materials and methods involved. Regarding the cholate family, Sun Z et all obtained a stable dispersion of graphene in water using sodium taurodeoxycholate as surfactant and claimed to reach a 0.71% of graphene in weight [218]. Ramalingam P et al, compared sodium cholate and sodium deoxycholate, the last one resulting five times more effective and reaching stable graphene dispersions up to 0.26% in weigth [184]. [Bis(2-ethyhexyl)sulfosuccinate, sodium salt] (AOT), octadecylamine (ODA) and ethylhexadecyldimethyl ammonium bromide (EDMB) were reported by Ioni Yu V et al to permit dispersions between 0.02% (w/w) and 0.05%(w/w) [94].Buzgaloet al reported results for a wide variety of surfactants: TX-100 and Pluronics P65, P84, P103, D127 and P123 as non-ionic, sodium cholate and sodium dodecyl sulfate as anionic and didecyldiethylammonium bromide and hexadecyltrimethylammonium bromide as cationic surfactants. The resulting dispersions for all these compounds presented concentrations between 0.03 and 0.18mg/mL [29]. Parvizet al studied 1-pyrenecarboxylic acid ($PyCO_2H$),1- pyrenebutyric acid (PyBA), 1-pyrenesulfonic acid sodium salt ($PySO_3H$) and 1,3,6,8-pyrenetetrasulfonic acid tetra sodium salt($Py(SO_3)_4$) resulting in dispersions between 0.1 and 0.7 mg/mL [169]. $PySO_3Na$ was compared to sodium dodecyl benzene sulphonate (SDBS) and polyvinylpyrrole, obtaining a five-fold higher dispersion of graphene for the SDBS.

Tecnalia has a large experience in nano-materials related research projects. The difficulty and importance of obtaining stable dispersions of well-known concentration of nanoparticles became clear in plenty of them. Furthermore, the research developed in this thesis required the use of graphene-like materials in liquid medium. Thus, **the study of the factors that must be handled to successfully achieve stable graphene dispersions and the conditions that lead to the optimization of these dispersions would be carried out and presented in Chapter 3.**

1.5 Graphene Functionalization

It has already been described how graphene presents a set of properties with an overwhelming potential for its application in several fields. However, some of its drawbacks, such as low dispersibility in organic solvents, inertness to reaction and zero band gap, limit its utilization. Some applications require these drawbacks to be overcome and some of the properties to be tuned. Functionalization of the carbonaceous structure of graphene is a path with a wide variety of possibilities. For this reason, there has been a huge increase in the number of research projects aimed at functionalization of graphene. Multiple attempts from different perspectives have been reported, that can be summarize in four main groups.

1.5.1 Covalent bonding

In a first group the functionalization by covalent bonding is contemplated. The main objectives aimed with this kind of functionalization are the improvement of the dispersibility of the graphene sheets and the addition of new properties related to the added groups. Functionalization of the carbon atoms in the lattice generaly perturbs the extended aromatic character of the graphene, enabling the control of its electronic properties.

This type of functionalization over pristine graphene includes the formation of covalent bonds between free radicals or dienophiles and the C=C bonds of the graphene. Diazonium salt and azomethine ylide are examples of reactives for each case. Graphrene Oxide presents an interesting alternative in the covalent bonding functionalization due to the multiple functional groups present on its surface, as stated in previous section. The wide chemistry of the epoxy, carboxyl and other groups on the GO allows the addition of chromophores, the covalent link to polymers and the addition of other organic molecules [77], [36].

1.5.2 Non-covalent bonding

The non-covalent functionalization of graphene techniques, form a second group. Different organic compounds are used in order to interact with the π-system of the graphene without disturbing its electronic network. This network is intimately related to the structure and thermal and electrical conductivities of the graphene sheets, therefore any disruption of it can lead to dramatic effects. These non-disruptive non-covalent functionalization techniques involving π-systems are pivotal to the stabilization of proteins, enzyme-drug complexes,

DNA-protein complexes, organic supramolecules and functional nanomaterials. Non-polar Gas-π interaction, H- π interaction, π- π interaction, cation-π interaction, π_{cation}- π interaction, anion- π interaction and graphene-ligand non-covalent interaction end the variability of the non-covalent functionalizations described up to date [77], [36].

1.5.3 Substitutional doping of graphene

The third group consists on the substitutional doping of graphene. It consists on the substitution of some of the carbon atoms from the honeycomb lattice by other ones, boron or nitrogen atoms mainly. The difference in electrophilic character in these atoms makes the doped graphene sheets to exhibit an n-type behavior or a p-type behavior. Furthermore, the control in the degree of the doping modification can be used to adjust the electrical properties of the graphene, thereby expanding remarkably the application of the graphene in nanoelectronics.

The N-doped graphene is the most studied one. The N can be incorporated in situ by CVD, arc discharge or solvothermal methods or during reduction, and replaces an O or C atom. N atoms use their three sp3 orbitals to incorporate into the sheet, what makes their lone pair electrons to conjugate with the graphitic π-system, leading in last place to an electron-rich graphene sheet with an n-type semiconductor behavior [118], [77].

1.5.4 Functionalization of graphene sheets with nanoparticles

In the last place goes the functionalization of graphene sheets with nanoparticles, which is one of the widest groups and most extensively studied. It is based on the dispersion of metallic or metal-oxide nanoparticles over the surface of graphene sheets. It presents great variety of applications in catalysis, optoelectronics and energy storage devices such as fuel cells, batteries and supercapacitors. The large active surface area per mass unit of the graphene among with its mechanical strength and high conductivity makes it an ideal substrate. Despite the difference in conductivity when compared to the pristine graphene, GO and rGO also stand out as great substrate for nanoparticle support.

Precious metal nanoparticles and quantum dots are both usually used for this functionalization. In the first case, the precursors tend to be metal salts, reduced in solvents that contain pristine graphene, GO or rGO and have a

great applicability in catalytic and magnetic materials. The quantum dots, in the second one, can be supported by reduction or spin casting processes and have a great interest in biological labeling, solar cells and light emitting devices. In the field of nanoparticle support, however, the deposition of metal oxide nanoparticles becomes particularly relevant due to the low cost and great availability of most of the employed metal oxide precursors. Tin oxides, cobalt oxides, titanium oxides, manganese oxides are widely used in applications in energy storing devices. They are usually synthesized by reduction processes, which must be closely controlled because of the great impact that different dispersion degrees over the sheet and different morphological structures can have in its final performance [77].

Functionalization processes with metal and metal-oxide nanoparticles are studied in Chapter 4 of this thesis. There are three different materials that result of particular interest,, for their great use in many applications and for the broad experience reached by Tecnalia with them: Cu, ZrO_2 and MnO_2.

Copper nanoparticles

Graphene and graphene derivatives have been used extensively in combination with copper for multiple applications and there are already hundreds of publications to this regard. The synergy between both materials can be obtained by ball-milling them, ultrasonicating them together in a solvent, growing graphene on copper substrates. However, few studies have been carried out for the plating of Cu nanoparticles over graphene-like materials by electroless method.

Xiao-Wing et al [137] presented in 2011 a study with several metal plated over graphene by electroless method, including Cu. In 2014, Chao Zhao et al [281] used the same technique to cover GNP with copper and introduced it in a Cu matrix, forming a GNP/Cu composite. They presented enhancements in tensile strength and Young modulus by 107% and 2% respectively, in 1.3%wt. Y. Peng and colaborators [172] presented a two-dimensional copper/reduced graphene oxide nanosheets nanocomposite. They effectively fabricated it by an ultrasound-assisted electroless copper plating process. They reported that the effect of ultrasound on electroless enhanced several features, including, the interfacial bonding, a key factor in the elaboration of graphene metal matrix composites (MMCs). Recently, Dadan Zhong et al [272] also fabricated Cu covered GNP by the electroless method and claimed that composites with the addition of 0.5% Cu-GNP exhibited an increase of 49% in yield strength when compared with pure Cu.

Zirconia nanoparticles

Graphene and other carbon allotropes are being studied in conjunction with zirconia (ZrO_2) too. Zirconia is a versatile oxide largely employed in many applications. It can be synthesized by a simple hydrothermal method [175], which shows important advantages from a kinetic, thermodynamic and technological point of view [174]. Nanoparticles of zirconia have been synthesized and characterized [20], [58] for many applications such as catalyst [30] and medical biosensors [74] even in combination with other metal oxides.

The combination of both carbon derived nanomaterials and zirconia is exploited in two different approaches: The nanocarbonaceous materials can be used as nanofillers into zirconia composites or they can be used as support for the growth of zirconia nanoparticles over its surface. Carbon nanotubes have also been extensively characterized and employed. Garmendia et al presented several studies regarding the synthesis of zirconia in the presence multiwalled carbon nanotubes (MWCNT) [72], [75] and the covering of MWCNT by zirconia [73]. They also studied the slip casting of nanozirconia/MWCNT composites using a heterocoagulation process to facilitate the dispersion of the nanotubes along the matrix [76]. Single walled carbon nanotubes were used as reinforcement in yttria stabilized zircona ceramics by Jung-Hoo Shin and Seong-Hyeon Hong [199] and MWCNT-zirconia composites were also studied by L. Melk et al reaching interesting results in the decrease of the wear rate [150]. The introduction of graphene as a reinforcement has also led to notable improvements on mechanical properties. F. Chen et al published an increase of a 61% in the fracture toughness of a graphene reinforced zirconia ceramic with a 0.01wt.% of graphene platelets [37]. H. Li and collaborators reinforced a zirconia coating with graphene nanosheets (1 wt.%) obtaining a 50% wear rate reduction and a decrease of 29% on the friction coefficient [125]. N. Laidani et al. characterized back in 2008 zirconia-carbon nanocomposite films [119].

As an example of the use of the graphene-like materials as support for zirconia nanoparticles, the work of J. Gong and his team can be mentioned. They synthesized zirconia nanoparticles over graphene nanosheets for a methyl parathion sensor [79]. The fields of sensors and medical applications are the main focuses of this kind of nanomaterials. Later, Teymourian et al [227] presented a hydrothermal method for the decoration of rGO with ZrO_2 nanoparticles, also for its performance as electrochemical sensing and biosensing platform. The hydrothermal method stands out for its simplicity and good results, and can be used not only for ZrO_2 but also for other metal nanoparticles [162].

Manganese Oxide Nanoparticles

Manganese oxide has been extensively studied for its catalytic activity. It is commonly used in electrochemistry and biological sensing due to this property. The term "manganese oxides", represented as MnOx, includes several compounds depending on the oxidation state of the manganese (MnO_2, MnO, Mn_2O_3). There are several synthesis methods for obtaining manganese oxide but the hydrothermal process is one of the most extended ones. The hydrothermal synthesis tends to favor obtaining MnO_2 but further oxidations states can be obtained by heat treatments [83]. They present their own crystal structure and some of them can even present different crystal phases. These crystal phase and crystal structure variations have to be considered when synthesizing manganese oxide, as they can affect the properties of the nanoparticles.

In order to enhance the properties of manganese oxide, it is combined with multiple carbonaceous supports, such as graphite [127], active carbon [114], CNT [67], carbon xerogel [164], GO [95], rGO [271] and of course, graphene [256]. Mixing these oxides with carbon materials adds conductivity, which is one of their main drawbacks.The MnO_x/C composites are extensively used in metal-air batteries, supercapacitors and fuel cells, as the manganese oxide play an important role on the Oxygen Reduction Reaction (ORR), key in these applications.

The functionalization of graphene-like materials by the controlled growth of metal and metal oxide nanoparticles will be studied in Chapter IV of this thesis. Copper, zirconia and manganese oxide nanoparticles will be grown and the resulting composites will be characterized. Furthermore, as the functionalization processes are always very oriented towards specific applications, their performance as metal matrix composites (Cu, ZrO2) and ORR catalyst (MnOx) will be also studied.

1.6 Graphene-Polymer Nanocomposites

1.6.1 Thermal properties of graphene and derivatives

Graphene, CNTs, graphite and similar carbon allotropes present an elevated basal plane thermal conductivity product of the strong covalent bonding between carbon atoms, their light atomic weight and their large crystalline domains. Graphene was the last one to be measured and was expected to present

the highest thermal conductivity. A non-contact Raman optothermal technique was used in UC Riverside for the first experimental studies of thermal conductivity of graphene, performed over large-area suspended graphene layers exfoliated from high-quality bulk graphite. The results showed that the thermal conductivity K can exceed 3000 W/mK near room temperature when large enough graphene flakes are measured [193].

In addition to the experimental measurements, fundamental thermal transport studies are highly relevant. Many groups have reported results on molecular dynamic simulations for thermal transport in graphene. These simulations require huge computational calculations, since in many cases the number of atoms has been decreased and the simulated domains are smaller than the micron scale phonon-phonon scattering mean free path. Due to the mentioned limitations, the calculated conductivity values vary between 50 and 9000 W/mK [189].

Table 1.1: Summary of the thermal conductivity values measured for different carbon allotropes at room temperature [88], [189]

Carbon Allotrope	Thermal Conductivity (W/mK)
Graphite	100-2000 (on plane)
Carbon Black	6-174
CNT	2000-6000
Diamond	2000
Graphene	50-9000

High basal plane thermal conductivity in graphene is dominated by the contribution from phonons, the energy quanta of lattice vibration waves. The phonon mean-free path for graphene was estimated in 775nm for room temperature. Due to the absence of interlayer phonon scattering in suspended monolayer graphene, it shows higher intrinsic basal plane thermal conductivity than that of graphite, what was confirmed by the thermal conductivity measurements at UC Riverside. The presence of additional layers in the graphene structure tends to reduce the values achieved for the monolayer: MLG, with an approximately 7 to 10 atomic planes of graphene, retains the outstanding thermal properties of the single layered graphene, whereas graphite, with up to infinite atomic planes of graphene, exhibits a thermal conductivity of 2000 W/mK at room temperature [189].

The conductivity is not only reduced by the aggregation of several layers but also by other factors that can cause a disruption in the electron cloud, such us: The functionalization of the graphene layers; the formation of covalent bonding

between the graphene and a polymer matrix or the support of graphene on a substrate. For example: 1) The 3000W/mK thermal conductivity for pristine graphene when suspended drops to approximately 600 W/mK when supported on a SiO_2 substrate [194], [193]. 2) X. B Li et al and K. D. Bi and collaborators have predicted that both compressive and tensile strains can suppress thermal conductivity up to 44% for 8% strain[21][128].

Once again, the diversity of results obtained for similar materials by different groups, when approaching the thermal performance of graphene derivatives, makes it clear that it is necessary to deeply characterize their nanostructure, sizes, thicknesses and atomic compositions. When facing the study of the applicability and performance of certain graphene-like material it is mandatory to evaluate its structure and morphology

1.6.2 Graphene and derivatives in epoxy resins

The impressive thermal and mechanical properties of graphene made it to be a clear target for research in the composite field. As filler, it is expected to lead to a significant improvement in the performance of many epoxy and polymer matrixes. Its great surface to volume ratio is desirable for its use as nanofiller, to enhance the thermal conductivity of polymer composites; although it is known that contact of graphene with an amorphous solid or organic matrix can suppress phonon transport.

The first detailed study of the morphology and properties of an exfoliated graphite nanocomposite was published by Pan Y. X. et al [166], dispersing platelets of 10nm thickness by an in situ polymerization of caprolactam. As the researches advanced, the distinction between graphene, graphite, GNP and multilayered graphene (MLG) proved to be necessary. This discrimination is needed as composites with nanofillers tend to show property enhancements at much lower loadings than those composites with micron-scale fillers . In the thermal conductivity research, it is generally accepted that graphene-like materials with a maximum of 10 layers will present a behavior close to pristine graphene .

In order to make the most out of the properties of nanomaterials and nanofillers it is necessary to use well defined methods that lead to appropriate dispersion and exfoliation when introducing them into epoxy matrixes. Furthermore, for most applications, a large-scale inexpensive production must be achieved in order to become interesting for industrial purposes.

For the incorporation of pure carbon materials such as graphene into polymer matrixes, three main approaches have been developed:

Solvent mixing: It consists in the mixing of colloidal suspension of graphene platelets with the chosen polymer. The polymer can be already in a solution itself or be dissolved into the colloidal suspension. Then, the suspension can be molded into a cast and the solvent removed, by evaporation for example. This technique, however, can cause the graphene to re-aggregate during the solvent elimination process, spoiling the composite‘s final properties. Thus, alternatively, using a non-solvent for the polymer, its chains can be precipitated causing the graphene to get encapsulated. Both processes can bring on the restacking of the graphene platelets. Some authors have employed surfactants to avoid this phenomenon and to facilitate the mixing . Nevertheless, the use of surfactants can affect many of the final composite properties.

In situ polymerization: In this process, the graphene filler is mixed with the required amount of monomers or a solution of monomers. Later, the monomers are polymerized in the presence of the graphene. In some cases, the polymerization process can be used to achieve the exfoliation of graphite [202], as the monomers get intercalated between graphene layers in the graphite. Good exfoliation levels have been reported with these techniques [201], [38], although isolated monolayers have yet to be achieved.

Direct mixing: This method consists in the direct addition of the graphene to the polymer matrix and the application of shear mechanical forces. Calandering and high shear mixing are the most used techniques for accomplish the required shear forces, both on its own or by a combination of both. S. G. Prolongo et al [178] presented a complete study of the application of these in situ processes to a GNP-Epoxy composite . They added 0.5wt% GNPs to an epoxy resine and applied three different shear conditions: Calandering, High-shear mixing and the combination of both; recommending the use of calander in front of high shear mixing, and not finding any advantages in the combination of both.

Finally, once the filler is dispersed, the morphology of the nanocomposite‘s microstructure would determine the enhancement of the final properties. Graphene and other graphene derivatives, present a layered structure that can be compared to certain silicates which have been widely investigated as composite fillers [170]. Three general states of platelet dispersion on short length scales have been suggested for these nanoclay-based composites: Phase separated, intercalated and exfoliated. Figure 1.2 roughs out the different morphologies.

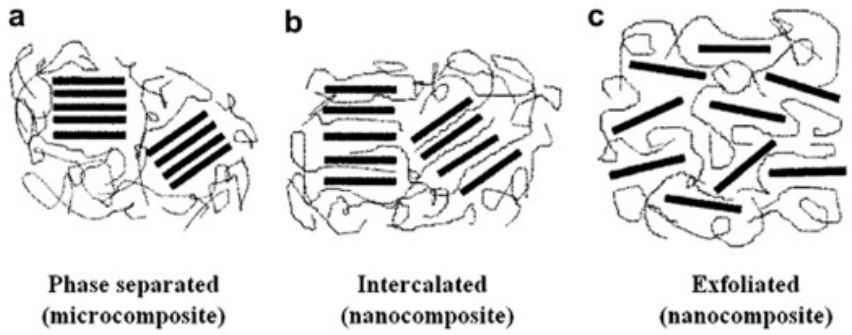

Figure 1.2: Scheme of three possible types of composite from the interaction of graphene and polymers: (a) phase- separated (b) intercalated and (c) exfoliated [7]

The higher the affinity of the graphene for the matrix, the more extended conformation they will adopt. Insufficient exfoliation will favor, on the other hand, the formation of large agglomerates and possibly a separated phase.

1.6.3 Fundamentals of Rheology characterization

The most used rheological techniques to study carbon nanofiller/epoxy nanocomposites are small amplitude oscillatory shear flow measurements. They have already been applied with great success for the study of CNT/epoxy nanocomposites by Chapartegi in her PhD thesis [34]. Typically these measurements involve a sample which is contained between two parallel plates (or between a cone and a plate), one part undergoing a small amplitude oscillation with a frequency (ω). The main feature to be noted is that the shear stress (σ_{21}) and the shear strain γ_{21} oscillate both with the same frequency, but with a phase difference of an angle δ. This angle is a key parameter to disclose the viscoelastic response of materials, since for an ideal elastic solid δ is 0 radians, whereas for merely viscous liquid δ takes a value of $\pi/2$.

The application of the general model of the linear viscoelasticity leads to define the following dynamic viscoelastic functions [24]:

Elastic or storage modulus (G'):

$$G' = \frac{\sigma_{21}^{o}}{\gamma_{21}^{o}} \cos\delta$$

Equation 1.1:Elastic modulus (G') according to the linear viscoelasticity model.

Viscous or loss modulus (G"):

$$G'' = \frac{\sigma_{21}^{o}}{\gamma_{21}^{o}} sen\delta$$

Equation 1.2:Viscuous modulus (G") according to the linear viscoelasticity model.

Complex shear modulus (G∗)

$$G^{*} = G' + iG''$$

Equation 1.3:Complex shear modulus (G∗) according to the linear viscoelasticity model.

Loss tangent (tanδ):

$$\tan\delta = \frac{G''}{G'}$$

Equation 1.4:Loss tangent (tanδ) according to the linear viscoelasticity model.

Complex viscosity (η∗):

$$\eta^{*} = \eta' + i\eta''$$

Equation 1.5:Complex viscosity (η∗) according to the linear viscoelasticity model.

The knowledge of the rheological properties of epoxy nanocomposites is fundamental for both their processing and the comprehension of their microstructure and dynamics. The rheological characterization also provides information about the formation of nanofiller structures and helps to optimize the thermal conductivity enhancement, as it will be further described in Chapter 5.

1.6.4 Application development: Thermal Interface Material

There are dozens of fields where the Epoxy/Graphene-like composites have great applicability. The combined characteristics of both materials make them suitable for a wide range of conditions and requirements. In first place, for similar outcomes, the use of a non-precious material such as graphene reclaims the attention of the global industry. Furthermore, its properties exhibit a potential that has yet to be admeasured. For now, graphene-based polymer composites are being studied for applications in energy storage devices[230], field effect transistors[57] and solar cells[213] among others. Taking advantage of the described thermal conductivity properties, researchers found in thermal interface materials (TIM) a great application for graphene- based epoxy composites [194].

The last chapter of this thesis will focus on their application as TIM. To evaluate its applicability as TIMs, it will be necessary: 1) To set the conditions for the successful introduction of the carbonaceous nanofillers into the epoxy resin. 2) To analyze the effect of different graphene-like nanofillers, different concentrations and different dispersion methods on the thermal conductivity of the final composite. 3) To study the rheological properties of the most promising sample to understand the behavior of the nanofiller inside the resin, its percolation limits and its handling conditions.

Chapter 2

Characterization of graphene and its derivatives

2.1 Approach Objectives and Experimental details

2.1.1 Approach

It exists an enormous variability inside the so called "graphene-like materials". They present big differences in size distributions, number of layers, lattice defects and even chemical composition. Furthermore, depending on the provider and the product, they can be supplied as isolated monolayers, in powder form or dispersed in some solvent forming a slurry. In Chapter I the description and nomenclature for some of the most relevant ones was presented. However, up to date, they are still not standardized, for what the characterization of these materials before employing them in further research is essential.

There are plenty of analysis tools that are used by researches in the characterization of graphene and graphene derivates [136]. In the first place, for the morphological characterization, Atomic Force Microscopy (AFM) and Scanning Electron Microscopy (SEM) are the most extended techniques.SEM images provide visual information about the form, shape and surface sizes of the platelets whereas AFM is mostly used to measure their thickness[124]. Paredes and its groups presented a study where pristine graphene and GO are differentiated by the thickness of their layers, as the functional groups interacted differently with the AFM tip than the carbon atom lattice. Transmission Electron Microscopy (TEM) is also employed: not only it offers morphological information about the sample but also allows measuring the total number of layers in a sample [112]. This technique was used by Hernandez et al. to accurately determine the thickness of graphene.

For the characterization of the structure and the evaluation of defects, X-ray diffraction and Raman spectroscopy are widely employed. The XRD creates a diffraction pattern characteristic of the studied substance that, in the case of graphene-like materials, is indicative of its interplanar distance and provides information about the amount of defects in the lattice. Raman spectroscopy, on the other hand, not only allows to clearly differentiate between graphene, GO and rGO, but also permits to evaluate the presence of defects in the carbon atom lattice[158],[112] , [116], [31] and presence of doping atoms [49] For graphene samples with few, it even allows to determine their number and orientation [65]. To this regard, UV-Visible spectroscopy is also used and has recently proved being able to provide information of the number of layers in a graphene sample. Z. Sun et al. [219] reported significant drops in transmittance from monolayer graphene to bilayer graphene and even higher for a six-layer graphene.

In this Chapter, a complete characterization of the four materials presented in the experimental details is aimed (Graphenea rGO, Graphenea GO, SkySpring GNP and AvanGraphene GNP). These graphene-like materials are used widely along the thesis and it is necessary to study their structural and morphological characteristics in order to predict their behavior and to evaluate their suitability for different applications. All the knowledge acquired about the samples in this Chapter would facilitate enormously the interpretations of results in further studies. AFM, XRD, Raman spectroscopy and Field Emission Scanning Electron Microscopy (FE-SEM) are used to characterize the four samples.

Due to the laminar structure of graphene-like materials, consisting in thousands of nanoplatelets, their performance in different applications would not only depend on their bulk properties, but also on the characteristics of those platelets. For the analysis of the particular properties and structure of individual platelets, a more selective methodology is needed. Aiming further comprehension of their nature and their particularities, a methodology that enables the traceability of an isolated platelet is developed. Selecting appropriate platelets, several techniques are applied over them to determine their specific characteristics and to correlate the information obtained.

2.1.2 Objectives

The main objective of this Chapter is to acquire great knowledge about four graphene-like materials that will be used along the thesis. Nanomaterials in general present noticeable variations between producers and batches. The industry around graphene production is still new and lacks of defined standardization. Thus, characterizing the particular graphene-like material that is employed for a particular study is a necessary step.

- To characterize the morphology and structure of four graphene-like materials and compare the results between them, understanding the reasons for those differences. Additionally, the results will be compared with the information provided by the suppliers in their datasheets.

- To study the effect of different spin-coating conditions on the dispersion of graphene-like materials over a Si/SiO_2. Also, to establish the spinning conditions to successfully disperse the material in order to obtain the deposition of isolated platelets.

- To present and validate a characterization methodology that enables the local analysis of a particular platelet and its traced characterization by different microscopes.
- To study the synergy between different characterization techniques when applied over a particular graphene-like platelet and to correlate the information obtained with them.

2.1.3 Experimental Details

Materials

In this Chapter, four different graphene-like materials are characterized: AvanGraphene GNP from Avanzare, xGnP GNP grade M from SkySpring, GO from Graphenea and rGO from Graphenea too.

AvanGraphene GNP: They are provided as a black powder. According to the supplier, these GNP have a lamellar structural morphology, with 2 x 5 μm^2 of surface and less than 10 nm in thickness, observed by TEM and SEM. The density of the bulk powder is less than 0.2g/cc. The carbon content in the material is 98.5%. They are presented as an alternative to the use of CNT and carbon nanofibers. Their use is oriented toward thermal conductivity enhancement.

SkySpring GNP: These GNP are provided as a black powder too. They consist of short stacks of graphene sheets with a platelet shape. Their thickness lays between 6 and 8 nm and the average particle diameter is 5 μm. The bulk density of these GNP is lower, 0.03-0,1 g/cc. The carbon content is 99.5 %. Oxygen content is showed in the datasheet, indicating it as $< 1\%$.

Graphenea GO: The GO are provided as a yellow-brown slurry of GO dispersed in water with a concentration of 0,5 mg/mL. No information is included about their surface size or their thickness but a detailed elemental analysis is supplied: Carbon (49-56%), Hydrogen (0-1%), Nitrogen (0-1%), Sulfur (0-2%), Oxygen (41-50%). The monolayer content is over 95%, however, it is indicated in the datasheet that dilution followed by slight sonication is required to obtain a higher percentage of monolayers as the GO flakes tend to agglomerate.

Graphenea rGO: Is provided in powder form and presents black color. Graphenea synthesizes this rGO via the chemical reduction of their GO. Thus,

Figure 2.1: SMA SPINNER 6000 Pro.

the GO just described is the precursor for the elaboration of this rGO. The reduction process eliminates a remarkable amount of functional groups, reestablishing the carbon atom lattice, so elemental analysis shows lower sulphur and oxygen contents, as expected: Carbon (77-87%), Hydrogen (0-1%), Nitrogen (0-1%), Sulfur (0%) and Oxygen (13-22%).

Datasheets for all the materials are presented in Annex I.

Characterization techniques

To avoid aggregation and to facilitate the study of individual platelets, the four graphene-like materials are deposited over Si/SiO substrates before the characterization. The deposition process is performed using a SMA SPINNER 6000 Pro (Figure 2.1).

Thickness measurements are performed using an AFM (Atomic Force Microscope) (Dimension 3100, with NanoScope IV electronics and NanoScope 5.31r1 software) (Figure 2.2). A Field Emission Scanning Electron Microscope

Figure 2.2: AFM Dimension 3100, with NanoScope IV electronics.

(FE-SEM) (NOVA NanoSEM 230 of FEI) in high vacuum conditions is used to examine the location, the distribution and the morphology of the platelets. Raman spectra are acquired on two different equipments: the Jobin-Yvon Labram, that was used for obtaining the spectra from the general samples and the Raman Imaging WITec Alpha 300R, for the mapping analysis of specific platelets. The measurements are made at 0,5mW and using a laser of 532nm of wavelength. For the X-Ray Diffraction (XRD) measurements a PANalytical XPert PRO MPD is used. The XRD analysis does not require the previous deposition of the sample over a substrate.

2.2 General characterization of graphite nanoplatelets and its derivatives

All the materials described above and characterized in this Chapter present a great tendency towards aggregation. Structural characterization, XRD measurements and Raman Spectroscopy, do not necessarily require separation between the platelets, even though Raman Spectroscopy can provide greater information if applied specifically to certain platelet. Nevertheless, morphological characterization, AFM and even FE-SEM, need the samples to be well dispersed and deposited over a substrate. To achieve better characterization results, a previous study on the deposition of these materials by spin-coating is performed.

2.2.1 Graphene deposition on SiO_2/Si substrates

Due to the importance of depositing the dispersed samples avoiding the formation of agglomerations of material, a study of deposition is carried out to ensure the correct separation between the platelets before applying the characterization techniques. The deposition is done using the spin-coating technique, consisting in dropping liquid over a substrate and rotating it, so that the liquid forms a layer over the substrate. In this case, the four samples are deposited on Si/SiO_2 substrates of 3x3cm^2. The goal of the study is to find the optimal conditions of rotation speed, acceleration and material quantity for obtaining a homogeneous dispersion of platelets along the substrate. For this, two different sets of experiments are carried through, using a GO dispersion and $Si0_2$/Si substrates in both cases. The GO dispersion is prepared adding 1 mL of GO slurry to 4 mL of isopropanol (0.1 mg GO/mL) and sonicating it by sonication bath for 5 minutes.

Effect of the acceleration ramp

The first set is performed to evaluate the effect of different ramps of acceleration in the deposition. One drop of 20 μL is dropped on the $Si0_2$/Si substrate and a spin coating process is done. The substrate is accelerated from 0 rpm to 2000 rpm with acceleration ramps for each experiment: 300 s, 400 s, 500 s and 600 s; what means longer times to reach the maximum speed, thus, a decreasing acceleration. After reaching the final velocity the process is continued for 1000 s. One last deposition is done using the same substrate and sample quantity but without performing any spinning process.

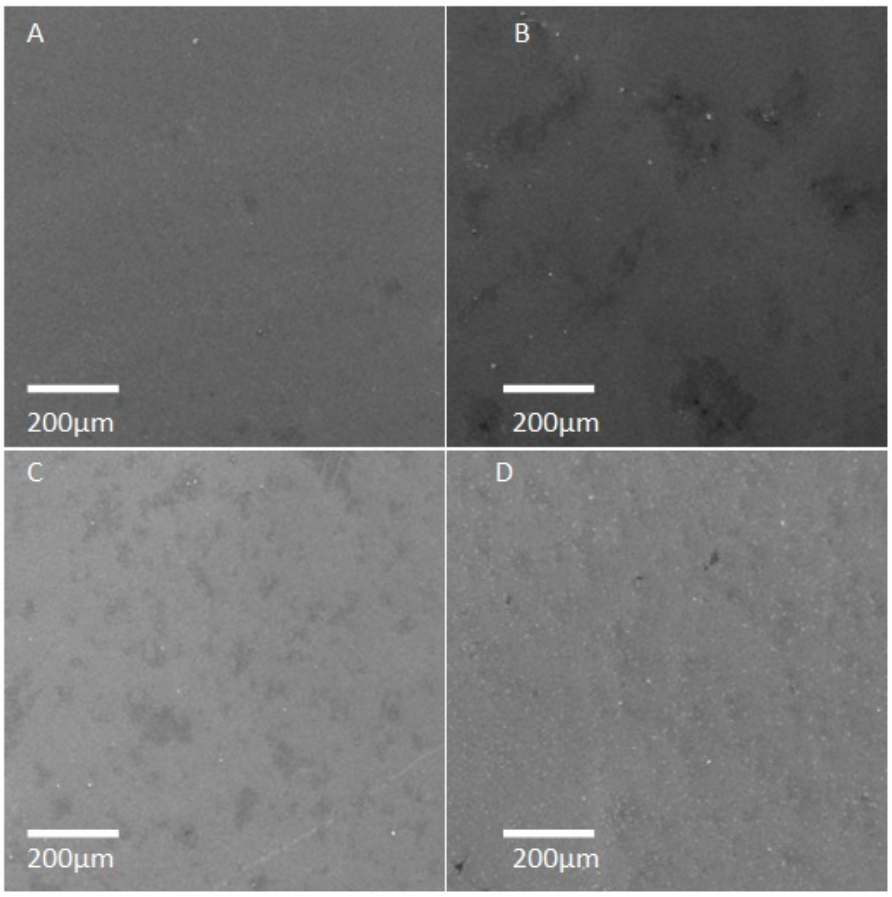

Figure 2.3: SEM images of GO deposited on Si/SiO substrates with an acceleration ramp of: (A) unspinned, (B) 400s, (C) 500s and (D) 600s.It is worth to note that in (B) and (C) there are GO agglomerations whereas in (A) and (D) there is hardly any.

Figure 2.3 compares the distribution of GO platelets for each condition. Figure 2.3 (A) corresponds to the unspinned sample and Figure 2.3 (B), (C), and (D) correspond to acceleration ramps of 400s, 500s, and 600s respectively. All the images are acquired with FE-SEM. The unspinned sample hardly shows any presence of GO in the middle of the substrate. Most of the GO appears aggregated in the borderline due the "coffee ring effect", a phenomenon that appears for the evaporation of a particle loaded liquid and that tends to agglomerate the particles forming a ring.The rest of the samples, the ones spinned, show a different behavior. The GO is deposited over the entire substrate surface. However, the agglomeration of platelets changes with the acceleration ramp. This aggregation of material can be seen in the images of Figure 2.3, where it

appears as black shapes. For the highest acceleration (ramp of 300 s, which is not shown in the figure) GO forms big agglomerated bulks. While acceleration decreases, these agglomerations start growing in number but decreasing in size. For the lowest acceleration there are almost any agglomerations and the substrate surface is covered mostly by separated GO platelets.

The best separation result is achieved with the longest acceleration ramp (600s).

Addition of multiple droplets

The second set of experiments is carried out to assess the results of adding new sample drops over an already spinned sample. Each process of spin coating is done with 20μL drops of the GO dispersion, with an acceleration ramp of 600s up to 2000rpm and kept at that velocity for additional 1000s. Five samples are analyzed, starting for just one droplet and repeating the process for two, three, four and five droplets, repeating the spin coating process after every addition.

Figure 2.4 compares the deposition of GO for the mentioned conditions. Figure 2.4 (A, B, C and D) present a SEM image of the substrate after the droplet addition and spin coating process repeated one, two, three and four times respectively. It can be appreciated that as the process is repeated a thick layer of multiple GO platelets starts growing. For the addition of two droplets, Figure 2.4 (B), this layer is not still continuous all over the surface. After the addition of the third droplet, Figure 2.4 (C), the layer covers most of the substrate and the individual platelets that form it are hardly distinguishable. For four and five droplets the layer keeps homogeneous and is presumable that gains thickness after every addition. Therefore, the deposition of up to two droplets would be preferable when studying isolated platelets while three or more might be more recommended for studies that require a continuous layer, like conductivity ones.

From both deposition studies, the conditions for a correct separation and deposition of the platelets are obtained. **For the following characterization studies, the samples will be dispersed in isopropanol with a concentration of 0.1mg/mL and sonicated for 5 minutes by sonication bath. Then, 20 μL of the dispersions will he deposited on a Si/SiO substrate of 3x3 cm^2. Finally, the spin coating process will be carried out with an acceleration ramp of 600 s, from 0 rpm to 2000 rpm.**

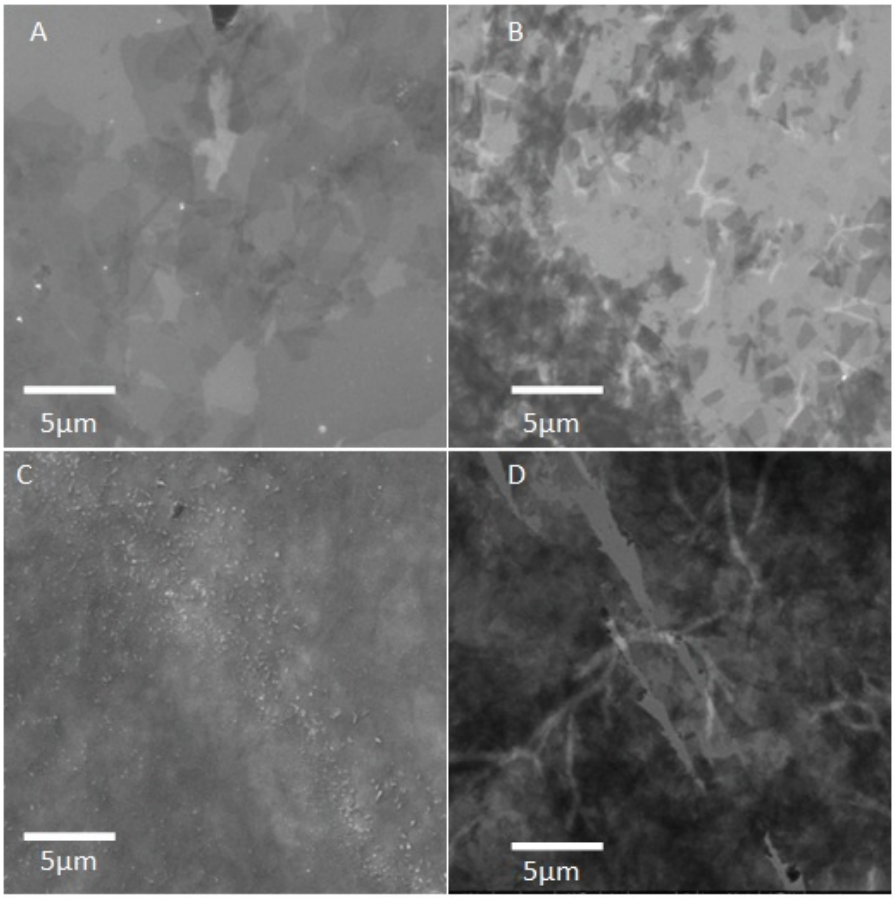

Figure 2.4: SEM images of GO deposited on Si/SiO substrate. Different number of droplets where used in the deposition: (A) one, (B) two, (C) three and (D) four

2.2.2 Morphological and structural characterization of graphene derivatives

A first general analysis is carried out over the four samples. This analysis will provide general information about their characteristics and will allow to confirm their classification as GNP, GO and rGO respectively. The morphology of the platelets is studied by SEM and AFM, evaluating the surface sizes, their roughness and their thickness (what allows to calculate the number of layers in the platelets). The structure, then again, is studied by both Raman spectroscopy and XRD, what provides information about the presence of defects in the carbon atom lattice and about the distance between sheets in the platelet.

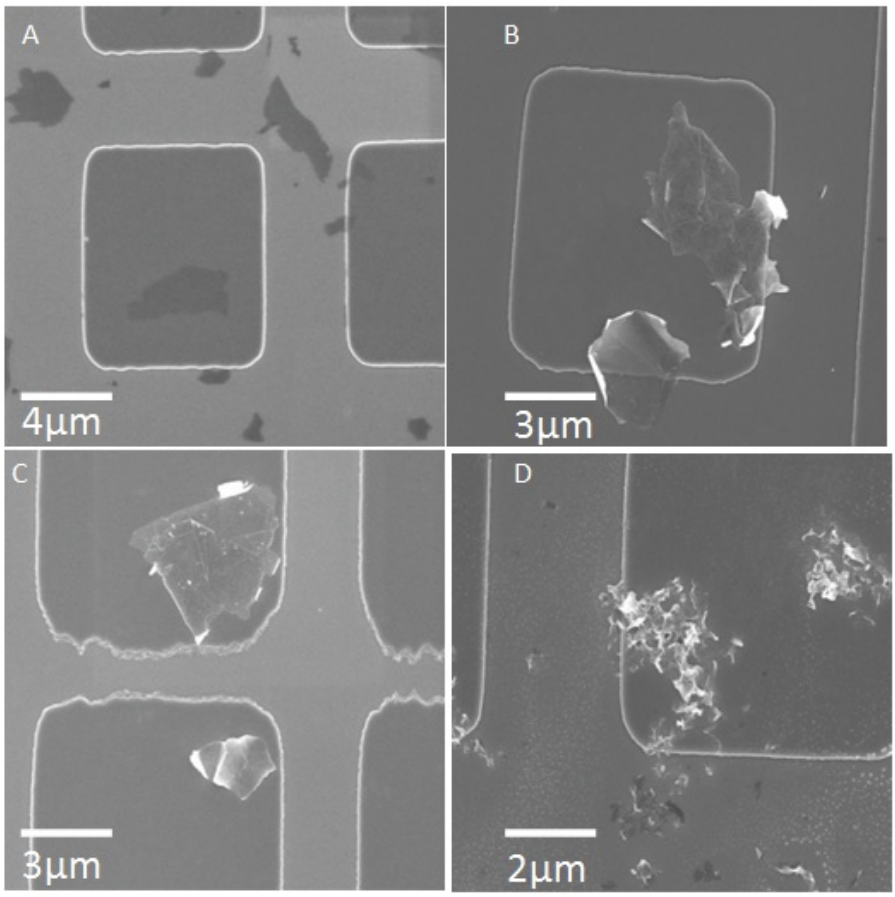

Figure 2.5: SEM images of: (a) A GO platelet. (b) Deposited GNP from SkySpring. (c) Deposited AvanGraphene GNP. (d) Aggregated rGO sheets.

Morphological analysis

To facilitate the analysis and to obtain more information about the samples, they are deposited on a Si/SiO_2 substrate following the spin-coating method and conditions developed in previous section. Once the samples are deposited, the characterization techniques are applied. A representative SEM image of the Graphenea GO is shown in Figure 2.5 (A). Most of the material is separated in clear, flat platelets and there is hardly any presence of agglomerated GO. The platelets present a rectangular-like shape with a wide range of sizes that go from 1.2x1.0 μm^2 to 14.5x7.3 μm^2. AFM measurements showed thicknesses from 1.2 nm to 4.2 nm. However, most of the platelets presented thicknesses under 1.5 nm, what confirms they are, in majority, monolayer [267]. Figure 2.5 (B) shows a SEM image of the GNP sample from SkySpring. These GNP do not present

separated monolayers but they appear as aggregations of many layers. Some agglomerations of several platelets can be found, indicating that the dispersion process did not separate them all. They show some irregular surfaces when compared to the GO platelets, than appeared flat and homogeneous. The size of the platelets go from 3.3x2.6 μm^2 to 9.3x5.8 μm^2. Later measurements with AFM showed that they present thickness between few tens of nanometers in the limits of the platelets and some hundreds in the middle of the bulky parts.

SEM image of AvanGraphene GNP is shown in Figure 2.5 (C). These GNP present smaller paltelets than the SkySpring GNP, with sizes from 1.59x1.44 μm^2 to 7.11x6.60 μm^2. Some agglomerations appeared, showing again the necessity of further dispersion to ensure the complete separation of the platelets. AFM measurements showed that these platelets present different thickness values, in a wide range, up to 500 nm, depending on the number of layers. Finally, the Figure 2.5 (D) shows a SEM image of Graphenea rGO. This sample is the one that most differs from the others. It presents very small platelets, with sizes from 0.6x0.75μm^2 to 5.1x2.6 μm^2. They are very rough and have highly irregular shapes, with high thickness dispersion.

Raman Spectroscopy

Raman spectroscopy can be used to determine the difference in structure between graphene, GO and rGO[215],[252] , [81]. The most prominent feature in the Raman spectra of monolayer graphene is the so-called G band appearing around 1580 cm_1. This band is generated by the in-plane vibrations of the sp^2 carbon atoms. In the case of a disordered sample or at the edge of a graphene sample, it can also be seen the so-called disorder-induced D band, at about half of the frequency of the G band (around 1350 cm_1). The D band is an indicator of the presence of carbon atoms with a sp^3 bonds in the basal plane. The position of the D and G bands and the relation between their intensities are good indicators of the structure of the sample and provide information about the defects on the sample. The D band vibration is due to the breathing modes of sp^2 atoms in the rings, which are only permitted in the presence of sp^3 hybridized carbon atoms[63]. Figure 2.6 compares the Raman spectra obtained for GO, rGO and the two different GNP samples.

GNP from Avanzare and GNP from SkySpring both present very similar spectra: the first one presents a G peak at 1582 cm^{-1} and the second one at 1581 cm^{-1}. Their G peaks are both very narrow and show high intensity, while for graphene this band tends to be wider. The positions match with the G band for graphite and the shape of the peak correspond to a graphitic structure [144].

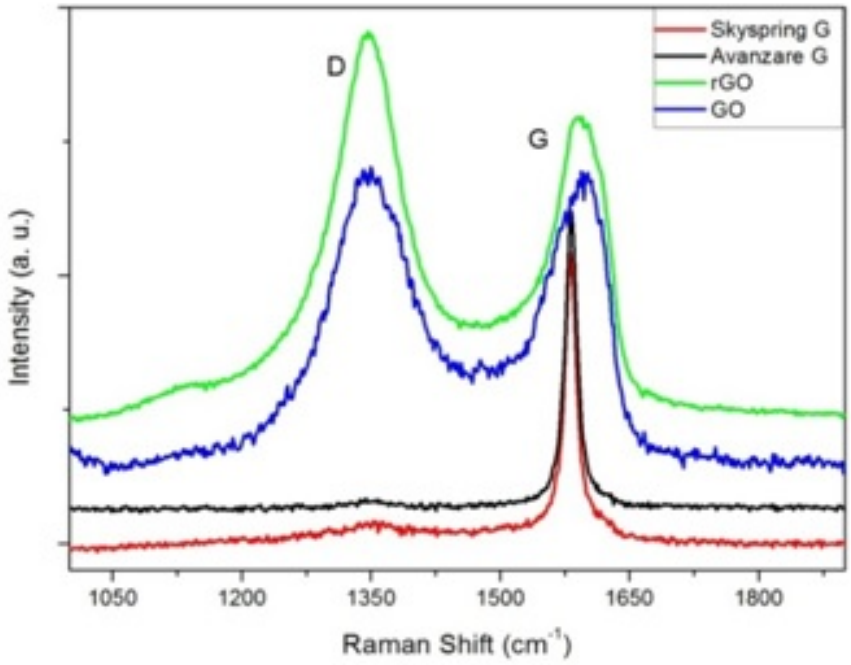

Figure 2.6: Raman spectra of GO (blue), rGO(green), AvanGraphene GNP (black) and SkySpring GNP (red)

None of the two samples present a D band, meaning that the amount of defects is very low for both of them. These results confirm the structure of the GNPs studied are closer to graphite than to graphene monolayer or MLG.

The G peak in the Raman spectrum of GO is broadened and shifted to 1598 cm^{-1}. The oxidation process breaks the carbon atom lattice of graphene and often leads to the isolation of double bonds, that resonate at higher frequencies when they are separated from the conjugated π-π lattice [117]. In addition, the D peak appears at 1348.41 cm^{-1} indicating the reduction in size of the in-plane sp ^{2} domains [215]. This two features in the Raman spectrum of GO clearly indicate a disruption of the carbon lattice due to the oxidation. In the Raman spectrum of rGO the G band downshifts to an intermediate position between GO and graphene (1590 cm^{-1}), what is attributed to graphitic <<self-healing>> [63], the recovery of some of the sp^2 domains induced by the reduction. The D band hardly shifts but increases its intensity, presenting a higher D/G ratio than the GO. Table 2.1 summarizes the positions of bands and their relation in intensities for the studied samples.

The reason for the higher I_D/I_G in rGO is explained by the effect of the

	D (cm_{-1})	G (cm_{-1})	I_D/I_G
Sky. GNP	X	1581	X
Avan. GNP	X	1582	X
GO	1348	1598	1
rGO	1347	1590	1.12

Table 2.1: Positions and intensity relations of D and G bands in Raman spectra for the four samples.

reduction process. While reducing the GO, up to 75% of the oxygen is eliminated, according to the producer. However, the reduction not only affects the oxygen groups but also the carbon atoms in the lattice, thus, generating defects in the structure that increase the intensity of the D band. The remarkable difference between rGO spectrum and the spectra from both GNP confirm that the reduction of the GO is far from completely recovering the full carbon atom lattice.

XRD

Finally, in the last characterization step, XRD measurements were performed for the rGO, the AvanGraphene GNP and the SkySpring GNP. Due to the aqueous nature of the GO sample (it is supplied as slurry) no measurements were carried out for it.

Figure 2.7 shows the spectra obtained for the three samples. The main peak corresponds to (0 0 2) reflection. This peak is related with the interplanar distance between layers by Braggs law (Equation 2.1.1), that gives the angles for coherent and incoherent scattering from a crystal lattice.

$n\lambda = 2d \sin\theta$

Where:

n: An integer

λ: Wavelength for X-rays

d: Interplanar distance

θ: Incidence angle.

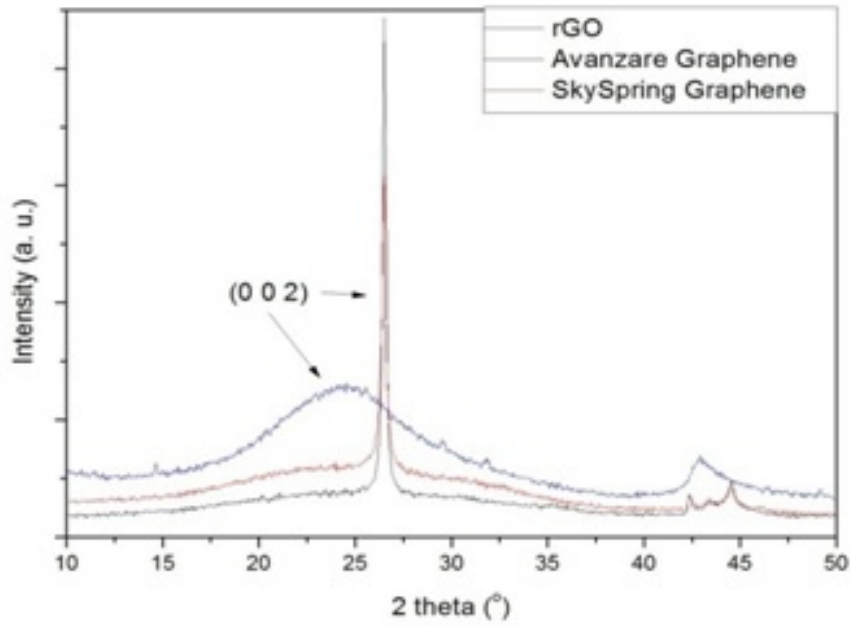

Figure 2.7: Diffractogram of rGO (blue), AvanGraphene GNP (black) and SkySpring GNP (red)

The position of the peaks and the interplanar distance calculated by Braggs law are presented in Table 2.2. The results show the same interplanar distance for both GNP, what makes great coherence. rGO sample, however, presents a slightly higher interplanar distance. This increase is probably related to the presence of residual oxygen groups and other defects that add disorder to the crystallinity of the system. The numerous lattice defects in the rGO and the resulting increased disorder make it (0 0 2) reflection to appear much wider than the ones for the GNP samples.

Sample	2θ	Interplanar distance (Å)
GNP (SkySpring)	26.4	3.36
GNP (Avanzare)	26.4	3.36
rGO	24.5	3.62

Table 2.2: XRD results for characterized samples

Comparison and classification

The application of AFM, Raman spectroscopy, FE-SEM and XRD over the four samples, a general characterization has been achieved. The information obtained about them enables their comparison and classification.

SkySpring GNP and AvanGraphene GNP presented very similar characteristics. No significant differences in structure have been found either, being both of them notably defect-free materials, with a clear graphitic structure. On the one hand, lateral sizes between 5 and 25μm are indicated for SkySpring in the datasheet and the FESEM results partially agree (no platelets over 10μm were found). According to the supplier their thickness values are between 6 and 10 nm, however, AFM measurements over the samples did not showed any platelet with a thickness below 30nm. On the other hand, lateral sizes around 2 μm are specified in the datasheet for AvanGraphene GNP and most of the platelets presented that size, even if some of them reached 7 μm. Thicknesses over 40nm were measured, while according to the datasheet it should be 10nm.

The characterization made over the GO and rGO samples supplied by Graphenea confirmed the specifications of the Datasheets. GO presented more defects, mostly related to oxygen functional groups, than rGO. The reduction process successfully eliminated some of them, restoring the carbon atom lattice. Most of the GO was dispersed in flat monolayers and presented big lateral sizes, up to 14 μm. rGO however, showed irregular surfaces of notable smaller sizes (5 μm). The rGO samples are obtained by the reduction of the same GO samples characterized in this work, so it is clear that the reduction process has a direct impact on its morphology, reducing the lateral size of the platelets and making them rougher.

To be able to study the morphological and structural effects of the reduction process over a GO platelet, it would be necessary a characterization process that allows the use of several techniques in sequence over the same platelet. A process with this feature is developed and presented in next section.

2.3 Local Analysis

General analysis techniques provide <<bulk>> characteristics of the studied samples, like the average sizes or the amount of functional groups. However, for some studies and applications these may not be enough and further characterization is needed.

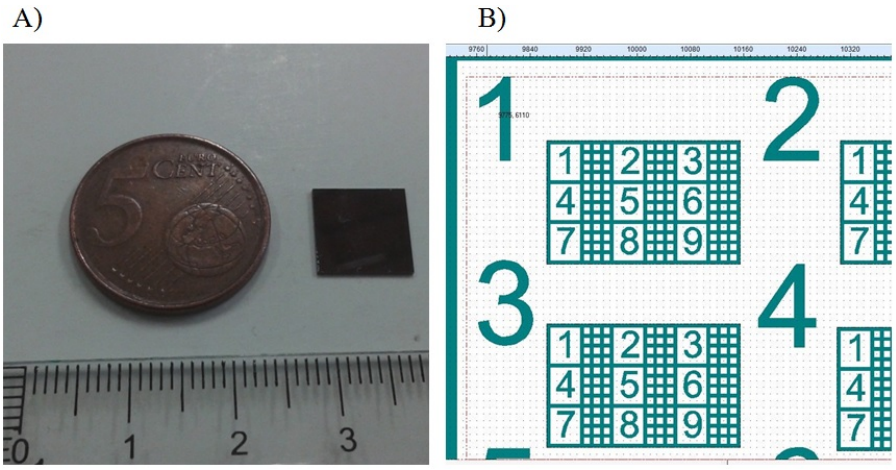

Figure 2.8: A. Patterned $Si0_2$/Si substrate. B. Image of the lithographed pattern.

To study the characteristics of certain platelet, the effects of oxidation/reduction processes over it or the impact of functionalization on its structure and morphology it is necessary a method that enables the local study and tracing of that platelet. Additionally, as multiple microscopes are needed to fully characterize it, the method has to allow an easy access for the different techniques.

In this section, an analysis procedure that allows the use of several analysis techniques over the same traced platelet to characterize it is developed. To evaluate the accomplishment of the method, it is applied to SkySpring GNP and to Graphenea GO.

2.3.1 Method description

Firstly, the graphene or graphene-like material needs to be dispersed in an appropriate media. The conditions for the dispersion are taken from the previous study: The platelets are dispersed in isopropanol (0.1 mg/mL) using a sonication bath (5 min). Then, 20 μL of the dispersion are taken and dropped on a Si/SiO substrate.

In order to localize individual platelets a pattern is made over Si/SiO substrates using standard lithography (Fig 2.8). This pattern consists in 10x10 μm squares with a nominal height of 90 nm, as presented in Figure 2.9. The whole pattern is numbered, and each square has a unique code that facilitates the localization of a given platelets over the analysis with different microscopes.

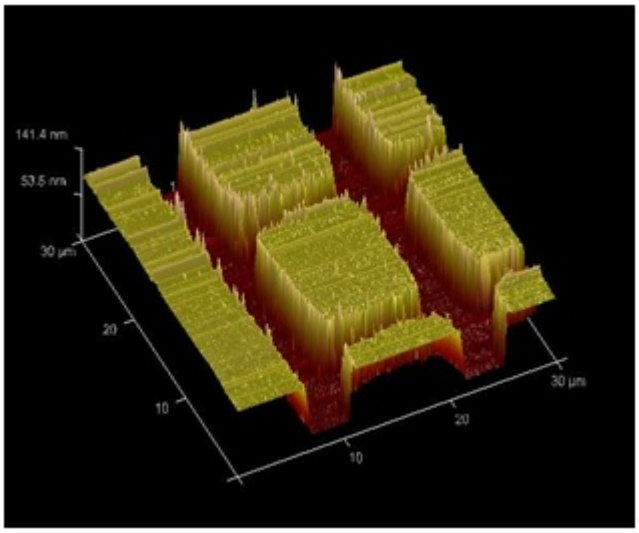

Figure 2.9: AFM image of the $Si0_2$/Si substrate used for the depositions.

For the convenient deposition of the platelets over the substrate, spin coating process is carried out with an acceleration ramp of 600 s, from 0 rpm to 2000 rpm.

Once the material is dispersed over the patterned substrate, the selection of the platelet takes place. FE-SEM is used to obtain morphological data about the platelets and allows to locate one with the desired aspect. Once selected, further analysis is carried out over the same platelet. The morphological information acquired with FE-SEM, is completed with the obtaining of its height profile by AFM and a Raman mapping is done to complete the structural information.

Thanks to the tracing of the platelet enabled by this technique, the morphological information of shape and thickness is directly correlated for each point of the platelet with the structural information that the Raman mapping presents. Furthermore, the technique enables the use of additional non-destructive microscopy techniques if required.

Two representative samples are analyzed by this method: SkySpring GNP and GO from Graphenea. The GO, due to its functionalized structure with high content of epoxide, hydroxyl and carboxyl groups, presents a great dispersibility and few-layered platelets, what makes it a perfect target for the analysis. The GNP from SkySpring exhibited better dispersibility than Avanzare GNP in the conditions applied , being the dispersibility a key factor when studying isolated platelets.

2.3.2 SkySpring GNP

SkySpring GNP are dispersed and deposited according to the described method. FE-SEM allowed the selection of two nanoplatelets deposited over a patterned square. They are chosen for presenting a large surface with clearly identified flat areas.

Figure 2.10presents three images obtained with each analytic technique for the two deposited platelets. The image in Figure 2.10 (a) is obtained with FE-SEM. It shows two 8x4 μm^2 platelets with a rough surface area and a flat one, in both cases. Surface roughness on graphite nanoplatelets arises as an important factor in for certain applications, like enhancing mechanical interlocking and load transfer with the matrix in composites, what leads to a better adhesion [106]. Figure 2.10 (b) is an image obtained with AFM and presents the height profile of both platelets. As the FE-SEM image suggested, the two flat surfaces correspond to the thinnest parts of the platelets. A profile of each zone is presented in Figure 2.11 (A and B). Figure 2.11 (A) presents a step of 32nm high between the $Si0_2$/Si and the graphite nanoplatelet, and even a thicker part on its left side. A graphene layer has an average thickness of 0.4nm so it gets confirmed that the platelet is multilayer, presenting between 100 and 500 graphene layers depending on the region.

The section of the other platelet, presented in Figure 2.11 (B), shows a thinner step of 23nm. This thickness will determine the results of the Raman spectra. 2.10 (C) shows a mapping of Raman made by multiple spectra obtained with an integration time of 0.4s and performing 130x130 spectra in an image size of 13x13μm^2. This mapping presents a color scale for the intensity of the spectra between 2500 cm^{-1} and 3000 cm^{-1}. Raman spectra provide information about the number of graphene layers, clearly identifying a single layer graphene, from a bi-layer one and from an up to five layer graphene mostly by the behaviour of the 2D peak, which has shown to be still a field of research [63]. However, as the AFM data confirmed, the deposited platelets presented too many layers in every part of the platelet to enable this comparison. Figure 2.11 (C) shows the obtained spectrum for the spot, which, as predicted, corresponds to graphitic material.

The accuracy of the local analysis of the platelets showed that, for certain regions, their lateral sizes are below 100nm. Measured values of 23nm and 32nm makes it reasonable to classify them as GNP and are closer to the 6-10nm described in their Datasheet. However, the presence of areas with more than 200nm indicates that the dispersion process needs to be improved.

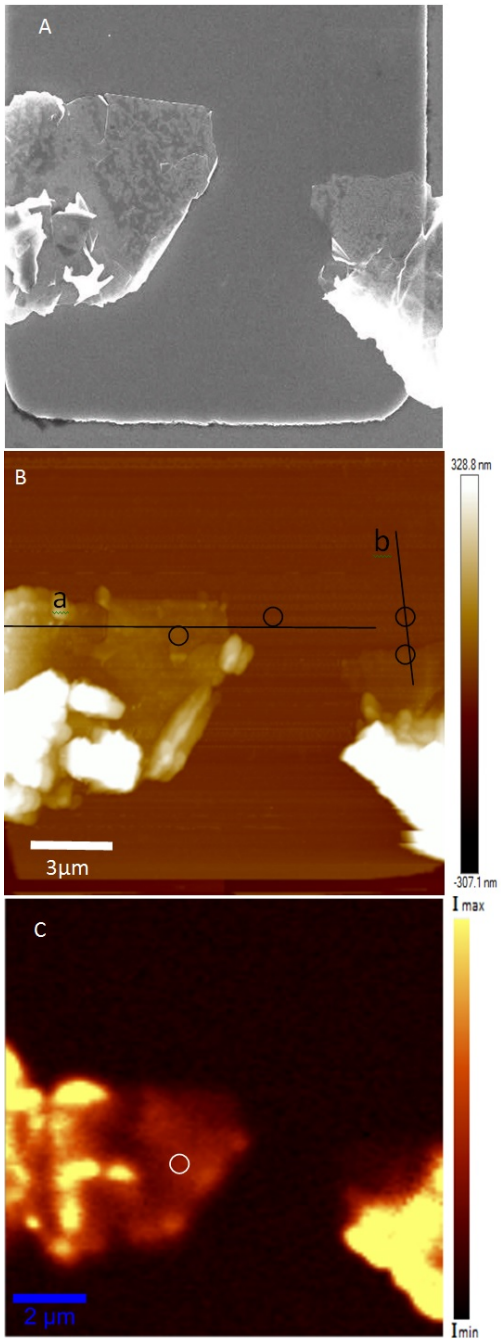

Figure 2.10: Images of two SkySpring GNP platelets obtained with: (A) FE-SEM, (B) AFM, (C) Raman Mapping color intensity propotional to the 2D band-

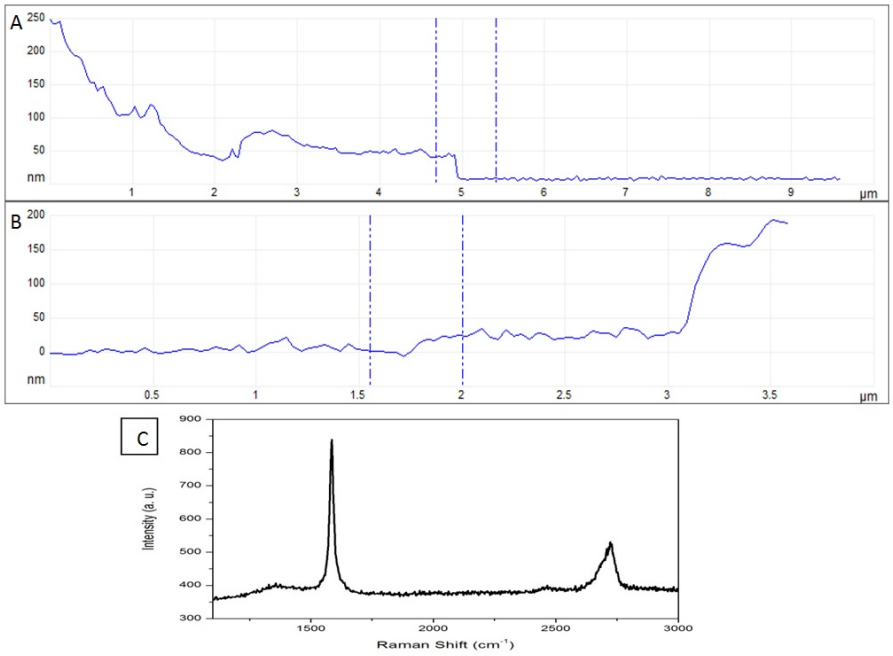

Figure 2.11: (A) and (B) AFM profiles corresponding to lines in Figure 2.5.1(B), (C) Raman spectrum for the spot in Figure 2.5.1 (C)

2.3.3 Graphenea GO

Graphenea GO is dispersed and deposited according to the described method. FE-SEM allowed the selection of one clear and well isolated platelet deposited over a patterned square. This platelet is chosen for its relatively large surface area, which is apparently flat. Figure 2.12 compares the images obtained with the three techniques of the procedure. The FE-SEM image in Figure 2.12 (A) shows a platelet of 6.3x3.8μm^2 that present two different areas. The first one covers most of the platelet and seems to be composed of just one layer. The second one is located in the right side of the platelet, where it seems that a second layer has been deposited on top of the first one.

Figure 2.12 (B) presents the height profile of the GO platelet obtained with AFM, a section of this profile is plotted in 2.13 (A). This section shows two steps in the platelet, of 1.3nm each. Minimum sheet thickness of 1nm has been measured [268] for GO. So it gets confirmed that there is a main platelet of one GO layer with a smaller monolayer deposited on its top, forming a GO bi-layer on its right side. The profile also shows that the bi-layer is more wrinkled than the monolayer, for this platelet.

Figure 2.12 (C) presents a mapping of Raman made by multiple spectra obtained with an integration time of 1s and performing 55x55 spectra in an image size of 11x11μm. This mapping presents a color scale for the intensity of the spectra between 1100 cm^{-1} and 1900 cm^{-1}. Two clear areas of different Raman behaviour can be differentiated in the platelet, one corresponding to the monolayer and the other corresponding to the bi-layer. An average of the Raman spectra for these two areas has been plotted in Figure 2.13 (B), where spectrum A is the average for the monolayer and spectrum B is for the bi-layer. The signal in both cases is quite low due to the small amount of material, however, it is enough to clearly identify the standard D and the G bands of GO. Furthermore, there is a clear difference in the intensity of the bands between the two spectra, being the bands of the bi-layer spectrum more intense than the bands of the monolayer one. This further confirms the presence of different number of layers in the platelet, clearly correlating the data obtained with the three microscopy techniques.

The structural and morphological properties measured by the local analysis of this GO, such as the large platelet size, the low number of layers in the platelet and the presence of functional groups in the structure highlight the convenience of its use in many applications.

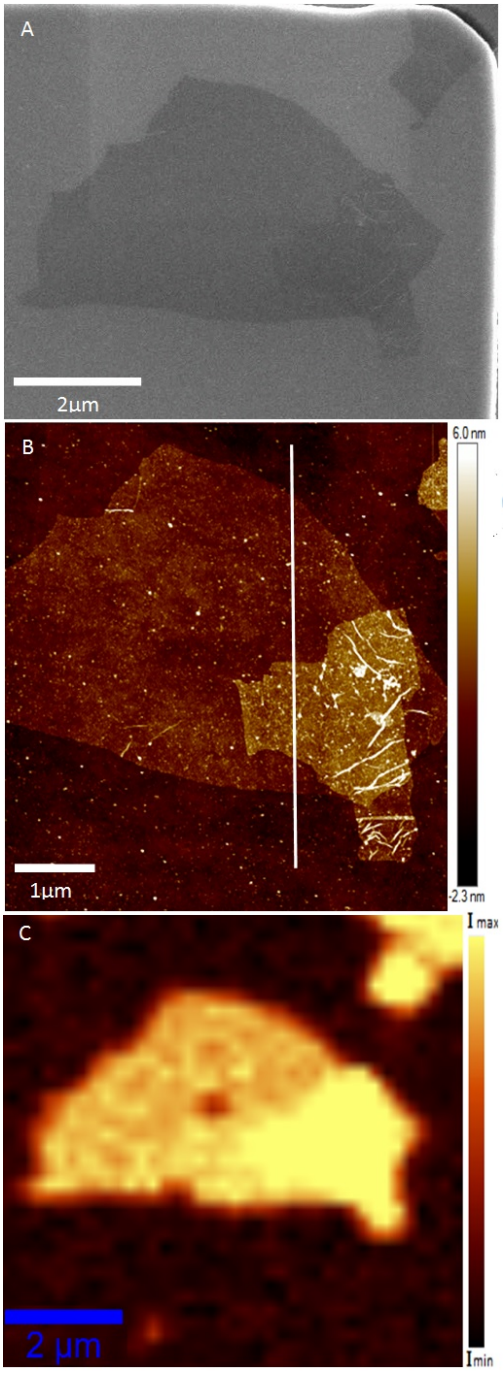

Figure 2.12: Images of Graphenea GO obtained with: (A) SEM, (B) AFM, (C) Raman Mappingcolor intensity proportional to D and G bands-

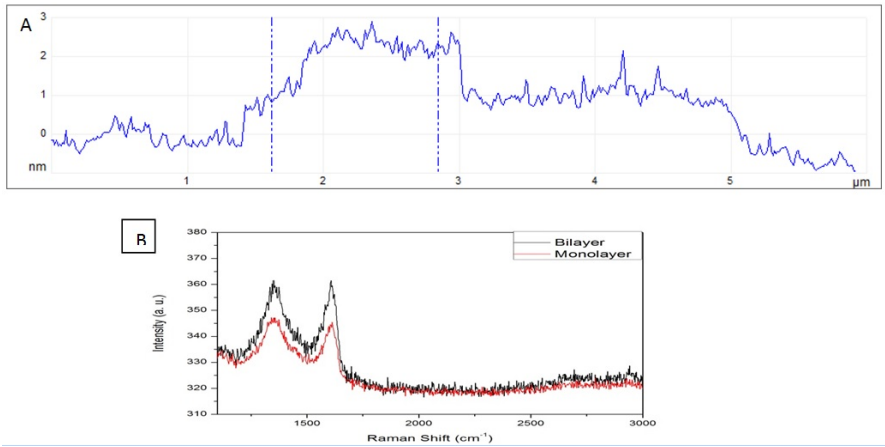

Figure 2.13: AFM profile corresponding to the line in Figure 2.12(B). (B) Raman spectra for the two layers of GO shown in Figure 2.12 (C)

2.4 CONCLUSIONS

Conditions for the deposition of isolated platelets along the surface of a Si/SiO_2 have been stablished

Deposition of the graphene-like materials in isopropanol and their dispersion over a Si/SiO_2 substrate by spin-coating has proved to be an appropriate method for the separation of their platelets. Steps and conditions are summarized in Table 2.3. It allowed the characterization of isolated platelets and stand out for the short times it requires, the its low cost and the simplicity of the equipment involved.

Table 2.3: Summarizes the conditions required for each step: Dispersion, deposition and spinning

Dispersion	Nanomaterial is added to isospropanol (0.1mg/mL) and sonicated for 5 minutes
Deposition	20μL are droped over a 3x3cm Si/SiO\textsubscript2 substrate
Spinning	Substrate is accelerated from 0 rpm to 2000 rpm in 600s and kept at 2000rpm for 1000 additional seconds.

It has been also found out that the repletion of the process over the same platelet, with additional droplets lead to the formation of a continuous layers, what could be interesting for certain characterizations and applications. The addition of three droplets of 0.1mg GO/ mL isopropanol proofs to be enough to form the continuous layer.

The general characterization of the materials is successfully achieved

Structure and morphology of all the studied materials have been characterized, confirming its classification according to the nomenclature proposed by Carbon and presented in Chapter 1. Morphological results are summarized in Tabla 2.4, that also includes the values provided by the supplier in their datasheets. Lateral size values agree with the datasheet, whereas some differences are appreciated in the thickness of both GNPs. As the GNP have a great tendency towards the agglomeration, the reason for these discrepancies in thicknesses is probably the aggregation of platelets after the sonication or during the spinning process. Raman spectroscopy results sustained the variation in chemical composition between samples marked in their datasheets. It

also pointed out the presence of defects in the carbon atom lattice of rGO, that could be later seen by FE-SEM.

A method for the local characterization of laminar nanomaterials has been developed and its performance has been successfully proven

The use of patterned Si/SiO_2 enabled the localization of isolated graphene-like platelets and their posterior characterization. Several non-destructive microscopy techniques were employed to study GO and GNP samples, what allowed correlating the information obtained by different techniques, for instance: AFM, FE-SEM and Raman spectroscopy. The studied GO platelet was confirmed to be formed by a monolayer area and a bi-layer area, with 1.3nm for each layer. Raman results over the same platelet supported this affirmation: The response was very different in intensity and the two areas could be clearly differentiated when mapping the surface of the platelet. D and G bands in GO increased remarkably their intensity from the monolayer to the bi-layer areas. As Raman mapping is a quicker technique than AFM, the relation established between the number of GO layers (up to two) and the intensity of D and G bands allows analyzing bigger surfaces in less time.

The method has also revealed some limitations concerning to the measures with AFM and Raman spectroscopy. Inadequately dispersed samples wont provide much information about the thickness of a monolayer when analyzing them with an AFM. Platelets with high roughness on its surfaces could present some difficulties too.It is suggested for future work that the functionalization of the $Si0_2/Si$ surface may facilitate the deposition of graphene and rGO in thin platelets and may help to avoid the formation of sample agglomerations.

Table 2.4: Summary of the properties characterize for Graphenea GO, Graphenea rGO, AvanGraphene GNP and SkySpring GNP

	Lateral size (μm)		Thickness (nm)		Interplanar distance (A)
	Datasheet	Experimental	Datasheet	Experimental	Experimental
SkySpring GNP	5, 10, 25	2.6 -9.3	6 - 10	> 0	3,36
Avangraphene GNP	2	1.44 - 7,11	10	> 40	3.36
Graphenea GO	x	1 - 14.5	x	1.2 - 4.2	x
Graphenea rGO	0.3	0.6 - 5.1	x	x	3,62

Chapter 3

Graphene Nanoplatelets Dispersion

3.1 Approach, objectives and experimental details.

3.1.1 Approach

The remarkable importance of graphene dispersions has already being stated in Chapter I. Its great properties stand out when the graphene monolayer remains un-stacked. The improvement of a method that allows the manipulation of this material without forcing its aggregation got the interest of many research groups[224]. And the dispersion of graphene in an appropriate solvent is the most promising one.

John Texter, in his last review about graphene dispersions, pointed out that many papers are published exploring the properties and applications of graphene dispersions[226]. Many of these applications require dispersion quantities far from the production at laboratory scale. Thus, the scalability of the dispersion processes appears as an additional requirement for the convenience of the studied methods.

The development of stable GNP dispersions in water is aimed, since it is widely used in a sort of processes and has a large applicability range. Using surfactants to stabilize carbonaceous nanoparticles in water is an effective way of ensuring long-term stability. The optimal surfactant concentration required for the GNPs used in this thesis is yet to be determined.

This chapter will focus on the experimental study of a sonication/centrifugation method for the obtaining of stable GNP dispersions in water by using a GNP:Surfactant appropiate ratio.

3.1.2 Objectives

The general objective of this chapter is to develop GNP-SDBS dispersions in water that present two main characteristics: 1) It must show long term stability and 2) GNP concentration in the dispersion must be well-known and as high as the materials allow. Higher concentrations tend to show less stability, for what different factors are studied in order to find the best conditions. Several steps are followed pursuing this goal:

- To evaluate the viability of SkySpring GNP and AvanGraphene GNP (both characterized in previous Chapter) to form SDBS stabilized GNP dispersions in water.

- To establish the most appropriate sonication method for the elaboration of concentrated GNP dispersions: Tip sonication or Bath sonication.
- To calculate the Absorption coefficient (α) for the particular GNP system studied in this work and to compare it with the value reported by other groups for similar systems.
- To establish and optimize a dispersion method that enables the obtaining of stable GNP dispersions in water with SDBS as surfactant.
- To individually study the effect of several factors in the dispersion method over the final GNP concentration, for instance, sonication time, surfactant concentration and centrifugation time.

3.1.3 Experimental details

Solvent

Deionized water is the solvent of choice for the study of graphene dispersion in this thesis. Its inexpensive, it can be obtained easily and, most important, it is widely used in the most variety of global industry processes.

Surfactant

SDBS is used as surfactant for the elaboration of the dispersions. It is represented in Figure3.1. It presents a hydrated sulfonate group attached to a benzene ring, with two aliphatic chains attached to the ring. When interacting with the graphene in small SDBS proportions, the SDBS molecules form a monolayer aggregate structure parallel to the surface, leading to a stable charged encapsulation layer on both sides of the suspended sheets.

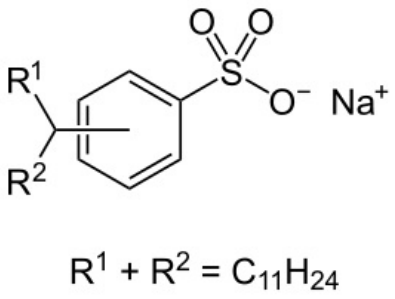

Figure 3.1: Chemical structure of the Sodium Dodecyl benzene Sulphonate

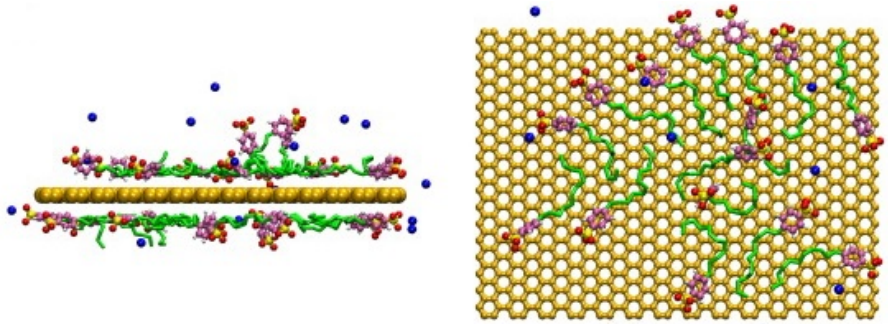

Figure 3.2: Side and front views of representative simulation snapshots for the self-assembly of SDBS surfactants absorbed on graphene sheets at low surface coverage. [216]

SDBS molecules tend to distribute uniformly on the graphene surface, maximizing the contact between molecules and surface and, oppositely, minimize the contact between the water molecules and the graphene hydrophobic surface. Haoyue Sun and Xiaoning Yang presented a deep molecular simulation study to this respect[216]. When the SDBS rates are increased, the molecules form hemimicelle aggregates between the water and the graphene (a general behavior for ionic surfactants with 12 methyl groups on carbon surfaces). Most of the SDBS molecules orient radially, however, some of them remain parallel to the graphene, leading to their hydrophobic tail groups facing the graphene surfaces. Furthermore, still for a high SDBS ratio, the arrangement of the SDBS molecule's head-group is so that they locate at the edge section of the graphene surfaces (Figure 3.2). When graphene presents more than one layer, the graphene-SDBS interactions slightly vary and a small amount of molecules adsorb on the step edge regions [216].

Graphite nanoparticles

Graphite nanoplates from two different companies are used.

The first ones are provided by SkySpring, by the name of "xGnP bulk dry powder Grade-M" GNP. Their morphological and structural properties are extensively described in Chapter II. They present platelet surfaces between $8.5\mu m^2$ and $54\mu m^2$, whereas, their typical surface area is from 120 m^2/g to 150 m^2/g, according to the supplier.

The second GNPs are purchased from Avanzare, with the technical name "Avangraphene". In Chapter II, the morphology and structure was also characterized. Their surface is slightly smaller, between $2.3\mu m^2$ and $47\mu m^2$. These

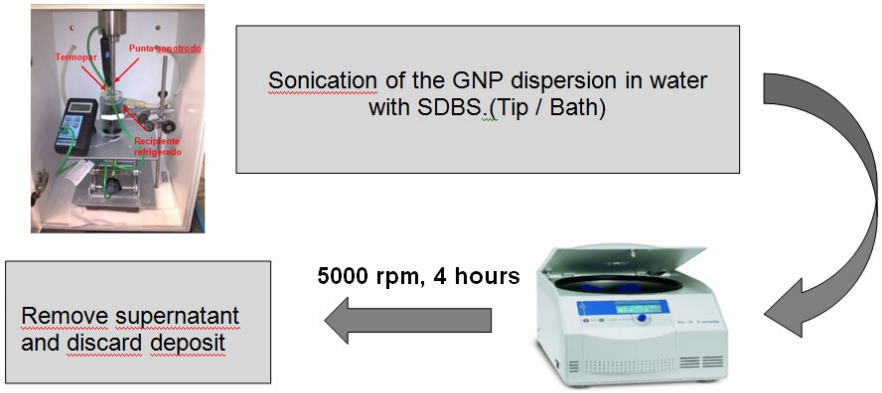

Figure 3.3: Schematic representation of the dispersion process applied to graphite nanoplates in water.

GNP are designed for their use as fillers for conductive polymers and present an exceptional electrical conductivity, according to the supplier.

They were both chosen for their price and the knowledge already acquired from previous work. Both present few layered defect-free structures with medium-large surfaces, what makes them suitable for many applications. They are used in several projects in Tecnalia including the elaboration of batteries, the development of paintings and mortars or water desalinization, and their reliability is proved. Furthermore, the description of Avangraphene points out its potential applicability in thermal management composites, a topic studied in the last chapter of this thesis.

Method to obtain GNP dispersions

Starting from the previous experience in Tecnalia in elaborating dispersions with different types of carbonaceous nanoparticles and the existing literature, a consistent method is presented for the obtaining of stable GNP dispersions. This method will be employed and optimized.

The dispersion method consists in three main steps: Exfoliation of the GNP in water with SDBS, centrifugation of the dispersion and separation of the supernatant from the deposited fraction. The method is schematized in Figure 3.3.

The agglomeration in GNPs can reach several hundreds of layers, thus, an activation energy must be provided to produce the separation. This energy

input will be provided by a sonication treatment. Sonication supplies sufficient energy activation so as to overcome the interlayer adhesion energy that keeps graphene layers bound. Ultrasonic frequencies over 20 kHz are applied to the sample. This triggers the creation and growth of bubbles in the liquid. These cavitation bubbles develop and grow until a critical diameter is reached, inducing their implosion. This collapse causes locally extreme conditions of very high local pressure and very high temperatures, which can lead to a splitting up of particle agglomerates[25]. Furthermore, sonication helps with the diffusion of the surfactants, facilitating them to reach the just exfoliated graphene layers before they re-aggregate. The sonication treatment will be applied by two different equipments: Ultrasonication tip and ultrasonication bath.

Long sonication treatments at high power output, however, can not only get over the π-π interactions between graphene layers but may also break those layers and reduce the size and surface area of the platelets. This drawback must be considered as it can be of great impact on certain applications where large platelets are preferable. For example, for the deposition of catalytic particles over GNP, bigger surface areas are preferable [154] and thermally conductive composites or electrically conductive devices made with GNP require of larger platelets [186].

Once the graphene layers separate and show their "fresh" surfaces, SDBS adsorbs onto it and prevent the flocculation.

The process then continues with the centrifugation of the dispersion. The centrifugation step is used to separate the most unstable GNP particles, normally those who remained aggregated after the sonication treatment, and ensure stability. After the centrifugation, two different phases are obtained: The precipitated particles and the stable dispersion. These two phases are separated by decantation in the final step of the method, and the liquid phase is kept as the stable GNP dispersion.

Characterization method

A wide variety of techniques have been employed to characterize graphene dispersions. Scanning electron microscopy (SEM) and transmission electron microscopy (TEM) have been extensively used in conjunction with atomic force microscopy (AFM) to study the morphology of graphene platelets, its surface area, its thickness and even their lateral size distributions. Raman spectroscopy has also proved its capability to determine not only the number of layers in

regular graphene flakes but also the amount of defects and the presence of functionalizations[64].

For measuring the concentration of a GNP dispersion, however, a quick technique that facilitates the analysis of samples in a short period of time is required. To this regard, optical absorption has proved to be the most useful and easily applied characterization method for estimating the overall extent of graphene dispersion, since the optical absorption can be related to the graphene concentration in a sample[226].

In this Chapter, UV-Vis Spectrophotometer Uvikon 992 from Kontron Instruments is used.

The morphological characterization is carried out with a SEM Model JOEL JSM-5910LV/ INCA300 that includes an Energy Dispersive Spectroscopy (EDS) device.

3.2 Graphene dispersion in water

The achievement of stable GNP dispersions at high concentrations requires the adjustment of many factors: The initial GNP concentration, the relation between GNP concentration and SDBS concentration, the sonication technique used for exfoliating the platelets and the duration of the sonication process. As a first step, these parameters must be screened and the most promising conditions experimentally sifted out. So, a set of 64 samples is prepared. These samples are clustered in 3 main groups: GROUP A, 24 samples with initial GNP concentration of 0.1 mg/mL; GROUP B, 24 samples with initial GNP concentration of 1 mg/mL and GROUP C, 16 samples with initial GNP concentration of 10 mg/mL. For each group both types of GNP are tested. Both sonications methods are also used in the preparation of the samples and different sonication times are tested. The relation between GNP and SDBS is set at 1:1, 1:10 and 1:30 w/w ratios. The real conditions for each test are summarized below in tables.

The elaboration of the 64 samples follows the method described in previous section: Sonication of GNP in water (20mL) in the presence of SDBS, centrifugation (5000rpm at 4h) and separation of the liquid phase by decantation. The evaluation of the samples is carried out by visual analysis at the initial time (t=0 days) and after one day (t=1days).

Various objectives are aimed with this test: a) To know the conditions that must be discarded because they conduct to low performance towards the dispersion of GNP in water; b) To determine the conditions that lead to the best GNP dispersion; c) To evaluate if there is any difference in the final sample when sonicated by sonication bath or sonicated by sonication tip; d) To evaluate if there is a different behavior between GNP from SkySpring and AvanGraphene GNP.

GROUP A: 0.1 mg/mL

Conditions for the first set of samples are summarized in Table 3.1 and Table 3.2. These samples correspond to the lowest initial GNP concentration, 0,1 mg/mL. The pictures corresponding to these samples are presented in Figure 3.4 and Figure 3.5.

The low GNP content in these samples becomes manifest at first sight, as most of them are totally transparent. Only samples 8, 11 and 12 show some coloration at t= 0 days, due to the presence of dispersed GNP. The three

of them are made with AvanGraphene GNP. However, after 1 day, the GNP precipitates in all of them, appearing a black solid phase at the bottom of the tubes. None of the SkySpring GNP samples show any presence of GNP.

The conditions used on these samples are discarded for low performance.

Table 3.1: Summary of dispersion conditions for initial Avanzare Graphite Nanoplates concentrations of 0.1mg/mL.

AvanGraphene GNP (0.1 mg/mL)			
N	Dispersion Method	Agitation time	GNP:SDBS Ratio (w/w)
1	Sonication tip	10 min	1:01
2			1:10
3			1:30
4		40 min	1:01
5			1:10
6			1:30
7	Sonication bath	2 hours	1:01
8			1:10
9			1:30
10		8hours	1:01
11			1:10
12			1:30

GROUP B: 1 mg/mL

The conditions for the second set of samples are summarized in Table 3.3 and Table 3.4. These samples correspond to the middle initial GNP concentration, 1 mg/mL. The pictures corresponding to these samples are presented in Figure 3.6 and Figure 3.7.

On the one hand, for the AvanGraphene GNP samples, coloration can be noticed in almost everyone, with the exception of numbers 13 and 16. Samples sonicated by sonication bath present a darker color. Among them, numbers 20 and 24 stand out. However, sample number 18, the one with 40 minutes of sonication tip and 1:30 GNP:SDBS (w/w) ratio appears as the sample with higher stability. Sample 23 also shows presence of GNP but the dispersion is not homogeneous and big aggregations can be distinguished. On the other hand, SkySpring GNP samples present much lower coloration. Sample number

Table 3.2: Summary of dispersion conditions for initial SkySpring Graphite Nanoplates concentrations of 0.1mg/mL.

SkySpring GNP (0.1 mg/mL)			
N	Dispersion Method	Agitation time	GNP:SDBS Ratio
33	Sonication tip	10 min	1:01
34			1:10
35			1:30
36		40 min	1:01
37			1:10
38			1:30
39	Sonication bath	2hours	1:01
40			1:10
41			1:30
42		8hours	1:01
43			1:10
44			1:30

53 exhibits the darker color among them but most of the GNP are precipitated after one day.

GROUP C: 10 mg/mL

The conditions for the third set of samples are summarized in Table 3.5 and Table 3.6. These samples correspond to the highest initial GNP concentration, 10 mg/mL. The pictures corresponding to these samples are presented in Figure 3.8 and Figure 3.9. Samples with 1:30 GNP:SDBS (w/w) ratio are not tested, because the amount of SDBS is too high and becomes really hard to solve in water.

Among the samples with an initial GNP concentration of 10vmg/mL there are four dispersions that stand out with a remarkable coloration: Samples 25, 27, 57 and 59.These four samples correspond to 10vmg/mL GNP, 10vmg/mL SDBS and sonication tip as dispersion method. They differ in the sonication time (10 min for samples 25 and 57 and 40 min for samples 27 and 59). The same behavior is shown in GNPs, provided by SkySpring and by Avanzare.

Even with lower sonication times, samples dispersed with ultrasonication tip reach higher coloration than those dispersed with ultasonication bath, which

Table 3.3: Summary of dispersion conditions for initial Avanzare Graphite Nanoplates concentrations of 1mg/mL.

AvanGraphene GNP (1 mg/mL)			
N	Dispersion Method	Agitation time	GNP:SDBS Ratio
13	Sonication tip	10 min	1:01
14	Sonication tip	10 min	1:10
15	Sonication tip	10 min	1:30
16	Sonication tip	40 min	1:01
17	Sonication tip	40 min	1:10
18	Sonication tip	40 min	1:30
19	Sonication bath	2 hours	1:01
20	Sonication bath	2 hours	1:10
21	Sonication bath	2 hours	1:30
22	Sonication bath	8 hours	1:01
23	Sonication bath	8 hours	1:10
24	Sonication bath	8 hours	1:30

Table 3.4: Summary of dispersion conditions for initial SkySpring Graphite Nanoplates concentrations of 1mg/mL.

AvanGraphene GNP (1 mg/mL)			
N	Dispersion Method	Agitation time	GNP:SDBS Ratio
45	Sonication tip	10 min	1:01
46	Sonication tip	10 min	1:10
47	Sonication tip	10 min	1:30
48	Sonication tip	40 min	1:01
49	Sonication tip	40 min	1:10
50	Sonication tip	40 min	1:30
51	Sonication bath	2 hours	1:01
52	Sonication bath	2 hours	1:10
53	Sonication bath	2 hours	1:30
54	Sonication bath	8 hours	1:01
55	Sonication bath	8 hours	1:10
56	Sonication bath	8 hours	1:30

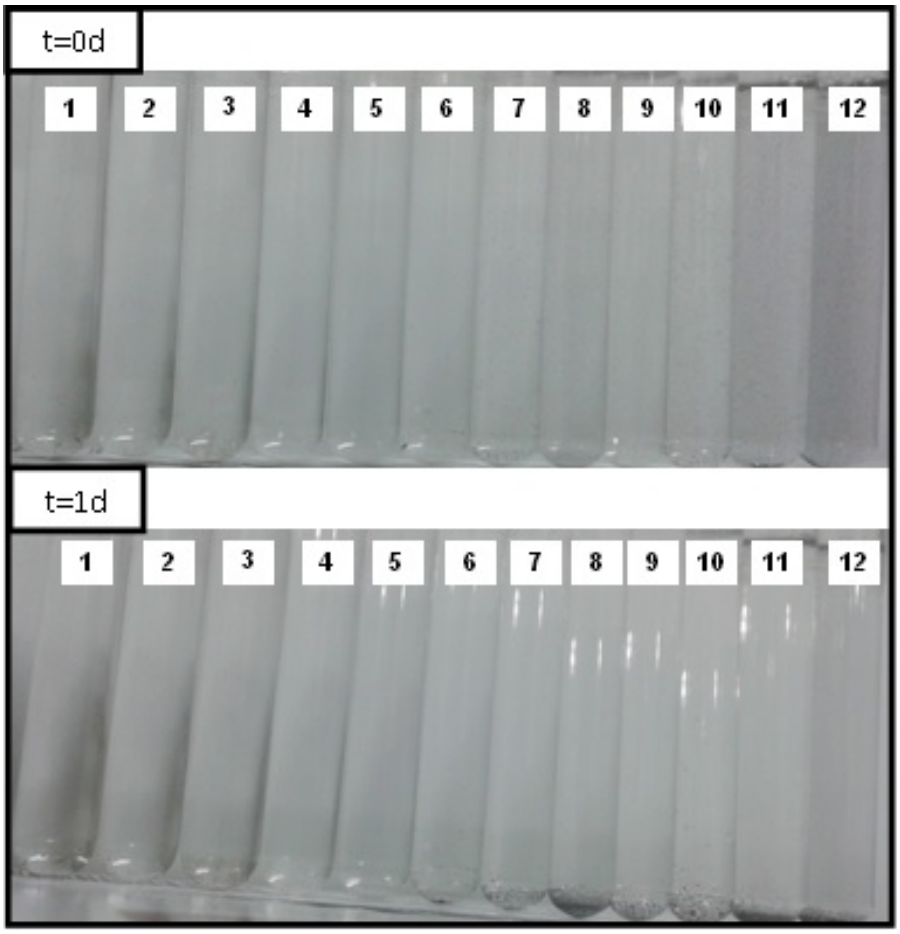

Figure 3.4: Images of Avanzare Graphite Nanoplatelets dispersions with intitial concentration of 0.1mg/mL. It shows the stability with images a time=0 days and time= 1day

suggests a more effective application of the energy towards the separation of aggregates for the tip rather than the bath. This effect is clearly observed in samples 59, 61 and 63. Starting out from the same graphene and SDBS concentrations, the sample dispersed with ultrasonication tip becomes darker (59) , despite the longer ultrasonication bath times for 61 and 63.

This set of samples also makes it clear that the 1:10 GNP:SDBS (w:w) relation for initial GNP concentrations of 10 mg/mL is completely unsuitable for the elaboration of dispersions. None of the samples with this relation showed any presence of GNP.

The results of this screen-study enable to determine the dispersion condi-

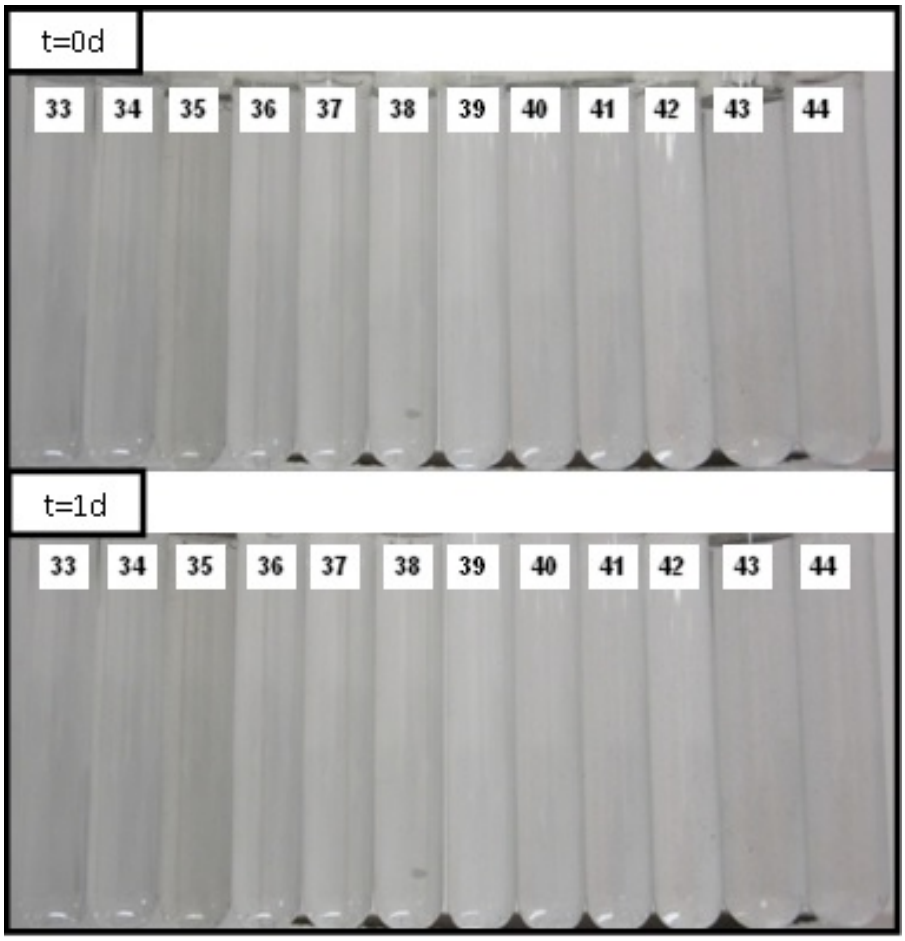

Figure 3.5: Images of SkySpring Graphite Nanoplatelets dispersions with intitial concentration of 0.1mg/mL. It shows the stability with images a time=0 days and time= 1day.

tions that will be used for further research. It established sonication tip, over sonication bath, as a simple, effective and quick method to disperse graphite nanoplates in water. Besides, it showed certain initial concentrations of SDBS and GNP that lead to stable dispersions in water.

For the following analysis, AvanGraphene GNP from Avanzare are chosen. Both of them (AvanGraphene and Skyspring) presented a similar behavior at the last set of samples and dark, stable dispersions were obtained with both. AvanGraphene GNP are preferred as they will be also employed in later Chapter for its incorporation in conductive resins. Furthermore, there was a higher availability of them in Tecnalia at the moment of this study. So, **the selected**

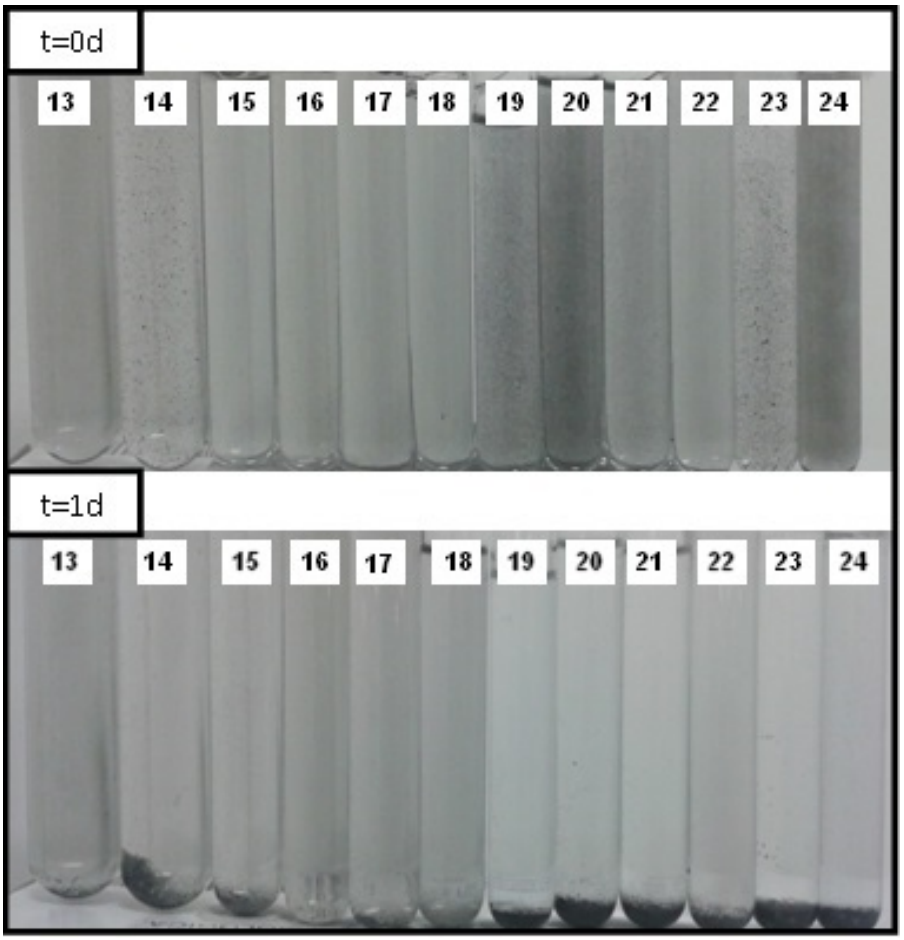

Figure 3.6: Images of Avanzare Graphite Nanoplatelets dispersions with intial concentration of 1mg/mL. It shows the stability with images a time=0 days and time= 1day

conditions are the ones corresponding to sample 27: 10mg/mL Avan-Graphene GNP, GNP:SDBS ratio 1:1, 40 minutes of sonication with sonication tip and 4 hours at 5000rpm.

As said, the material, sonication technique and conditions settled with this experiment are the basis for further analysis. In order to evaluate and optimize the parameters that lead to better GNP dispersions in water, it is necessary to establish and tune up a more accurate technique than the visual analysis: Optical absorption with UV-Vis Spectrophotometer.

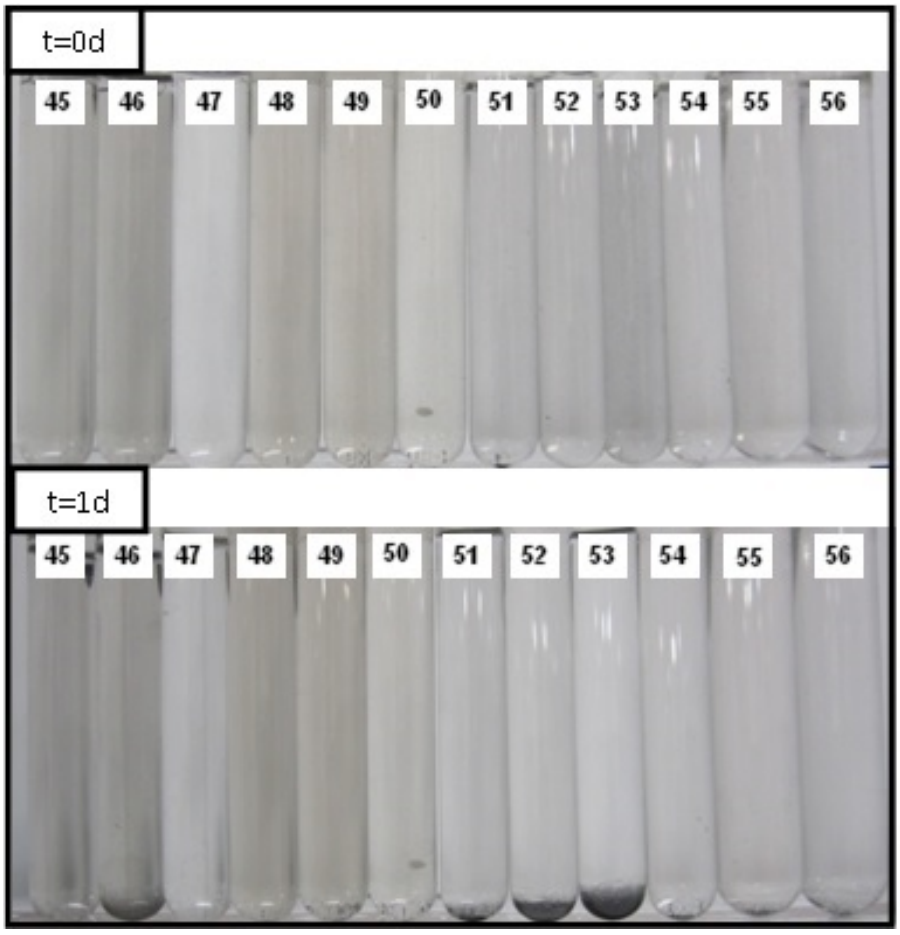

Figure 3.7: Images of SkySpring Graphite Nanoplatelets dispersions with intitial concentration of 1mg/mL. It shows the stability with images a time=0 days and time= 1day.

3.3 Relation between Absorbance and graphene concentration

The optical absorption allows measuring the absorbance for a given dispersion. The Absorbance is a parameter that has an extended use in the characterization of nanoparticle dispersions and their concentrations. According to the law of Lambert-Beer law (Eq. 3.2.1.1), the absorbance of any certain dispersion varies linearly with its concentration for a certain wavelength.

$$A = \alpha l C$$

Table 3.5: Summary of dispersion conditions for initial Avanzare Graphite Nanoplates concentrations of 10mg/mL.

AvanGraphene GNP (10 mg/mL)			
N	Dispersion Method	Agitation time	GNP:SDBS Ratio
25	**Sonication tip**	**10 min**	**1:01**
26	Sonication tip	10 min	1:10
27	**Sonication tip**	**40 min**	**1:01**
28	Sonication tip	40 min	1:10
29	Sonication bath	2 hours	1:01
30	Sonication bath	2 hours	1:10
31	Sonication bath	8 hours	1:01
32	Sonication bath	8 hours	1:10

Table 3.6: Summary of dispersion conditions for initial SkySpring Graphite Nanoplates concentrations of 10mg/mL.

SkySpring GNP (10 mg/mL)			
N	Dispersion Method	Agitation time	GNP:SDBS Ratio
57	**Sonication tip**	**10 min**	**1:01**
58	Sonication tip	10 min	1:10
59	**Sonication tip**	**40 min**	**1:01**
60	Sonication tip	40 min	1:10
61	Sonication bath	2 hours	1:01
62	Sonication bath	2 hours	1:10
63	Sonication bath	8 hours	1:01
64	Sonication bath	8 hours	1:10

Equation 3.2.1.1. Law of Lambert-Beer.

Where:

A: Absorbance

C: Concentration

α: Absorption coefficient of the system

L: Width of the system.

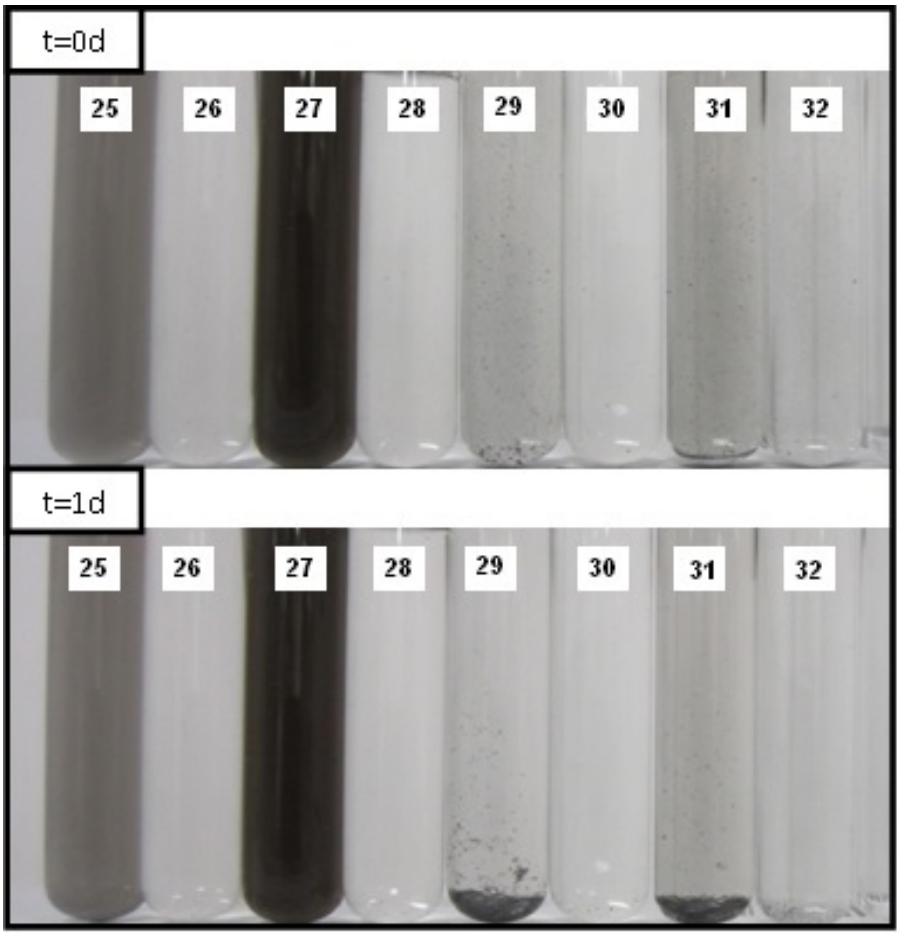

Figure 3.8: Images of Avanzare Graphite Nanoplatelets dispersions with intitial concentration of 10mg/mL. It shows the stability with images a time=0 days and time= 1day.

The spectrum of a dispersion consists in the absorbance measured for every wavelength (λ), generally between 200nm and 800nm. Each system will present a certain spectrum according to its physical properties and its interaction with the light. The nature of the nanoparticles and their morphology can lead to variations on it. Figure 3.10 presents an example of a typical absorbance spectrum for the studied system: Graphite nanoplates dispersed in water by SDBS.

The first thing to notice is the lack of peaks for most of the wavelengths. The spectrum is almost flat and featureless for λ values between 800 and 400nm. This behavior is expected for a quasi 2-dimensional material such as graphite nanoplatelets[146]. However, below 350nm, a high absorption band is observed

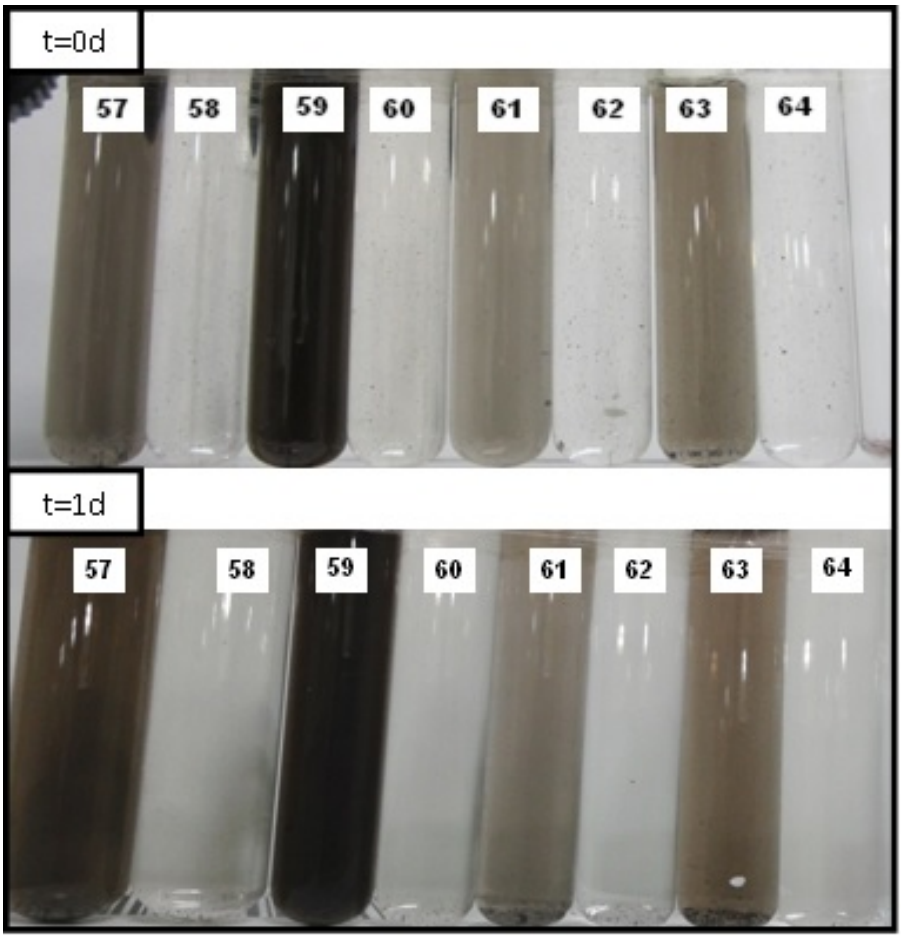

Figure 3.9: Images of SkySpring Graphite Nanoplatelets dispersions with intitial concentration of 10mg/mL. It shows the stability with images a time=0 days and time= 1day.

and the spectrum becomes irregular. This absorption peak and the later "noisy" behavior are related to the effect of the surfactant[140].

Generally, the experimental points used for the calculation of the concentration by the law of Lamber-Beer correspond to the peaks of maximum absorbance. On these peaks the resolution of the technique becomes higher. However, for this type of spectra, the peak around 280nm can not be used to measure the concentration of GNP, as it is related to the surfactant and not to the nanoparticles. Another wavelength must be selected to measure and compare the concentration of different samples. The main groups researching this topic employ λ=660nm. That point is far enough from the peak to ensure

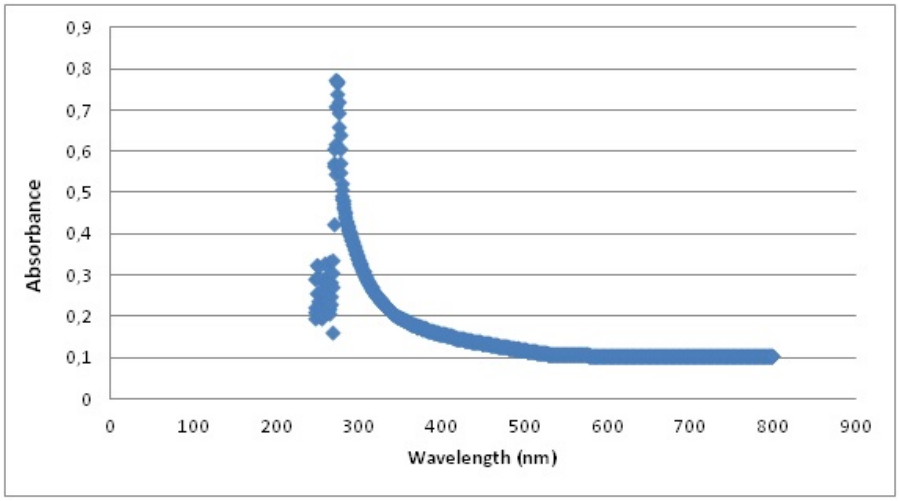

Figure 3.10: Absorbance as a function of the wavelength for graphite nanoplatelets dispersions in water stabilized with SDBS. Example of behavior.

no interferences from the surfactant, so λ=660nm will be used in this work.

In order to calculate the concentration of nanoparticles in a dispersion using the law of Lambert-Beer, it is necessary to know the absorption coefficient of the system, α. Each system presents different α, depending on the nanoparticles and their morphology. Furthermore, in a certain system, α varies with the wavelength, for what is necessary to know the value of α for the wavelength that will be used in the experimental measurements. The choice of λ=660nm facilitates the approximation to the topic; previous work has been done by other groups to this regard and some values for α at that wavelength have been calculated: α= 1390 mL mg^{-1} m^{-1} for Lotya et al [140] and α=1660 mL mg^{-1} m^{-1} for Sriya et al [50].

However, some authors pointed out that the differences in the graphitic material experimentally employed in the calculus of α can lead to variations in it [146]. Furthermore, the experience of the research groups at Tecnalia showed that many morphological differences can be found not only between nanoparticles from different companies but also between nanoparticles from the same company and different batches. Therefore, an experimental calculation of α for the system (AvanGraphene GNP and SDBS in water) studied in this chapter is necessary.

3.3.1 Experimental calculation for α at λ=660nm

The calculation of α for this system requires to elaborate a dispersion and experimentally measure two things: The absorbance of the sample at 660nm and the amount of GNP dispersed in it.

First, a dispersion of AvanGraphene GNPs and deionized water is prepared. The conditions for this dispersion are taken for the best results achieved in previous section: Initial GNP concentration of 10mg/ml and SDBS concentration of 10 mg/mL; 40 minutes of tip sonication and centrifugation at 5000 rpm for 4 hours. After the centrifugation process, the precipitated fraction is discarded and the supernatant is kept and labeled as GNP-Sample-1. The process is repeated to obtain 2 additional samples.

The next step consists in measuring the GNP concentration in the dispersion. An appropriate filter of well-known weight is required. A polyvinyliden fluoride filter with a pore size of 0.45 μm from MILIPORE is employed in this case. A measured volume of the supernatant is filtered and repeatedly washed with deionized water until complete elimination of the surfactant. The filter is then dried to eliminate any presence of the solvent. Finally, the dried filter is weighed and the GNP quantity is calculated by difference.

This method used to evaluate the GNP concentration in the dispersion includes two main error sources: A) The presence of SDBS that may remain in the filter after the multiple washes and B) The loss of certain amount of GNP during the filtering process. To avoid the first error source, it is necessary to repeat the washing step several times with large volumes of solvent. To prevent the second source of error a filter must be consciously chosen so as its pores size is small enough for the GNP to fit across them. The AvanGraphene GNPs used in this study have been already characterized in Chapter II by Scanning Electron Microscopy and Atomic Force Microscopy. The size evaluations of the platelets showed a minimum lateral size of 1.5 μm for what a filter with a pore size of 0.45 μm was considered suitable enough to avoid any significant losses. However, the two mentioned sources of error must be taken into account and the experimental result should be compared with the results in bibliography to ensure its reliability.

The GNP concentration for GNP-Sample-1 and the additional 2 samples is measured, saving an aliquot of each for the calculation of α. These aliquots are serially diluted and the absorbance is measured for each dilution. α is then calculated for each sample using the linear relationship. The results are

Table 3.7: Samples for the calculation of α .

Sample	Absorbance	[GNP] (mg/mL)	Calculated α (mL g^{-1} m^{-1})
GNP-Sample-1	1.503	0.0719	2088
GNP-Sample-2	1.499	0.0721	2079
GNP-Sample-3	1.507	0.0717	2101

collected in Table 3.7. The 3 values obtained for α in each sample are used to statistically calculate its value.

With Equation 3.2.1.1 α **is calculated to be 2089 mL g^{-1} m^{-1},** with a standard deviation of 9.01.

This value is higher than those presented by Lotya and even Sriya. Various values of α are obtained by distinct groups due to variations in the morphology of the material used in each study. Despite the difference between the three of them, the value calculated in this work is considered consistent enough and will be used to characterize de GNP concentration of future samples. Furthermore, it is in reasonable agreement with the average absorption coefficient presented by Hernandez et al for graphite/graphene in different solvents (2064 mL $g^{-1}m^{-1}$)[90].

3.3.2 Characterizing the GNP concentration by Optical Absorption

With an extinction coefficient already calculated for the system of study, the concentration and stability of the dispersions can be measured. The first dispersion to be analyzed is the one whose conditions stood out in section 3.2 (Initial AvanGraphene GNP and SDBS concentrations of 10 mg/mL, 40 minutes of tip sonication and centrifugation at 5000 rpm for 4 hours).

The obtained dispersion (the decanted supernatant after the centrifugation) is analyzed with UV-Vis spectrophotometer to measure its absorbance. Measurements are carried out for 21 days to study the stability. The absorbance is used with the determined α to calculate the GNP concentration in the sample. Figure 3.11 shows the GNP concentration, as a function of time.

The GNP concentration at time=0 is 0.073 mg/mL. This concentration is nearly a 50% higher than that reported by Lotya et all. for the same system

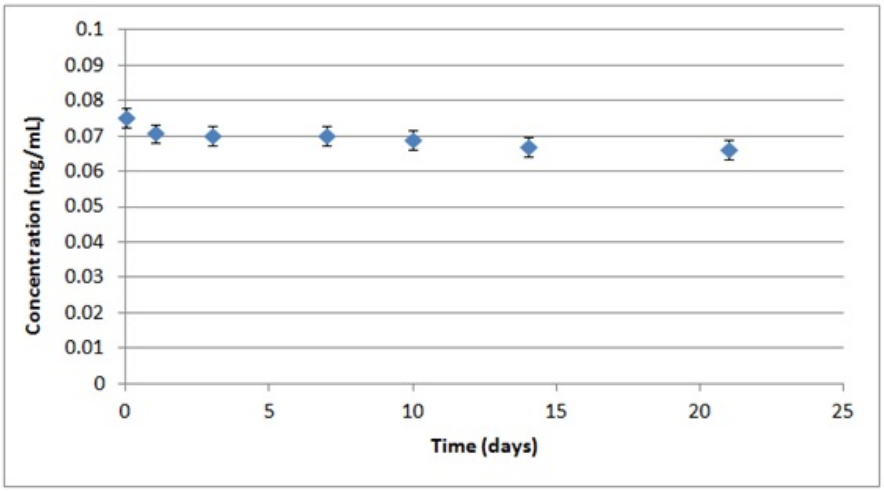

Figure 3.11: Concentration of a GNP dispersion in water as a function of the time.

(0.05 mg/mL) [140] . However, is lower than that reported by Sriya et al (0.2 mg/mL) [50] and the one recently reported by Y. Song et al [211] (0.1 mg/mL) and Uddin et al [233] (1.5 mg/mL). The concentration in the studied sample is relatively close to most of the reported dispersions but is remarkably far from the concentration achieved by Uddin and its group. The difference is explained by the dispersion method. In this case, the AvanGraphene GNPs are dispersed with SDBS in water, whereas Uddin method included the addition of SDBS to a GO dispersion, before reducing it with hydrazine, forming a so called SDBS-S-Graphene, which is later dispersed in water. Furthermore, it did not include a centrifugation step.

For the evaluated time, the dispersion presents a good stability. There is an initial 5.4% GNP loss during the first 24 hours. For the next six days, the sample suffers an additional 1.3% loss. In the last 14 days, the sample losses another 5.4%. It is considered a remarkable estability, however, it cannot be compared since no data about similar stability studies has been found.

It becomes necessary to study and adjust the factors involved in the dispersion process in order to optimize them towards a higher concentrated GNP dispersion in water. Three key factors will be studied and optimized: Sonication time, surfactant concentration and centrifugation time.

3.4 Optimization of the GNP dispersion in water

3.4.1 Effect of the sonication time in the final concentration

In this section the effect of the sonication time on the final GNP concentration is studied for the system GNP in water stabilized by SDBS. Longer sonication times entail more energy applied to the sample, thus, higher exfoliation and better dispersions are expected.

A group of five GNP dispersions with the same initial conditions are prepared: Those conditions are summarized in Table 3.8. Its dispersion is sonicated for different periods of time, from 20 minutes to 120, also summarized in the same table.

After the sonication process, each sample was centrifuged at 5000rpm for 4 hours. The resulting dispersions were characterized by UV-Vis spectroscopy, as the direct relation between absorbance and GNP concentration has already been established in Section 3.2.1. The absorbance is measured at 660nm and appropriate dilution was applied to those samples whose absorbance were higher than 1. Figure 3.12 gathers the absorbance results for each sample.

Table 3.8: Summarizes the dispersion conditions applied to each sample.

Dispersion	Sonication time (min)	[GNP]o (mg/mL)	[SDBS]o (mg/mL)	Volume (mL)
A	20	10	10	20
B	40	10	10	20
C	70	10	10	20
D	100	10	10	20
E	120	10	10	20

The results show a notable increase of the absorbance with the sonication time. For the same initial conditions, Sample E, with 120 minutes of sonication, doubles the absorbance of Sample A, with just 20 minutes. For the range of sonication times analysed, absorbance shows a linear relationship with the sonication time, and confirms that the final concentration of GNP dispersion in water can be heavily modulated varying the sonication times.

The obtained data do not show a saturation point. Analysis with longer sonication times were aimed. However, some limitations related with the high heating of the dispersions during the sonication with the tip hindered further analysis.

Admitting the limitations of the process, 120 minutes are taken as the sonication time that provides best results.

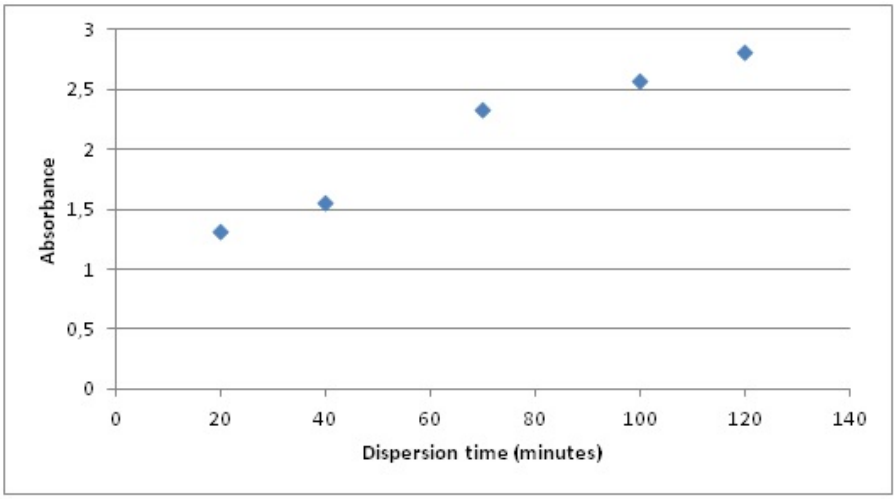

Figure 3.12: Absorbance at time=0 days and λ=660nm as a function of the sonication time in the tip

3.4.2 Surfactant concentration adjustment

The concentration of SDBS used to favor the dispersion and stabilization of the GNP is a main factor in the achievement of successful results. A lack of SDBS can lead to an undercover of the carbonaceous surface of the GNP, leading to an increase in the interface energy between GNP and the water medium and subsequently, to a destabilization of the dispersion. An excess can also affect negatively to the stability due to an oversaturation effect. To this point, the critical micelle concentration (CMC) must be considered as a benchmark. CMC, in colloidal chemistry, is defined as the concentration of surfactant above which micelles form. The so called micelles consist in an aggregate of the surfactant molecules. Generally, the formation of micelles facilitates the dispersion and stabilization of suitable nanoparticles. In the case of SDBS and graphene, it has been even described an exfoliation effect[212].

The effect of the SDBS concentration over GNP dispersions in water is studied in order to find an optimal SDBS concentration that leads to higher GNP concentrations. Different SDBS concentrations are used in the preparation of stable GNP dispersions and their concentrations are measured by their absorption at 660nm wavelength.

According to bibliography, the CMC of SDBS is at 0,544mg/mL (1.59mMolar) [147]. Therefore, values of SDBS concentration for the samples are chosen around it, above and below the CMC. Table 3.9 summarizes the SDBS concen-

trations for each sample, being sample 3 the one that corresponds to the CMC of SDBS.

For the preparation of each sample, the next steps are followed: 1) 10mg/mL of GNP and the chosen amount of SDBS are mixed in 20mL of deionized water by ultrasonication tip for 40 minutes, as these were the conditions found out to lead to best dispersions at initial studies.2) The dispersion is centrifuged for 4 hours at 5000 rpm. The precipitated portion is rejected and the supernatant is kept.

Table 3.9: Summary of the GNP dispersions in water. The SDBS concentration is presented both in molar concentration and in mg/mL for better understanding.

Sample	SDBS Concentration (mMolar)	SDBS Concentration (mg/mL)
1	0.29	0.1
2	0.72	0.25
3	1.6	0.56
4	1.7	0.6
5	1.8	0.64
6	2	0.7
7	2.2	0.75
8	2.9	1

The absorbance for each sample is measured at 660nm wavelength right after the centrifugation (time=0 days). For samples of absorbance above 1, a dilution is carried out to suit the value between 1 and 0 (where the linear relation for the law of Lambert-Beer is valid). Dilution is carried out with water and SDBS at the same concentration than the original sample. The absorbance results are plotted in Figure 3.13.

From the lowest concentration of SDBS, the absorbance increases rapidly as the concentration grows: From values of 0.15 for SDBS concentration of 0.1mg/mL and 0.63 for 0.25mg/mL, to the highest value of absorbance (2.32) at a SDBS concentration of 0.64mg/mL (1.80mMolar). The point for the CMC, which lays between the mentioned values, presents and absorbance of 1.2. Values above 0.64mg/mL quickly decrease to values around 1 and even lower for the highest SDBS concentration.

The results evidence a notable peak of absorption for a SDBS concentration of 0.64mg/mL, slightly above the CMC. This effect of maximum GNP concentration was at first supposed to be at the CMC. An explanation for this shift

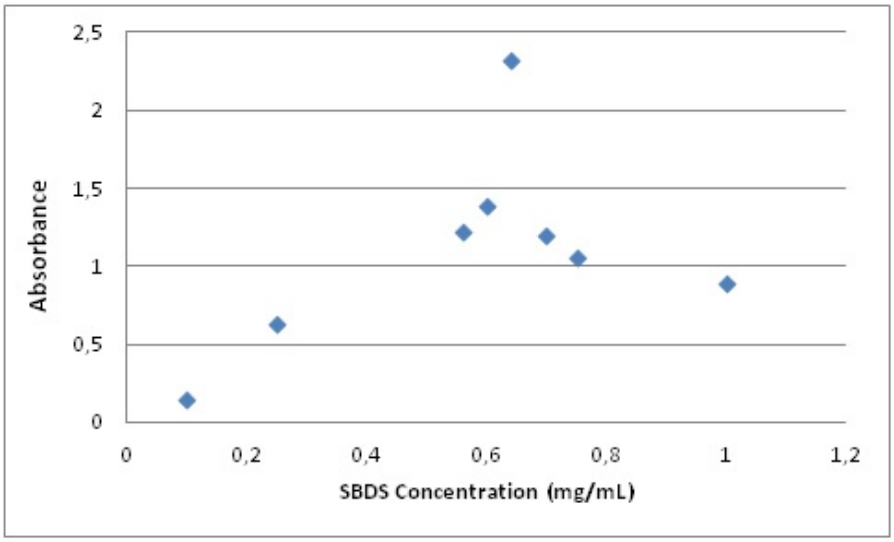

Figure 3.13: Absorbance at time=0 days and λ=660nm as a function of the SDBS concentration in the dispersion

could relay in the interaction between GNP and the SDBS. The alkyl chains in the SDBS are of great importance when forming the micelles. In the presence of GNP, these chains tend to interact with the carbon atoms of the GNP and adsorb over its surface. Thus, a higher amount of SDBS molecules would be necessary to form a micelle, so the CMC increases.

From these results, a SDBS concentration of 0,64mg/mL can be stablished as the optimal amount to obtain the highest GNP concentration in a stable GNP dispersion in water.

3.4.3 Effect of the centrifugation time in the final concentration

Centrifugation is a separation process commonly applied to dispersions. It uses high angular velocities to favor sedimentation. During the centrifugation process, the dispersed particles suffer sedimentation and precipitate from the suspension, differentiating two phases: The precipitated phase, formed by the sedimented particles, and the supernatant, formed by the stable liquid dispersion.

Two factors can be adjusted when employing this technique: Rate (angular velocity) and time. The effect of centrifugation rates over dispersions of graphene and graphene derived materials is well-known and widely described in bibliography[104],[141]. The rate to which dispersions are centrifuged will determine the cutoff size of the platelets that stay in the supernatant, as the average lateral flake size decreases as the centrifugation rate is increased. This means that centrifugation at high rates results in the separation of small flakes, that remain dispersed, from large flakes, which sediment out[106]. 5000 rpm is the highest centrifugation rates studied by these groups and leads to the most stable dispersions.

Just after the sonication, there are GNP aggregates that remain in suspension despite being unstable in middle-term. The centrifugation allows an acceleration of the sedimentation process that otherwise would have required several days. Up to now, the conditions of 5000rpm for 4 hours resulted in dispersions that have proved to remain relatively stable for, at least three weeks, as it has been explained in previous paragraphs.

In this work, the centrifugation step is being used to ensure the stability of the resulting supernatant. Without varying the centrifugation rate, the effect of shorter centrifugation times on the GNP concentration and their stability is studied. The goal is to obtain high concentrated GNP dispersions without losing stability. Additionally, it is aimed to optimize the dispersion method by reducing the centrifugation time (which is, by far, the longest step).

Five samples are prepared to evaluate this effect. The samples are prepared under the same conditions used on previous analysis: 10 mg/mL GNP, 10 mg/mL SDBS, 40 min sonication time. The centrifugation rate is kept at 5000rpm but different centrifugation times are applied to every sample. Conditions for each sample are summarized on Table 3.10.

Table 3.10: Summary of the samples and their centrifugation times at a 5000rpm rate.

Sample	Centrifugation time at 5000rpm (h)	Sonication time (min)	[GNP]o (mg/mL)	[SDBS] (mg/mL)	Volume (
A	0.5	40	10	10	20
B	1	40	10	10	20
C	2	40	10	10	20
D	3	40	10	10	20
E	4	40	10	10	20

The absorbance of the samples is measured at 660nm. To study their stability, the absorbance is measured at t=0 hours and time=480 hours. The results for these measurements are presented in Table 3.11.

Table 3.11: Summary of the samples and their absorbance at different times.

Sample	Absorbance (t = 0h)	Absorbance (t = 480h)	Loss of Absorbance (\%)
A	3.125	2.247	28.1
B	2.481	1.967	20.7
C	2.119	1.765	16.7
D	1.684	1.479	12.2
E	1.492	1.330	10.9

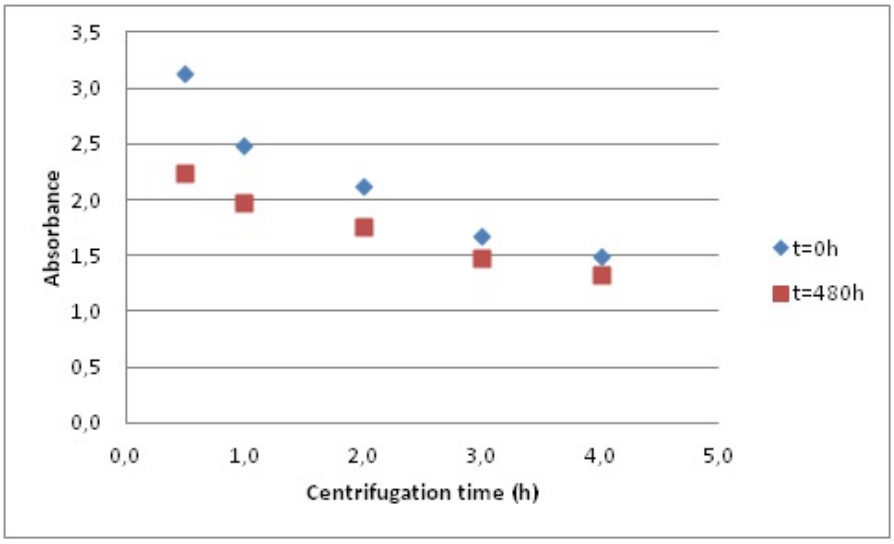

Figure 3.14: Absorbance at t=0h and t=480h for samples with different centrifugation times.

Sample A, presents the highest absorbance. The results for time=0h show a noteworthy decrease on the absorbance as centrifugation time increases. There is a loss of 52.25% when comparing sample A (0,5h centrifugation) and sample E (4h centrifugation). However, the stability increases with the centrifugation time. The percentage of absorbance lost for sample A is the largest (28.1%), whereas sample E shows the lowest of the cluster (10,9%). Results are plotted in Figure 3.14for better understanding.

Both effects can be clearly identified: 1) Shorter centrifugation times lead to more concentrated dispersions. 2) Longer centrifugation times ensure long-term higher stability.

This opens the possibility for adjusting the concentration of a GNP dispersion by controlling the centrifugation time and prepare high-concentrated

dispersions for applications that only require short-term stability.

3.5 Study of an optimized graphene dispersion in water

Along Chapter III, the influence of several factors over the concentration and stability of GNP dispersions in water has been studied and optimized. In this last section, the optimized parameters are used to elaborate a GNP dispersion in order to evaluate the improvement achieved when compared to the initial one (Section 3.3.2). The stability of this optimized dispersion is also studied, from t=0 days to t=21 days. To calculate the GNP concentration, the experimentally calculated value for α will be employed (α=2089 $mLg^{-1}m^{-1}$). Furthermore, the stability of the dispersion is also studied up to 21 days.

The conditions for the dispersion are summarized in 3.12. Centrifugation time is set to 1 hour. It has already been observed that a time of 0.5 hours results in higher values of absorbance. However, the stability showed is lower, for what longer time is chosen in order to achieve better stability results.

Table 3.12: Dispersions conditions for the optimized GNP dispersion in water.

[GNP]o (mg/mL)	[SDBS] (mg/mL)	Volume (mL)	Sonication time (min)	Centrifugation tim
10	0.64	20	120	

Just after the centrifugation and the separation of the supernatant, the periodic measurement of the absorbance begins. Figure 3.15. shows the relation between time and concentration, calculated by applying Lambert-Beer equation.

Thank to the parameter optimization carried out during this study, the concentration results calculated for this dispersion, present higher values than the first one measured in Section 3.3.2. The GNP concentration at t=0 days increases from 0.072 mg/mL to 0.178 mg/mL, a remarkable increase. Regarding the stability, during the first 2 days the sample experiments the main material loss, decreasing the concentration from 0.178 mg/mL to 0.145 mg/mL, i.e. a 18%. For the next 18 days, the concentrations drops just 0.013 mg/mL, from 0.145 mg/mL to 0.132mg/mL, an additional 7.3%, which makes a total loss of 25.3% of the GNP in 21 days. This behavior matches with the analysis carried out in Section3.3.1.

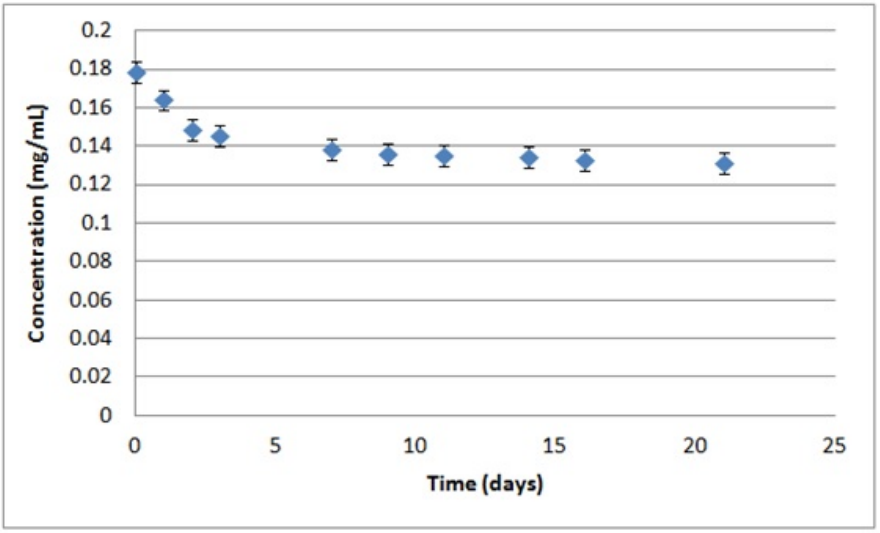

Figure 3.15: Concentration of the GNP dispersion in water as a function of time.

The achievement of 0,178 mg GNP/mL at t=0 days sets the obtained concentration over the value stablished by Y. Song et al [211] (0.1 mg/mL) and very similar to Sriya et al [50] (0.2 mg/mL). These studies, nevertheless, do not include a stability analysis, for what the duration of the GNP dispersed in the solution is unknown.

Finally, the morphology of the GNP on the dispersion is analyzed by SEM. The method tuned in Chapter II is followed: A droplet of 20 μL from the GNP dispersion is dropped over a Si/SiO substrate. The substrate is spun with an acceleration ramp of 600 s from 0 rpm to 2000 rpm. Once 2000 rpm are reached, it keeps spinning for 1000 s. This method proved in Chapter II that it avoids the reaglomeration of separated GNP platelets during its deposition over the Si/SiO substrate. Once the platelets are deposited over the substrate, they are analyzed by SEM. Figure 3.16 shows a representative image of the GNP.

The SEM analysis shows a remarkable reduction in the size of the GNP. The morphological study performed in Chapter II over AvanGraphene GNP showed platelets up to 7.11 x 6.60 μm^2. However, the GNP dispersed in the sample exhibit smaller surfaces, under 4.5 x 3.2 μm^2.

This reduction can be directly related to the combination of three effects: 1) The separation of layers in the platelets by the dispersion process, 2) The surface breakage caused by the application of long tip-sonication times and

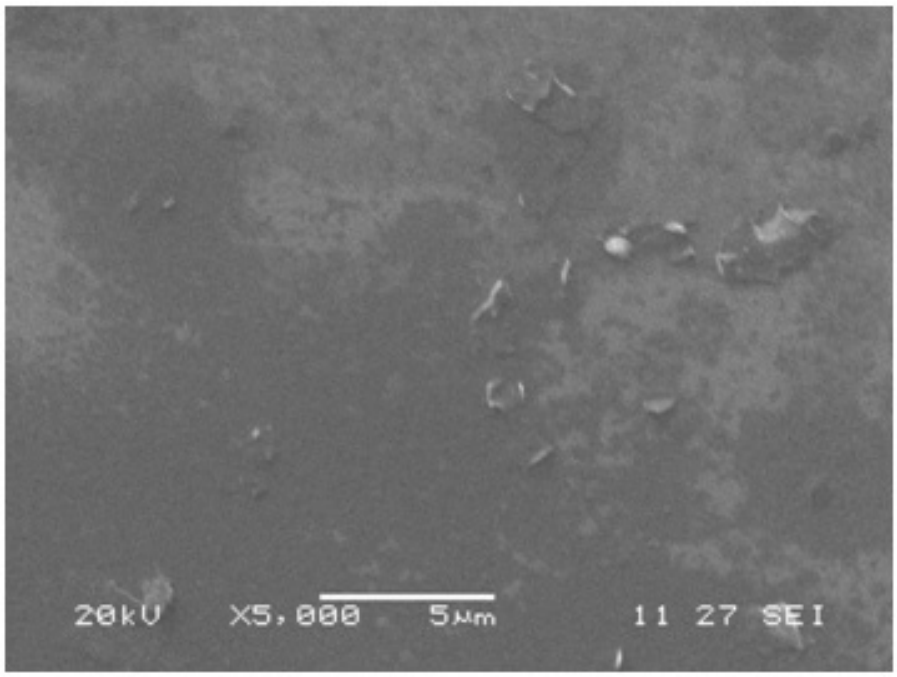

Figure 3.16: SEM image of representative GNP in the dispersion.

3) The separation of the largest platelets by the centrifugation process. The extent of each factor on the reduction of the platelet size will be topic for further studies.

3.6 Conclusions

SkySpring GNP and AvanGraphene GNP are suitable for their dispersion in water when stabilized with SDBS surfactant

Both have been successfully dispersed in deionized water using SDBS as surfactant. They present similar behaviors for low and medium initial concentrations (0.1 mg/mL and 1 mg/mL), with small presence of GNP on the final dispersions. However, for greater initial concentrations the resulting dispersions present more GNPs. This study was used to determine the conditions that enabled further analyses: 20 mL deionized water, 10mg GNP/mL, 10 mg SDBS/ mL, 40 min of sonication tip and 4h centrifugation at 5000rpm. It also showed that shorter periods of sonication with tip (40 min) are more effective towards the dispersion than longer periods with sonication bath (8h).

The absorption coefficient, α, for the system AvanGraphene GNP and SDBS in water has been experimentally calculated.

α, a key parameter for the determination of the amount of GNP in a dispersion was experimentally calculated to be 2089 mL g^{-1} $^{-1}$, with a standard deviation of 9.01. Other authors reported their own calculations for the same system. Table 3.13 presents these values, which are lower than that obtained in this work. The differences in morphology and structure between GNPs could explain the variation between the three studies.

Table 3.13: α values reported by other research teams, in agreement with the value calculated in this work.

Author	α (mL g^{-1} m^{-1})	Reference
Lotya et al	1390	[140]
Sriya et al	1660	[50]
Present work	2089	

The optimal SDBS concentration has been established.

Several concentrations of SDBS were tested in order to find the one that leads to higher GNP dispersion. 0.64 mg SDBS /mL has been established as the optimal for the stabilization of AvanGraphene GNP dispersions in water, leading to the highest GNP concentration.

The effect of sonication times and centrifugation times have been described.

On the one hand, increasingly longer sonication times were studied and it was confirm that they have a direct impact on the final concentration of the GNP dispersions. Longer sonication times lead to higher concentrations, at least up to 120 minutes (the longest time tested). On the other hand, longer centrifugation times reduce the final GNP concentration of the dispersions. However, this dispersions centrifugated for short times present lower stability, as long centrifugations ensure the complete sedimentation of unstable platelets.

The presented dispersion method has proven to lead to stable GNP dispersions. Furthermore, the dispersion conditions have been successfully optimized to obtain higher GNP concentrations with remarkable stability.

At the beginning of this study, stable dispersions with GNP concentrations of 0.072 mg/mL were achieved, validating the method proposed. The carried out optimization process concluded in obtaining dispersions with 0.178 mg GNP/mL. Is not only a noteworthy increase but it also betters some of the reported values (Table 3.14). The optimized conditions are the following: 20 mL deionized water, 10 mg/mL GNP, 0.64 mg/mL SDBS, 120 minutes of sonication tip and 1 hour centrifugation at 5000rpm. In addition to the high concentration, great stability was achieved too, since 74.7% of the material remain dispersed after 21 days.

Table 3.14: Summary of the GNP concentrations in water achieved by other groups with the SDBS concentration they used

Author	GNP Concentration (mg/mL)	SDBS concentration	Reference
Lotya et al	0.05	0.5 mg/mL	[140]
Sriya et al	0.2	2%w/v	[50]
Song et al	0.1	17.5 mg/mL	[211]
Present work	0.178	0.64 mg/mL	

Chapter 4

Graphene functionalization with metal and metal oxides

This chapter gathers the studies carried out on the functionalization of graphene-like materials with different nanoparticles. Three different types of nanoparticles are grown over the carbonaceous substrates: Copper, Zirconia and Manganese oxide. The performance of the metal-graphene composites and the metal oxide-graphene composites on different applications are also analyzed. On the one hand, Copper and Zirconia composites are aimed to form a metal matrix composite (MCC) with bronze. On the other hand, the catalyst activity of the Manganese oxide composite towards the Oxigen Reduction Reaction (ORR) is studied for its potential use in metal-air batteries.

For a better comprehension, the chapter is divided in two different sections regarding the final application aimed with the functionalization.

4.1 Introduction: Approach, Objectives and Experimental details

4.1.1 Approach

As stated in Chapter I, graphene is suitable for many types of functionalizations in order to adapt to a wide variety of applications. One of the fields in which functionalized graphene started to be studied is the Metal Matrix Composites (MMC). MMCs are attracting the attention of the scientific community for structural applications due to its high specific resistance and its thermal and electric conductivities. There are still few publications relating MMC with graphene. Some groups have published studies of the interfacial structure metal/graphene for Al, Cu and Ni, predicting mechanical properties for Al/graphene and temperature effects in thermal conductivity for Cu/Graphene and Ni/graphene[209],[257] , [207] , [33].

Wang et al. are currently working in the fabrication of MMCs of Al-Graphene and in the study of its mechanical properties and the strengthening mechanism in the graphene platelets[248]. Bartolucci and his team[19] prepared and studied Al-Graphene composites made by a ball-milling dispersion followed by hot pressing and extrusion. A reduction in hardness is reported compared to pure Al. An analogous process was followed by S. J. Yan to make aluminum alloys reinforced by graphene nanoflakes. The main goal was to enhance aluminums alloys properties without sacrificing the ductility. They reported a remarkable increase in both tensile and yield strengths keeping the ductility performance.

Graphene/Zirconia composites have also been studied and synthesized by several techniques for different applications. Plasma spraying technique was used by Honqqing et al. [125] to produce Graphene NanoSheets (GNS)/ZrO_2 composites for the increase of wear resistance and the lowering of the friction coefficient. Liu et al. [133] prepared GNP reinforced zirconia toughened alumina nanocomposites using Spark Plasma Sintering, increasing %40 the fracture toughness of the resulting material just by the addition of 0.8% vol. GNP. Ceria-Zirconia/Graphene composites were synthesized by wet impregnation methods for its catalytic activity towards the synthesis of dimethyl carbonate [188]. The addition of graphene to zirconia/alumina composites by ball milling also showed the reinforcing effect of graphene, enhancing the toughness [134]. Additionally, other graphene derivatives have been used with zirconia too: Tao Yang et al. [262] presented an interesting study comparing

Zirconia/rGO composites synthesized by one-step electrodeposition and stepwise electrodeposition, both leading to different nanostructures that displayed different electrical conductivities. According to this study, the globular morphology of the zirconia nanoparticles in one of the samples resulted in larger surface area and higher electrical conductivity. Spark plasma sintering was reported by Jung-Hoo et al. [200] as a successful technique for the elaboration of ytttria-stabilized zirconia/rGO comoposites. Electrochemical techniques have been used by Mudila et al. [153] and Virendra et al. [205] for the synthesis of zirconia composites, in these cases with GO. Furthermore, GO/zirconia composites have also been prepared by "one pot mild method [167].

Copper has also been used as versatile matrix in the MMC fabrication with graphene and graphene-like materials. Bin Li et al. used a ball milling technique to successfully produce Cu/Graphene composites [23]. Later, W. J. Kim et al [113] used the same technique in combination with high-ratio differential speed rolling to disperse MLG particles into Cu matrix. The obtained 1 vol.% MLG/Cu composites presented a noteworthy strength increase. E. K. Athanassiou and R. N. Grass reported the synthesis of Graphene/Cu nanoparticles by a reducing flame synthesis that used Cu-2-ethythexanoate as precursor [12], [197], [236]. Sanggeun et al. employed the same technique [123] and improved the process [55]. Y. Tang et al. [222] achieved great results by preparing GNS-Ni/Cu composites too. They firstly synthesized GNS-Ni hybrids by an in situ chemical reduction method. Secondly, they added these hybrids to a Cu matrix, achieving the GNS-Ni/Cu composites by spark plasma sintering. For additions of only 1,0% vol% GNSs, a 61% increase in Youngs modulus (132 GPa) and a 94% improvement in yield strength (268 MPa) were reported. Also, Liu Aiping et al. [132] and Zhao Yo Cheng et al. [258] separately reported the synthesis of Cu/Graphene composites by liquid phase reduction reaction. In addition to the improvement in mechanical properties, several authors like Nieto [155] et al. and Lei Zhang et al. [276] pointed out the thermal conductivity enhancing potential of Graphene/Cu composites. Jagannadham carried out several studies to this regard [96]. He used an electrodeposition technique to produce plated Graphene/Copper composites and achieved a 116% increase on thermal conductivity for Graphene loadings of 14%wt. and even a 131% increase for 35%wt Graphene [97]. Thermal conductivity increases were also reported for similar composites with carbonaceous nanomaterials like MWCNT/Cu [44], [45] and Graphite/Cu [26], with a 140% increase compared to regular copper.

The results are certainly promising. However, all things considered, for a better understanding on the behavior of graphene and graphene-like nanofillers in MMCs, further investigation has yet to be accomplished.

There are two necessary topics that must be front faced when introducing nanofiller into a MMC: 1) The thermal stability. The elaboration of MMCs often involves the use of high temperatures in which carbonaceous materials would decompose. It is necessary to ensure the stability of the filler inside the metal matrix during its manufacturing. 2) The wettability of the metal over the filler. The tendency of graphene and its derivatives towards aggregation is well-know and already described. A good interaction between the platelets and the metal matrix is required to ensure a homogeneous dispersion of the filler along the composite. Furthermore, a big interaction between the reinforcement graphene and the metal matrix would lead to a better charge transfer.

In this section, the introduction of graphene-like materials in a well-known industrial bronze is studied. The introduction of these nanofillers aims the improvement of the thermal conductivity keeping the mechanical properties of the original bronze. As it is required in the elaboration of many metal products, high temperatures are applied during its processing and modeling. For the studied industrial bronze, temperature treatments up to 1100°C are applied.

In order to fulfill the two requirements just mentioned above, namely thermal stability and wettability, the covering of the graphene-like materials with copper nanoparticles and with zirconia nanoparticles is proposed. On the one hand, copper is present in the composition of the bronze (the original bronze contains between a 14,2%wt. and a 21%wt. of copper) for what the wettability is ensured, whereas zirconia is expected to favor the wettability for its metal nature. On the other hand, the thermal stability of the employed graphene derivatives is expected to improve with the covering of these nanoparticles.

A first step requires selecting the most suitable graphene-like material for its introduction in the MMC. The most important feature to be evaluated at first is their thermal stability, a key factor that could limit the use of some of them. Then, the functionalization processes need to be studied and settled to ensure a complete and homogeneous covering of the platelets, which favors its wettability and stability. The growth of copper nanoparticles is carried out by a plating electroles method and the growth of zirconia nanoparticles by a hydrothermal method. Finally, once the conditions for the functionalization of an appropriate graphene-like nanofiller is established, the elaboration of a MMC with the industrial bronze using the self-made graphene-metal compound is attempted in order to evaluate its impact on the thermal conductivity of the bronze and on its physical properties.

4.1.2 Objetives

The main objective of this section is to study the use of functionalized graphene nanofillers to enhance the thermal conductivity of an industrial bronze without reducing mechanical properties. In order to achieve this goal, several steps must be accomplished:

- To study the thermal stability of different graphene derivatives in order to evaluate its potential use as nanofiller in bronze (which requires high temperatures for its elaboration)
- To perform the functionalization of the selected graphene derivative with Cu nanoparticles by an electroless method for different initial conditions.
- To characterize the morphology, homogeneity and distribution of the obtained Cu nanocomposites in the graphene/Cu nanocomposite.
- To study the functionalization of the selected graphene derivative with ZrO_2 nanoparticles by an hydrothermal method for different initial conditions.
- To characterize the morphology, homogeneity and distribution of the obtained ZrO_2 nanoparticles in the graphene-derivative/ ZrO_2.
- To study and compare the retardation effect of the Cu and ZrO_2 functionalizations over the thermal decomposition of the functionalized graphene derivative.
- To perform a preliminary study on the incorporation of functionalize graphene-like material into a bronze matrix.
- To study the effect of the addition of the nanocomposite on the thermal and mechanical properties of the bronze MMC.

4.1.3 Experimental details

Graphene derivatives

Three different graphene-like materials are initially proposed for its use in this section: AvanGraphene GNP, Graphenea GO and Graphenea rGO. All of them have already been presented and thoroughly characterized in Chapter 2.

Characterization

The thermal stability can be studied by Thermal Gravimetric Analysis (TGA). In this technique the sample is heated in different atmospheres and the weight loss for each temperature is measured. It allows simulating the conditions in which the nanoadditives would be added to the bronze, permitting to predict its behavior.

The morphological characterization of the grown nanoparticles is carried out with a SEM Model JOEL JSM-5910LV/ INCA300 that includes a Energy Dispersive Spectroscopy (EDS) device.

Growth of Cu nanoparticles

An electroless plating method is employed for covering the platelets with Cu nanoparticles. For the process, which is explained in detail later, SDBS ($C_{12}H_{25}C_6H_4SO_3Na$) (Aldrich, tech. quality), $CuSO_45H_2O$ (Aldrich, ReagentPlus >99%), NaOH (Aldrich, reagent grade >98%), Potassiu sodium tartrate tetrahydrate (Aldrich, ACS reagent 99%) and HCHO (Aldrich, ACS reagent 37 wt. % in H_2O, contais 10-15% methanol as stabilizer to prevent polimerization) are used.

Growth of ZrO_2 nanoparticles

A simple hydrothermal synthesis is used for covering the platelets with ZrO_2 nanoparticles. The details are explained later. NAOH (Aldrich),SDBS ($C_{12}H_{25}C_6H_4SO_3Na$) (Aldrich, tech. quality) and $Zr(OH)_4$ are employed in the synthesis.

Bronze MMC elaboration

An Elin 50Kw-15KHz induction oven from GH is used for the metal fusion. It has a spire of 100mm in diameter. The fusion process is carried out in a Morgan Salamander A1 model graphite melting pot, covered in its inside by a boron nitride layer. Pictures of both tools are presented in Figure 4.1.

4.2 Selection of the carbonaceous material

GO, rGO and GNP are the graphene-like materials evaluated for its covering with nanoparticles and its future introduction in a bronze MMC.Two key factors have been pointed out to this regard: wettability and thermal stability.

Figure 4.1: Images of the GH. Elin oven and the Morgan Salamander melting pot.

As the platelets must be covered by a continuous nanoparticles layer, their nature would not have an impact on the final wettability. The thermal stability, nevertheless, can be a limiting factor when selecting the material. A thermal analysis has been done to study their thermal behaviour.

The melting point for different carbon allotropes can vary depending on their structure, the strength of the atom-atom bonds and the presences of van der waals forces, what is indicative of different thermal behaviors and thermal stability. J. Lin et al. studied the stability of graphite finding no weight loss in the range of 100°C to 800°C[131] under air atmosphere. This absence of weight loss indicates a great stability for the temperature range. However, as already stated, GNP and other graphene derivative nanostructures present different thermal stabilities. According to different groups[269],[40] , [279]. GO presents a main weight loss around 200°C due to the presence of carboxilic groups in the structure. Y. Guo and its team deepened in this effect studying the thermal stability of two rGO with different amount of defects[86]. The reduction eliminates functional groups and restores the sp2 hybridized carbon structure. The data presented show that the more effective the reduction, the higher the thermal stability. Less reduced rGO decompose at lower temperatures.

Different authors have already asserted the capacity of carbonaceous nanomaterials, such as carbon nanotubes [199] and graphene platelets [269], to "survive" high temperature sintering processes. From the three different graphene-like materials have been characterized along this thesis (GNP, GO and rGO), according to the bibliography and the theoretical models, GNP should present

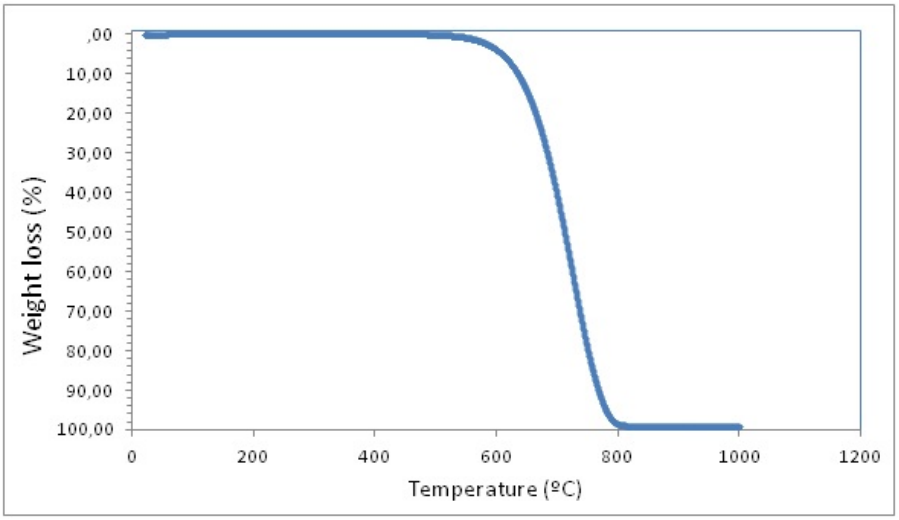

Figure 4.2: TGA curve for AvanGraphene GNP under air atmosphere and 5°C/min ramp.

the best thermal stability. Thus, the study will begin with the evaluation of this material.

AvanGraphene GNP are analyzed by TGA, setting a temperature range from room temperature to 1300°C, with a rise ratio of 5°C/min and under air atmosphere. Figure 4.2 shows the results for the described analysis. GNP presented a remarkable stability for temperatures under 550°C, where they did not suffer any weight loss. At 570°C, however, the decomposition of the material begins, as indicated by the weight loss. The carbon atoms in the structure of the platelets react with the oxygen in the air forming CO_2 and CO, what causes the weight loss. There is a continuous and rapid decrease on the weight between 570°C and 800°C, where 100% of the material disappeared. The test was stopped at 1000°C as no rests of GNP were present.

The thermal stability of the GNP is high when compared with the results published for similar materials: graphite nanosheets (380°C) and GO (200°C). The temperature achieved by the GNP without decomposing is remarkable. However, the TGA analysis took more than 3 hours and a half to complete the heating process (due to the 5°C/min ramp). These conditions are not similar to the ones that would suffer the nanofiller when introduced to the metal matrix, where the temperature is already above 1000°C and, therefore, the heating is remarkably faster. Thus, to emulate at its best the conditions in which nanoadditives are mixed with the metal matrix, the test will be carried out in a temperature range from 20°C to 1300°C with a temperature increase of 50°C/min,

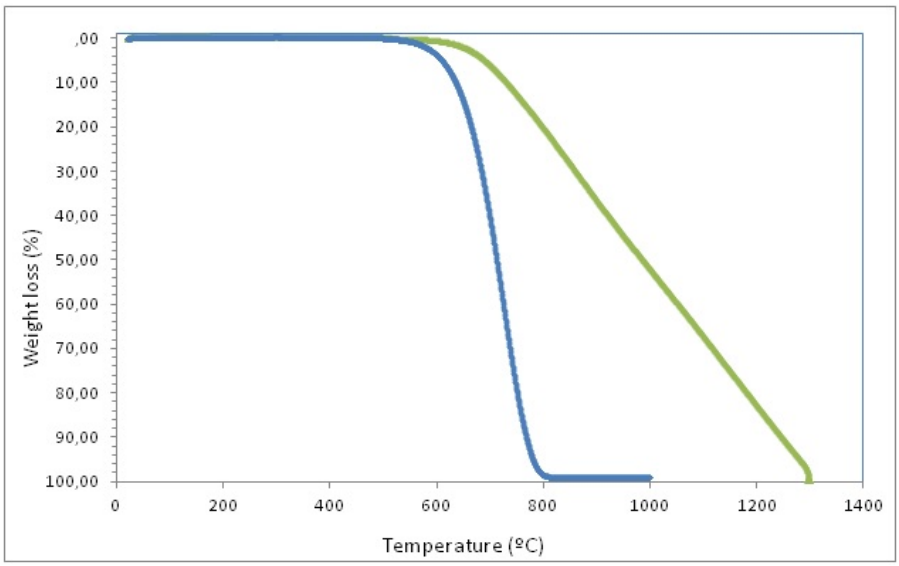

Figure 4.3: TGA curve for AvanGraphene graphite nanoplates under air atmosphere with 5°C/min ramp (blue) and 50°C/min ramp (green).

under air atmosphere. It is the highest acceleration ramp available in the TGA, closer to the rapid heating inside the MMC during its elaboration. Figure 4.3 presents the results of the two TGA analysis done over AvanGraphene GNP at 5°C/min and 50°C/min heating ratios.

The temperature at which the weight loss begins is slightly higher for the sample tested at 50°C/min ramp. Both samples lose practically the 100% of their mass, however, the sample heated at 5°C/min limits this loss between 570°C and 800°C whereas the other sample begins the loss at 600°C and ends it around 1300°C. The difference in the mass percentage lost at temperatures over 570°C is related to the capacity of the O_2 molecules to reach the carbon atoms and react. At a high speed heating ramp, the material presents more stability due to its inability to decompose fast enough. This result indicates that rapid changes in the temperature of the material during the fabrication of the MMC could avoid the disintegration of the graphite nanoplatelets.

The 50°C/min heating ramp not only emulated the sintering conditions more precisely but it also resulted in better stability results for the GNP. Thus, the same conditions are applied to the GO and rGO samples to evaluate the thermal stability.

A comparison of the TGA results for GNP, GO and rGO with a heating ramp at 50°C/min under air atmosphere is presented in Figure 4.4. The behav-

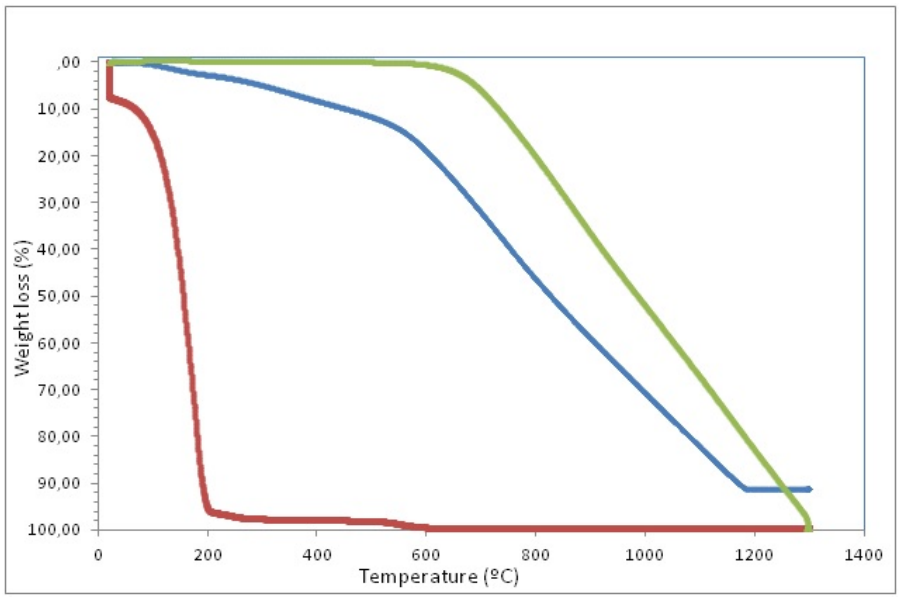

Figure 4.4: TGA curve for three graphitic materials: Graphenea GO (red), Graphenea rGO (blue) and Avanzare AvanGraphene (green). With a 50°C/min ramp and under air atmosphere.

ior of the samples presents clear differences. GO, as previously explained in the characterization chapter, is provided as slurry. It shows a loss weight of almost 100% between 0 and 200°C were not only there is a total loss of solvent (water) but also the decomposition of the carbon atom structure. After this initial and sharp loss, a second one is noticed, slower, between 200°C and 530°C, until the complete elimination of GO.

For the rGO sample, the loss of the carbon atoms begin around 150°C and continues for the whole heating process (up to 1000°C). For GNP, nonetheless, the loss does not start until 600°C. This marked difference is directly related to the defects in the carbon atom lattice and the presence of functional groups in the structure. The Raman characterization carried out in Chapter II allows to know the amount of defects and functional groups in the samples and to correctly evaluate its impact on the thermal stability.

Functional groups and defects are vastly present in the structure of GO, what makes the weight loss to appear at lower temperatures. The reduction process to obtain rGO from GO eliminates most of the functional groups and restores the carbon lattice, reducing the amount of defects, thus, the weight loss, despite starting around the same temperature, remains until over 1000°C.

Meanwhile, GNP hardly present any functional group and suffer presents lattice defects, for what it remains stable up to 600°C.

The understanding of the role of defects and functional groups in the carbon atom lattice during heating process will be very important to correctly evaluate the thermal stability of the synthesized samples.

From the results obtained with the thermal stability study of the graphene-like materials, GNP can be clearly identified as the most stable and resistant to heating treatments. As pointed out at the beginning, thermal stability is a key factor for the selection of the appropriate nanomaterial. Thus, the two functionalization processes studied in these sections will use AvanGraphene GNP as carbonaceous substrate.

4.3 Graphene functionalization with Cu

This section studies the functionalization process followed for the obtaining of good quality GNP covered by copper nanoparticles. Tecnalia has previous experience in copper/carbon composites. Several articles have been published on the manufacture[18] and characterization of Cu/carbon nanofibers composition with great results[138]. A electroless plating technique has been successfully used by its researchers[17] for the elaboration of the composites[16]. However, its use over GNP was still to be attempted in Tecnalia.

This technique, also known as autocatalytic plating, has been massively employed in the printed circuit industry as well as in the obtaining of protective thin films. Some groups around the world have successfully employed electroless plating for the covering of GNP with Cu, as stated in Chapter I. However, they used different conditions than the ones employed in this work. Peng et al. [172] and Zhao et al. [281] as carbonaceous substrate to functionalize used graphene oxide nanosheets (GOS) and GO respectively instead of GNP. The functionalization carried out by Liu et al. [132] consisted in the immersion of a Cu foil in the electroless bath in the presence of graphene and is later slowly removed. The electroless method followed here is analogous to the one used by Barcena for the convering of carbon nanofibers [15]

The process consists on a reduction-oxidation chemical reaction that leads to the deposition of metallic particles on the top of the substrate. Over non-activated substrates, such as GNP, it is necessary to catalyze the surface prior to the coating process. Predominantly, the activation is carried out by adsorbing

Sn and Pd ions on the substrate surface. The ions are attached to the substrate by immersing it into $SnCl_2$/HCl colloidal solution (called sensitization step) and $PdCl_2$/HCl colloidal solution (called activation step).

After the surface of the substrate is activated, the metal particles are deposited by a last step called <<Plating step>>, that requires the use of the following agents:

Solvent: The medium were the graphene will be dispersed and the reaction takes place. For these samples, deionized water is used. Furthermore, a surfactant is used as surfactant to facilitate and to ensure the correct dispersion of the graphene. In chapter III it was ascertained the reliability of SDBS for the successful dispersion of GNP in water. Thus, SDBS is used to avoid the aggregation of the platelets during the functionalization process.

Metallic salt: Is used as the source for metallic ions. $CuSO_45H_2O$ is employed in this case.

Buffering agent: It is required to control the pH of the solution, a key factor for the correct development of the reaction. NaOH is used.

Complexing agent: Is used for complexing the metal salt in order to improve its solubility in the solution. It prevents the metallic salt from reacting with other agents, thereby avoiding precipitation. Sodium and Potassium tartrate is employed.

Reducing agent: Reduces the metallic ions to metal on the substrate surface. HCHO is used for this synthesis.

The whole electroless method is resumed in Figure 4.1.2.3 to facilitate its global understanding. The process requires about 12 hours to obtain the final product. The quantity obtained depends strongly on the initial concentration of graphite nanoplates.

As expected, the control of the temperature and even more the pH of the plating bath are of great importance for the correct and controlled deposition of the metal. Different bath processes require different conditions, already compiled in several manuals[171],[145]. Furthermore, Dr. Barcena, researcher at Tecnalia Research & Innovation, also developed a study on copper plating process, in which this work is based.

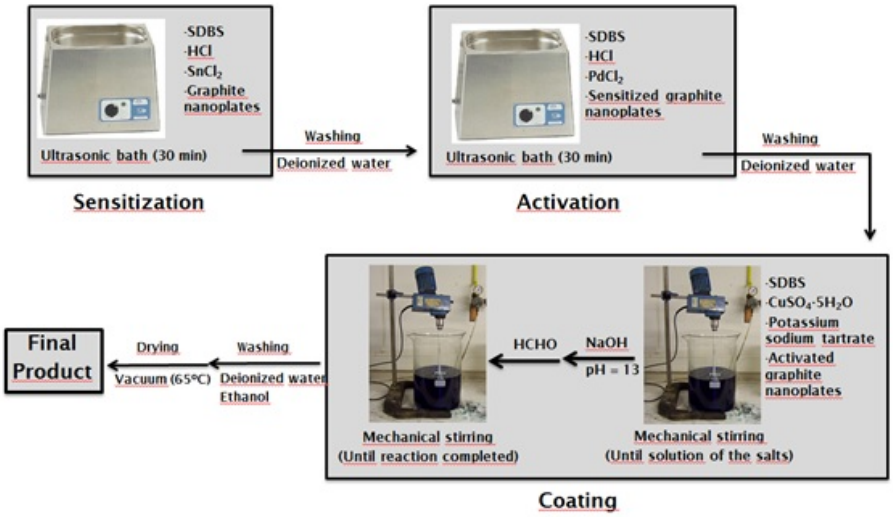

Figure 4.5: Resume of the electroless method for covering surfaces with metal Cu.

After some preliminary tests and based on the current bibliography, pH=13 and 25°C were the chosen conditions for the plating bath process.

The composition and conditions of sensitization bath are resumed in Table 4.1 For all the prepared samples, the graphite nanoplates were immersed in the sensitization bath while ultrasonicated in bath for 30 minutes. The bath consists in an aqueous colloidal dispersion of $SnCl_2$ particles in HCl. SDBS is used to facilitate the deagglomeration of the graphite nanoplates. Homogeneous black dispersions are obtained. Afterwards, the solutions were vacuum filtered and washed carefully with distilled water.

Table 4.1: Sensitization bath composition.

Products	Parameters
Hydrochloric Acid- HCl	100mL / L
Tin Chloride-$SnCl_2$	25g / L
Sodium dodecylbenzenesulfonate- SDBS	0,175g / L
Time (min)	30
Temperature (°C)	22

After the graphite nanoplates were sensitized and well washed, a second bath treatment was required, which was in fact the activation step. The graphite nanoplates are immersed into an aqueous colloidal suspension of $PdCl_2$

particles in HCl. Table 4.2 resumes the composition and conditions of the bath. During the activation bath the graphite nanoplates were also bath sonicated and after the 30 minutes treatment the resulting black dispersion was also vacuum filtered and washed with deionized water, as performed with the sensitization bath.

Table 4.2: Activation bath composition.

Products	Parameters
Hydrochloric Acid- HCl	1,25 mL /L
Tin Chloride-$PdCl_2$	0,625mg / L
Sodium dodecylbenzenesulfonate- SDBS	0,175g / L
Time (min)	30
Temperature (°C)	22

This two-step activation process is easy and cost effective. Both sensitization and activation solutions are reusable for several treatments. It can be reused until the metal-ions are consumed, that it is noticed when the solution turns transparent, being then necessary to prepare a new one.

Once the graphite nanoplates were activated, the coating step takes place. It consists in a reduction-oxidation reaction where copper sulphate is the source of the Cu ions. Table 4.3 resumes the composition of the bath employed in this step. NaOH and formaldehyde are used as pH buffer and reducing agent respectively, whereas potassium sodium tartrate is the complexing agent that eases the solubility of the copper ions and prevents it from side-reacting with other agents. It is very important that all the compounds of the coating bath are well dissolved before adding the activated graphite nanoplates, for what continuous and energetic stirring is mandatory.

Table 4.3: Coating bath composition

Products	Parameters
Copper sulphate-$CuSO_4$	10 g/L
Potassium sodium tartrate-NaK(COO)2(CHOH)2•$4H_2O$	2 g/L
Sodium Hydroxide- NaOH	Until pH=13
Formaldehyde-HCHO	30 mL/L
Time (min)	Until complete reaction
pH	13
Temperature (°C)	22

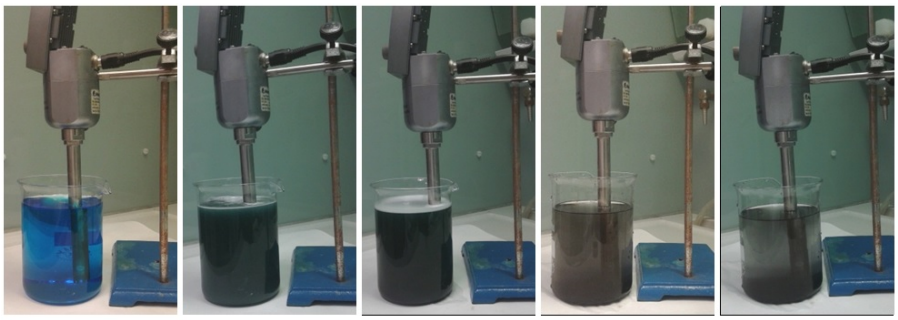

Figure 4.6: Evolution of reduction-oxidation reaction over time: a) before adding graphite nanoplates, b) 0 minutes, c) 10 minutes, d) 25 minutes and e) 35 minutes.

The mechanism of copper decomposition consists on the reduction of copper ions on the activated surface of the graphite nanoplates. The electrons are captured by the reducing agent. Both anodic and cathodic reactions are:

Equation 4.3.1. (anodic reaction)

$$HCHO + OH^{-} \rightarrow HCOO^{-} + H^{2}$$

Equation 4.3.2. (cathodic reaction)

$$Cu^{2+} + 2HCOO^{-} + 3H^{2} \rightarrow Cu^{0} + 2HCHO + 2H^{+}$$

Equation 4.3.3. (Complete reaction)

$$Cu^{2+} + H^{2} + 2OH^{-} \rightarrow Cu^{0} + 2H_{2}O$$

The end of the reaction can be identified by the end on the bubble and the clarification of the solution (this clarification can be partially hidden by the black color of the graphite nanoplates). The process is shown in Figure 4.6 To the end of the reaction all the copper from the salt is converted to metallic copper over the platelet surface.

After the reaction is completed, the graphite nanoplates covered with Cu are carefully vacuum filtered and washed several times with water and ethanol, ensuring a last washing process with ethanol to facilitate the drying process. The use of high temperatures can favor the oxidation of the metal Cu leading to oxides such as $Cu^{2}O$ or CuO. Therefore 65°C was the used temperature for

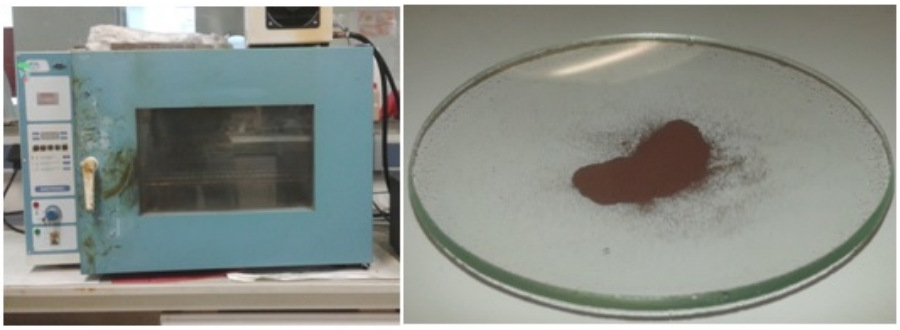

Figure 4.7: Purification process: a) Heater and b) macroscopic appearance of composite powders after coating.

the drying step, for a period that varies on the sample and could last up to 8 hours.

The result aimed with the electroless deposition is to obtain a uniform and homogeneous covering of metal Cu over the whole surface of the GNP. The lack of covering on some platelet areas would expose them to direct contact with the metal matrix, decreasing the wettability. Moreover, those areas would be unprotected by the metal layer when suffering a heat increase.

4.3.1 Study of GNP/Cu ratio

The relation between the amount of copper salt and the initial amount of graphite nanoplates can significantly affect the morphology and the homogeneity of the Cu layer. Maintaining the quantities and concentrations of the rest of components, three samples with decreasing GNP concentrations were synthesized. Conditions are summarized in Table 4.4

Table 4.4: GNP concentration for each sample.

Sample	Graphite nanoplates initial concentration
Gr-Cu-1	1 g/L
Gr-Cu-2	0,2 g/L
Gr-Cu-3	0,05 g/L

Assuming a complete reaction, it is clear that higher fraction of graphite nanoplates leads to a lower weight percent of copper and, subsequently, to thinner coatings. The effect is clearly illustrated in Figure 4.8, where a macroscopic image of samples Gr-Cu-1, Gr-Cu-2 and Gr-Cu-3 are displayed. The

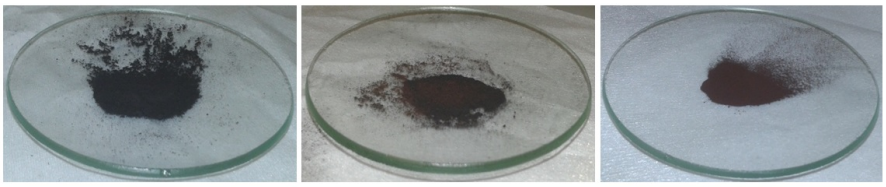

Figure 4.8: Macroscopic images of Gr-Cu-1, Gr-Cu-2 and Gr-Cu-3 samples.

difference in color from graphite nanoplates (black) and metal copper (brown-orange) enables an optical inspection to provide qualitative information about the amount of metal in the composite. Sample Gr-Cu-3 presents a clear brownish color, where hardly any presence of black can be noticed, whereas sample Gr-Cu-1 shows an opposite appearance, with a prevailing presence of black powder. Gr-Cu-2, as expected, lies in the middle with a semi-black semi-brown color.

4.4 Morphologic characterization

Further morphological characterization is, of course, required and the three samples where studied by Scanning Electron Microscopy (SEM).

Two SEM images of sample Gr-Cu-1 are displayed in Figure 4.9 The first one, offers an overall perspective of the graphite nanoplate. Graphite nanoplates are predominant in the sample and hardly any presence of metal copper can be found to this magnification. Figure 4.9 B (x20000), shows the presence of Cu all over the platelet. The metal copper has been deposited forming small sphere particles with approximately 200nm.

In this sample, metal copper growths quite homogeneously over the graphite platelets, with no huge agglomerations. However, as it can be noticed, a complete coating of the platelet is not reached and several areas of carbonaceous surface are exposed. The aim of total covering of the GNP is valuable for a correct thermal protection.

Figure 4.10 shows two SEM images for sample Gr-Cu-2. Image 4.10 (a) provides an integrated perspective of the mixture. The graphite nanoplates in this sample are quite aggregated. For a magnification of 1000x, Cu agglomerates can be seen too, what makes a notable difference with sample Gr-Cu-1 and confirms what stated with the optical analysis.

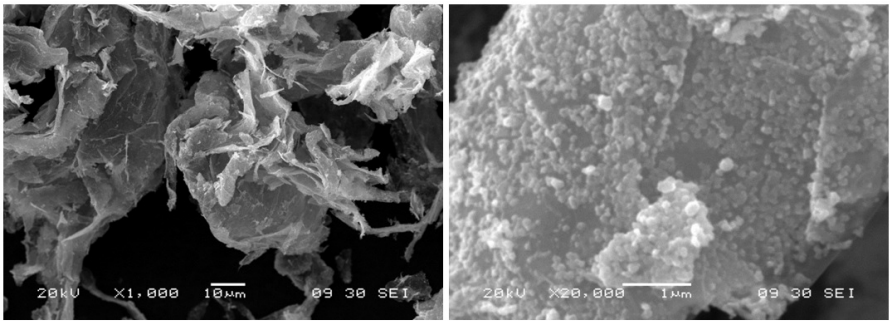

Figure 4.9: SEM images of Gr-Cu-1 at (a) 1.000x, (b) 20.000x

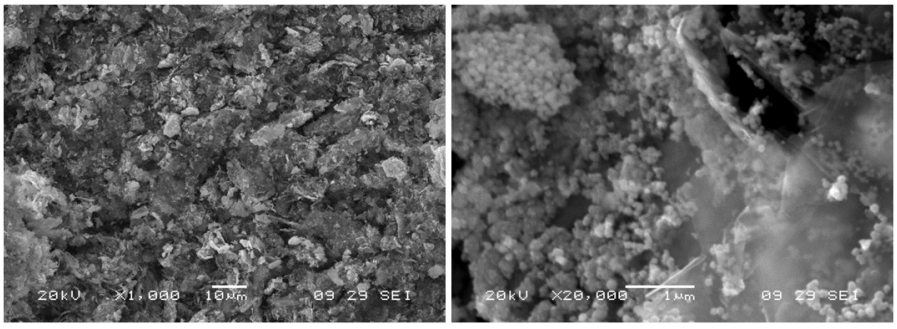

Figure 4.10: SEM images of Gr-Cu-2 at (a) 1.000x, (b) 20.000x

When focusing on a single platelet, image "b", the larger amount of copper metal is still observed. Cu adopts the morphology of small particles with sizes between 350nm and 150nm. Despite the noteworthy presence of Cu, not all the surface of the platelet is covered. There are some areas where the absence of metal particles is notable. Some aggregates of Cu particles up to 2μm can be also found.

The SEM images of the last sample, Gr-Cu-3, are presented in Figure 4.11. This sample corresponds to the one with the lowest amount of graphite nanoplates, for what is no surprise to find the highest amount of Cu in the images. The graphite nanoplates observed in image "a" are surrounded by copper metal, which forms aggregates of few microns in size and are randomly distributed, what gives an impression of inhomogeneity. However, when focusing deeper into one platelet, image "b", an homogenous layer of Cu nanoparticles grown over the graphite nanoplate can be found. No spots of carbonaceous material are exposed, being a good indicator of a full coverage.

In the three cases the obtaining of GNP platelets covered by Cu nanoparticles has been achieved. Clearly identifiable sphere-like Cu nanoparticles have

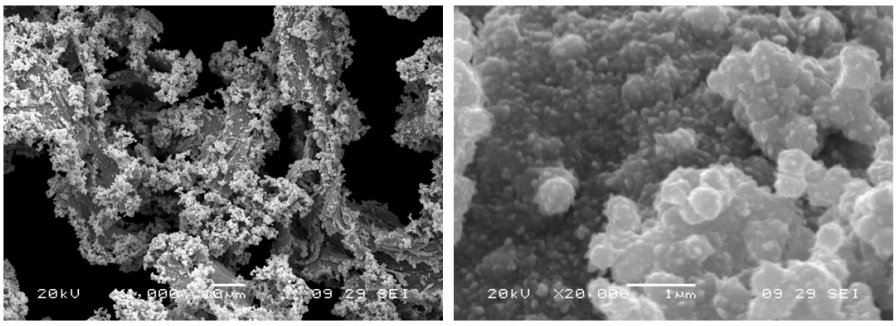

Figure 4.11: SEM images of Gr-Cu-3 at (a) 1.000x, (b) 20.000x

successfully grown on the surface of the platelets, leading to Cu/GNP composites.

The results also evidence the importance of the Cu salt:GNP ratio. Uncovered GNP areas, that where pointed out as a main drawback, appeared on samples Gr-Cu-1 and Gr-Cu-2. In order to obtain a continuous Cu layer over GNP, the Cu salt (the precursor) in the initial reaction needs to be high. If the Cu salt is not high enough, some GNP surface areas will remain uncovered after the functionalization.

The explanation for the presence of uncovered areas is related to the electroless plating growth mechanism. Cu nucleates from Pd catalytic particles previously adsorbed on the platelet surface during the activation step. Once the first Cu atoms begin to nucleate over Pd, the next Cu atoms will grow over that nucleus. This growth happens in three dimensions, [195], [61], leading to the spherical morphology found for the three samples. The spherical morphology was expected and is in clear agreement with the results reported by several author in similar Cu electroless plating over carbonaceous surfaces [281], [272], [15]. The sizes vary between reports due to the slight difference in the functionalization conditions.

Figure 4.12 presents the TGA results for GNP/Cu composites compared to pristine GNP. The conditions used are the ones established in Section 4.2 (50°C/min and air atmosphere). Resutls for GNP are presented in green where as Gr-Cu-1 is purple, Gr-Cu-2 dark-blue and Gr-Cu-3 light-blue.

The three GNP/Cu sample initially suffer a weight increase. Gr-Cu-1 begins this increase at 240°C, reaching a maximum of 3% weight increase at 348°C. Gr-Cu-2 begins the increase at 201°C, reaching a maximum of 12% weight increase at 342°C. Finally, Gr-Cu-3 begins the increase also at 240°C, reaching

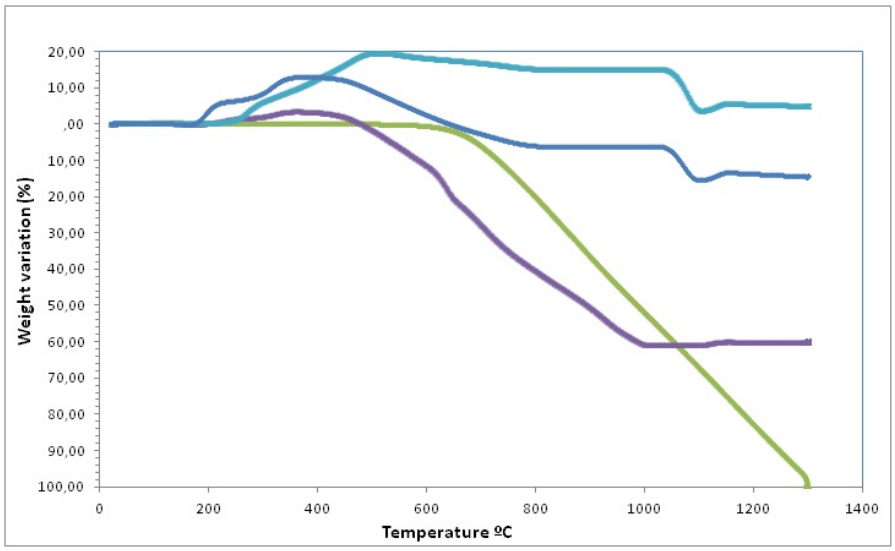

Figure 4.12: TGA curve for samples Gr-Cu-1 (purple), Gr-Cu-2 (dark-blue) and Gr-Cu-3 (light-blue) compared to plain GNP (green). With a 50°C/min ramp and under air atmosphere.

a maximum of 20% weight increase at 500°C. The increase in weight is a direct effect of the Cu oxidation, following the reactions described in Equations 4.4.2 and 4.4.3, clearly indicating the higher presence of Cu on Gr-Cu-3, followed by Gr-Cu-2, and Gr-Cu-1 being the sample with lowest Cu quantity, as expected. However, the amount of copper in each sample can not be totally quantified because some GNP loss might be occurring at the same temperature.

Equation 4.4.2

$$2Cu + O_2 \rightarrow 2CuO$$

Equation 4.4.3

$$2Cu + 1/2\ O_2 \rightarrow Cu^2O$$

All the GNP/Cu samples, despite the Cu covering, present clear weight losses for temperatures bellow 600°C. The decomposition of the carbon atom lattice of the GNP is the reason for these losses. Nevertheless, plain GNP begin their decomposition at 600°C. This reduction in the decomposition temperature must be attributed to the increase of defects in the graphene lattice during the plating process.The lack of accuracy determining the percentage of GNP in the

samples makes it impossible to confirm with the TGA the amount of GNP in the residues at 1300°C.

Attending to the TGA results and the SEM images, **Gr-Cu-3 sample would be the most appropriate one for its introduction as nanofiller in the bronze MMC**. It showed the most homogeneous Cu covering of the GNP samples. The nanoparticles covered the complete surface, with no exposed GNP areas. Moreover, this sample thermally decomposed at the highest temperature.

4.5 Graphene-ZrO_2 synthesis

Functionalization process for the covering of GNP with zirconia nanoparticles is described and studied in this section. The aimed objective is to cover the graphene nanoplatelets with ZrO_2 nanoparticles in order to achieve an increase in the wettability and the temperature of decomposition. The synthesis method chosen for the functionalzation is hydrothermal reaction. Tecnalia already worked on the synthesis of Zr and ZrO_2 over carbonaceous supports for several years, principally over CNT. The research team in Tecnalia accomplished the functionalization of CNTs by hydrothermal reaction. However, none synthesis over GNP has been carried out yet.

Few studies have been published on the hydrothermal synthesis of ZrO_2 over graphene-like materials. Some authors work with GO as precursor, which is oxidized during the reaction, leading to ZrO_2/rGO composites [163]. Graphitic sources have also been employed for the functionalization with zirconia [228]. Non hydrothermal synthesis of ZrO_2/GNP composite has been reported to our concern.

Hydrothemal synthesis, as its name suggests, implies a chemical reaction in a regime of high temperature and high vapor pressure in the presence of water. The pressure must be above 1 atm whereas temperature should surpass 100°C. These conditions usually require the use of a special reaction reactor called autoclave that will be explained later in detail.

The reaction requires 4 different compounds for a correct performance:

Solvent: The medium in which the reaction will take place. The selection of an appropriate solvent is very important, as its boiling temperature will affect the vapor pressure and the equilibrium of the reaction. In this case, deionized water is employed.

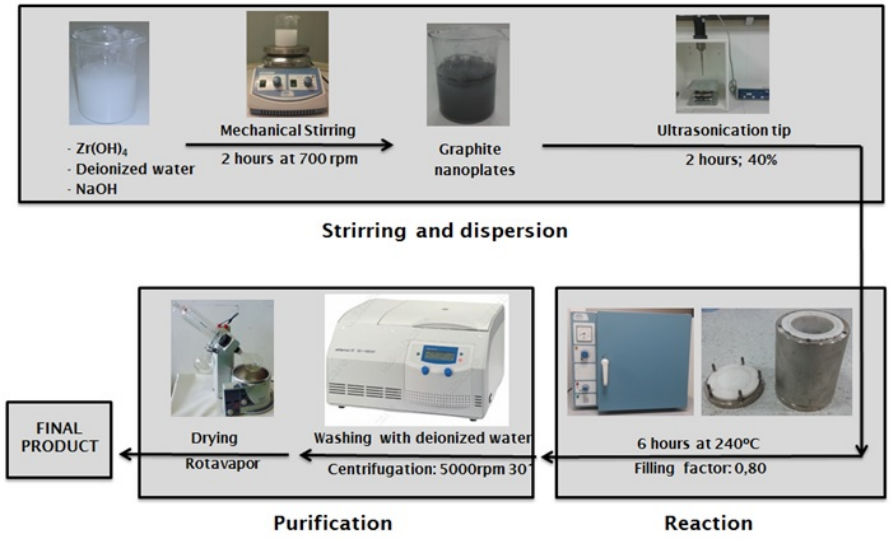

Figure 4.13: Resume of the hydrothermal reaction for the deposition of ZrO_2 over graphite nanoplates.

Precursor: Is used as the source of the metal. Can take the form of a salt. In this reaction, $Zr(OH)_4$ is employed.

Support: The material that will be covered by the metal. In the absence of a support material, the metal product would be obtained as a powder. AvanGraphene GNPs were used as support.

Buffering agent: pH must be kept under certain values to ensure the correct development of the reaction. As this reaction requires basic conditions, NaOH is used.

Figure 4.13 shows an schematic representation of the whole process.

The description to the general hydrothermal reaction of a zirconium hydroxide is presented in Equation 4.5.1[176].

Equation 4.5.1

$$Zr(OH)_y{}^{(z-y)+} + (z\text{-}y)OH^- \rightarrow ZrO_2 + \tfrac{z}{2}H_2O$$

The formation of ZrO_2 in hydrothermal solutions takes place by a solubilisation-reprecipitation process that requires sufficient degree of saturation. From the

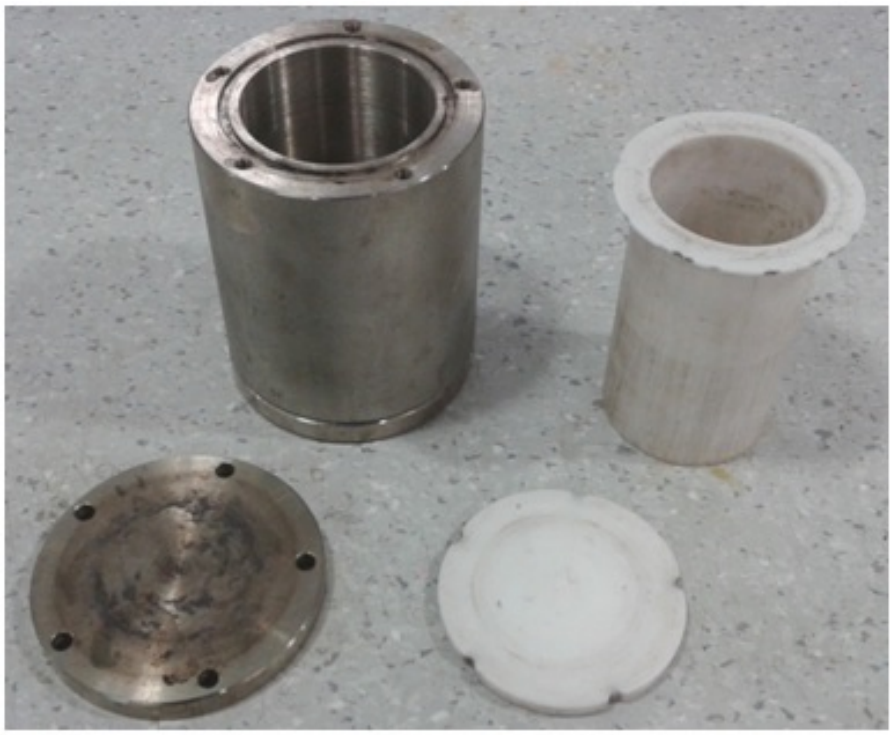

Figure 4.14: Image of the custom-made autoclave used in the hydrothermal synthesis.

equation is deduced that an increasing degree of hydratation <<y>> of the initial precursor favors the reaction towards the formation of the ZrO_2.Thus, $Zr(OH)_4$ stands out as a proper precursor to obtain higher quantities of the oxide.

An increase in the temperature of the reaction favors the equilibrium to the formation of the oxide [176]. Hydrothermal reactor, is used to facilitate these conditions. An autoclave is a cylindrical metal container, of indirect heating and autogenous pressure, where the reagents are introduced for the reaction. It possess two closures in both ends that allow a correct maintenance of the temperature and pressure values on the inside. Figure 4.14 presents an image of the used self-made autoclave. For its high thermal and corrosive resistance, AISI stainless-steel was employed for its elaboration. The use of products that can attack the steel in the long run made it mandatory the introduction of a Teflon vessel tightly set on its inside. Teflon has greater performance against corrosion than steel and it resist temperatures up to 275°C.

The closure is adjusted by five spherical head screws. The overpressure

inside the autoclave during the reaction presses heavily against the closure. It makes it significantly important to ensure a correct lock of the reactor, for what the autoclave was tested three times under working conditions before guaranteeing its correct operability. The autoclave presents an internal effective volume of 220mL.

According to the bibliography found and the previous experience of our group in the synthesis of ZrO_2, the conditions of the reaction were set as it follows: 240°C, 6 hours of reaction and a filling factor of 0,8. The filling factor is defined as the fraction of volume of the autoclave filled with the solvent. Among with the temperature, the filling factor will define the vapor pressure of the system inside the autoclave during the reaction.

John N Fox presented a study correlating the filling factor of the autoclave and the temperature with the vapor pressure for water [66]. The vapor pressure at certain conditions depends on the solvent of choice, being necessary to study the behavior of each new solvent of mixture of solvents. According to the study, with a filling factor of 0,80, at 240°C, the obtained water-vapor pressure is approximately of 500 bar.

The hydrothermal synthesis, from the reactants to the final product, can be summarized in three main steps: Stirring and dispersion, reaction and purification. During the stirring and dispersion step, $Zr(OH)_4$ is completely dissolved into the solvent (water) by mechanical stirring at 700 rpm during 2 hours. The pH must be adjusted to 12-13 by adding NaOH to the solution. Graphite nanoplates are then added to the solution and dispersed. For their dispersion, ultrasonication tip has been proved to be a proper method and 2 hours at a tip power of 40% are applied.

Next, the mixture is placed in the autoclave to begin with the reaction step. Ensuring its correct closure, the autoclave is located in an oven and heated to 240°C for 6 hours. After this time, the must be cooled down to room temperature to avoid spatter from the overpressure when opening it.

Finally, the graphite nanoplates-ZrO_2 compound must be purified. The product is washed with 1 L of deionized water by vacuum filtration. Then it is centrifuged to 5000rpm for 30 minutes. The centrifugation process is repeated three times to ensure the total elimination of the NaOH. As the last step, the remaining solution is rotavapored until it is totally dried.

Parallel to the work done over the covering of GNP with metal copper, the aimed objective with the hydrothermal reaction of $Zr(OH)_4$ is to obtain a

Figure 4.15: Macroscopic images of (a) Gr- ZrO_2-1 and (b) Gr- ZrO_2-2 samples.

homogeneous and uniform covering of ZrO_2 over the surface of the platelets. In this case, as the filling factor of the autoclave has a key role, its volume would be a limiting factor. For a 220ml autoclave, 176ml of deionized water are used. 1,79g of $Zr(OH)_4$ are dissolved in each synthesis for a 0,06M concentration. The rest of the conditions for the synthesis have already been described.

Two different samples were synthesized: Gr-ZrO_2-1 and Gr-ZrO_2-2. They vary in the initial GNP concentration and their conditions are summarized in Table4.5. Assuming a complete reaction, it is clear that higher fraction of graphite nanoplates leads to a lower weight percentage of ZrO_2, what would lead to thinner coatings.

Table 4.5: Graphite nanoplates concentration for each sample.

Sample	Graphite nanoplates initial concentration
Gr-ZrO_2-1	0,18 g/L
Gr-ZrO_2-2	1,8 g/L

4.6 Morphologic characterization

Figure 4.15 presents a macroscopic image for samples Gr- ZrO_2-1 and Gr-ZrO_2-2. The black color from the GNP is turned grayish by the presence of zirconia. As expected, sample Gr-ZrO_2-1 presents a brighter color than Gr-ZrO_2-2, what is indicative of a higher amount of zirconia. Only as a qualitative analysis but it provides a clear idea of the effect on the variation of the Graphite Nanoplates:$Zr(OH)_4$ ratio over the composition of the final product.

Further morphologic analysis is carried out by SEM. SEM images for sample

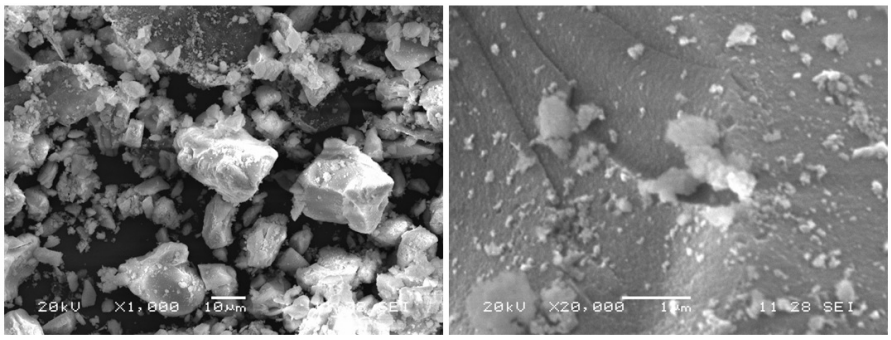

Figure 4.16: SEM images of Gr-ZrO_2-1 at (a) 1.000x, (b) 20.000x .

Gr-ZrO_2-1 are displayed in Figure 4.16. The first one shows an overall perspective of the synthesized product. Two different structures can be differentiated: 1)Zirconia particles of sizes between 2μm and 20μm. These particles present granular shapes and indicate that the ZrO_2 not only grows over the nucleation points on the surface of the nanoplatelets, but also grows forming isolated ZrO_2 nanoparticles not adsorbed on the GNP surface. 2) Zirconia particles under 1 μm in size and attached to the GNP surface. These particles are remarkably smaller than the ones that appear isolated.

A closer look to the surface of a graphite nanoplatelet is presented in the second image in Figure 4.16 The presence of a zirconia layer over the platelet is confirmed in this image. The layer is homogeneous and fully covers the surface of the platelet, with no holes on the covering. The covering is found over the vast majority of the platelets in the product. Some ZrO_2 particles also appear attached to the covering layer. Their sizes vary between 50nm and the few microns. It is not clear if these particles have grown over the zirconia layers or have attached later to it. However, in any case, they dont disrupt the continuity of the layer.

Figure 4.17 presents two SEM images of sample Gr-ZrO_2-2. The GNP:ZrO_2 ratio is higher than in sample Gr-ZrO_2-1, what can be clearly seen in the first image. Most of the ZrO_2 appears attached to the surface of the nanoplates. Few big isolated zirconia particles of sizes around 10μm are also present in the sample.

Not a clear covering layer of ZrO_2 can be found. The absence of this layer is confirmed in Figure 4.17 (b). The closer look on the graphite nanoplatelets evidences that no complete layer has been achieved during the synthesis. Few areas exhibit some ZrO_2 covering and some agglomerations of zirconia nanoparticles

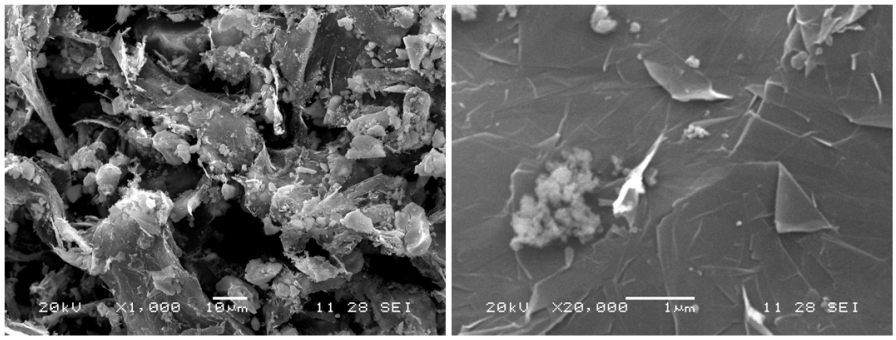

Figure 4.17: SEM images of Gr-ZrO_2-2 at (a) 1.000x, (b) 20.000x.

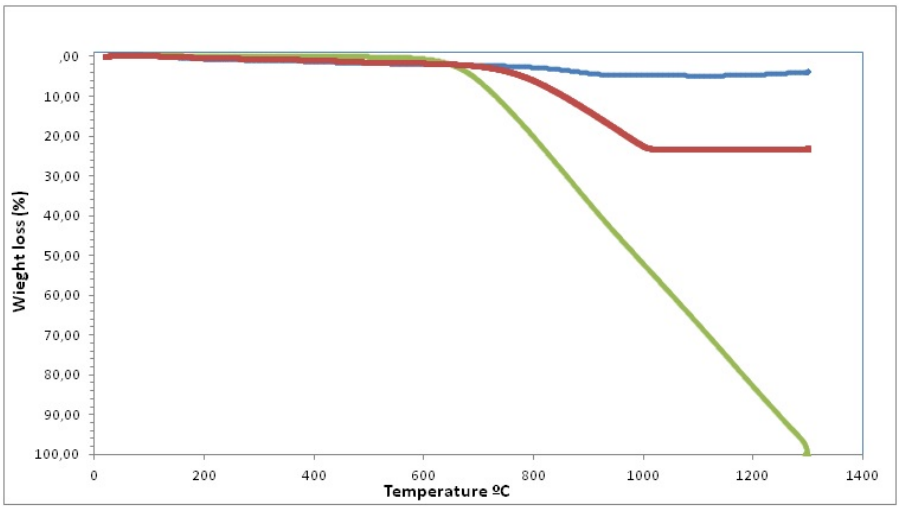

Figure 4.18: TGA curve for samples Gr-ZrO_2-1 (blue) and Gr-ZrO_2-2 (red) compared to plain graphite nanoplates (green). With a 50°C/min ramp and under air atmosphere.

are present over the surface. The $Zr(OH)_4$:GNP ratio for this sample proves to be inadequate to attain the complete covering aimed. The morphology obtained agrees with the results presented in studies from other groups [175] and from Tecnalia [72], [75]. The size, however, is high when compared to those studies. The synthesis conditions would have to be tuned and further researched if smaller nanoparticles were required.

Figure 4.18 presents the results of the TGA analysis for the two samples of Zirconia/GNP composites (Gr-ZrO_2-1 in blue and Gr-ZrO_2-2 in red) G. A TGA curve for plain GNP (green) is included to facilitate the interpretation of the results.

The first thing to be noticed when comparing these results is the slight decrease in weight for both samples between 270°C and 650°C. As commented before, these losses are related to the defects on the carbon lattice. They indicate that the hydrothermal synthesis of ZrO_2 nanoparticles over graphite nanoplates introduces some degree of defect on the graphite structure, as the non-treated graphite nanoplates do not exhibit this loss.

The second remarkable aspect to interpret is the retardation of the main weight loss of the composite samples. Plain graphite nanoplates begin a weight loss around 600°C. This loss corresponds to the transformation of the sp^2 bonded C atoms of the lattice into CO_2 and CO. For the same weight loss to happen in the two composite samples, 730°C must be overcomed. These results are a significant delay in the initiation of the decomposition of the GNP. In sample Gr-ZrO_2-2 this decomposition begins at 730°C whereas in sample Gr-ZrO_2-1 it starts at 760°C, due to a more effective covering of the platelets. Therefore, the retardation effect has been measured and confirmed for this set of samples.

Attending to the TGA results and the SEM images of the two ZrO_2 samples, **Gr-ZrO_2-1 would be the most appropriate one for its introduction as nanofiller in the bronze MMC**. Sample Gr-ZrO_2-2 did not achieve a complete covering of the platelets, resulting in a lot of exposed GNP areas. Regarding the TGA results, Gr-ZrO_2-1 presented the main weight loss at higher temperatures than Gr-ZrO_2-2.

4.7 Preliminary tests on the introduction of coated GNP into bronze

After the experimental study of the functionalization processes and the thermal behavior of the composite samples GNP/Cu and GNP/ZrO_2, it is necessary to select one in order to introduce it into bronze. The morphological analysis of the Cu-GNP and ZrO_2-GNP open a possible issue that could affect the application of these composites. The densities of both Cu (around 8,7g/cm^3) and ZrO_2 (around 5,7g/cm^3) are remarkably higher than the density of GNP (around 0,0017g/cm^3). This difference has a huge impact on the weight relation of the components in the composite. As SEM images evidenced, a notable amount of metal or metal oxide is required to ensure a complete and homogeneous covering of the GNP. However, despite the volumes being in similar order of

magnitude, the weight percentage of the covering metal or metal oxide is much higher. This effect should be taken into account when approaching TGA results. Furthermore, later applications of the composites would be also affected by this, as high masses of metal and metal oxide might be needed to be added to MMC just for small additions of graphite nanoplatelets.

On the one hand, the coating process with Cu is fast and easily scalable. The morphological analysis of the GNP-Cu samples demonstrated that, adjusting the relation between reactants and GNP, complete and relatively homogeneous Cu coatings can be achieved. However, the thermal performance of the composite does not delay the decomposition of GNP. Also, the electroless coating process provokes the introduction of defects in the sp^2 carbon atom lattice, lowering the decomposition temperature of the GNP. Cu covered GNP demonstrated to start the decomposition process at lower temperatures than pure GNP.

On the other hand, the ZrO_2 covering of GNP is a process that requires high temperatures (over 150°C) for several hours. Added to the necessity of keeping high pressures too, it becomes more difficult to scale. Nevertheless, the conditions required are easily assumed from an industrial perspective. The ZrO_2 coat demonstrated to be continuous and complete along the GNP surface, with certain presence of ZrO_2 microparticles.

The coating, furthermore, successfully delayed the decomposition temperature for GNP. Sample Gr-ZrO_2-1, the sample with the best coating, the GNP begins its decomposition at 760°C, being 600°C the temperature at which the sp^2 carbon atom lattice begins its decomposition for pure GNP at the same heating conditions. The early mass loss due to the presence of defects in the lattice is hardly appreciated, what indicates that the coating process respects the structure of the GNP.

Therefore, it is concluded that the ZrO_2 coating is more effective than the Cu coating when aiming an increase in the decomposition temperature of GNP. Furthermore, the conditions for sample Gr-ZrO_2-1 presented the best results from the two samples studied.

4.7.1 Elaboration of bronze/GNP MMC

Zirconia covered GNP is the selected material for its introduction into an industrial bronze. A bronze composite with a GNP concentration below 1% wt. is aimed. The conditions for the elaboration of the GNP/ZrO_2 composite are the

Figure 4.19: Sample image of a testing tube made out of GNP/ZrO_2 and bronze MMC.

ones described for sample Gr-ZrO_2-1, selected for ensuring a complete covering of the platelets and the delay on the decomposition temperature.

Zirconia covered GNP are introduced in a melting pot. Then, a cylinder of solid bronze is introduced too and the melting pot is heated over 1000°C. This temperature is reached as fast as possible (less than 5 minutes). Once the bronze is melted, the sample is mixed with an iron rod to homogenize it. The sample is finally cooled in the same melting pot.

Test tubes as the one presented in Figure 4.19 are prepared with the elaborated MMC for its mechanical characterization.

The composition of the materials and the conditions of the processes can not be described in further detail for industrial property reasons.

4.7.2 Issues

At this point, the nanocomposite ZrO_2/GNP is already evaluated as suitable for its introduction in bronze to elaborate a MMC. The potential for thermal

conductivity enhancement has already been established in the approach and the mechanical properties of the MMC have to be measured, in order to study if the introduction of GNPs in the bronze has a negative effect over them. However, at this point, when approaching the experimental elaboration of the MMC, some issues were detected that prevented these tests from being carried out.

1) It has already been described above that there is a remarkable difference in density between copper, zirconia and GNP, of around three orders of magnitude. This has a great impact on the melting step, which requires the bronze rod and the GNPs to be poured into a melting pot. Due to the density difference, the GNP volume required to achieve just a 1%wt. is so big that it is not possible to introduce it in the pot with the bronze rod.

2) TGA results showed that the GNP%wt. in the GNP/ZrO_2 is below 5%. Thus, the introduction of 1g of GNP (for example), implies the introduction of more than 95g of ZrO_2, what changes remarkably the composition of the original bronze.

3) The synthesis of GNP/ZrO_2 for the SEM and TGA analysis was carried out at laboratory scale and was not up-scaled. However, the material for the elaboration of MMC specimens required of big amounts of composite, what required very long synthesis times. The process was not viable. This long elaboration times, limited the test tube sizes. Tests were performed for the obtaining of two mechanical properties: Elastic Limit and the stretching. However, the small size of the test tubes made it impossible to obtain reliable data.

So, the initial idea of evaluating the effect of the introduction of GNP on the mechanical properties of a well-known bronze, could not be achieved.

4.8 Conclusions

AvanGraphene GNP presents the best thermal stability of the three graphene like materials studied.

Thermal stability study was carried out over Graphenea GO, Graphenea rGO and AvanGraphene GNP. For heating ramps of 50°C/min, rGO begins its decomposition at 150°C , GNP at 600°C and GO loses most of his mass before 200°C. The obtained data, along with the characterization performed in Chapter 2, allow ascertaining the relation between the carbon atom lattice structure and the thermal stability. The lack of defects in AvanGraphene GNP when compared to GO and rGO make its thermal decomposition temperature to reach the highest values. Table 4.6 summarizes the main thermal stability results.

Table 4.6: Presents the main weight losses for GO, rGO and GNP.

Graphenea GO		Graphenea rGO		AvanGraphene GNP	
T. Range (°C)	%wt. Loss	T. Range (°C)	%wt. Loss	T. Range (°C)	%wt. Loss
20 - 200	97	150 - 1180	92	600 - 1300	100

GNP/Cu nanocomposites has been successfully accomplished by electroless method.

Cu nanoparticles have been grown over the GNP surface. The functionalization was carried out under different initial conditions and the objective of forming a homogeneous and continuous layer of Cu nanoparticles over GNP was achieved. The effect of GNP:Cu salt on the formation of this layer was experimentally evaluated. Cu nanoparticles with spherical morphology and radius below 1μm were obtained. Results are summarized in Table 4.7.

GNP/ZrO_2 nanocomposite has been successfully accomplished by hydrothermal synthesis.

ZrO_2 nanoparticles have also been grown over the GNP surface. The conditions for the growth of a homogenous and continuous layer of ZrO_2 have been established. The obtained ZrO_2 particles presented a disparity of sizes: from few nanometers to over 20μm. Results are summarized in Table 4.7.

Thermal decomposition temperature for GNP has been retarded.

Table 4.7: Resume of the conditions for the developed functionalization and the resulting morphologies in the final GNP/ metal or GNP/metal oxide composites.

Nanoparticle	Synthesis method	$[GNP]_o$ (g/L)	Morphology	Size	Platelet Covering
Cu	Electroless plating	1	Spherical	200nm	Not complete
Cu	Electroless plating	0,2	Spherical	150-300nm	Not complete
Cu	Electroless plating	0,05	Spherical	100nm-1μm	Complete
ZrO_2	Hydrothermal Reaction	0,18	Irregular	Few nm- 10 μm	Complete
ZrO_2	Hydrothermal Reaction	1,8	Irregular	50nm-Few μm	Infimun

The functionalization of GNP with an homogeneous layer of ZrO_2 demonstrated to significantly delay the main thermal decomposition of the GNP. The best results achieved a delay of 160°C for a 50°C/min ramp under air atmosphere, from 600°C decomposition of plain GNP to 760°C of the GNP/ ZrO_2 composite.

Several issues for the elaboration of GNP/ ZrO_2 / Bronze MMC have been localized.

The preliminary study of the introduction of GNP/ ZrO_2 into bronze showed particular issues that have been noted. These technical issues are related with the dimensional differences between nanocomposites and regular metallurgy tools and test tubes.

Manganese Oxide

4.9 Introduction: Approach, Objectives and Experimental details

4.9.1 Approach

The research on functionalization with nanoparticles continues in this section. GNP is chosen to be functionalized with MnO_2 nanoparticles by hydrothermal reaction. As stated in Chapter 1, the hydrothermal synthesis has been successfully used previously by some groups for the funtionalization of different carbonaceous materials, including graphene, with manganese oxides.

The reason for choosing MnO_2 is related to its promising performance on different energy storage devices, like metal-air batteries, fuel cells and supercapacitors.

MnO_2 has been widely investigated as one of the most promising catalysts for oxygen reduction reaction (ORR) in an alkaline medium. ORR is of great significance to metal-air based batteries and fuel cells, however, the cathodic activation, ohmic and mass transport losses, the requirement of high activation energy for O_2 reduction and the relatively high O=O bond strength have collectively hampered the ORR kinetics[102].

For this reasons, catalysts are required in order to lower the energy barrier of O_2 and increase the electrokinetics of ORR. Up to date, Pt-based catalysts have been used for its efficiency and stability. However, the scarcity of Pt reserve, its high cost and its sensitivity to carbon monoxide poisoning has opened a research field in order to find an alternative.

Alternative catalysts should satisfy some requirements such as extended number of active sites, catalytic activity, conductive channels, interconnectivity, etc. To this regard, MnO_2 presents a high catalytic activity, specific capacitance and it is inexpensive, abundant and environmentally friendly.

MnO_2 crystals present a variety of morphologies and crystal-structures which have proved to be of great significance in the catalytic activity towards the ORR. However, the activity and mechanism by which the ORR takes place in these materials remain to be fully demonstrated. Since the catalytic process for oxygen reduction involves the reduction and oxidation of surface manganese species[28] , the number and activity of these redox centers would be important factors to define the catalytic performance. Therefore, a material with distorted

structure would likely provide more active sites, and so, amorphous manganese oxides, which contain much more structure distortions than crystalline manganese oxides, might present higher catalytic activity for the oxygen reduction reaction. Based on this fact, Yang et al. [260] have proposed the utilization of a nanoporous amorphous manganese oxide, synthesized from low-temperature aqueous redox routes, as an electrocatalyst for the oxygen reduction reaction in alkaline solutions. It was found that this oxide catalyzes the 2-electrons pathway for the reduction of molecular oxygen. The significant catalytic activity was attributed to the high surface area and concentration of lattice defects in the amorphous material.

Recently, several groups studied the electrochemical performance of manganese oxides structures as oxygen reduction electrodes. L. Feng and its groups[60] carried out a study of the catalytic activity of two different morphology structures for the α-MnO_2. They asseverate that incompact structures are beneficial to improve the transmission rate and transfer abilities of the species involved in the reduction reaction. Thus, hollowed or tunneled structures could have better performances than more compact ones. To this regard, G.G. Kumar et al. [13] described the manner in which α-MnO_2particles arrange in nanotube shapes, with tunnels that can easily accommodate molecular oxygen through bridge-mode. On the other hand, there is still controversy in the influence of the crystal structures. α-MnO_2 proves to have better catalytic properties than β-MnO_2 or amorphous MnO_2[253] and was accepted as the structure with the best catalytic performance. However, recent studies[235] show better results for the ϵ-MnO_2 when compared to α-MnO_2. Some authors even present results where MnO_2 nanosheets have better catalytic activity towards the ORR than α-MnO_2 and δ-MnO_2. Zhang et al. have investigated [277] MnO_2 materials with different crystal structure (α-MnO_2, β-MnO_2, and δ-MnO_2) as the cathode catalysts in microbial fuel cells MFC. In the study β-MnO_2 was proved to be the most effective catalyst with a maximum power density of 466 ± 19 mW m^{-3}.

However, the poor electrical conductivity of manganese oxides leaded to some limitations in its applicability. A developed strategy to overcome this setback consists in supporting the MnO_2 nanoparticles onto the surface of electrically conductive substrates. Carbon materials not only can increase the electronic conductivity of the electrode, but also has relatively good ORR catalytic activity in the alkaline media. Uniform distribution of the MnO_2 into carbon is essential to high ORR catalytic activity. Recent studies[280] demonstrated that the mechanically mixed MnO_2/Conductive Carbon Support catalyst exhibit worse electrocatalytic activity towards the ORR than those in which the MnO_2 is generated directly on its surface. Researchers have tried to support the

MnO_2 on carbon by using a chemical method instead of by simply mixing the two materials together. The chemical method can greatly increase the uniform distribution and make it possible to achieve a good contact between manganese oxide and carbon[217]. Hence, there is actually a good variability in the materials tested for the MnO_2/Conductive Carbon Support catalysts. As pointed out by Narah Ominde et al. [160] the deposition process in which MnO_2 grows onto carbon supports may affect the porous structures of this support and have a role in the catalysis due to the importance of the surface area.

Y. Zhan et al. (X) and Y. Lv et al. [142] both reported MnO_2/CNT catalysts prepared by chemical reactions over the nanotubes surface, achieving promising results headed to the Pt/C catalysts substitution. H. Gao and its group[71] synthesized carbon microspheres (CM) loaded with manganese oxide reacting the CMs with $Mn(NO_3)_2$. This catalyst show a high catalytic activity towards the ORR, however, the reaction undergoes a $2e^-$ pathway, what is less desirable than the $4e^-$ pathway. C. Shi et al. [196] and H.-Y. Park et al. [168] presented different composites both involving layered manganese oxide and graphene oxide. C. Shi et al. stated that the MnO_2 nanosheets present higher catalytic activity than other MnO_2 crystal structures. MnO_2/Active Carbon has also been subject of research by P. Zhang et al. [278] and its proposed by them as a good alternative catalyst to Pt. In a similar direction go Jang-Soo Lee and its group[122], for whom the lack of electrical conductivity of the MnO_2 as opposed to the carbon as well as the available active sites exposed is key in the catalysis. This group got great results with Ketjenblack carbon/MnO_x composites, getting electrodes that exhibit a peak power density of $190mW/cm^2$.

Graphene has also been used as support for the MnO_2, forming high performance MnO_2/Graphene catalysts. The combination of the high surface area (theoretical values of $2610m^2/g$), an elevated mobility of charge carriers, high conductivity, unique graphitized basal plane structure and potential low manufacturing cost makes graphene sheets a promising candidate for a cathode catalyst support in air-metal batteries, Q.Wen et al. [249] synthesized MnO_2 nanoparticles directly over reduced graphene oxide platelets by a redox reaction with $KMnO_4$ under microwave irradiation. The results reached by them even exhibits higher performance than the Pt/C catalysts. Yong Qian et al. [180] and Jiajia Wu et al. [253] both reported catalytic activity of rGO/MnO_2 towards the $4e^-$ pathway, reaching this last group a ca. 130 mV shift of the half-wave potential in the positive direction. Regarding the use of doped graphene, Ma and its group recently reported the catalytic activity of sulfur doped graphene derived from cycled-sulfur batteries [143], whereas Gong et al. demonstrated that

graphene nanoribbons doped with boron and nitrogen are efficient catalyst towards the ORR [80]. Quin et al. [181], Guo et al [85] and Ratso et al. [185] also pointed towards the substitution of carbon atoms by nitrogen atoms. In the case of Quin and its group the substitution was done over holey graphene and also proved its catalytic activity. Some combination between N-doped graphene and MnO_2 have been reported recently with noteworthy improvements towards the catalysis of ORR [**?**], [**?**]. Additionally, Jiajia et al. studied the effect of MnO_2 crystal structure on the catalytic activity, standing out the α-MnO_2 nanowires as the ones with the best performance. In this concern, G. G. Kumar[13] and its group also reported an enhancement on the catalytic activity towards the ORR for α-MnO_2 nanowires/ Graphene Oxide composites. Finally, Jang-Soo Lee[121] presented an inviting Ionic-Liquid rGO/Mn_2O_3 composite in which the $4e^-$ and the $2e^-$ pathways can be tuned with the relative amount of Mn_2O_3 and graphene.

Up to the latest technology progress, MnO_2 as a catalyst and graphene materials as support have also been reported as efficient alternatives in the Li-Air batteries[101],[243] . In this chapter, the elaboration of MnO_2-GNP nanocomposites is aimed. The effect that the presence of GNP has over the morphology and structure of in-situ synthesized MnO_2 will be studied and the catalytic activity of the most promising MnO_2-GNP will be evaluated.

4.9.2 Objectives

In this subChapter the elaboration of GNP- Manganese Oxide composites is studied for its potential use in metal-air batteries as ORR catalysts. This research requires the fulfillment of several intermediate sub-objectives:

- To study the synthesis of manganese oxide nanoparticles by hydrothermal method and the functionalization of AvanGraphene GNP surface with them.
- To characterize the morphology of the obtained Manganese Oxide nanoparticles and to compare the effect that the presence of GNP has. Also, evaluate the homogeneity and distribution of the nanoparticles over the GNP.
- To study the crystal structure of the obtained Manganese Oxide nanoparticles.
- To compare the thermal performance of the GNP/Manganese Oxide composites when compared to plain GNP and plain Manganese Oxide.

- To assess the catalytic activity of GNP/Manganese Oxide composite towards the ORR, in order to evaluate the viability of its application in metal-air batteries.

4.9.3 Experimental details

Materials

AvanGraphene from Avanzare are the GNP selected for the functionalization study. They have been largely characterized in Chapter 2 and chapter 3 and they are known to present an appropriate structure with large-surfaced platelets and a proven stability in water with the presence of SDBS. They are chosen over rGO and GO for their higher electrical conductivity, an important property for the performance in metal-air batteries.

The functionalization process is made by a hydrothermal method. For the synthesis $MnSO_4H_2O$ (Panreac, analysis quality), $KMnO_4$ (Probus, analysis quality) and dodecylbenzenesulfonic acid sodium salt ($C_{12}H_{25}C_6H_4SO_3Na$, SDBS) (Aldrich, tech. quality) are employed. For washing purposes, absolute ethanol (Scharlau, extra pure) is used.

Morphological/Structural Characterization

In order to characterize the morphological and structural properties of the functionalized GNP, three different characterization techniques are employed:

SEM (Scanning Electron Microscopy)INSPECT F-50 (FEI Company) is used to evaluate the the distribution of MnO_x over GNP, the homogeneity of the covering and the size and morphology of the MnO_x particles.

A thermogravimetric analysis (TGA) is carried out using a TG.DTA92 thermobalance, to obtain information about the composition of the samples. The samples are heated from room temperature to 1000°C with a heating ramp of 5C°/min in air atmosphere.

Finally, the crystallographic phase of the MnO_x particles is studied by X-Ray Diffraction (XRD) (Bruker D8 Advance) in the 2? from 0 up to 75° using CuKα radiation.

Figure 4.20: Image of the ALS-RRDE-3A.

Electrochemical Characterization

RDE: ALS-RRDE-3A apparatus connected to a Biologic VMP3 multichannel potenciostat is used in order to carry out Hydrodynamic Voltammetry measurement. Image 4.20 shows an image of this equipment. 3mm Glassy Carbon (GC) working electrode, Platinum wire as counter electrode and RHE electrode as reference electrode were used. A dispersion/ink of 5mg of MnO_x/Graphene powder in 10ml (1:3 Isopropanol-water) adding 0,10ml of Dupont D521 Nafion dispersion (5% wt. polymer content) was prepared followed by ultrasonically dispersing for 30 min. 5μl of this dispersed suspension was pipetted (in 1μl drops) onto the top of the GC working electrode surface and dried rotating at 100 rpm in RDE at room temperature, waiting 30 min. for dry between drop and drop.

The experiments were conducted in KOH 1M at 25°C electrolyte. First, Cyclic Voltammetry (CV) for conditioning the catalyst and Linear sweep Voltammetry (LSV) at 1600rpm (scan rate=20mV/s) for background current correct in deaerated (Ar) electrolyte was carried out. Then, linear sweep voltamme-

try (LSV) at 20 mV/s with different rotation rates (400, 625, 900, 1225, 1600, 2500) in O_2 bubbled media were carried out in order to know the ORR activity of the catalyst.

Background current correction: At lower potential scan rates, the effect of impurities and the formation of surface oxides suppress the measured ORR activity; at scan rates above 20mV/s, capacitive current effects are higher. The background current is measured by running the ORR sweep profile (20 mV/s and 1600 rpm) in Arpurged KOH 1M either before or after the ORR measurements to account for capacitive current contributions. This background current is subtracted from the experimental ORR current to eliminate any contributions of capacitive current.

4.10 MnO_2 Synthesis

This section describes de synthesis of manganese oxide nanostructures over the surface of GNP. MnO_2 can get easily supported by a simple in-situ hydrothermal method. The fundamentals for a hydrothermal synthesis have already been described in section 4.1.4, as well as the required equipment.

Four different compounds are required for a correct performance of this hydrothermal reaction:

Solvent: The medium where GNP are dispersed and the reaction takes place. The solvent chosen will affect the pressure conditions. For these samples, deionized water is used. In this case, the deionized water will also act as a reactant in the synthesis.

Oxidant Agent: Oxidizes the metal ions to form the metal oxide. In this case $KMnO_4$ is used.

Precursor: Is used as the source for the metal ions. Can take the form of a salt. In this reaction, $MnSO_4$ is employed

Support: The material over which metal oxide nanoparticles will grow. GNP are used.

Surfactant: (SDBS) Is used to separate and stabilize the support material in order to guarantee a maximum exposed surface.

Table 4.8: Summarizes the conditions for the hydrothermal synthesis of MnO_2.

Products	Parameters
Potassium permanganate - $KMnO_4$	0,005 M
Manganese sulphate - $MnSO_4$	0,005 M
Sodium dodecylbenzenesulfonate- SDBS	Same amount than GNP
Time	12 h
Temperature	160 °C

The general conditions for the synthesis are described in Table 4.8 The whole process consists in three main steps. The first one consists on the dispersion of the graphite nanoplates and the dissolution of the rest of the compounds in the solvent. Then, in the reaction step, the dispersion is poured into a Teflon autoclave with a 0,8 filling factor and is heated to 160°C. At this temperature the Reaction 4.2.2.1 occurs:

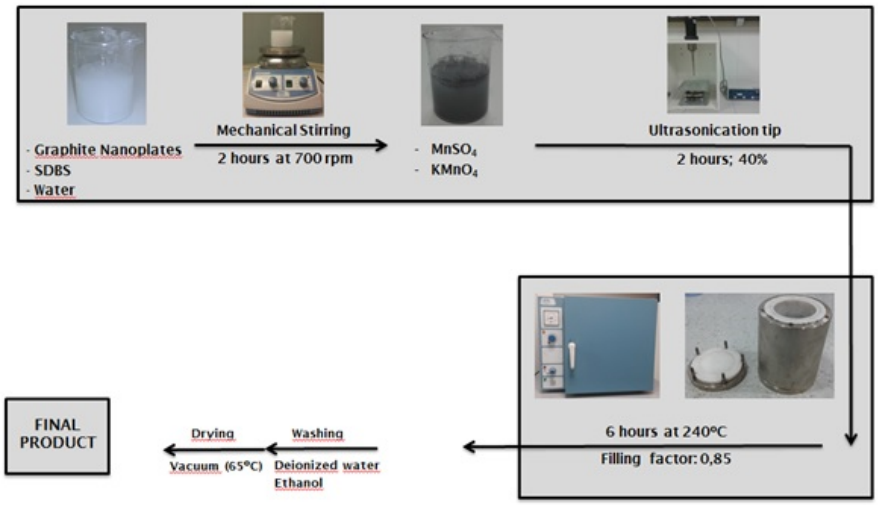

Figure 4.21: Schematic representation of the hydrothermal reaction for the synthesis of MnO_2-Graphite nanoplates.

$$2KMnO_4 + 3MnSO_4 + 2H_2O \rightarrow 5MnO_2 + 2H^2SO_4 + K_2SO_4$$

Reaction 4.2.2.1

The autoclave with the solution is kept at that temperature for 12 hours to ensure the complete reaction of the reactants. Afterwards, in the purification step, the mixture washed several times with water and ethanol under vacuum filter, until complete elimination of impurities, and dried at 80°C. The whole process is schematized in Figure 4.21.

Following this method, five samples are synthesized. It is known that the ratio between the support graphitic material and the oxidant agent agent affects the morphology and later performance of the MnO_2-GNP composite. Thus, different relations between both of them were tested, with $KMnO_4$:GNP ratios from 1:2,5 to 2,5:1. A fourth sample is synthesized in the absence of graphite nanoplates and is used as a blank reference. Regular GNP are also employed for comparison with the modified ones. Table 4.9 summarizes the initial graphene and SDBS conditions for each sample.

For the prepared samples, the used autoclave has 220ml of capacity. Accordingly, 176mL of deionized water is required to achieve a filling factor of 0,8. The resulting pressure has already been described in section 4.1.4.

Table 4.9: Summary of the synthesized Graphene-MnO_2 samples.

Sample	Graphene	SDBS	$KMnO_4$:Graphite nanoplates
GNP	100\%	X	X
Blank	X	X	X
$GrMnO_{-1}$	0,0543 g	0,0543 g	2,5 : 1
$GrMnO_2$-2	0,1359 g	0,1359 g	1:01
$GrMnO_2$-3	0,438 g	0,438 g	01:02,5

4.11 Morphological characterization

Depending on the reaction conditions,the synthesis method employed to form the MnO_2 nanoparticles can lead to the obtaining of various structures. Thus, to fully evaluate the obtained nanoparticles, it is necessary to study their structure by SEM. Furthermore, as described in the approach, not only the crystal phase but also the nanostructure of the oxide would have a great impact on its catalytic activity.

Figure 4.22 includes three SEM images of the sample Blank at increasing magnitudes. This sample corresponds to the synthesis reaction in absence of GNP. This lack of substrate for the growth of the oxide has a great impact on its morphology. The manganese oxide has grown in the shape of irregular rods with polyhedral morphology. The length of the rods slightly from 1μm to 5 μm. Their thickness is in the range of 150-300nm.These rods, along with nanowires, are one of the common morphologies for the MnO_2 to take under hydrothermal conditions.

SEM images for sample $GrMnO_2$-1, are presented in Figure 4.23. The structure varies notably from the blank sample. In this case, the sample present two different morphologies: Long acicular wires and agglomerations of <<nanospheres>>. The acicular wires have various microns in length but a thickness of only around 30nm. The sphere-alike nanoparticles present radius under 100nm.Nanosphers grow over the graphene platelets forming a continuous and rather homogeneous covering, as it can be appreciated in the top of Figure 4.23A .The oxide wires completely surround the platelets forming intricate nets around it. The grow of two kinds of nanostructures happens as this is the sample with the highest $KMnO_4$:Graphene ratio. Low presence of GNP favors the nanostructures with low width to length relations (with wire shape). In the absence of enough nucleation spots over the graphene surface for its growth as nanospheres, the tendency of the oxide is to grow over itself.

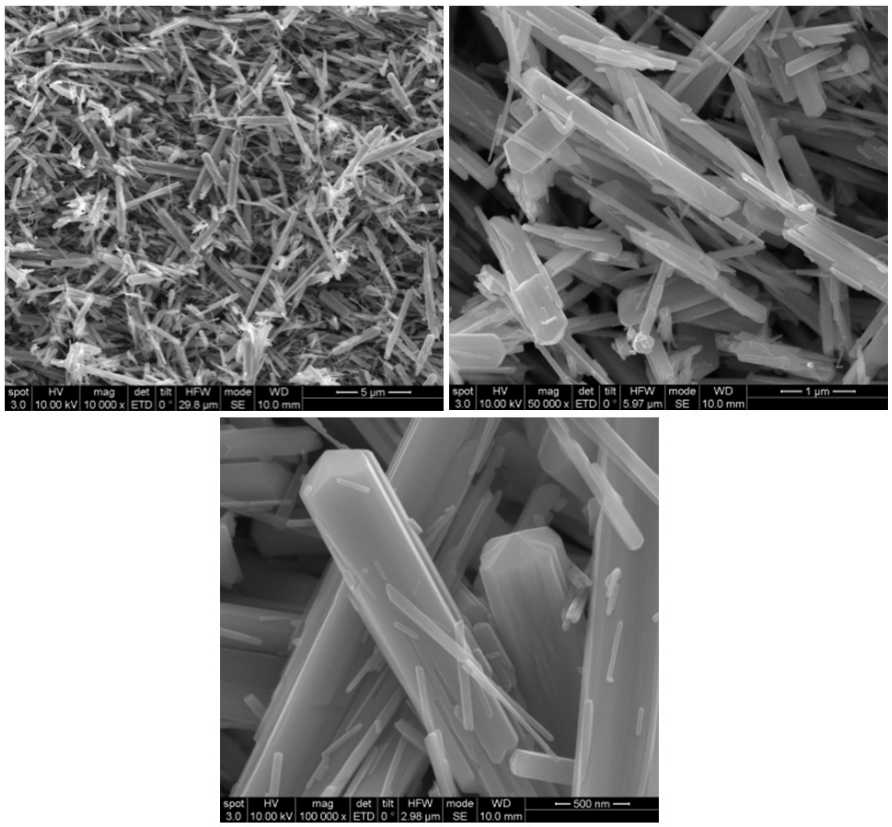

Figure 4.22: SEM photograph of sample Blank at 10.000x (a), 50.000x (b) and 100.000x (c) magnitudes.

In the structure of the manganese oxide in sample $GrMnO_2$-2, the preparation with a $KMnO_4$:Graphene ratio of 1:1, the substitution of nanowires by nanospheres is higher. Figure 4.24 shows the SEM images of this sample at different amplifications. At the highest magnification, Figure 4.24C some nanowire structures of 500nm length and 20nm width are seen. However, most of the oxide is forming big agglomerations of nanospheres. The agglomerations are located mostly in the edge of the graphene platelets, what points out the defects on the graphene structure as nuclear points of preference for the growth of the manganese oxide.

SEM images of sample $GrMnO_2$-3 are presented in Figure 4.25. The $KMnO_4$:Graphene relation ups to 1:2,5. Mostly agglomerated nanospheres can be found, with a very low presence of nanowires. These spheres present a radius between 50nm and 100nm. Even though there is still a preference for the growth at the edge of

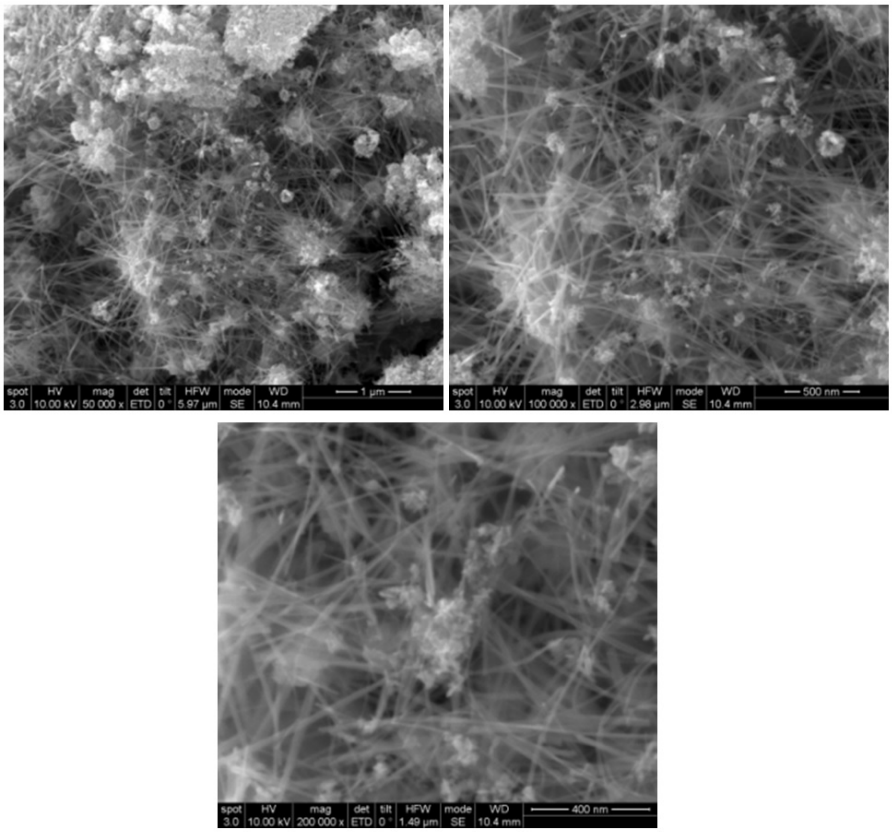

Figure 4.23: SEM photograph of sample $GrMnO_2$-1 at 50.000x (a), 100.000x (b) and 200.000x (c) magnitudes.

the graphene platelets (Figure 4.25A) there is also a growth over the surface of the platelets (Figures 4.25 B and C), achieving a better cover of the graphene.

Spherical nanostructures proved to be obtained for higher amount of GNP substrate. This kind of morphologies present better catalytic activities due to the higher Surface:Mass ratio when compared to nanorods.

Only one MnO_2/GNP sample will be further characterize and compared with plain GNP and plain MnO_2. The sample chosen is $GrMnO_2$-3, with the highest amount of GNP, for the reason just explained.

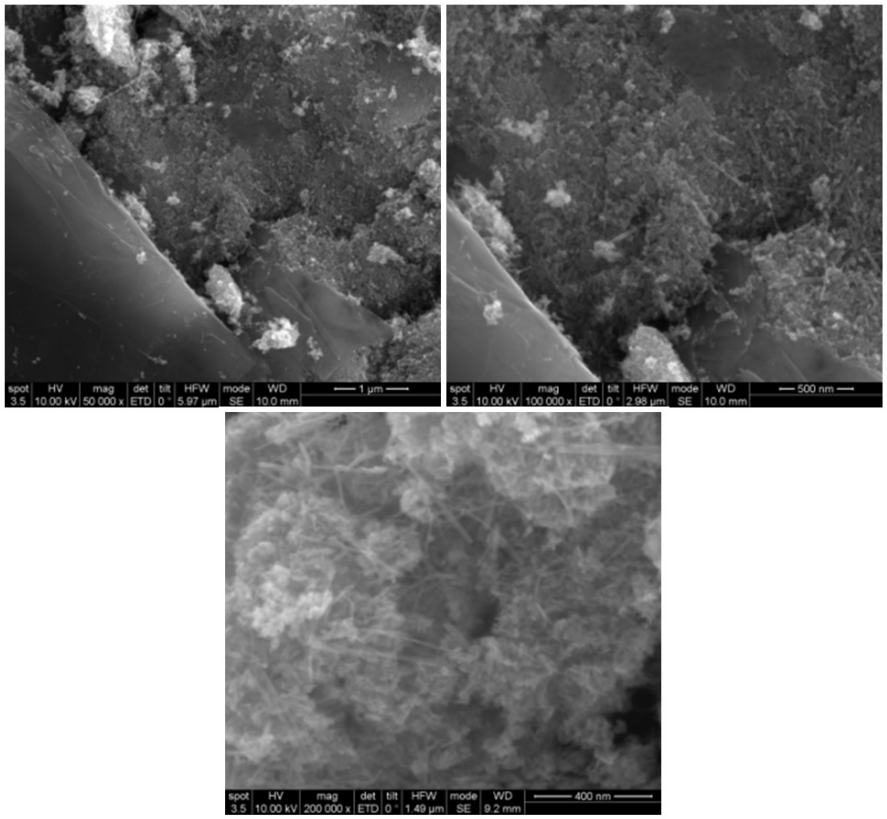

Figure 4.24: SEM photograph of sample GrMnO$_2$-2 at 50.000x (a), 100.000x (b) and 200.000x (c) magnitudes.

4.12 Determination of the crystal structure for sample GRMnO$_2$-3

In order to determine the crystalline structure of the plain MnO_2 sample and the MnO_2/GNP sample, XRD analysis is performed. The XRD pattern for MnO_2 is showed in Figure 4.26. From the XRD pattern, sample MnO_2 is indexed to be pure β-MnO_2 (pyrolusite, with lattice constants a=4,398A, b=4,3983A and c=2,873A). The broad diffraction peaks in the XRD pattern indicate small crystallite size for this sample. β-MnO_2 is one of the polymorphs that MnO_2 can show based on the different configurations of its basic octahedral unit [MnO_6][43]. It presents (1x1) tunnels composed of single chains of the octahedral[246].

The XRD pattern for MnO_2/GNP (Figure 4.27) shows an almost X-ray

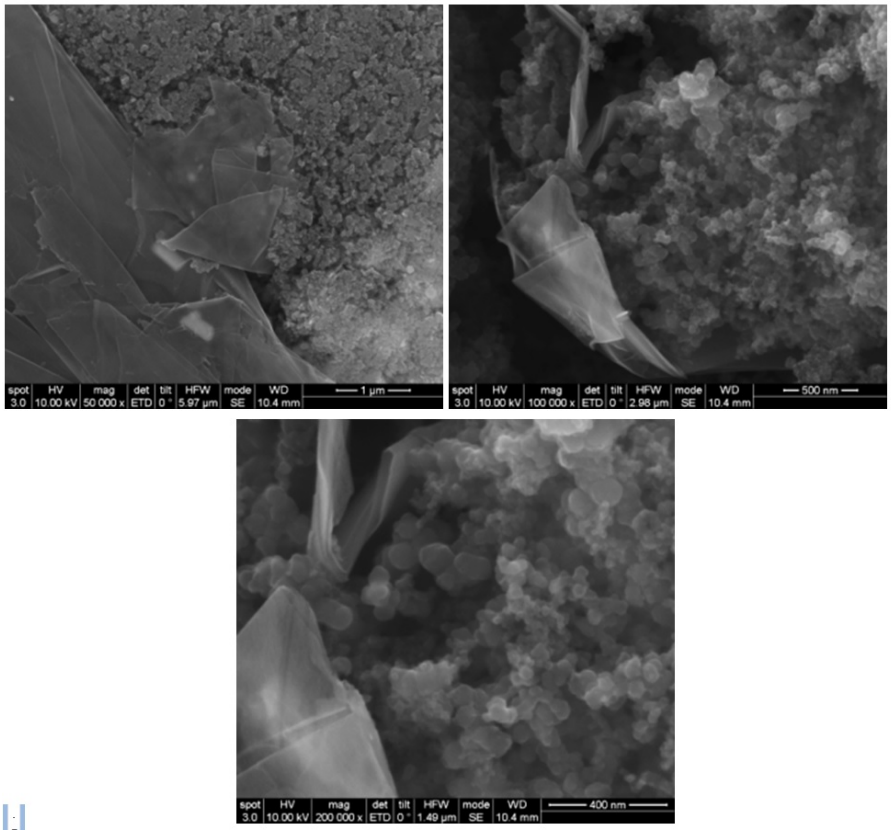

Figure 4.25: SEM photograph of sample $GrMnO_2$-3 at 50.000x (a), 100.000x (b) and 200.000x (c) magnitudes.

amorphous structure, also with small crystalline domains. The use of an amorphous structure as catalyst can be more favorable over crystalline manganese oxide structures due to the higher surface area and the bigger amount of available active sites exposed to oxygen molecules [260]. As ascertained with the SEM analysis, the MnO_2/GNP granular structure offers a larger surface area than the nanorods from MnO_2. Furthermore, amorphous structures present large concentrations of lattice defects, what makes them efficient electrocatalysts for ORR in alkaline solutions, according to Yang et al.

4.13 Thermal characterization

Thermo gravimetric analysis are carried out over the three samples with a heating ramp of 5°c/min and under air atmosphere. Figure 4.28 shows the

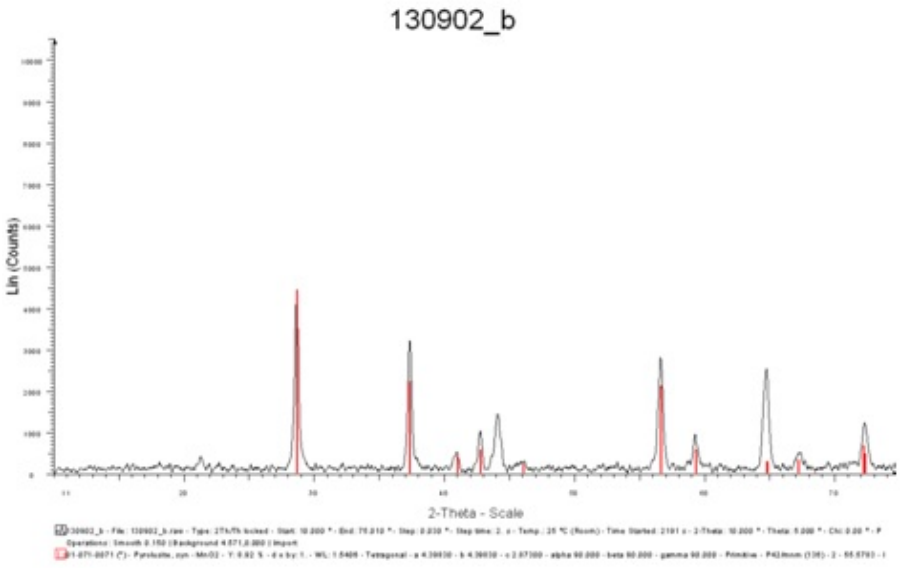

Figure 4.26: XRD pattern for MnO_2, corresponding to pyrolusite.

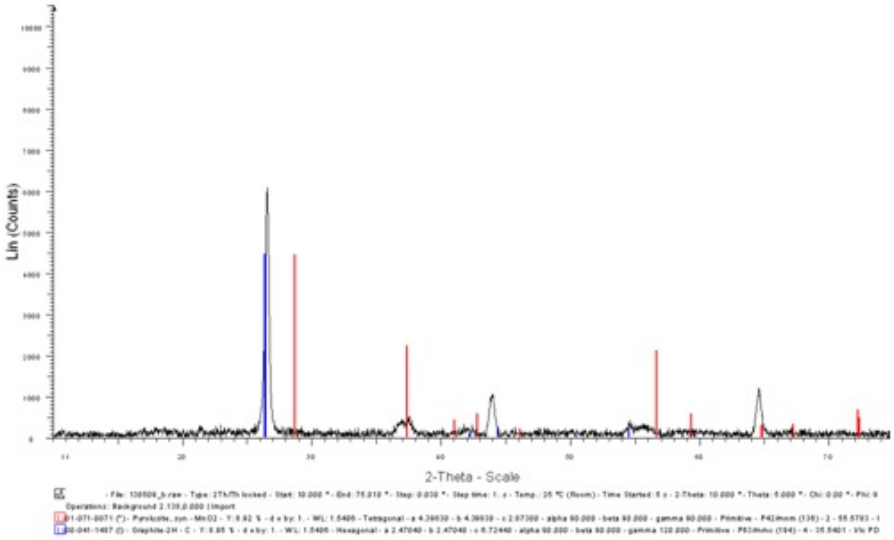

Figure 4.27: XRD pattern for sample $GrMnO_2$-3, indicating and amorphous structure.

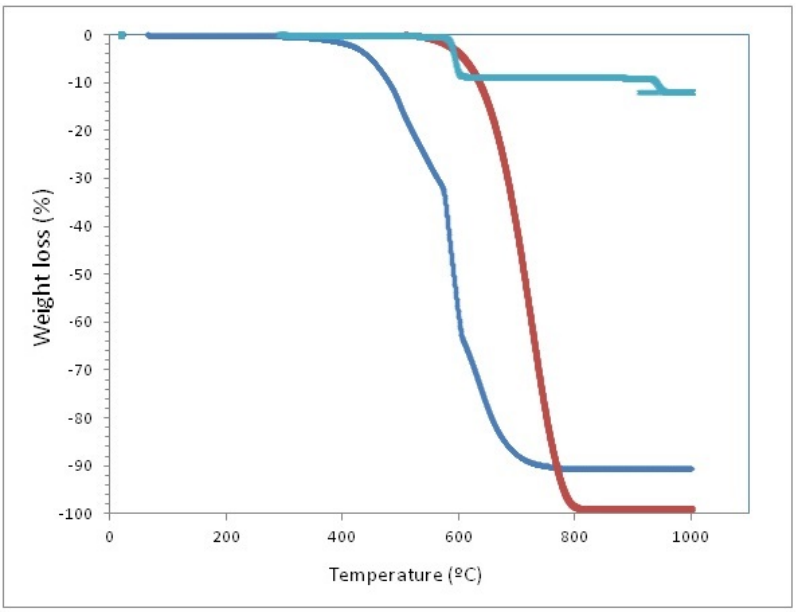

Figure 4.28: . TGA results for plain GNP (Red), plain MnO_2 (green) and $GrMnO_2$-3 (blue), with a heating ramp of 5°C/min and under air atmosphere.

TGA curves for the GNP, the MnO_2 and the MnO_2/GNP.

On the one hand, plain GNP with no manganese oxide, presents a foremost weight loss of 99% in the range of 550 to 800°C, which is attributed to the decomposition of its carbon structure. In the other hand, plain MnO_2 without graphene, the β-MnO_2 graphene nanorods, present a weight loss of 8% between 580 and 620°C. This loss at a temperature higher than 500 °C corresponds to the transformation of MnO_2 to Mn_2O_3, according to the reaction: $2MnO_2(s) \rightarrow Mn_2O_3(s) + 1/2\ O_2(g)$ [234]. This transformation starts at higher temperatures for pyrolusite (β-MnO_2) than for the other oxides[120].

For the MnO_2/GNP there is an initial weight loss before 300°C attributed to the loss of adsorbed solvent molecules and the content of sulphates ions from the hydrothermal reaction. There is a main weight loss of an 85% from 450°C to 700°C. This loss is ascribed to both the phenomena already described for plain MnO_2 and plain GNP. The decomposition of the carbon structure, however, is drifted to lower temperatures. This is due to the oxidation reaction that takes place during the MnO_2 synthesis and that affect the carbon lattice, introducing numerous defects that facilitate the thermal decomposition.

4.14 Characterization of the electrochemical properties

In order to evaluate MnO_2/GNP ORR activity, Rotating Disc Electrode (RDE) experiments are performed over GrMnO_2-3 sample. Plain MnO_2 without graphene and GNP without MnO_2 are also studied by RDE to enable a better comprehension of the catalytic activity. Furthermore, PtC (20%Pt on Vulcan XC-72) is also measured, as it is known that Pt based catalyst presents excellent ORR activity and the reaction takes place via one pathway or 4 electrons process.

The linear sweep voltagrams (LSV) show the morphology of the curves, ORR onset potential vs NHE and the diffusion limiting current (Steady state zone) for all the tested samples. Figure 4.29 shows LSV curves for all samples at different rotating rates. It can be seen that curve morphology of ref MnO_2/GNP and the Pt/C are similar, they have a great increase of the current density until reach to steady state or the diffusion limited current density zone. The onset potential for the MnO_2/GNP is 80mv aprox. greater than Pt (+0,1V vs NHE) and the diffusion limited current density (3 mA/cm^2 for 1600rpm) is lower than the Pt/C(4 mA/cm^2 for 1600rpm). This MnO_2/GNP behavior in ORR is promising and demonstrate that graphene improve the ORR activity if MnO_2 growth homogeneously around the Graphene platelets. There is no observed ORR activity for MnO_2 and GNP samples. This demonstrates that the composite the both materials dont have activity separately but together the ORR activity increases significantly. The graphene provides great surface area and conductivity enhancing the ORR activity of the MnO_2 catalyst.

When studying the catalytic activity towards the ORR, it is also important to ascertain that the reaction takes place via four-electron pathway.

Orr is a multi electron reaction that may proceed via two different pathways such as direct four-electron pathway (commonly referred as and the two-electron pathway (commonly referred as partial reduction). In direct four-electron pathway, O_2 is directly reduced into water molecules without the formation of hydrogen peroxide (H_2O_2) intermediate. In the less efficient two-step two-electron pathway, O_2 undergoes a two-electron reduction and H_2O_2 is formed as an intermediate. Four-electron pathway is highly preferable, owing to the reduction in lower energy loss and direct reduction of O_2 without any intermediates. Both reactions are described ahead and the schematic mechanism is presented in Figure 4.30 [214].

Mechanism 1

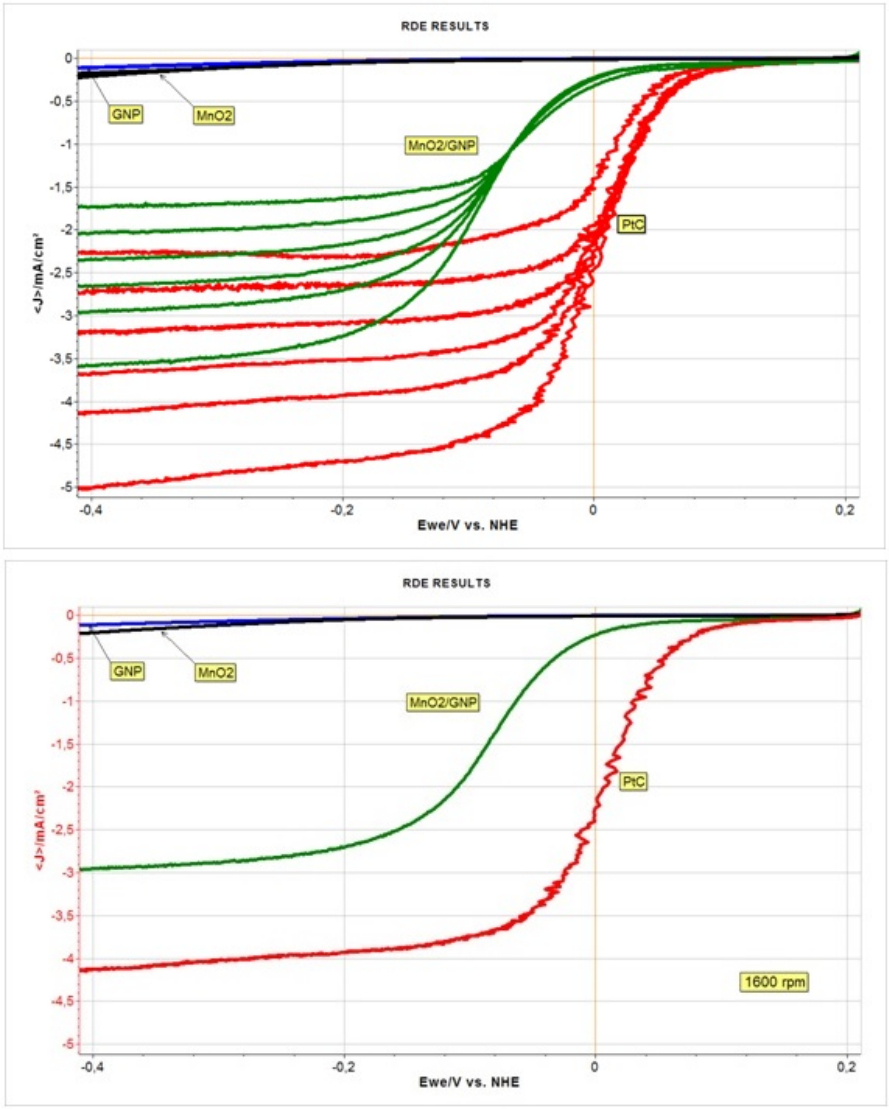

Figure 4.29: Linear sweep voltagrams for $GrMnO_2$-3 (green), PtC (red), plain MnO_2 (black) and plain GNP (blue).

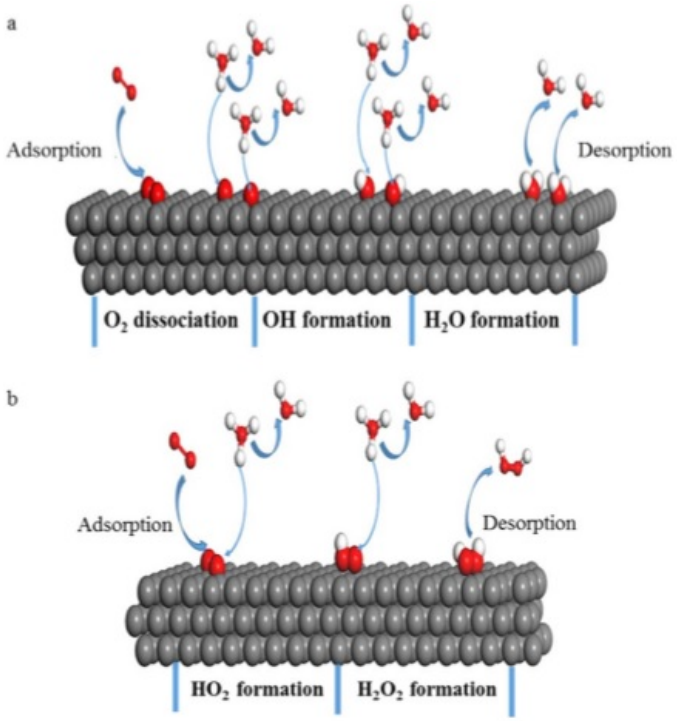

Figure 4.30: Mechanism schematics based on the work of Zhang et al. [274] of a) full reduction and b) partial reduction of oxygen

$O_2 \rightarrow *O_2 + *O_2 + e^- + H^+ \rightarrow *OOH *OOH + e^- + H^+ \rightarrow *OH + *OH$

$2*OH + 2e^- + 2H^+ \rightarrow 2H_2O$

Mechanism 2

$O_2 \rightarrow *O_2 + *O_2 + e^- + H^+ \rightarrow *OOH *OOH + e^- + H^+ \rightarrow *O + H_2O *O + e^- + H^+ \rightarrow *OH$

$*OH + e^- + H^+ \rightarrow H_2O$

The LSV curves recorded at different rotating rates can be utilized to construct Koutecky-Levich (K-L) plots according to K-L equation in order to calculate de number of electrons (n) involved in ORR and also ik kinetic current can be calculated:

Equation 4.15.1:Koutecky Levich Equation

$$\frac{1}{i} = \frac{1}{i_k} + \frac{1}{0.62nFC0Dov^{-\frac{1}{6}}\omega^{\frac{1}{2}}}$$

Where:

I: measured current density

i_k : kinetic current density

n: number of electrons transferred per O_2 molecule

F: Faraday constant (96,485 $Cmol^{-1}$)

ω:angular velocity of rotation.

CO: Saturated concentration of O_2

D_0: Diffusion coefficient

v: viscosity

For the performed tests, CO= $1{,}1x10^{-6}$ mol/cm^3 in KOH 1M , D0 in 1M KOH solution $1.7610^{-5}cm^2\ s^{-1}$, and ?)= 1M KOH are cited as 110^{-2} $cm^2\ s^{-1}$.The results after applying K-L are presented in Figure 4.31.

K-L MnO_2/GNP and PtC plots are in parallel to the $4e^-$ pathway process but the kinetic current density ik is different. Pt has the greater ik (23 mA/cm^2) because ORR is faster with this catalyst, also n is close to 4 that corroborated ORR mechanism taking place via $4e^-$ with this catalyst. MnO_2/GNP sample plot is parallel to the $4e^-$ reference plot too but izzzz (11 mA/cm^2) is lower than the Pt, approximately a half (n≈3,1) which means that partially ORR is via $4e^-$ or is possible that ORR is via $2e^-$ but HO_2- reduction/disproportionation to OH- is faster for this sample.

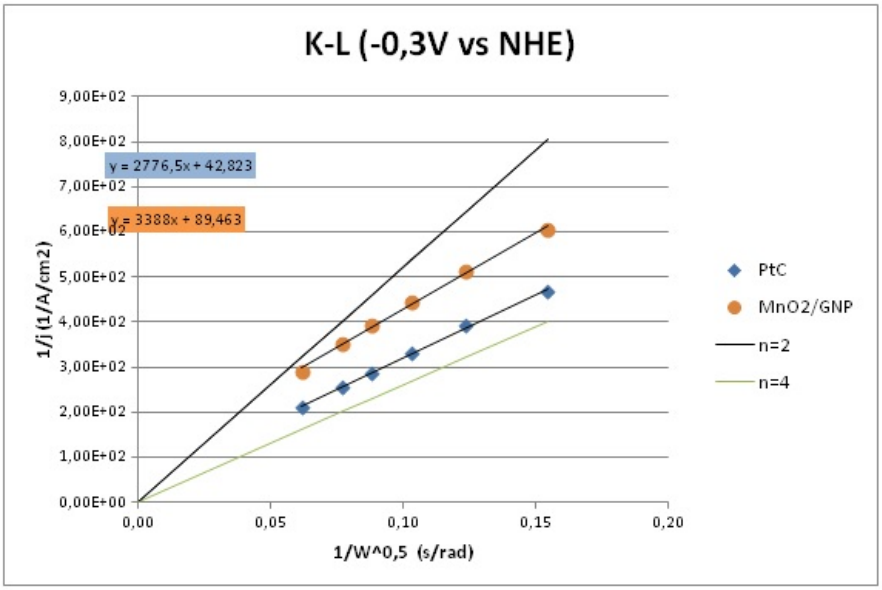

Ref	E(V)	DO2(Cm^2s^{-1})	CO2($molcm^{-3}$)	nu(Cm2S-1)	a (pendiente)	1/a	n (electrones)	enada en ori	K (mA/cm2)
PtC	-0,3	1,76E-05	1,10E-06	0,010	2776,500	3,602E-04	3,75	42,8	23,36
MnO2/GNP	-0,3	1,76E-05	1,10E-06	0,010	3388,000	2,952E-04	3,08	89,5	11,17

Figure 4.31: Plotted results after the use of K-L over the RDE results for sample $GrMnO_2$-3(orange) and PtC (blue).

4.15 Conclusions

MnO_2 nanoparticles have been successfully synthesized by simple hydrothermal method

MnO_2 nanoparticles were obtained by a two step hydrothermal synthesis consisting in 1) a mixing/dispersion in water and assisted by SDBS and 2) a reaction at 240 °C for 6 hours with a homemade autolave with a filling factor of 0,85. The reaction, when carried out in the presence of GNP, lead to the functionalization of their surface.

The morphology of the obtained MnO_2 nanoparticles was measured and compared

Several morphologies were identified for different GNP concentrations. The relation between the amount of manganese salts for the reaction and the amount of dispersed GNP proved to be a determining factor in the growth of the nanoparticles. In absence of GNP, MnO_2 grew as long rods. With an increasing presence of GNP, MnO_2 nanospheres begin to appear and for the highest amount of GNP tested, most of the MnO_2 was forming nanospheres. The explanation behind this behavior is the amount of nucleation spots available for the growth of MnO_2. When large GNP areas are available, the MnO_2 tends to use it to grown in small spheres. When their surfaces are lacking, MnO_2 grows over itself forming rod-like and wire-like morphologies, with high length to width ratios. Furthermore, it has been ascertained that MnO_2 has a greater tendency towards the edges of the GNP rather than their surfaces. A summary of the morphological characterization is presented in Table 4.10.

Table 4.10: Summary of the morphological properties measured for the synthesized samples

$KMnO_4$:GNP	Morphology	Sizes
No GNP	Rods	Length: 1-5 μ Thickness: 150-300nm
2,5:1	Wires > Spheres	Wires (Length: 2 μ Thickness: 30nm) Spheres (100nm radiu
1:1	Spheres >> Wires	Wires (Length:500nm Thickness: 20nm) Spheres (100nm rad
1:2,5	Spheres	50-100nm radius

The crystal structure of the synthesized MnO_2 nanoparticles has been determined

XRD analysis was carried out over MnO_2/GNP composite from sample Gr-MnO_2-3 and over the plain MnO_2 sample. On the one hand, plain MnO_2 was

indexed to be pure β- MnO_2 (pyrolusite), with small crystallite size. On the other hand, MnO_2 from sample Gr-MnO_2-2 exhibited an amorphous structure, also with small crystalline domains.

Thermal stability of MnO_2/GNP composites and plain MnO_2 has been studied.

Thermal stability analysis were successfully carried out by TGA over the mentioned samples and compared to the results obtained in Section 4.2 for plain GNP, at 5°C/min and under air atmosphere. The most remarkable feature is the reduction of the decomposition temperature for the MnO_2/GNP, that drops from 600°C to 450°C. GNP begins its decomposition at lower temperatures due to the introduction of defect in the carbon atom lattice during the hydrothermal reaction.

Chapter 5

Graphene based thermally conductive polymer composites

5.1 Introduction: Approach, Objectives and Experimental Details

5.1.1 Approach

One of the many applications of carbon nanofillers/ epoxy resin nanocomposites is to enhance the thermal conductivity of electronic devices, where heat dispersion is very important. The reliability of electronic devices is highly dependent on the operating temperature as they heat up during operation, thus, fast heating dissipation is desirable and is achieved usually by adding thermal conductivity fillers [190], also called Thermal Interface Materials (TIMs). Plain epoxy resins usually present a thermal conductivity between 0.17 W/mK and 0.22 W/mK and, for TIMs thermal conductivities in the range of 1-5 W/mK are desirable. So, carbon nanofillers are used to enhance it. (NOTE: some authors provide the filler content of their samples in %wt. while other do it in %vol. what difficults the comparison between results).

Graphene and graphene-derivatives are promising fillers for epoxy composites due to its great thermal conductivity and its high aspect ratio, and stand out when compared to other commonly used fillers, as lower loadings are required to achieve similar results. For example, conductivity values between 0.35 W/mK and 0.65 W/mK were reported by L. Fan et all[59] for Al2O3/epoxy composites with a loading of 50 wt%, whereas, R. Moriche et al [152] published a value of 0.65W/mK for an epoxy resin loaded with a 10%wt. of GNP, introduced by sonication and calander.

The comparison between graphene and other carbon allotropes is necessary, especially with CNT. For instance, Jukubinek et al [100] reported a maximum thermal conductivity value of 0.29 W/mK at 300K, reached by their epoxy/MWCNT composites of volume fractions up to 0.04. The thermal conductivity is not very much enhanced even increasing dramatically the MWCNT concentration: For epoxy/MWCNT buckypapers containing 47%wt. MWCNT a thermal conductivity of 0.40 W/mK at 300K, which represents an increase of around 100% with respect to neat epoxy, was reported by Chapartegi et al[35].The low thermal conductivity of composites that contain MWCNTs has been explained by the very low thermal conductance of the nanotube-polymer interface [151]. In this sense, the high thermal conductivity (1.4 W/mK at 300K) observed for a microwave cured epoxy/MWCNT composite has been suggested to be due to the improvement of the interfacial bonding [88]. The

latter is a rather exceptional result and as a matter of fact the thermal conductivity of polymer/graphene composites is in general (not only for epoxies) higher than that of polymer/MWCNT composites [108] [204], [109]. A modest 3-fold increase was found by Esposito et al [187] for epoxy/graphene composites prepared using acetone to disperse expanded and sonicated graphite. But, as reported in the review of Kim, Abdala and Macosko [108], a 30-fold increase in thermal conductivity was attained by incorporating 25%vol. of few nanometer thick graphite platelets to an epoxy resin via solution polymerization. A similar enhancement was obtained by Haddon et al[87], who reported a thermal conductivity of 6.4 W/mK for a 25% vol. of graphene platelets loading in an epoxy matrix. With a 10%wt. of graphene a 4,01W/mK value was reported by Fu et al [68]. A combination of graphene and MLG with XDXDXD were loaded at a 10 vol% into an epoxy by K. M. F. Shahil and A.A. Balandin[193], resulting in a thermal conductivity of 5.1 W/mK. To my best knowledge, the highest thermal conductivity value ever reported is 12.4 W/mK, obtained with a epoxy/graphene composite elaborated with commercial graphene submitted to high pressures during dispersion to close the gaps between adjacent platlets [203]. More recent experiments have not been able to achieve higher values. Haiquing et al reported a 0.56W/mK conductivity with the addition of 5%wt. graphene nanosheets [264] and , with the same amount of GNP (5%wt.), Li et al achieved 0.70W/mK conductivity [130]. All these results are summarized in Table 5.1

Table 5.1: Summary of the thermal conductivities achieved by several groups in the filed of epoxy composites.

Filler	Loading	Thermal cond. (W/mK)	Reference
Al_2O_3	50%wt.	0.35-0.65	[59]
GNP	10%wt.	0.65	[152]
MWCNT	0.04%vol.	0.29	[100]
MWCNT	47%wt.	0.4	[35]
GNP	25%vol.	6.4	[87]
G	10wt.	4.01	[68]
G+MLG	10%vol.	5.1	[193]
G	Not specified	12.4	[203]
G Nanosheets	5%wt.	0.56	[264]
GNP	5%wt.	0.7	[130]

In addition to the thermal conductivity, when studying a material for its use as TIM is necessary to make a rheological characterization. The rheological behavior of nano-reinforced fluids plays an important role during the manufacturing process, and thus on the performance of the final products. Despite the

extensive literature in the rheology of CNT based materials, much less has been reported on the rheology of graphene and graphene derivatives. Very recently Francesco del Giudice and Amy Q Shen presented a study on the shear rheology of GO dispersions, but emphasizing mostly in aqueous dispersions [53]. Focusing on the epoxy composites, M. Martin-Gallego and its team [148] reported some years ago a comparison between CNT epoxy composites and graphene epoxy composites, mainly centered in the mechanical properties. Panta Jojibabu et al [99] also presented a rheological study comparing different carbon nanofillers in epoxy adhesive joints and Marialaura Clausi [46] et al, focused in the differences of steady-shear rheological properties for GNPs with different morphologies.

But, there are very few studies that combine the rheological and thermal conductivity analysis of graphene/epoxy composites. However, both fields are closely related. It is well known that the greatest thermal conductivity is achieved when a network of the filler is formed within the polymer matrix, i.e. when the system reaches the percolation threshold. Martin-Gallego et al, ascertained that the rheological percolation of graphene in epoxy matrix is over a 1.5%wt. Li and its group, on a more recent study, did not found evidences of thermal percolation for samples below a 5%wt. graphene [130].

There are two main strategies to analyze the formation of this filler network: 1) To analyze the thermal conductivity of samples with increasing filler concentration and 2) To study the rheological response of the dispersion in the liquid state. In both cases a jump on the properties should be found when the system passes from a non-percolated state to a percolated one. In this chapter, both research paths will be followed.

5.1.2 Objectives

The general objective of this chapter is to evaluate the potential use of the graphene-like materials as fillers in TIMs. The materials have already been characterized and studied along this thesis and their properties presumably fit the conditions required for a good performance in this field. Bibliographic reports, furthermore, confirm the good results obtained by different carbon allotropes, and graphene derivatives are expected to score even better.

The specific objectives to achieve in every step of this study are the following:

- To study the compatibility between an epoxy resin and the different graphene-like nanomaterials that have been characterized and used in previous chapters.
- To establish the proper method and conditions for the elaboration of solid epoxy specimens that meet the requirements for the thermal conductivity characterization.
- To investigate the effect of different mixing techniques on the thermal and rheological properties of epoxy resins filled with graphene-like nanofillers.
- To study the effect of different graphene derivatives on the thermal conductivity of epoxy composites.
- To compare the thermal conductivity enhancement of a graphene-like nanofiller with a regular carbonaceous filler like graphite.
- To study the rheological properties of epoxy resin filled with graphene-like nanofillers.
- To evaluate the formation of a nanofiller network and to establish the rheological and thermal percolation threshold of the graphene/epoxy system.
- To develop a composite of epoxy and graphene-like nanofiller and compare its thermal and rheological performance with a commercial epoxy resin, in order to evaluate its applicability as TIM.

5.1.3 Experimental Details

Epoxy Resins

Epoxy resin is a versatile thermosetting polymer with its molecule consisting of two or more 1,2-epoxide groups. The most commonly used epoxy is diglycidyl ether of bisphenol A (DGEBA), which is characterized by the presence of two epoxide groups5.1. The epoxide group is subjected to a variety of chemical reactions to obtain different epoxy resin structures. Commonly used cross-linking agents for generation of cross-linked structures are aliphatic amines, aromatic amines, polyamines and anhydrides. The degree of the cross-linking as well as the inter-chain bond nature provides cross-linked epoxies attractive properties like high degree of adhesiveness with many substrates, high tensile and flexural strength, good chemical and corrosion resistance and satisfactory electrical properties [190].

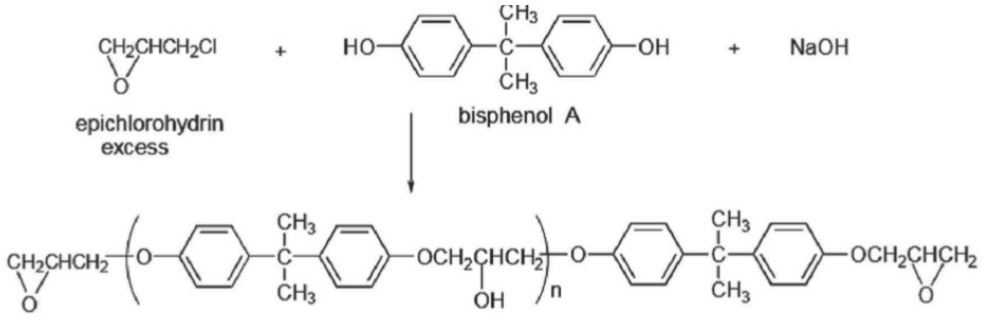

Figure 5.1: Schematic synthesis of DGEBA [190]

Two different epoxy adhesives from the same company are employed and compared in this chapter: ECCOBOND 55 Unfilled General Purpose Epoxy Adhesive and ECCOBOND 285 Thermally Conductive Epoxy Paste Adhesive, both provided by Henkel.

The first one, ECCOBOND 55 is a regular two component DGEBA for multiple applications. The second one, ECCOBOND 285, is a commercially available thermally conductive adhesive with a high percentage of alumina as filler, which is obtained by adding this alumina filler to the ECCOBOND 55. ECCOBOND 55 is then an earlier step in the elaboration of ECCOBOND 285. No information about the thermal conductivity of ECCOBOND 55 is provided in its datasheet, whereas ECCOBOND 285 presents a higher thermal conductivity due to the thermal conductivity enhancer added.

ECCOBOND 55,as a plain epoxy resin, would be filled with different graphene-like materials at different %wt. loadings and compared with the commercially available ECCOBOND 285, which is already used in industry for thermally conductive properties.

Datasheets for both materials are presented in Annex 2

Graphene-like materials

Five different graphene-like materials are studied in this chapter: Avanzare AvanGraphene GNP, Graphenea rGO, Graphenea GO, Graphenea Dry GO and Scharlab Graphite.

Avanzare AvanGraphene GNP, Graphenea rGO and Graphenea GO have been presented, characterized and applied several times along the thesis. All

the information and knowledge about this materials gathered during previous studies will be useful to understand their behavior and results in this chapter. Because of their pure carbonaceous nature GNPs, presents high thermal conductivity enhancement potential. In addition, some authors [239] y [129] pointed out that the presence of functional groups on the surface of the graphene layers could improve the interfacial bonding between epoxy and filler, achieving better dispersion. For this reason the three types of graphene derivatives (GNP, rGO and GO) will be used.

Graphenea Dry GO is the dried version of Graphenea GO. Graphenea GO, as explained, is provided as slurry with a concentration of 0.5 mg/mL. This slurry, when slowly dried, leads to the agglomeration of the GO platelets, resulting in a sheet formed by the superposition of thousands of GO platelets. This material is offered by Graphenea as an alternative to the regular GO slurry for applications where presence of water must be avoided.

When studying the use of nanomaterials it is advisable to compare the results with the ones that could be obtained with their macro-sized counterpart. In this case, the thermal conductivity results achieved with the graphene derivatives must be compared with the ones that could be obtained with regular graphite. Scharlab Graphite will be used for this porpoise. This graphite is a (INCLUIR DηLLES TECNICOS lateral size, orgien, tamao de los platelets, etc.) NOTANOTA

Nanofiller introduction techniques

Several techniques are currently being used for the incorporation of graphene-like nanofillers to epoxy resins with different degree of succes [221], [32] y [9]. The technique and the conditions for introducing these nanomaterials into resin have a great impact on the performance of the final composite. It can affect not only the structure of the nanomaterial but also its agglomeration grade and the homogeneity of its distribution over the matrix. It is reported that highly dispersed fillers tend to present better properties enhancement than poorly dispersed filler particles [190]

In this chapter, three of the most reported techniques for the introduction of nanofiller in epoxy matrixes are used: Calender mixing, High-shear mixing with Cowles disk and Solvent pre-mixing by ultrasonication.

Calender: Calendering is used commercially for dispersing pigments in inks, paints and cosmetics. It results in nearly pure shearing as opposed to other

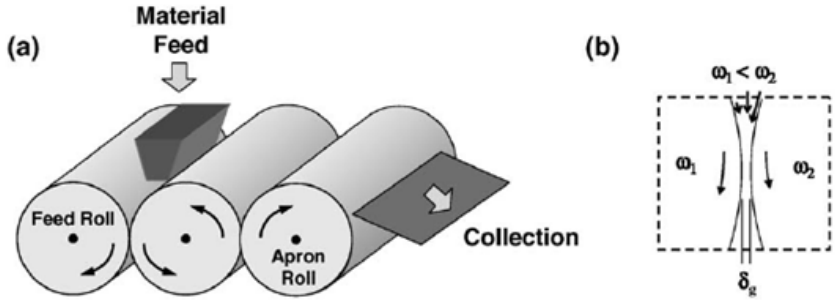

Figure 5.2: (a) Schematic diagram showing the general configuration of a three-roll mill. (b) Region of high shear mixing between the feed and the center rolls[229].

types of mills, which rely on compressive impact as well as shear. Its configuration is illustrated in Figure 5.2 (a) and consists of three adjacent cylindrical rolls where each turns at a different velocity, from the slowest one, where the material is fed, to the fastest one, where the dispersion is collected. The first and the third rolls rotate in the same direction while the center roll, with an intermediate velocity, rotates in the opposite direction.

The dispersing effect results from the high shear stresses generated in the gap between the adjacent cylinders, as shown in Figure 5.2 (b).The narrow gap between the rolls, δg, combined with the mismatch in angular velocity of the adjacent rolls, ω1¡ω2, results in very high shear forces.

The particular conditions employed for calander in this chapter are described ahead: The nanofiller is added into the resin and mixed with a glass rod for 5 minutes. The mix is then submitted to the calender process summarized in Table 5.2.

Table 5.2: Summary of the steps in the calendaring process.

Repetitions	**Gap 1 (νm)**	**Gap 2 (νm)**	**Speed (rpm)**
1	120	40	250
1	60	20	250
1	45	15	250
2	15	5	250

Mechanical stirring with Cowles disk: The high shear forces required to disperse the graphene in the epoxy resin are generated by a mechanical stirrer with an attached Cowles disk. This kind of disk present a geometry (Figure

Figure 5.3: Geometry of the Cowles disk[3].

5.3) that makes it suitable to apply high shear in highly viscous mediums.The geometry is so that is generates what is known as the doughnut effect (Figure 5.4).

The doughnut-like flow pattern is formed when a channel begins to form around the shaft and a part of the disk becomes visible. It is a signal of maximum mechanical power in the millbase and is developed because the millbase is accelerated outwards from the tip of the disk. When hitting the wall of the container, the stream is divided into two parts: The one going downwards flows back to the middle of the disk along the bottom of the dispersion container and rises up to hit the disk once again. The second part flowing upwards has the same circular path, which is limited by the force of gravity and the rheological properties of the millbase.

The particular conditions employed for Cowles disk in this chapter are described ahead: The resin is poured into a cylindrical container with 7cm in diameter and 13cm height. A Cowles disk with 3cm in diameter is submerged into the resin at 5mm over the bottom of the container and starts rotating at 9000rpm. The nanofiller is then added slowly over the agitated resin. When the addition is completed, the agitation will continue for 35 minutes.

Solvent pre-mixing by ultrasonication: In this technique, the nanofiller is not directly dispersed into the resin by shear forces but it is dispersed into

Figure 5.4: Doughnut-like flow pattern [3]

a chosen solvent. In the present study, exploiting the knowledge in GNP dispersions developed in previous chapters, ultrasonication tip will be the method employed to prepare it. After the sonication process in a suitable solvent, the dispersion is incorporated to the resin. Thus, the selected solvent should be compatible both with the resin and the nanofiller. Once incorporated, the solvent is eliminated from the mixture by heating or submitting to vacuum conditions, for what the solvent should have a lower boiling point than the resin.

The particular conditions employed for solvent pre-mixing in this chapter are described ahead: Acetone is the chosen solvent for its compatibility both with the nanofiller and the ECCOBON55. The nanofiller is dispersed into the acetone, with a concentration of 10 mg/mL, by ultrasonication tip for 40 minutes at 40%. Then, the dispersion is poured into the resin and vigorously mixed with a glass rod for 5 minutes.

Thermal characterization

The thermal conductivity measurements are carried out using a Hot Disk Thermal Constants Analyser TPS 2500 S (Figure 5.5).

The basic principal of the system is to supply a constant power to an initially isothermal sample via a Hot Disk sensor and during a limited heating period follow the resulting temperature increase by using the sensor also as a resistance

Figure 5.5: Image of the Hot Disk Thermal Constants Analyser TPS 2500 S.

thermometer. The dynamic features of the temperature increase, reflected in resistance increases of the sensor, is precisely recorded and analysed so that both the thermal conductivity and the thermal diffusivity can be determined from one single transient recording.

For these measurements an electrically insulated Hot Disk sensor is sandwiched between two identical samples of the same composition. The Hot Disk sensor consists of an electrically conducting pattern in the shape of a double spiral etched out of a thin sheet of Nickel with the radius 2.001mm. The Nickel foil is chosen because of its high and well-known temperature coefficient of resistivity. The conducting pattern is supported on both sides with a thin electrically insulating material. The sensor act as the heat source (heating the sample) and temperature monitor (recording the temperature increase of the sample) simultaneously.

Rheological characterization

For the rheological characterization of the composites a Thermo Scientific Haake RheoStress 6000 is used (Figure 5.7). It enables measurements in dynamic, stationary and transitory regimen. Its rotation and oscillation torques operate from 200nNm to 200mNm (with a torque resolution of 0,5nNm at the lowest torque) and its oscillation frequencies from 10^{-5} Hz to 100 Hz. This equipment presents a minimum angular velocity of 10^{-7} min^{-1} and a maximum of 4500 min^{-1}, with an internal angular resolution of 12 nrad. Samples can be studied in the range of -80°C to 500°C.

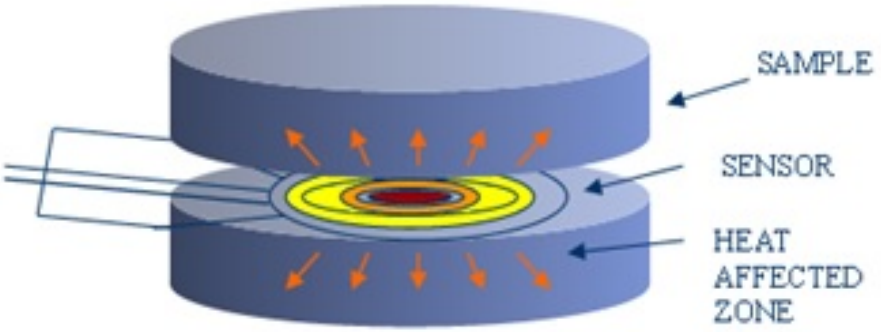

Figure 5.6: Schematic of the sensor sandwiched between two similar samples. (Graphene Commercialisation & applications 2013. Balandin Group, UC Riverside / Presenter: P. Goli)

Figure 5.7: Image of the Thermo Scientific Haake RheoStress 6000

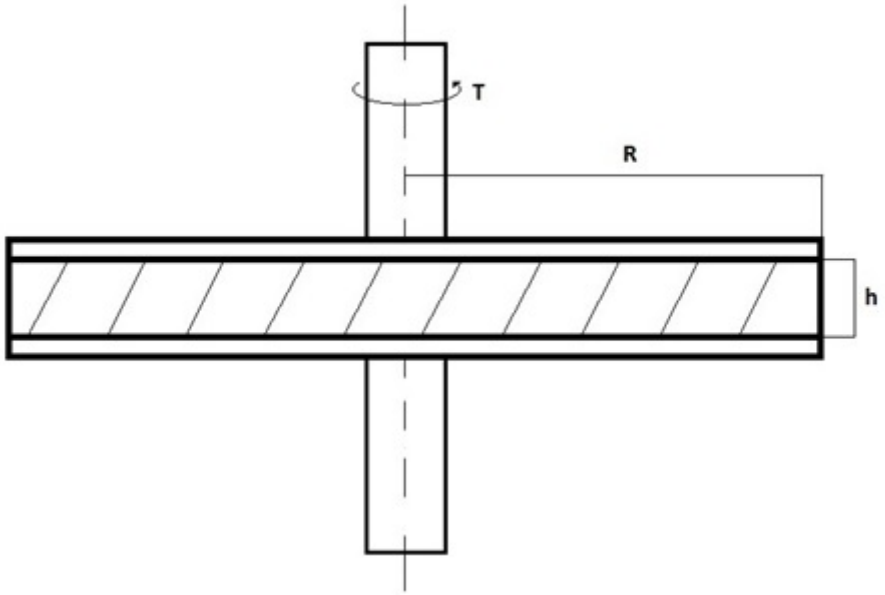

Figure 5.8: Schematic representation of the parallel-plate sensor. Where <<R>> is the radius of the disks, <<T>> is the torque applied for the rotation and <<h>> is the distance between disks, filled with sample.

Measurements under controlled strain in oscillatory and rotational modes can be performed with the Thermo Scientific Haake RheoStress 6000. The temperature is controlled by a Peltier module, which provides fast cooling and heating times. Sensors with different geometries can be used in this device. For the results presented in this work, the sensor employed is the parallel-plate. A schematic representation of the sensor is presented in Figure 5.8. The sample is placed between two parallel disks of radius <<R>>. <<h>> is the distance between both disks. One of them rotates at an angular velocity Ω with a torque T, whereas the other holds firm.The shear-rate GAMMAPUNTO depends on the distance to the rotation axis. This value would be maximum at the edge of the sample and 0 at the center. The same happens with the shear-stress τ. Generally, the value at the edge is considered in both cases.

For <<h>> values where R>>h, both Equation 5.1 and 5.2 are satisfied.

Equation 5.1

$$\gamma^{o} = \frac{\Omega R}{h}$$

Equation 5.2

$$\sigma = \frac{2T}{\pi R^3}$$

The rheological measurements in this chapter are carried out using parallel plates of 40mm diameter (R=20mm) and 1 mm gap (h=1mm). Except when stated otherwise, all the measurements are performed at room temperature (27°C). The characterization is performed using steady state flow tests and oscillatory test. The viscosity, which is the ratio between the shear stress and the shear rate, is evaluated in shear rate range between 0.1 and 100 Hz. Dynamic sweeps at 1Hz are carried out at an oscillation strain selected in the linear viscosity region. The storage moduli (G') and the loss moduli (G") as a function of time are measured. Gel point is determined by the crossover of the storage and loss moduli (G'=G").

5.2 Elaboration of epoxy composites with graphene-like nanofillers

In order to evaluate the thermal performance of different graphene-like nanofillers for its use in TIMs there are some previous studies that must be carried out. The thermal conductivity measurements require solid specimens of sizes above 40x40x3mm. So, as a first step, it is necessary to establish the conditions for the proper elaboration of these specimens with the plain epoxy resin, without fillers. Secondly, the compatibility between the fillers and the resin must be ascertained, aiming an homogeneous dispersion along the structure of the specimen.

These two unavoidable points are developed ahead, before the thermal and rheological characterizations.

5.2.1 Specimen elaboration with ECCOBOND 285

The rheological properties of the composites can be studied without the elaboration of solid specimens. However, the measurement of the thermal conductivity with the technique described requires solid specimens to be accomplished. To

this regard, this first section will focus on establishing the conditions for the successful elaboration of specimens with plain epoxy resins. The epoxys used in this thesis are composed of two different parts: The resin and the hardener (catalyst). Proper specimens will require 1) homogeneous mixing of the catalyst and the resin, 2) correct curing of the mixture and 3) absence of defects like air bubbles or roughness on the surface.

To begin with, ECCOBOND285 is used to establish the conditions for a successful specimen elaboration method. The datasheet of ECCOBOND 285 provides a thermal conductivity value (1.44 W/mK), **The approximation of the specimens to that value will be taken as an indicator for the reliability of the manufacturing method**. The thermal conductivity of each specimen is measured in four separated points along its surface, to ensure its homogeneity, and each measurement is repeated three times. Furthermore, a visual inspection of the specimens and an insight view of its lateral profile after a cut are carried out too, helping to confirm the absence of air bubbles and defects.

The manufacturing process of the ECCOBOND 285 samples consists in two main steps. In the first one, the epoxy resin is vigorously mixed with the required amount of catalyst and the mixture is degased in order to eliminate any possible air bubbles that could have entered the matrix during the mixing process. In the second step, the mixture is cured attending the specifications of the catalyst. Two samples are prepared, one by hand mixing and the other by mechanical mixing.

The thickness of the specimen is controlled by the size of the mold. For the thermal conductivity measures to be admissible with the Hot Disk Thermal Constants Analyser TPS 2500 S with a 2.001 mm radius sensor, the surface of the sample must be above 40x40mm and the thickness above 3mm.

A more detailed description of the manufacturing process follows:

1- A mixture is prepared adding 50g of ECCOBOND 285 and 1,75g of Catalyst 9 (3.5:100) weight ratio catalyst:resine

2- The mixture is blended during 10 minutes (hand mixing or Mechanical mixing).

3- The mixture is degased in a vacuum chamber during 10 minutes at 0.7 atm.

4- The mixture is poured into a 40x40x3mm mold, degased for additional 10 minutes and cured at room temperature (20°C) for 24h (following datasheets specifications for ECCOBOND 285 and Catalyst 9 mixtures).

Additionally, due to the high viscosity noticed on ECCOBOND 285 during its handling, a third specimen is prepared. This last sample is submitted to mechanical mixing in combination with simultaneous degasification. Table 5.3 summarizes the elaboration conditions for each ECCOBOND285/Catalyst 9 specimens and their thermal conductivity.

Table 5.3: Summary of the manufactured ECCOBOND 285/ Catalyst 9 samples and the measured thermal conductivity for each.

Sample	Resin	Catalyst	Mixing process
A	ECCOBOND 285	Catalyst 9	Hand mixing (10min) + Vacuum degas (10 min
B	ECCOBOND 285	Catalyst 9	Mechanical mixing (10min) + Vacuum degas (10 min
C	ECCOBOND 285	Catalyst 9	Simultaneous mechanical mixing and vacuum degas (10min

The conductivity results obtained for samples A and B (1.025W/mK and 1.088 W/mK respectively) are far from the 1.44 W/mK specified in the datasheet for ECCOBOND 285/Catalyst 9 mixtures. Thus, the conditions used in their elaboration do not fit the requirements needed. The reason for this lower conductivity can be better explained by direct observation of the specimens:

Figure 5.9 shows images of the specimens made from samples A, B and C, including a lateral image showing the profile of specimen C. Due to its high viscosity, resin ECCOBOND 285, presents problems during the gasification process. The consequences of these problems can be appreciated in the specimens of samples A and B. There is a massive presence of bubbles and irregularities all over the material. The thermal conductivity of both specimens is measured exploiting the areas with less imperfections, but the results differ heavily with the one provided in the datasheet and are far unreliable.

Nevertheless, sample C presents a flat surface where no presence of air bubbles can be found. The lateral cut of the specimen does not show any imperfections in its profile either. Furthermore, the measured thermal conductivity value of 1.44 W/mK measured agrees with the information provided in the datasheet. The thermal conductivity measurement is made on four different areas of the surface and repeated three times for each. A value of 1.44 W/mK is obtained in all of them. These results allow concluding that **the elaboration process employed for specimen C (simultaneous vacuum**

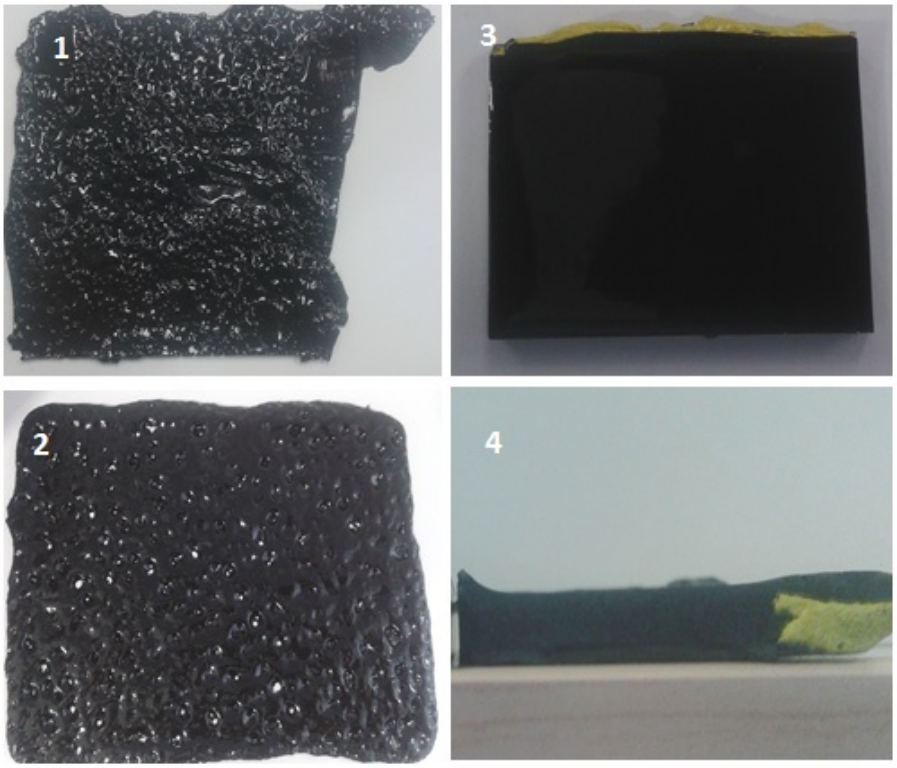

Figure 5.9: ECCOBOND 285 sample: (1) sample A, (2) sample B, (3) sample C and (4) lateral view of sample C.

degas and mechanical mixing of catalyst and resin for 10 minutes) is appropriate for the nature of ECCOBOND 285.

5.2.2 Specimen elaboration with ECCOBOND 55

Once the conditions for the elaboration of ECCOBOND 285 specimens are established, the same research on ECCOBOND 55 results easier. Furthermore, the absence of alumina filler in ECCOBOND 55 when compared with ECCOBOND 285 makes it way less viscous, what eases both the mixing with catalyst and the degas steps.

The process followed for the elaboration of ECCOBOND 55 is based on the conditions established in previous section. However, due to the big difference in viscosity noticed in handling, two different specimens are prepared: One with vacuum degas and the other without it:

1- A mixture is prepared adding 50g of ECCOBOND 55 and 6.75g of Catalyst 9 (13.5:100) weight ratio catalyst:resine

2- The mixture is blended during 10 minutes by hand mixing.

3- The mixture is degased in a vacuum chamber during 10 minutes at 0.7 atm (just for one of the samples).

4- The mixture is poured into a 40x40x3mm mold, degassed for additional 10 minutes (just for one of the samples) and cured at ambient temperature (20°C) for 24h.

Pictures of the specimens and their profiles are shown in Figure 5.10. It can be noticed that the morphology heavily varies from that of ECCOBOND 285, principally the color. This difference is related to the absence of alumina in ECCOBOND 55. However, when comparing both ECCOBOND 55 specimens, with and without degassing, no differences can be appreciated. Neither showed any presence of bubbles or defects. Table 5.4 summarizes the conditions and thermal conductivity results for the two samples. In both cases the thermal conductivity is 0.21 W/mK. As in the case of ECCOBOND 285, the measurements where made over 4 different spots and repeated three times.

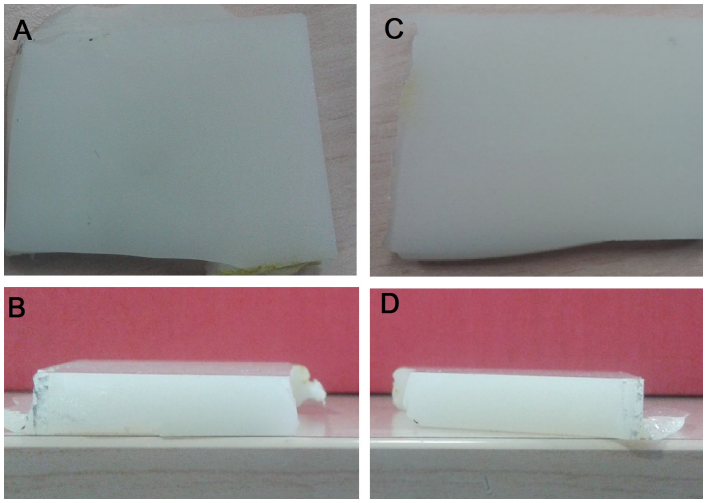

Figure 5.10: ECCOBOND 55 specimens with 40x40mm surface and 3.5mm thickness. A and B correspond to the degassed specimen whereas C and D correspond to the undegased one

Due to the different viscosity properties of the ECCOBOND 55, just hand mixing processes proof to be successfully employed in the manufacturing of the

specimens. Air bubbles present in ECCOBOND 55 during the first step of elaboration are noticed to spontaneously leave the system after the mixing process. However, it is expected an increase in the viscosity when adding graphene-like nanofillers to ECCOBOND 55. The increase in viscosity could difficult the partial self-degasing process perceived for ECCOBOND 55, for what further specimens would be submitted to a vacuum degas process of 10 min at 0,7 atm to ensure the total elimination of possible air bubbles.

Table 5.4: Summary of the manufactured ECCOBOND 55/ Catalyst 9 samples and the measured thermal conductivity for each.

Sample	Resin	Catalyst	Mixing process	Thern
A	ECCOBOND 55	Catalys 9	Hand mixing (10min) + Vacuum degas (10 min)	
B	ECCOBOND 55	Catalys 9	Hand mixing (10min) + No Vacuum degas	

To conclude, these preliminary studies have enabled to establish two main points:

A) The reference thermal conductivity values of ECCOBOND 285 and ECCOBOND 55, 1.44 W/mK and 0.21 W/mK respectively. 0.21 W/mK is the value that must be increased by the addition of nanofiller, whereas 1.44 W/mK is the value that must be approached by the use of graphene derivatives instead of alumina.

B) The conditions for a reliable elaboration of specimens of graphene derivatives/ ECCOBOND 55 composites, which are: 10 minute vigorous hand mixing between the resin and the catalyst, pouring of the sample in a 40x40x3mm mold, degasification for 10 minutes at 0.7 atm and curing at 20°C for 24 hours

5.2.3 Change in the hardener

During previous section Catalyst 9 has been used as hardener both with ECCOBOND 285 and ECCOBOND 55. Hereinafter, however, Catalyst 11 will be used, by recommendation of the provider. Resin ECCOBOND 285 nowadays is extensively used in industry, especially as adhesive in electronic systems, along with Catalyst 11 as hardener. Thus, the study of the composite with this catalyst results of greater interest.

Conditions for the correct proportions of both catalysts are described in the datasheet for each resin. Although there is a difference in the weight relation required by each catalyst, it would hardly affect the developed process

for specimen elaboration. The datasheet of ECCOBOND 285 also indicates that the thermal conductivity for the systems ECCOBOND285/Catalyst 9 and ECCOBOND285/Catalyst 11 are the same.

The specimen elaboration process settled in previous chapter is applied to both ECCOBOND 285/Catalyst 11 and ECCOBOND 55/ Catalyst 11 systems, obtaining, as expected, the same homogeneous and defect-free specimens. Furthermore, the thermal conductivity measured for ECCOBOND55/Catalyst 11 is also 0.21 W/mK, for what the reference values from both systems remain unchanged.

5.2.4 Graphene-like materials and resin compatibility

Five graphene-like materials are selected for its incorporation into ECCOBOND55. Their compatibility with the matrix is studied in this section.

AvanGraphene GNP: This material has already been extensively described and characterized along the thesis. Its compatibility with the resin is tested by Cowles disk mixing. Figure 5.11 shows an image of the specimen with a load of 6.9% in weight. The GNP does not show any incompatibility and the specimen elaboration process success for this filler.

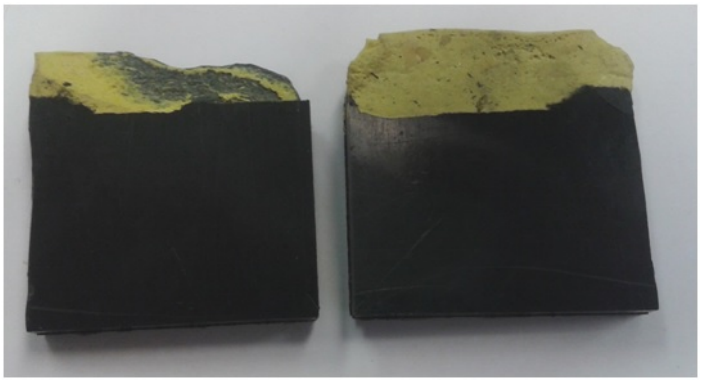

Figure 5.11: Image of ECCOBOND 55- AvanGraphene GNP specimen.

Graphenea GO: This material, again, has been extensively studied along the thesis. It is provided as a slurry, mixed with water, in weight percentages always bellow 5%. The presence of such a high relation of water brings compatibility problems with the resin. Figure 5.12 shows an image of a specimen elaborated by Cowles disk and a 5% of GO in weight. The specimen is completely irregular and fractures grow all along its structure. This result repeats

itself when mixing the GO slurry and the resin by other mixing techniques for what it is attributed to the water-resin incompatibility. Thus, when using GO slurry to elaborate specimens, is necessary to include a first step of evaporation of the major part of water.

Figure 5.12: Image of ECCOBOND 55- GO specimen.

Graphenea Dry GO: Considering the compatibility problems presented by the GO slurry, it was decided to test Graphenea Dry GO. The compatibility results with the resin, however, were not positive neither, as the nanofiller does not disperse correctly into the resin. Figure 5.13 shows the image of a specimen made by hand mixing a 0.08% of dry GO in weight. The dry GO sheets are clearly visible on the surface of the specimen, proving a complete lack of homogeneity. Further tests with Cowles disk mixing improved the dispersion of the nanofiller but also lead to irregular and inhomogeneous specimens.

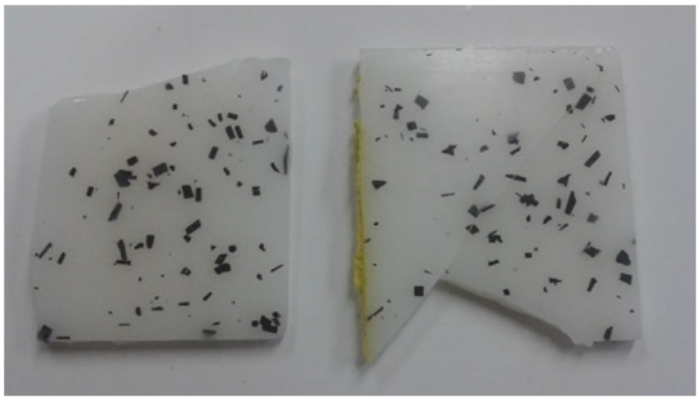

Figure 5.13: Image of ECCOBOND 55- Dry GO specimen.

Graphenea rGO: Similarly to AvanGraphene GNP and Graphenea GO, this rGO has been deeply described and characterized in previous chapters. Its

compatibility with the resin is evaluated by solvent pre-mixing, using acetone as the solvent for the first dispersion. Figure 5.14 shows an image of the specimen with a load of 9.68% in weight. The high price of the rGO when compared to GNP or graphite strongly limits the amount that can be added to the specimens. The rGO does not show any incompatibility and the specimen elaboration process success for this filler.

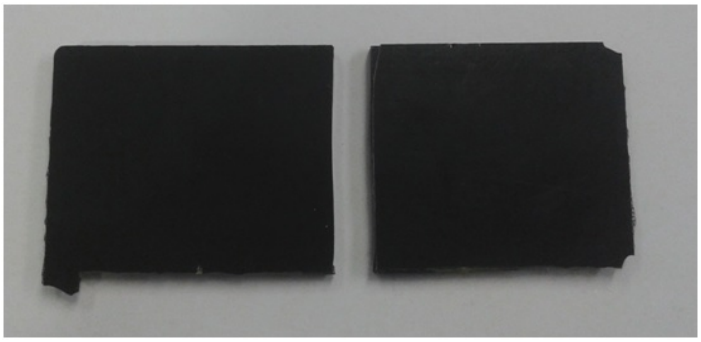

Figure 5.14: Image of ECCOBOND 55- rGO specimen.

Scharlab Graphite: The objective aimed with the use of graphite is to evaluate its performance when compared to GNP (more expensive and less produced by the industry). Its compatibility with the resin is ascertained with the elaboration of a simple hand mixed specimen. Figure 5.15 presents an image of the specimen with a 6.9% load of graphite in weight. Graphite doesnt show any incompatibility and the specimen elaboration process success for this filler.

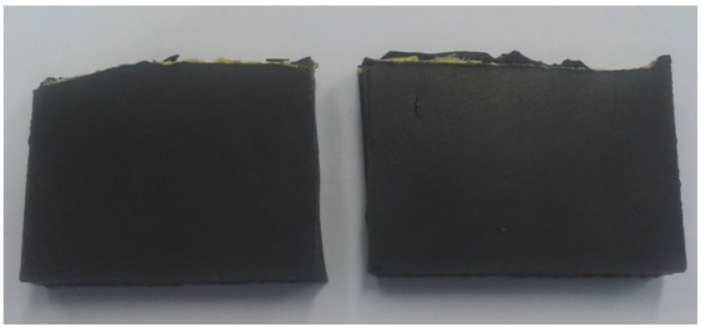

Figure 5.15: Image of ECCOBOND 55- Graphite specimen.

The compatibility tests discard Graphenea Dry GO as suitable filler for ECCOBOND55, as no homogeneous samples has been achieved. Graphenea GO can be used in small proportions and previously evaporating some of its water content.

5.3 Thermal characterization of graphene filled epoxy specimens

Thermal conductivity is a key aspect for the performance of a TIM. Due to the superior thermal conductivity of graphene, graphene/epoxy composites are promising candidates for high-performance TIM.In this section, the effect of different graphene-like nanofillers is studied. The nanomaterials have been chosen regarding the compatibility with the epoxy resin established in section 5.2.3: Graphenea GO, Graphenea rGO and Avanzare GNP. The effect of Scharlab Graphite will also be analyzed for comparison.

Additionally, the effect of different mixing techniques will be studied. The mixing techniques have an important role on the proper dispersion of the nanomaterials in the epoxy matrix. The aggregation of nanoparticles hinders their potential for thermal conductivity enhancement, which presents better results when they are well dispersed and deagglomerated around the matrix. As mentioned, three mixing techniques are compared: Calander, Cowles disk and solvent pre-mixing.

To achieve these results, several sets of tests have been carried out, classified and presented below.

5.3.1 Effect of the nanofiller

The study of the effectiveness of the different nanofillers has been notably hampered by their huge difference in price and availability. The lower availability and remarkably higher prices of rGO and GO when compared to GNP limited the load percentages achieved.

Three specimens have been elaborated. The technique chosen for their preparation is the solvent pre-mixing, as it is the one that requires less amount of material. The conditions for each sample are summarized in Table 5.5. Samples A and B, with 1%wt. rGO and 0.91%GO, respectively increased the thermal conductivity of plain epoxy resin to 0.25 W/mK, a 19% increase. The value achieved with the rGO is in agreement with the 21% increase reported by Pu et al [**?**] for 1%wt.rGO. Sample B (GO) clearly surpasses the 4.8% increase presented in 2015 by Wang et al for 1%wt. GO mixed by sonication [244]. On the other hand, sample C, with 1%wt. of GNP, reached thermal conductivity values of 0.32 W/mK, a 52% increase. This result is a remarkable achievement

for the low percentage of nanofiller added to the composite. In 2016 Moriche et al reported 0.65W/mK for an epoxy composite with 10%wt., what is 200% higher but employing 1000% more GNP.

Table 5.5: Thermal conductivity and loading for epoxy composites with rGO, GO and GNP

Sample	Material	Load (%wt.)	Thermal Con. (W/mK)
A	rGO	1	0.25
B	GO	0.91	0.25
C	GNP	1	0.32

The obtained values clearly point out GNP as the best thermal conductivity enhancer nanofiller in epoxy composites. Not only is more inexpensive and more available, but it also leads to better conductivity. This result agrees with the characterization carried out in Chapter 2. Avanzare GNP presented less lattice defects and close to none functional groups in its structure what, according to theoretical models [157], leads to better thermal transport along its platelets. Some authors pointed out that the functionalization of GNP [179] or its oxidation [239] helped to form a stronger bonding between the filler and the polymer, thus, improving some of the properties, mostly mechanical ones [129]. For the thermal conductivity, the reduction in thermal transport inside the carbon atom lattice due to the presence of functional groups proves to have more effect in the final results than the stronger bonding filler-epoxy.

5.3.2 Effect of the dispersion techniques

The effectiveness of the three different dispersion techniques is studied in this section. The same nanofiller is dispersed in the same concentration by three techniques and their efficiency will be measured comparing the enhancement in thermal conductivity that each one reaches. For this tests, Avanzare GNP is chosen as nanofiller. Firstly, because it demonstrated to provide the highest thermal conductivity results in previous section. Secondly, because its availability and prize make it more suitable for higher loadings.

Three specimens are elaborated: One with calander, other with Cowles disk and the last one with solvent pre-mixing in acetone. The concentration of GNP in the epoxy nanocomposite is 6.9%wt. for each. Conditions and thermal conductivity results for the three samples are summarized in Table 5.6.

Obtained results show a clear difference between solvent pre-mixing and the other two techniques: Sample F presents a thermal conductivity value of 0.41

Table 5.6: Summary of thermal conductivity results for different mixing methods

Sample	Mixing method	Thermal conductivity (W/mK)
D	Calander	1.1
E	Cowles	1
F	Solvent pre-mixing	0.41

W/mK, a 95% increase. Despite being a noteworthy result, is far from the obtained with Samples D and E, which is above 1 W/mK. Thus, this technique, with acetone as solvent, is discarded for further tests because of for its poor lower result. To follow the analysis, Samples D and E are compared. Sample E, mixed by Cowles disk, reached a thermal conductivity value of 1 W/mK, whereas Sample D, mixed by calander, reached 1.1 W/mK. Both are extraordinary results for just a 6,9%wt. GNP loading. Despite not reaching the highest enhancement ever achieved (12.4 W/mK for the addition of a non-specified quantity of pristine Graphene [203]), it patently increased the lasted reported values for GNP/Epoxy composites: 0.65 W/mK [152]; 0.56 W/mK [264] and 0.7 W/mK [130]. The promising results achieved with both techniques encourages further analysis over these compositions and brightens the applicability of GNP as nanofiller in TIM.

textbfFrom this study, solvent pre-mixing is discarded as a mixing technique for future work. On the other hand, calander and Cowles present similar and very successful results. Notwithstanding calander provided better thermal conductivity enhancement, the values obtained are so close that Cowles disk is not to be discarded.

5.3.3 Thermal conductivity enhancing properties of GNP

The great thermal conductivity results achieved for GNP mixed by Cowles disk and calander, motivated a deeper study of the effect of the nanofiller concentration on the final conductivity of the composite. Starting from 1%wt. GNP load, a set of specimens were prepared with increasing amount of nanofiller, by both techniques, and their thermal conductivities are measured. Conditions and results for each specimen were summarized in Table 5.7.

The behavior of the thermal conductivity increase is noteworthy, as there is a change of trend for the highest concentration. The thermal conductivity results are plotted in Figure 5.16 as a function of the GNP concentration. In

Table 5.7: Thermal conductivity results for different GNP loadings mixed by calander and Cowles.

GNP Load %wt.	Technique	Thermal Conductivity	Technique	Thermal Conductivity
1	Calander	0.33	Cowles	0.34
3	Calander	0.58	Cowles	0.59
5	Calander	0.65	Cowles	0.67
6.9	Calander	1.1	Cowles	1

both cases, the three lower concentrations (1, 3 and 5%wt.) mark a convex trend towards saturation, but for 6.9%wt. the thermal conductivity jumps. This can be due to the formation of a percolated network for the highest concentrated composite. When a filler network or a filler-polymer network is formed within the polymer matrix, the greatest enhancement is achieved. Some authors have already studied the percolation point for GNP/epoxy composites [148]. In their 2016 study, Li et al reported that none thermal percolation was found for GNP/epoxy systems for composites with a %wt. load below 5% GNP. In this thesis, however, GNP concentrations up to 6.9%wt. are studied and **thermal percolation point is found to be between 5%wt. and 6.9%wt.** (pointed in Figure 5.16 with a red dotted line). For CNT/Polymer systems, a relation between the thermal percolation and the rheological percolation has been studied an proposed by Ares et al [11], thus, an analogous study will be carried out in this work.

5.3.4 Final comparison between GNP, Graphite and Commercial Epoxy

To conclude the thermal characterization section, it is necessary to compare the performance of the nanofiller (GNP) with its macro or micro scale counterpart, in this case graphite. Scharlab graphite is chosen for this study and its compatibility with ECCOBOND 55 has been ascertained in section 5.2.3. Three specimens with increasing graphite loadings are prepared by calander mixing. The conditions and conductivity values are summarized in Table 5.8 along with the previously obtained results for GNP/epoxy composite, ECCOBOND 55 and ECCOBOND 285.

Specimens with graphite loading from 7 to 20 %wt. are elaborated. These concentrations exceed those tested for GNP, however, their thermal conductivity values remain way below. Around 300% improvement is achieved for

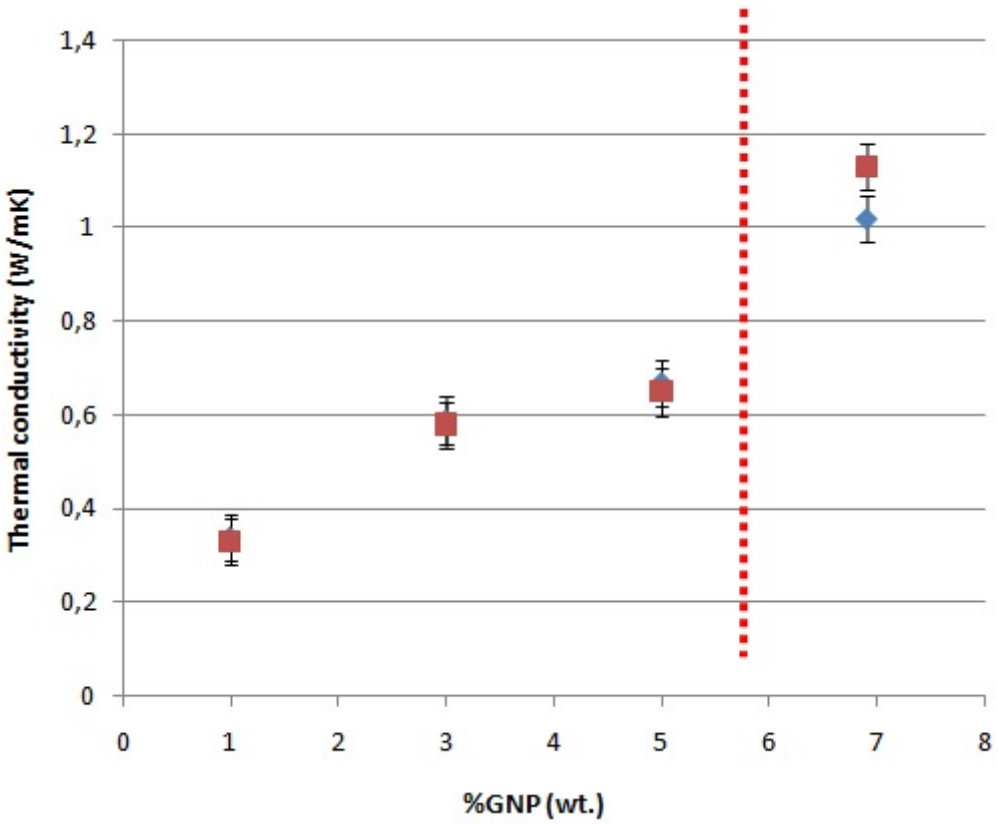

Figure 5.16: Thermal conductivity as a function of the concentration. The change in trend between 5 and 6.9% , marked with the red line, suggests the formation of a percolated network.

Table 5.8: Summary of the thermal conductivity values for the studied specimens and the two references: ECCOBOND285 and ECCOBOND55

Sample	Material	Loading %wt.	Thermal Conductivity (W/mK)
A	Graphite	7	0.45
B	Graphite	11	0.7
C	Graphite	20	0.85
D	GNP	6.9	1.1
ECCOBOND 55	None	0	0.21
ECCOBOND 285	Al2O3	50	1.44

the specimen with 20%wt. graphite (0.85W/mK), whereas 425% enhancement (1.1W/mK) is achieved for just a 6.9%wt. GNP addition. The nanosized nature of GNP proves to be more effective towards the elaboration of highly conductive composites. Some authors pointed out that the structure of graphene sheets, with thinner layers compared to graphite, facilitates the formation of 3D networks in the epoxy matrix resulting in pathways for heat conduction and improving the thermal conductivity [220]. The lower thicknesses values measured experimentally for Avanzare GNP in Chapter 2 and the results obtained for GNP and Graphite in this section agree with the explanation proposed by Tang et al. So, **GNP is established as better thermal conductivity enhancing nanofiller for epoxy resins than graphite.**

The performance of the elaborated 6.9%wt. GNP/ epoxy composite must be compared with the two reference conductivity values settled at the beginning of this section. When compared to plain ECCOBOND 55, the conductivity enhancement is exceptional. The correct addition of just 6.9%wt. of GNP by calander leaded to a 425% increase, and reached the 1-5W/mK range proposed [190] for the proper efficiency of a TIM. ECCOBOND 285 has a thermal conductivity of 1.44 W/mK, a 33% higher than the GNP/epoxy composite. This higher conductivity, however, comes to the cost of adding 50%wt. Al_2O_3, when just a 6.9%wt. GNP is used in the other case. The difference in filler loadings nature and quantities could have a great impact on the rheological properties of the final composite, which is, as stated before, a key factor towards the industrial use of TIMs. Thus, the rheological properties of the samples must be analyzed to complete the applicability of GNP/Epoxy composites as TIMs.

5.4 Rheological characterization of graphene filled epoxy specimens

There are very few reported studies regarding the rheological and thermal analysis of GNP/epoxy nanocomposites, what makes this type of research a novelty and an interesting topic by itself. Furthermore, the good thermal conductivities achieved in previous section, if accompanied by favorable rheological results, could settle the basis for the industrial application of this kind of nanocomposites.

Two different types of rheological measurements are carried out: 1) Viscosity measurements in continuous shear flow and 2) Small amplitude oscillatory

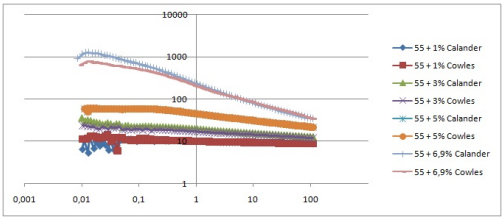

Figure 5.17: Viscosity as a function of the shear rate for samples mixed by calander and Cowles.

shear (SAOS) flow tests to analyze the curing process. The equipment used and the conditions for the measurements have already been described in previous sections.

5.4.1 Viscosity measurements in continuous shear flow

The continuous shear flow analysis is performed with the aim to characterize the behavior of epoxy resin reinforced with different concentration of GNPs and to determine the relation of the viscosity with the concentration. Moreover, in order to optimize the manufacturing and the industrial processing of epoxy/GNP nanocomposites it is important to know if the behavior is Newtonian or non-Newtonian.

As neither Cowles nor calander were discarded in previous sections as successful mixing techniques, samples mixed with both of them are analyzed. Then again, samples of plain epoxy (ECCOBOND 55) with GNP concentrations of 1, 3, 5 and 6.9 %wt. are prepared. For these preparations, the samples are not mixed with hardener because no curing process is required for the analysis. Their viscosity is measured for shear rates γ between 0.1 and 100 s^{-1}. The results are plotted in Figure 5.17.

The first thing to notice when analyzing the viscosity results is that samples from both mixing techniques are virtually equal. When looking at the viscosity as a function of the shear rate, a horizontal line (constant viscosity) indicates a Newtonian fluid and the decreased viscosity with increasing shear rate is defined as shear thinning, a non-Newtonian behavior. For the epoxy/GNP system, concentrations of 3%wt. and below exhibit a Newtonian behavior. The viscosity increases from 10 Pas for 1%wt.GNP to 20 Pas for 3%wt. GNP. However, samples with 5 and 6.9%wt. show shear thinning behavior, which is more accentuated for the highest concentrated mixture. These results differ from those recently presented by Jojibabu [99]: for the same GNP/Epoxy system, since

this author found a shear thinning behavior even with low GNP concentrations, 0.2%wt. and 0.5%wt. A very low effect in the viscosity when increasing the GNP load from a 0.2%wt. to a 2%wt is also reported. The difference probably lies in variations in morphology between the GNPs used in the two studies. Larger GNP platelets favor the stratification effect [179], which combined with the tendency of the GNP to align with the flow field [111], could lead to smaller viscosity increments due to the slide of GNP particles with each other.

Additionally, there is a remarkable feature in the continuous shear flow results that must be noticed. Viscosity suffers a noteworthy jump from 5 to 6.9%wt. GNP, related with the formation of a 3D network of GNP inside the epoxy matrix. This abrupt viscosity increase can be studied using the Carreau model Equation 5.3. Applying this model to the samples that exhibite shear thinning behavior, two main values are obtained: γ and η_o. In the studied epoxy composites, for very low shear rate values, there is a region in which the material has a Newtonian response. When increasing the shear rate, the shear thinning behavior appears. γ and η_o are, respectively, the shear rate and the viscosity for that behavior change. Of course, for samples with a Newtonian behavior, $\eta_o = \eta$ in the whole shear rate range.

$$\eta = \frac{\eta_0}{1 + \left(\tau_0 \dot{\gamma}_{21}\right)^{\alpha}}$$

Equation 5.3: Carreau model

The plot of η_o as a function of the concentration is presented in Figure 5.18 for samples mixed with calender and Cowles disk. **The presence of a huge increase in η_o between concentrations of 5 and 6,9%wt. ascertains that the percolation threshold is between these two concentration values** This results agrees with the statement presented by Martin-Gallego et al [148], who pointed that the rheological percolation for Epoxy/GNP systems should appear for loadings over 1,5%wt. Furthermore, this rheological percolation value agrees with the thermal percolation experimentally measured in the previous section.

Finally, the effect of temperature on the viscosity of 6.9%wt. GNP /epoxy composite and commercial ECCOBOND285 is studied and presented. Only the sample mixed by calander will be analyzed. Figures 5.19 and 5.20 show the results from room temperature (27°C) to 65°C. To the difference of the

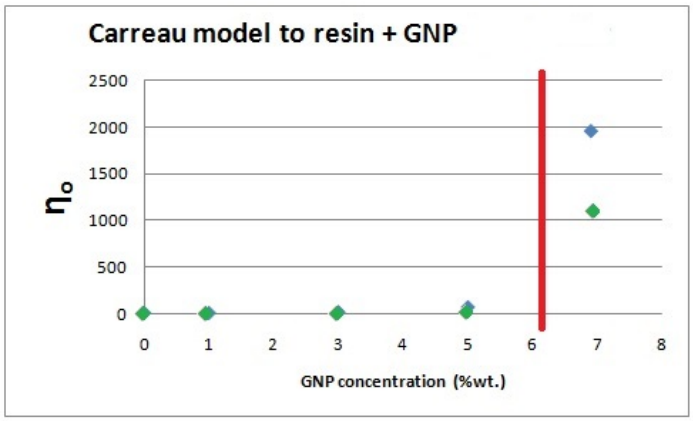

Figure 5.18: Carreau Model applied to 6.9%wt. GNP composites mixed by calander (blue) and Cowles disk (green). The percolation threshold, which stands for the huge viscosity increase, is marked with the red line

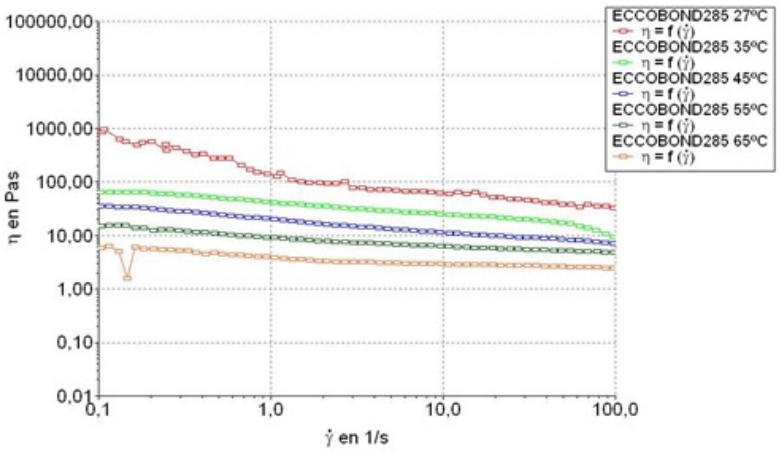

Figure 5.19: Viscosity as a function of shear rate for ECCOBOND 285 at different temperatures

prepared dispersion, ECCOBOND 285 displays a more shear thinning response at 27°C and low shear rates, with respect to the other temperatures. This impedes the application of the time-temperature superposition (TTS), indicating a thermorheological complexity in the analyzed range of temperatures. Face to ECCOBOND 285, 6.9%wt. GNP/ Epoxy shows a thermorheological simple behavior, which can be considered as a symptom of the homogeneity of the dispersion.

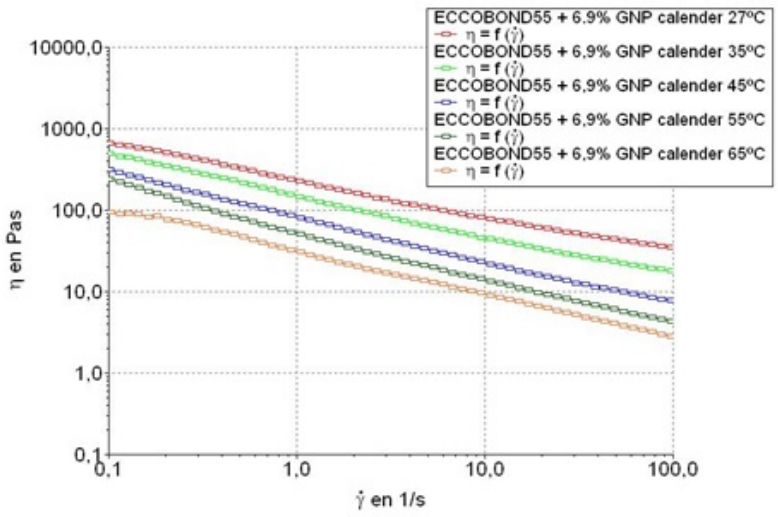

Figure 5.20: Viscosity as a function of shear rate for 6.9%wt.GNP epoxy at different temperatures mixed by calander

5.4.2 Small amplitude oscillatory shear (SAOS) flow tests

SAOS flow tests are widely used to study the curing processes of resin systems. How a resin cures is a feature of maximum relevance, especially when aiming its use in industrial applications. It is known that the curing process of resins can be affected by the presence of carbonaceous nanofillers. The addition of CNTs to an epoxy matrix accelerates the cure reaction of the resin, according to several authors ([34], [254]), whereas carbon nanofibers are reported to have no effect on the process [255]. Guo et al reported that at lower concentrations of expanded graphite, the composite with expanded graphite had a lower activation energy (E_a) before the gelation and a higher one after the gelation [84]. GO has been reported to catalyze the curing reaction of epoxy resins [182]. And graphene produces a decrease on epoxy group conversion for epoxy composites cured by UV irradiation [149].

The respective curing processes of the commercial ECCOBOND 285, the neat ECCOBOND 55 and the two elaborated 6.9%wt. GNP/Epoxy dispersion are studied analyzing the time evolution of the elastic modulus, G', and viscous modulus, G". The curing process implies the transition from a liquid state, where G" > G', to a solid state, at which both moduli are constant and G' > G".The measurements are carried out at 120C and a constant frequency of ω=1Hz. The results are presented in Figure 5.21 (ECCOBOND 55 and ECCOBOND 285) and Figure 5.22 (6.9%wt. GNP by calander and Cowles).

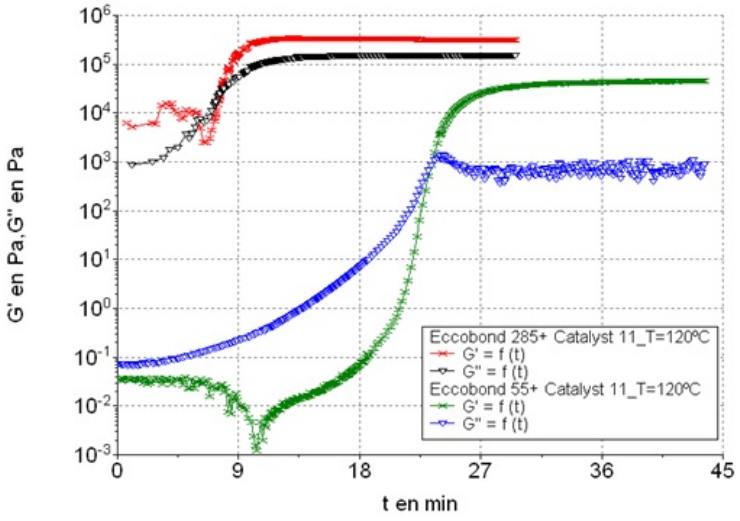

Figure 5.21: (SAOS) flow results for ECCOBOND 55 and ECCOBOND 285 at 120°C

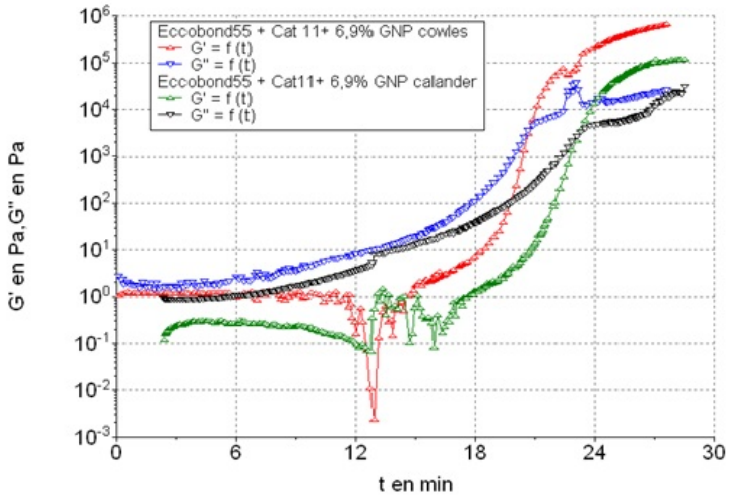

Figure 5.22: (SAOS) flow results for 6,9%GNP epoxys mixed by Cowles and calander at 120°C. The crossover G'=G" marks the curing time.

An estimation of the curing time can be expressed as the time for the G'=G" crossover. Attending to this effective criterion, the curing time of the four samples analyzed can be evaluated. On the one hand, commercial ECCOBOND 285 has a shorter curing time (8.5 min) than ECCOBOND 55 (22 min). This implies shorter "open time" for ECCOBOND 285. "Open time" is defined as the time in which the composite still flows and can be handled, before its solidification. GNP loaded composites, on the other hand, lowered the curing time of plain ECCOBOND 55, to values of 21 min for the Cowles mixed sample and 19 for the one mixed by calander. Both still remain way over the 8.5 min found for ECCOBOND 285, what means they have longer "open times". This is a remarkable advantage of the GNP loaded samples for their industrial application in geometries with difficult access or complicated structures, where longer handling times are required. Table 5.9 resumes the curing times for studied samples.

Table 5.9: Summary of the curing time at 120°C for the studied samples

Sample	Curing time (min) (120°C)
ECCOBOND 55	8.5
ECCOBOND 285	22
ECCOBOND 55 + 6.9%wt. (calander)	19
ECCOBOND 55 + 6.9%wt. (Cowles)	21

5.5 Conclusions

Compatibility study between different graphene derivatives and epoxy resin has been carried out.

The compatibility between five different graphene-like materials from three different companies (GNP from Avanzare, Graphite from Scharlab and rGO, GO in slurry and Dry GO from Graphenea) and a regular epoxy resin (ECCOBOND 55) has been studied. GNP and graphite, with similar structures and compositions, showed great compatibility and homogeneous samples were achieved. GO, in its two versions, slurry and dried, presented great difficulty for its mixture into the epoxy matrix. The presence of water in the slurry lead to many defects, fractures and irregularities in the surface of the composite specimens. Its elimination, resulted in GO dried film-like flakes that did not disperse correctly, resulting in very inhomogeneous samples.

A method for the elaborations of graphene-loaded epoxy composites has been stablished

Thermal conductivity measurements carried out with a Hot Disk sensor required the elaboration of 40x40x3mm smooth samples with no presence of air bubbles in their structure. The conditions that lead to specimens which satisfied the requirements were studied and established as it follows:

1- A mixture is prepared adding 50g of ECCOBOND 55 and 6.75g of Catalyst 9 (13.5:100) weight ratio catalyst:resine

2- The mixture is blended during 10 minutes by hand mixing.

3- The mixture is degased in a vacuum chamber during 10 minutes at 0.7 atm (just for one of the samples).

4- The mixture is poured into a 40x40x3mm mold, degassed for additional 10 minutes (just for one of the samples) and cured at ambient temperature (20°C) for 24h.

Thermal conductivity of epoxy composites loaded with several materials has been measured and compared

Several thermal conductivity measurements were carried out, leading to successful comparisons between several factors. The first one is the effect of

the nanofiller: For similar concentrations of rGO, GO and GNP mixed by solvent pre-mixing method, GNP stood out as the one with the best thermal conductivity enhancement capability for the studied system, improving their results in 25%. Secondly, the effect of different mixing methods was compared. Between calender, stirring with Cowles disk and solvent pre-mixing, the worst thermal conductivity results were for solvent pre-mixing, by far. The other two techniques led to similar results, even if calender brought about slightly higher thermal conductivity. **A thermal conductivity of 1,1 W/mK was achieved for a 6.9%wt. GNP load**, bettering some of the results recently reported by other groups. Finally, GNP was compared to graphite, in order to evaluate the effect of a nanofillller when opposed to a similar macro material. GNP resulted in higher thermal conductivities even for lower concentrations. Table 5.10 summarizes compositions and results.

Table 5.10: Thermal conductivity results considering filler loadings and mixing techniques for the studied epoxy matrix composites.

Material	Mixing	Load (%wt.)	Thermal Con. (W/mK)
rGO	Solvent	1	0.25
GO	Solvent	0.91	0.25
GNP	Solvent	1	0.32
GNP	Solvent	6.9	0.41
GNP	Cowles	6.9	1
GNP	**Calander**	**6,9**	**1,1**
Graphite	Calander	7	0.45
Graphite	Calander	11	0.7
Graphite	Calander	20	0.85

A rheological study was carried out on the properties of GNP loaded epoxy composites

The effect of GNP nanofiller over the rheological properties of an epoxy matrix was studied by viscosity measurements in continuous shear flow. It was ascertained that for samples with 1 and 3%wt. GNP, the composite maintains the Newtonian behavior of the original epoxy. For higher loadings, however, samples showed a shear thinning behaviour when measured in the range of 0.1 to 100 s^{-1} shear rates. When comparing the viscosity of samples dispersed by calander and Cowles disk the results are virtually equal. Shear thinning behaviours appear at the higher loadings in both cases and the changes in viscosity follow the same trend. When studying the curing times, however, some differences appeared. The composite mixed by calander presented a shorter

curing time (19 minutes) than the one mixed by Cowles (21 minutes). This slight difference, along with the small variation in thermal conductivity, confirm that both mixing techniques lead to different GNP dispersion results.

Percolation threshold for the GNP-Epoxy system is found

A remarkable jump in thermal conductivity was found between 5%wt. GNP and 6.9%wt.GNP composites. This jump is related to the formation of a thermal percolation network of GNP inside the matrix. GNP nanofiller helps to form 3D networks in the epoxy, resulting in pathways for heat conduction, what results in significant thermal conductivity increase. The few studies presented by other authors about the thermal percolation pointed towards these results, but none determined the range in which the threshold was formed. Furthermore, viscosity results also showed a noteworthy rise in the viscosity of GNP-epoxy composite loaded with a 5 and a 6.9%wt. GNP. Then again, this jump is related to the rheological percolation threshold. Thus **results confirm that for GNP-epoxy systems, the percolation threshold is between 5%GNP and 6.9%GNP**. It is suggested for future work to determine the exact concentration for the formation of the percolation network and to investigate on the relation between the rheological and the thermal percolation.

Finally, the main goal of the chapter, the elaboration of a GNP based Thermal Interface Material (TIM), has been successfully achieved

GNP was studied for its potential use as nanofiller in TIMs. ECCOBOND 55 a plain epoxy matrix, was filled with several amounts of GNP and mixed by different techniques in order to elaborate a composite that fulfilled the rheological and thermal requirements for a TIM. ECCOBOND 285, a commercial TIM composed of ECCOBOND 55 + around 50% of alumina, was used for comparison purposes. 6.9%GNP composites were compared with the commercial TIM. To begin, the incorporation of GNP led to an increase in the thermal conductivity of the original epoxy, from 0.21 W/mK of ECCOBOND 55 to 1,1W/mK. This result is close to the conductivity value 1.44W/mK of ECCOBOND 285 and is achieved with just a 6.9%wt. loading, compared to the 50%wt. of the commercial TIM. The benefits of adding smaller amounts of filler were ascertained by the rheological characterization. In both cases, the addition of respective fillers gave rise to a shear thinning behaviour above a shear rate of $0.1s^{-1}$. However, the GNP composite exhibited a lower viscosity than ECCOBOND 285, what is advantageous towards the industrial application. Regarding curing times, values close to the 22 minutes of ECCOBOND 55 were kept for the GNP composites. Samples mixed by Cowles disk presented

a curing time of 21 minutes and calander mixed samples, 19 minutes. Commercial ECCOBOND 285, on the other hand, has a curing time of 8,5 minutes. Longer curing times entail longer handling times, what can be beneficial when the adhesives are applied to complex geometries or when there is a difficult access to the point of application. **Considering these advantages and the great thermal conductivity results obtained with low nanofiller loadings, GNP epoxy composites arise as an efficient and reliable thermal interface material.**

Table 5.11: Rheological and thermal properties for commercial ECCOBOND 285, ECCOBOND 55, and GNP loaded epoxys

Sanple	ECCOBOND 55	ECCOBOND 285	ECCOBOND 55 + 6.9%GNP Cowles	ECCOBOND 55 6.9%GNP Caland
Viscosity (Pas) RT, Shear rate $10s^{-1}$	10	250	81	83
Rheological behaviour	Newtonian	Pseudoplastic	Pseudoplastic	Pseudoplastic
Gel Time (min)	22	8.5	21	19
Thermal C. (W/mK)	0.21	1.4	1	1.1

Bibliography

[1] http://ec.europa.eu/programmes/horizon2020/en/h2020-section/fet-flagships last visited on april 2016.

[2] http://spectrum.ieee.org/nanoclast/semiconductors/nanotechnology/europe-invests-1-billion-to-become-graphene-valley last visited on april 2016.

[3] http://www.doseuro.com/pdf/opuscoloem.pdf.

[4] http://www.graphenecanada2015.com/gc/topics.php last visited on april 2016.

[5] http://www.iso.org/iso/iso$_c$*atalogue*/*catalogue*$_t$*c*/*catalogue*$_t$*c*$_b$*rowse.htm*?*commid* = 381983*lastvisitedonapril*2016.

[6] A. K. Geim, K. S. N. The rise of the graphene. *Nature Materials* (2007), VOL 6.

[7] Alexandre, M., and Dubois, P. Polymer-layered silicate nanocomposites: preparation, properties and uses of a new class of materials. *Materials Science and Engineering: R: Reports 28*, 1 (2000), 1–63.

[8] An, C. J., Jang, S., Kang, K. M., Kim, S. J., Jin, M. L., and Jung, H.-T. A combined graphene and periodic au nanograte structure: Fundamentals and application as a flexible transparent conducting film in a flexible organic photovoltaic cell. *Carbon 103* (2016), 488–496.

[9] An, J.-E., and Jeong, Y. G. Structure and electric heating performance of graphene/epoxy composite films. *European Polymer Journal 49*, 6 (2013), 1322–1330.

[10] Arcelus, N. G. *Desarrollo de un nuevo material nanocompuesto de circona con nanotubos de carbono recubiertos para aplicaciones ortopédicas.* PhD thesis, 2009.

[11] Ares, A., Arboleda-Clemente, L., Garcia, X., and Abad, M. J. Enhanced thermal conductivity of rheologically percolated polyamide 12/polyamide 6/multi-walled carbon nanotubes composites. *IberReo15 Coimbra* (2015).

[12] Athanassiou, E. K., Grass, R. N., and Stark, W. J. Large-scale production of carbon-coated copper nanoparticles for sensor applications. *Nanotechnology 17*, 6 (2006), 1668.

[13] Awan, Z., Nahm, K. S., Xavier, J. S., et al. Nanotubular mno 2/graphene oxide composites for the application of open air-breathing cathode microbial fuel cells. *Biosensors and Bioelectronics 53* (2014), 528–534.

[14] Bagri, A., Mattevi, C., Acik, M., Chabal, Y. J., Chhowalla, M., and Shenoy, V. B. Structural evolution during the reduction of chemically derived graphene oxide. *Nature chemistry 2*, 7 (2010), 581–587.

[15] Barcena, J. *NOVEL METAL MATRIX COMPOSITES: COPPER REINFORCED BY CARBON NANOFIBERS FOR THERMAL MANAGEMENT OF HIGH POWER ELECTRONICS.* PhD thesis, 2008.

[16] Barcena, J., Martines, R., de Cortzar, M., Egizabal, P., Maudes, J., Caro, I., and Coleto, J. Powder metallurgy based manufacture of copper/carbon nanofibers composites. *European international powder metallurgy congress and exhibition, Euro PMManheim, Germany* (September 2008 through 1 October 2008), Code 105569.

[17] Barcena, J., Maudes, J., Coleto, J., Baldonedo, J. L., and de Salazar, J. M. G. Microstructural study of vapour grown carbon nanofibre/copper composites. *Composites Science and technology 68*, 6 (2008), 1384–1391.

[18] Barcena, J., Seddon, R., Coleto, J., Lloyd, J., and Neubauer, E. Carbon nanofibers reinforced copper matrix composites: manufacture, thermal and mechanical characterisation. *ASM International, Member/Customer Service Center Materials Park OH 44073-0002 United States* (2010).

[19] Bartolucci, S. F., Paras, J., Rafiee, M. A., Rafiee, J., Lee, S., Kapoor, D., and Koratkar, N. Graphene–aluminum nanocomposites. *Materials Science and Engineering: A 528*, 27 (2011), 7933–7937.

[20] Behbahani, A., Rowshanzamir, S., and Esmaeilifar, A. Hydrothermal synthesis of zirconia nanoparticles from commercial zirconia. *Procedia Engineering 42* (2012), 908–917.

[21] Bi, K., Chen, Y., Chen, M., and Wang, Y. The influence of structure on the thermal conductivities of low-dimensional carbon materials. *Solid State Communications 150*, 29 (2010), 1321–1324.

[22] Bianco, A., Cheng, H.-M., Enoki, T., Gogotsi, Y., Hurt, R. H., Koratkar, N., Kyotani, T., Monthioux, M., Park, C. R., Tascon, J. M., et al. All in the graphene family–a recommended nomenclature for two-dimensional carbon materials, 2013.

[23] Bin, L. Preparation and properties of graphene/cu composites.

[24] Bird, R. B., Armstrong, R. C., and Hassager, O. Dynamics of polymeric liquids. vol. 1: Fluid mechanics.

[25] Bittmann, B., Haupert, F., and Schlarb, A. K. Ultrasonic dispersion of inorganic nanoparticles in epoxy resin. *Ultrasonics sonochemistry 16*, 5 (2009), 622–628.

[26] Boden, A. *Copper Graphite Composite Materials*. PhD thesis, Freie Universität Berlin, 2015.

[27] Bonaccorso, V. F., Novoselov, K., Roche, S., Bøggild, P., Borini, S., Koppens, F., Palermo, V., and Pugno, N. www. rsc. org/nanoscale.

[28] Brenet, J. Electrochemical behaviour of metallic oxides. *Journal of Power Sources 4*, 3 (1979), 183–190.

[29] Buzaglo, M., Shtein, M., Kober, S., Lovrinčić, R., Vilan, A., and Regev, O. Critical parameters in exfoliating graphite into graphene. *Physical Chemistry Chemical Physics 15*, 12 (2013), 4428–4435.

[30] Caillot, T., Salama, Z., Chanut, N., Aires, F. C. S., Bennici, S., and Auroux, A. Hydrothermal synthesis and characterization of zirconia based catalysts. *Journal of Solid State Chemistry 203* (2013), 79–85.

[31] Cançado, L. G., Jorio, A., Ferreira, E. M., Stavale, F., Achete, C., Capaz, R., Moutinho, M., Lombardo, A., Kulmala, T., and Ferrari, A. Quantifying defects in graphene via raman spectroscopy at different excitation energies. *Nano letters 11*, 8 (2011), 3190–3196.

[32] Chandrasekaran, S., Seidel, C., and Schulte, K. Preparation and characterization of graphite nano-platelet (gnp)/epoxy nano-composite: Mechanical, electrical and thermal properties. *European Polymer Journal 49*, 12 (2013), 3878–3888.

[33] Chang, S.-W., Nair, A. K., and Buehler, M. J. Geometry and temperature effects of the interfacial thermal conductance in copper–and nickel–graphene nanocomposites. *Journal of Physics: Condensed Matter 24*, 24 (2012), 245301.

[34] Chapartegui, M. *Novel Nanocomposites Manufactured by Dispersion of Carbon Nanotubes in Thermostable Polymers: Characterization, Properties and Applications*. PhD thesis, 2011.

[35] Chapartegui, M., Barcena, J., Irastorza, X., Elizetxea, C., Fiamegkou, E., Kostopoulos, V., and Santamaria, A. Manufacturing, characterization and thermal conductivity of epoxy and benzoxazine multi-walled carbon nanotube buckypaper composites. *Journal of Composite Materials 47*, 14 (2013), 1705–1715.

[36] Chen, D., Feng, H., and Li, J. Graphene oxide: preparation, functionalization, and electrochemical applications. *Chemical reviews 112*, 11 (2012), 6027–6053.

[37] Chen, F., Jin, D., Tyeb, K., Wang, B., Han, Y.-H., Kim, S., Schoenung, J. M., Shen, Q., and Zhang, L. Field assisted sintering of graphene reinforced zirconia ceramics. *Ceramics International 41*, 4 (2015), 6113–6116.

[38] Chen, G., Wu, C., Weng, W., Wu, D., and Yan, W. Preparation of polystyrene/graphite nanosheet composite. *Polymer 44*, 6 (2003), 1781–1784.

[39] Chen, J., Chen, L., Zhang, Z., Li, J., Wang, L., and Jiang, W. Graphene layers produced from carbon nanotubes by friction. *Carbon 50*, 5 (2012), 1934–1941.

[40] Chen, M., Yin, J., Jin, R., Yao, L., Su, B., and Lei, Q. Dielectric and mechanical properties and thermal stability of polyimide–graphene oxide composite films. *Thin Solid Films 584* (2015), 232–237.

[41] Chen, S., Cai, W., Piner, R. D., Suk, J. W., Wu, Y., Ren, Y., Kang, J., and Ruoff, R. S. Synthesis and characterization of large-area graphene and graphite films on commercial cu–ni alloy foils. *Nano letters 11*, 9 (2011), 3519–3525.

[42] Cheng, C.-K., Lin, C.-H., Wu, H.-C., Ma, C.-C. M., Yeh, T.-K., Chou, H.-Y., Tsai, C.-H., and Hsieh, C.-K. The two-dimensional nanocomposite of molybdenum disulfide and nitrogen-doped graphene oxide for efficient counter electrode of dye-sensitized solar cells. *Nanoscale research letters 11*, 1 (2016), 1–9.

[43] Cheng, F., Shen, J., Ji, W., Tao, Z., and Chen, J. Selective synthesis of manganese oxide nanostructures for electrocatalytic oxygen reduction. *ACS applied materials & interfaces 1*, 2 (2009), 460–466.

[44] Chu, K., Guo, H., Jia, C., Yin, F., Zhang, X., Liang, X., and Chen, H. Thermal properties of carbon nanotube–copper composites for thermal management applications. *Nanoscale research letters 5*, 5 (2010), 868.

[45] Chu, K., Wu, Q., Jia, C., Liang, X., Nie, J., Tian, W., Gai, G., and Guo, H. Fabrication and effective thermal conductivity of multi-walled carbon nanotubes reinforced cu matrix composites for heat sink applications. *Composites Science and Technology 70*, 2 (2010), 298–304.

[46] Clausi, M., Santonicola, M. G., Laurenzi, S., DAmore, A., Acierno, D., and Grassia, L. Steady-shear rheological properties of graphene-reinforced epoxy resin for manufacturing of aerospace composite films. In *AIP Conference Proceedings* (2016), vol. 1736, AIP Publishing, p. 020024.

[47] Crochet, J., Clemens, M., and Hertel, T. Quantum yield heterogeneities of aqueous single-wall carbon nanotube suspensions. *Journal of the American Chemical Society 129*, 26 (2007), 8058–8059.

[48] Cruz, S., Girão, A. F., Gonçalves, G., and Marques, P. A. Graphene: The missing piece for cancer diagnosis? *Sensors 16*, 1 (2016), 137.

[49] Das, A., Pisana, S., Chakraborty, B., Piscanec, S., Saha, S., Waghmare, U., Novoselov, K., Krishnamurthy, H., Geim, A., Ferrari, A., et al. Monitoring dopants by raman scattering in an electrochemically top-gated graphene transistor. *Nature nanotechnology 3*, 4 (2008), 210–215.

[50] Das, S., Wajid, A. S., Shelburne, J. L., Liao, Y.-C., and Green, M. J. Localized in situ polymerization on graphene surfaces for stabilized graphene dispersions. *ACS applied materials & interfaces 3*, 6 (2011), 1844–1851.

[51] Dasgupta, K., Joshi, J. B., and Banerjee, S. Fluidized bed synthesis of carbon nanotubes–a review. *Chemical Engineering Journal 171*, 3 (2011), 841–869.

[52] De Parga, A. V., Calleja, F., Borca, B., Passeggi Jr, M., Hinarejos, J., Guinea, F., and Miranda, R. Periodically rippled graphene: growth and spatially resolved electronic structure. *Physical review letters 100*, 5 (2008), 056807.

[53] Del Giudice, F., and Shen, A. Q. Shear rheology of graphene oxide dispersions. *Current Opinion in Chemical Engineering 16* (2017), 23–30.

[54] Dhakate, S., Chauhan, N., Sharma, S., and Mathur, R. The production of multi-layer graphene nanoribbons from thermally reduced unzipped multiwalled carbon nanotubes. *Carbon 49*, 13 (2011), 4170–4178.

[55] Dong, X. C., Su, C. Y., and W J, Z. Large-scale graphene films prepared by chemical reduction. *Chemical Physics 12*, 7 (2010), 2164–2168.

[56] Dudek, I., Skoda, M., Jarosz, A., and Szukiewicz, D. The molecular influence of graphene and graphene oxide on the immune system under in vitro and in vivo

conditions. *Archivum immunologiae et therapiae experimentalis 64*, 3 (2016), 195–215.

[57] Eda, G., and Chhowalla, M. Graphene-based composite thin films for electronics. *Nano Letters 9*, 2 (2009), 814–818.

[58] Espinoza-González, R., Mosquera, E., Moglia, Í., Villarroel, R., and Fuenzalida, V. M. Hydrothermal growth and characterization of zirconia nanostructures on non-stoichiometric zirconium oxide. *Ceramics International 40*, 10 (2014), 15577–15584.

[59] Fan, L. *Proc. Electron. Compon. Conf.* (2004).

[60] Feng, L., Xuan, Z., Zhao, H., Bai, Y., Guo, J., Su, C.-w., and Chen, X. Mno 2 prepared by hydrothermal method and electrochemical performance as anode for lithium-ion battery. *Nanoscale research letters 9*, 1 (2014), 290.

[61] Feng, Y., and Yuan, H. Electroless plating of carbon nanotubes with silver. *Journal of Materials Science 39*, 9 (2004), 3241–3243.

[62] Fernandez-Merino, M. J., Guardia, L., Paredes, J. I., Villar-Rodil, S., Solis-Fernandez, P., Martinez-Alonso, A., and Tascón, J. M. D. Vitamin c is an ideal substitute for hydrazine in the reduction of graphene oxide suspensions. *The Journal of Physical Chemistry C 114*, 14 (2010), 6426–6432.

[63] Ferrari, A. C. Raman spectroscopy of graphene and graphite: disorder, electron–phonon coupling, doping and nonadiabatic effects. *Solid state communications 143*, 1 (2007), 47–57.

[64] Ferrari, A. C. Raman spectroscopy of graphene and graphite: disorder, electron–phonon coupling, doping and nonadiabatic effects. *Solid state communications 143*, 1 (2007), 47–57.

[65] Ferrari, A. C., and Basko, D. M. Raman spectroscopy as a versatile tool for studying the properties of graphene. *Nature nanotechnology 8*, 4 (2013), 235–246.

[66] Fox, J. N. Measurement of the vapour pressure curve of water. *Physics Education 28*, 3 (1993), 190.

[67] Fu, Y., Yu, J., Zhang, Y., and Meng, Y. Graphite coated with manganese oxide/multiwall carbon nanotubes composites as anodes in marine benthic microbial fuel cells. *Applied Surface Science 317* (2014), 84–89.

[68] Fu, Y.-X., He, Z.-X., Mo, D.-C., and Lu, S.-S. Thermal conductivity enhancement of epoxy adhesive using graphene sheets as additives. *International Journal of Thermal Sciences 86* (2014), 276–283.

[69] Fukushima, T., and Aida, T. Ionic liquids for soft functional materials with carbon nanotubes. *Chemistry-A European Journal 13*, 18 (2007), 5048–5058.

[70] Gallastegui, A. G. *Nuevas nanoestructuras basadas en nanotubos de carbono modificados con grupos funcionales para aplicaciones biomédicas: tesis doctoral.* PhD thesis, 2009.

[71] Gao, H., Li, Z., and Qin, X. Synthesis of carbon microspheres loaded with manganese oxide as air cathode in alkaline media. *Journal of Power Sources 248* (2014), 565–569.

[72] Garmendia, N., Arteche, A., Garcia, A., Bustero, I., and Obieta, I. Xrd study of the effect of the processing variables on the synthesis of nanozirconia in the presence of mwcnt. *Journal of composite materials 43*, 3 (2009), 247–256.

[73] Garmendia, N., Bilbao, L., Muñoz, R., Goikoetxea, L., García, A., Bustero, I., Olalde, B., Garagorri, N., and Obieta, I. Nanozirconia partially coated mwnt: nanostructural characterization and cytotoxicity and lixivation study. In *Key Engineering Materials* (2008), vol. 361, Trans Tech Publ, pp. 775–778.

[74] Garmendia, N., and Moreno, R. Colloidal processing of nanozirconia-mwcnt composites for biomedical applications.

[75] Garmendia, N., Sanstacruz, I., Moreno, R., and Obieta, I. Influence of the addition of multiwall carbon nanotubes in the sintering of nanostructured yttria-stabilized tetragonal zirconia polycrystalline. *International Journal of Applied Ceramic Technology 9*, 1 (2012), 193–198.

[76] Garmendia, N., Santacruz, I., Moreno, R., and Obieta, I. Slip casting of nanozirconia/mwcnt composites using a heterocoagulation process. *Journal of the European Ceramic Society 29*, 10 (2009), 1939–1945.

[77] Georgakilas, V., Otyepka, M., Bourlinos, A. B., Chandra, V., Kim, N., Kemp, K. C., Hobza, P., Zboril, R., and Kim, K. S. Functionalization of graphene: covalent and non-covalent approaches, derivatives and applications. *Chemical reviews 112*, 11 (2012), 6156–6214.

[78] Ghosh, S., Bao, W., Nika, D. L., Subrina, S., Pokatilov, E. P., Lau, C. N., and Balandin, A. A. Dimensional crossover of thermal transport in few-layer graphene. *Nature materials 9*, 7 (2010), 555–558.

[79] Gong, J., Miao, X., Wan, H., and Song, D. Facile synthesis of zirconia nanoparticles-decorated graphene hybrid nanosheets for an enzymeless methyl parathion sensor. *Sensors and Actuators B: Chemical 162*, 1 (2012), 341–347.

[80] Gong, Y., Fei, H., Zou, X., Zhou, W., Yang, S., Ye, G., Liu, Z., Peng, Z., Lou, J., Vajtai, R., et al. Boron-and nitrogen-substituted graphene nanoribbons as efficient catalysts for oxygen reduction reaction. *Chemistry of Materials 27*, 4 (2015), 1181–1186.

[81] Graf, D., Molitor, F., Ensslin, K., Stampfer, C., Jungen, A., Hierold, C., and Wirtz, L. Raman imaging of graphene. *Solid State Communications 143*, 1 (2007), 44–46.

[82] Green, A. A., and Hersam, M. C. Solution phase production of graphene with controlled thickness via density differentiation. *Nano letters 9*, 12 (2009), 4031–4036.

[83] Gu, X., Yue, J., Li, L., Xue, H., Yang, J., and Zhao, X. General synthesis of mno x (mno 2, mn 2 o 3, mn 3 o 4, mno) hierarchical microspheres as lithium-ion battery anodes. *Electrochimica Acta 184* (2015), 250–256.

[84] Guo, B., Wan, J., Lei, Y., and Jia, D. Curing behaviour of epoxy resin/graphite composites containing ionic liquid. *Journal of Physics D: Applied Physics 42*, 14 (2009), 145307.

[85] Guo, D., Shibuya, R., Akiba, C., Saji, S., Kondo, T., and Nakamura, J. Active sites of nitrogen-doped carbon materials for oxygen reduction reaction clarified using model catalysts. *Science 351*, 6271 (2016), 361–365.

[86] Guo, Y., Sun, X., Liu, Y., Wang, W., Qiu, H., and Gao, J. One pot preparation of reduced graphene oxide (rgo) or au (ag) nanoparticle-rgo hybrids using chitosan as a reducing and stabilizing agent and their use in methanol electrooxidation. *Carbon 50*, 7 (2012), 2513–2523.

[87] Haddon, H. 2. *Progress in Material Science* (20011).

[88] Han, Z., and Fina, A. Thermal conductivity of carbon nanotubes and their polymer nanocomposites: a review. *Progress in polymer science 36*, 7 (2011), 914–944.

[89] Hasan, T., Torrisi, F., Sun, Z., Popa, D., Nicolosi, V., Privitera, G., Bonaccorso, F., and Ferrari, A. Solution-phase exfoliation of graphite for ultrafast photonics. *physica status solidi (b) 247*, 11-12 (2010), 2953–2957.

[90] Hernandez, Y., Nicolosi, V., Lotya, M., Blighe, F. M., Sun, Z., De, S., McGovern, I., Holland, B., Byrne, M., Gun'Ko, Y. K., et al. High-yield production of graphene by liquid-phase exfoliation of graphite. *Nature nanotechnology 3*, 9 (2008), 563–568.

[91] Huh, S. H. *Thermal reduction of graphene oxide.* INTECH Open Access Publisher, 2011.

[92] Hummers Jr, W. S., and Offeman, R. E. Preparation of graphitic oxide. *Journal of the American Chemical Society 80*, 6 (1958), 1339–1339.

[93] Iijima, S. Helical microtubules of graphitic carbon nature 354: 56–58. *Find this article online* (1991).

[94] Ioni, Y. V., Tkachev, S., Bulychev, N., and Gubin, S. Preparation of finely dispersed nanographite. *Inorganic Materials 47*, 6 (2011), 597–602.

[95] Jafta, C. J., Nkosi, F., le Roux, L., Mathe, M. K., Kebede, M., Makgopa, K., Song, Y., Tong, D., Oyama, M., Manyala, N., et al. Manganese oxide/-graphene oxide composites for high-energy aqueous asymmetric electrochemical capacitors. *Electrochimica Acta 110* (2013), 228–233.

[96] Jagannadham, K. *J. Vac. Sci. Technol. 30* (2012), 03D109.

[97] Jagannadham, K. *Metall. Mater. Trans. A 44* (2013), 552.

[98] Jiao, L., Zhang, L., Wang, X., Diankov, G., and Dai, H. Narrow graphene nanoribbons from carbon nanotubes. *Nature 458*, 7240 (2009), 877–880.

[99] Jojibabu, P., Jagannatham, M., Haridoss, P., Ram, G. J., Deshpande, A. P., and Bakshi, S. R. Effect of different carbon nano-fillers on rheological properties and lap shear strength of epoxy adhesive joints. *Composites Part A: Applied Science and Manufacturing 82* (2016), 53–64.

[100] Jukubinek, J. 1. *Mat. Res. Soc. Symp.* (2007).

[101] Kalubarme, R. S., Ahn, C.-H., and Park, C.-J. Electrochemical characteristics of graphene/manganese oxide composite catalyst for li-oxygen rechargeable batteries. *Scripta Materialia 68*, 8 (2013), 619–622.

[102] Kannan, M., et al. Current status, key challenges and its solutions in the design and development of graphene based orr catalysts for the microbial fuel cell applications. *Biosensors and Bioelectronics 77* (2016), 1208–1220.

[103] Kennedy, G. L. Acute and subchronic toxicity of dimethylformam ide and dimethylacetamide following various routes of administration. *Drug and chemical toxicology 9*, 2 (1986), 147–170.

[104] Khan, U., O'Neill, A., Lotya, M., De, S., and Coleman, J. N. High-concentration solvent exfoliation of graphene. *Small 6*, 7 (2010), 864–871.

[105] Khan, U., ONeill, A., Porwal, H., May, P., Nawaz, K., and Coleman, J. N. Size selection of dispersed, exfoliated graphene flakes by controlled centrifugation. *Carbon 50*, 2 (2012), 470–475.

[106] Khan, U., ONeill, A., Porwal, H., May, P., Nawaz, K., and Coleman, J. N. Size selection of dispersed, exfoliated graphene flakes by controlled centrifugation. *Carbon 50*, 2 (2012), 470–475.

[107] Khan, U., Porwal, H., ONeill, A., Nawaz, K., May, P., and Coleman, J. N. Solvent-exfoliated graphene at extremely high concentration. *Langmuir 27*, 15 (2011), 9077–9082.

[108] Kim, H., Abdala, A. A., and Macosko, C. W. Graphene/polymer nanocomposites. *Macromolecules 43*, 16 (2010), 6515–6530.

[109] Kim, H. S., Bae, H. S., Yu, J., and Kim, S. Y. Thermal conductivity of polymer composites with the geometrical characteristics of graphene nanoplatelets. *Scientific reports 6* (2016).

[110] Kim, J., Kwon, S., Cho, D.-H., Kang, B., Kwon, H., Kim, Y., Park, S. O., Jung, G. Y., Shin, E., Kim, W.-G., et al. Direct exfoliation and dispersion of two-dimensional materials in pure water via temperature control. *Nature communications 6* (2015).

[111] Kim, K.-S., Rhee, K.-Y., Lee, K.-H., Byun, J.-H., and Park, S.-J. Rheological behaviors and mechanical properties of graphite nanoplate/carbon nanotube-filled epoxy nanocomposites. *Journal of industrial and engineering chemistry 16*, 4 (2010), 572–576.

[112] Kim, K. S., Zhao, Y., Jang, H., Lee, S. Y., Kim, J. M., Kim, K. S., Ahn, J.-H., Kim, P., Choi, J.-Y., and Hong, B. H. Large-scale pattern growth of graphene films for stretchable transparent electrodes. *nature 457*, 7230 (2009), 706–710.

[113] Kim, W., Lee, T., and Han, S. Multi-layer graphene/copper composites: Preparation using high-ratio differential speed rolling, microstructure and mechanical properties. *Carbon 69* (2014), 55–65.

[114] Koganovskii, A., and Kaninskaya, R. Low-temperature regeneration of activated carbon modified with manganese oxides. *Khim. Tekhnol. Vody 3* (1981), 437.

[115] Koh, W. S., Gan, C. H., Phua, W. K., Akimov, Y. A., and Bai, P. The potential of graphene as an ito replacement in organic solar cells: An optical perspective. *IEEE Journal of Selected Topics in Quantum Electronics 20*, 1 (2014), 36–42.

[116] Kudin, K. N., Ozbas, B., Schniepp, H. C., Prud'Homme, R. K., Aksay, I. A., and Car, R. Raman spectra of graphite oxide and functionalized graphene sheets. *Nano letters 8*, 1 (2008), 36–41.

[117] Kudin, K. N., Ozbas, B., Schniepp, H. C., Prud'Homme, R. K., Aksay, I. A., and Car, R. Raman spectra of graphite oxide and functionalized graphene sheets. *Nano letters 8*, 1 (2008), 36–41.

[118] Kuila, T., Bose, S., Khanra, P., Mishra, A. K., Kim, N. H., and Lee, J. H. Recent advances in graphene-based biosensors. *Biosensors and Bioelectronics 26*, 12 (2011), 4637–4648.

[119] Laidani, N., Micheli, V., Bartali, R., Gottardi, G., and Anderle, M. Optical and mechanical characterization of zirconia–carbon nanocomposite films. *Thin solid films 516*, 7 (2008), 1553–1557.

[120] Lamaita, L., Peluso, M. A., Sambeth, J. E., Thomas, H., Mineli, G., and Porta, P. A theoretical and experimental study of manganese oxides used as catalysts for vocs emission reduction. *Catalysis today 107* (2005), 133–138.

[121] Lee, J.-S., Lee, T., Song, H.-K., Cho, J., and Kim, B.-S. Ionic liquid modified graphene nanosheets anchoring manganese oxide nanoparticles as efficient electrocatalysts for zn–air batteries. *Energy & Environmental Science 4*, 10 (2011), 4148–4154.

[122] Lee, J.-S., Park, G. S., Lee, H. I., Kim, S. T., Cao, R., Liu, M., and Cho, J. Ketjenblack carbon supported amorphous manganese oxides nanowires as highly efficient electrocatalyst for oxygen reduction reaction in alkaline solutions. *Nano letters 11*, 12 (2011), 5362–5366.

[123] Lee, S., Hong, J., Koo, J. H., Lee, H., Lee, S., Choi, T., Jung, H., Koo, B., Park, J., Kim, H., et al. Synthesis of few-layered graphene nanoballs with copper cores using solid carbon source. *ACS applied materials & interfaces 5*, 7 (2013), 2432–2437.

[124] Li, D., Müller, M. B., Gilje, S., Kaner, R. B., and Wallace, G. G. Processable aqueous dispersions of graphene nanosheets. *Nature nanotechnology 3*, 2 (2008), 101–105.

[125] Li, H., Xie, Y., Li, K., Huang, L., Huang, S., Zhao, B., and Zheng, X. Microstructure and wear behavior of graphene nanosheets-reinforced zirconia coating. *Ceramics International 40*, 8 (2014), 12821–12829.

[126] Li, J., Ye, F., Vaziri, S., Muhammed, M., Lemme, M. C., and Östling, M. A simple route towards high-concentration surfactant-free graphene dispersions. *Carbon 50*, 8 (2012), 3113–3116.

[127] Li, L., and Lafdi, K. Composite films prepared by immersion deposition of manganese oxide in carbon nanotubes grown on graphite for supercapacitors. *Journal of materials science 46*, 22 (2011), 7328.

[128] Li, X., Maute, K., Dunn, M. L., and Yang, R. Strain effects on the thermal conductivity of nanostructures. *Physical Review B 81*, 24 (2010), 245318.

[129] Li, Y., Tang, J., Huang, L., Wang, Y., Liu, J., Ge, X., Tjong, S. C., Li, R. K. Y., and Belfiore, L. A. Facile preparation, characterization and performance of noncovalently functionalized graphene/epoxy nanocomposites with poly (sodium 4-styrenesulfonate). *Composites Part A: Applied Science and Manufacturing 68* (2015), 1–9.

[130] Li, Y., Zhang, H., Porwal, H., Huang, Z., Bilotti, E., and Peijs, T. Mechanical, electrical and thermal properties of in-situ exfoliated graphene/epoxy nanocomposites. *Composites Part A: Applied Science and Manufacturing 95* (2017), 229–236.

[131] Lin, J., Zhang, P., Zheng, C., Wu, X., Mao, T., Zhu, M., Wang, H., Feng, D., Qian, S., and Cai, X. Reduced silanized graphene oxide/epoxy-polyurethane composites with enhanced thermal and mechanical properties. *Applied Surface Science 316* (2014), 114–123.

[132] Liu, a. P., and Lu, B. Preparation electrode copper nanowires modified graphene composites and its application. *CN 104569097 A 04*, 09 (2015).

[133] Liu, J., Yan, H., Reece, M. J., and Jiang, K. Toughening of zirconia/alumina composites by the addition of graphene platelets. *Journal of the European Ceramic Society 32*, 16 (2012), 4185–4193.

[134] Liu, J., Yan, H., Reece, M. J., and Jiang, K. Toughening of zirconia/alumina composites by the addition of graphene platelets. *Journal of the European Ceramic Society 32*, 16 (2012), 4185–4193.

[135] Liu, W.-W., Chai, S.-P., Mohamed, A. R., and Hashim, U. Synthesis and characterization of graphene and carbon nanotubes: A review on the past and recent developments. *Journal of Industrial and Engineering Chemistry 20*, 4 (2014), 1171–1185.

[136] Liu, W.-W., Chai, S.-P., Mohamed, A. R., and Hashim, U. Synthesis and characterization of graphene and carbon nanotubes: A review on the past and recent developments. *Journal of Industrial and Engineering Chemistry 20*, 4 (2014), 1171–1185.

[137] Liu, X.-W., Mao, J.-J., Liu, P.-D., and Wei, X.-W. Fabrication of metal-graphene hybrid materials by electroless deposition. *Carbon 49*, 2 (2011), 477–483.

[138] Lloyd, J., Barcena, J., and Clegg, W. Microstructural characterization of copper/carbn nanofibre composites. *17th International Conference on Composite Materials, ICCM-17 Edinburgh; United Kingdom* (July 2009 through 31 July 2009), Code 85394.

[139] Lotya, M., Hernandez, Y., King, P. J., Smith, R. J., Nicolosi, V., Karlsson, L. S., Blighe, F. M., De, S., Wang, Z., McGovern, I., et al. Liquid phase production of graphene by exfoliation of graphite in surfactant/water solutions. *Journal of the American Chemical Society 131*, 10 (2009), 3611–3620.

[140] Lotya, M., Hernandez, Y., King, P. J., Smith, R. J., Nicolosi, V., Karlsson, L. S., Blighe, F. M., De, S., Wang, Z., McGovern, I., et al. Liquid phase production of graphene by exfoliation of graphite in surfactant/water solutions. *Journal of the American Chemical Society 131*, 10 (2009), 3611–3620.

[141] Lotya, M., King, P. J., Khan, U., De, S., and Coleman, J. N. High-concentration, surfactant-stabilized graphene dispersions. *ACS nano 4*, 6 (2010), 3155–3162.

[142] Lv, Y., Li, H., Xie, Y., Li, S., Li, J., Xing, Y., and Song, Y. Facile synthesis and electrochemical properties of mno 2/carbon nanotubes. *Particuology 15* (2014), 34–38.

[143] Ma, Z., Dou, S., Shen, A., Tao, L., Dai, L., and Wang, S. Sulfur-doped graphene derived from cycled lithium–sulfur batteries as a metal-free electrocatalyst for the oxygen reduction reaction. *Angewandte Chemie International Edition 54*, 6 (2015), 1888–1892.

[144] Malard, L., Pimenta, M., Dresselhaus, G., and Dresselhaus, M. Raman spectroscopy in graphene. *Physics Reports 473*, 5 (2009), 51–87.

[145] Mallorly, M. Electroless plating - fundamentals and applications. *Edited by: Mallory, Glenn O.; Hajdu, June B, William Andrew Publishing/Noyes* (1990).

[146] Mañes, J. L., Guinea, F., and Vozmediano, M. A. Existence and topological stability of fermi points in multilayered graphene. *Physical Review B 75*, 15 (2007), 155424.

[147] Manousaki, E., Psillakis, E., Kalogerakis, N., and Mantzavinos, D. Degradation of sodium dodecylbenzene sulfonate in water by ultrasonic irradiation. *Water Research 38*, 17 (2004), 3751–3759.

[148] Martin-Gallego, M., Bernal, M., Hernandez, M., Verdejo, R., and López-Manchado, M. A. Comparison of filler percolation and mechanical properties in graphene and carbon nanotubes filled epoxy nanocomposites. *European Polymer Journal 49*, 6 (2013), 1347–1353.

[149] Martín-Gallego, M., Verdejo, R., Lopez-Manchado, M., and Sangermano, M. Epoxy-graphene uv-cured nanocomposites. *Polymer 52*, 21 (2011), 4664–4669.

[150] Melk, L., Rovira, J. J. R., Antti, M.-L., and Anglada, M. Coefficient of friction and wear resistance of zirconia–mwcnts composites. *Ceramics International 41*, 1 (2015), 459–468.

[151] Moniruzzaman, M., and Winey, K. I. Polymer nanocomposites containing carbon nanotubes. *Macromolecules 39*, 16 (2006), 5194–5205.

[152] Moriche, R., Prolongo, S., Sánchez, M., Jiménez-Suárez, A., Chamizo, F., and Ureña, A. Thermal conductivity and lap shear strength of gnp/epoxy nanocomposites adhesives. *International Journal of Adhesion and Adhesives 68* (2016), 407–410.

[153] Mudila, H., Rana, S., and Zaidi, M. Electrochemical performance of zirconia/graphene oxide nanocomposites cathode designed for high power density supercapacitor. *Journal of Analytical Science and Technology 7*, 1 (2016), 3.

[154] Nie, R., Wang, J., Wang, L., Qin, Y., Chen, P., and Hou, Z. Platinum supported on reduced graphene oxide as a catalyst for hydrogenation of nitroarenes. *Carbon 50*, 2 (2012), 586–596.

[155] Nieto, A., Bisht, A., Lahiri, D., Zhang, C., and Agarwal, A. Graphene reinforced metal and ceramic matrix composites: a review. *International Materials Reviews 62*, 5 (2017), 241–302.

[156] Notley, S. M. Highly concentrated aqueous suspensions of graphene through ultrasonic exfoliation with continuous surfactant addition. *Langmuir 28*, 40 (2012), 14110–14113.

[157] Novoselov, K. S., Fal, V., Colombo, L., Gellert, P., Schwab, M., Kim, K., et al. A roadmap for graphene. *Nature 490*, 7419 (2012), 192–200.

[158] Novoselov, K. S., Geim, A. K., Morozov, S. V., Jiang, D., Zhang, Y., Dubonos, S. V., Grigorieva, I. V., and Firsov, A. A. Electric field effect in atomically thin carbon films. *science 306*, 5696 (2004), 666–669.

[159] Nuvoli, D., Valentini, L., Alzari, V., Scognamillo, S., Bon, S. B., Piccinini, M., Illescas, J., and Mariani, A. High concentration few-layer graphene sheets

obtained by liquid phase exfoliation of graphite in ionic liquid. *Journal of Materials Chemistry 21*, 10 (2011), 3428–3431.

[160] Ominde, N., Bartlett, N., Yang, X.-Q., and Qu, D. Investigation of the oxygen reduction reaction on the carbon electrodes loaded with mno 2 catalyst. *Journal of Power Sources 195*, 13 (2010), 3984–3989.

[161] ONeill, A., Khan, U., Nirmalraj, P. N., Boland, J., and Coleman, J. N. Graphene dispersion and exfoliation in low boiling point solvents. *The Journal of Physical Chemistry C 115*, 13 (2011), 5422–5428.

[162] Onyszko, M., Urbas, K., Aleksandrzak, M., and Mijowska, E. Reduced graphene oxide and inorganic nanoparticles composites–synthesis and characterization. *Polish Journal of Chemical Technology 17*, 4 (2015), 95–103.

[163] Onyszko, M., Urbas, K., Aleksandrzak, M., and Mijowska, E. Reduced graphene oxide and inorganic nanoparticles composites–synthesis and characterization. *Polish Journal of Chemical Technology 17*, 4 (2015), 95–103.

[164] Orge, C., Órfão, J., and Pereira, M. Composites of manganese oxide with carbon materials as catalysts for the ozonation of oxalic acid. *Journal of hazardous materials 213* (2012), 133–139.

[165] Pan, F., Zhang, W., Ma, J., Yao, N., Xu, L., He, Y.-S., Yang, X., and Ma, Z.-F. Integrating in situ solvothermal approach synthesized nanostructured tin anchored on graphene sheets into film anodes for sodium-ion batteries. *Electrochimica Acta 196* (2016), 572–578.

[166] Pan, Y.-X., Yu, Z.-Z., Ou, Y.-C., and Hu, G.-H. A new process of fabricating electrically conducting nylon 6/graphite nanocomposites via intercalation polymerization. *Journal of Polymer Science Part B: Polymer Physics 38*, 12 (2000), 1626–1633.

[167] Pang, H., Lu, Q., and Gao, F. Graphene oxide induced growth of one-dimensional fusiform zirconia nanostructures for highly selective capture of phosphopeptides. *Chemical Communications 47*, 42 (2011), 11772–11774.

[168] Park, H.-Y., Shin, T. J., Joh, H.-I., Jang, J. H., Ahn, D., and Yoo, S. J. Graphene-oxide-intercalated layered manganese oxides as an efficient oxygen reduction reaction catalyst in alkaline media. *Electrochemistry communications 41* (2014), 35–38.

[169] Parviz, D., Das, S., Ahmed, H. T., Irin, F., Bhattacharia, S., and Green, M. J. Dispersions of non-covalently functionalized graphene with minimal stabilizer. *Acs Nano 6*, 10 (2012), 8857–8867.

[170] Paul, D., and Robeson, L. M. Polymer nanotechnology: nanocomposites. *Polymer 49*, 15 (2008), 3187–3204.

[171] Paunovic, M. Modern electroplating. *Ed. By Mordechay S, Paunovic, John Willey and Sons* (2000).

[172] Peng, Y., Hu, Y., Han, L., and Ren, C. Ultrasound-assisted fabrication of dispersed two-dimensional copper/reduced graphene oxide nanosheets nanocomposites. *Composites Part B: Engineering 58* (2014), 473–477.

[173] Penuelas, J., Ouerghi, A., Lucot, D., David, C., Gierak, J., Estrade-Szwarckopf, H., and Andreazza-Vignolle, C. Surface morphology and characterization of thin graphene films on sic vicinal substrate. *Physical Review B 79*, 3 (2009), 033408.

[174] Piticescu, R., Monty, C., and Millers, D. Hydrothermal synthesis of nanostructured zirconia materials: Present state and future prospects. *Sensors and Actuators B: Chemical 109*, 1 (2005), 102–106.

[175] Piticescu, R., Monty, C., Taloi, D., Motoc, A., and Axinte, S. Hydrothermal synthesis of zirconia nanomaterials. *Journal of the European Ceramic Society 21*, 10 (2001), 2057–2060.

[176] Piticescu, R., Monty, C., Taloi, D., Motoc, A., and Axinte, S. Hydrothermal synthesis of zirconia nanomaterials. *Journal of the European Ceramic Society 21*, 10 (2001), 2057–2060.

[177] Prasai, D., Tuberquia, J. C., Harl, R. R., Jennings, G. K., and Bolotin, K. I. Graphene: corrosion-inhibiting coating. *ACS nano 6*, 2 (2012), 1102–1108.

[178] Prolongo, S., Jimenez-Suarez, A., Moriche, R., and Ureña, A. In situ processing of epoxy composites reinforced with graphene nanoplatelets. *Composites Science and Technology 86* (2013), 185–191.

[179] Prolongo, S., Moriche, R., Jiménez-Suárez, A., Sánchez, M., and Ureña, A. Advantages and disadvantages of the addition of graphene nanoplatelets to epoxy resins. *European Polymer Journal 61* (2014), 206–214.

[180] Qian, Y., Lu, S., and Gao, F. Synthesis of manganese dioxide/reduced graphene oxide composites with excellent electrocatalytic activity toward reduction of oxygen. *Materials letters 65*, 1 (2011), 56–58.

[181] Qin, L., Ding, R., Wang, H., Wu, J., Wang, C., Zhang, C., Xu, Y., Wang, L., and Lv, B. Facile synthesis of porous nitrogen-doped holey graphene as an efficient metal-free catalyst for the oxygen reduction reaction. *Nano Research 10*, 1 (2017), 305–319.

[182] Qiu, S., Wang, C., Wang, Y., Liu, C., Chen, X., Xie, H., Huang, Y., and Cheng, R. Effects of graphene oxides on the cure behaviors of a tetrafunctional epoxy resin. *Express Polym Lett 5*, 9 (2011), 809–818.

[183] Ramalingam, P., Pusuluri, S. T., Periasamy, S., Veerabahu, R., and Kulandaivel, J. Role of deoxy group on the high concentration of graphene in surfactant/water media. *RSC Advances 3*, 7 (2013), 2369–2378.

[184] Ramalingam, P., Pusuluri, S. T., Periasamy, S., Veerabahu, R., and Kulandaivel, J. Role of deoxy group on the high concentration of graphene in surfactant/water media. *RSC Advances 3*, 7 (2013), 2369–2378.

[185] Ratso, S., Kruusenberg, I., Joost, U., Saar, R., and Tammeveski, K. Enhanced oxygen reduction reaction activity of nitrogen-doped graphene/multiwalled carbon nanotube catalysts in alkaline media. *International Journal of Hydrogen Energy 41*, 47 (2016), 22510–22519.

[186] Ray, N., Fleischmann, M., Weckbecker, D., Sharma, S., Pankratov, O., and Shallcross, S. Electron-phonon scattering and in-plane electric conductivity in twisted bilayer graphene. *Physical Review B 94*, 24 (2016), 245403.

[187] Romeli, D., Barigozzi, G., Esposito, S., Rosace, G., and Salesi, G. High sensitivity measurements of thermal properties of textile fabrics. *Polymer Testing 32*, 6 (2013), 1029–1036.

[188] Saada, R., Kellici, S., Heil, T., Morgan, D., and Saha, B. Greener synthesis of dimethyl carbonate using a novel ceria–zirconia oxide/graphene nanocomposite catalyst. *Applied Catalysis B: Environmental 168* (2015), 353–362.

[189] Sadeghi, M. M., Pettes, M. T., and Shi, L. Thermal transport in graphene. *Solid State Communications 152*, 15 (2012), 1321–1330.

[190] Saleem, H., Edathil, A., Ncube, T., Pokhrel, J., Khoori, S., Abraham, A., and Mittal, V. Mechanical and thermal properties of thermoset–graphene nanocomposites. *Macromolecular Materials and Engineering 301*, 3 (2016), 231–259.

[191] Sekitani, T., Noguchi, Y., Hata, K., Fukushima, T., Aida, T., and Someya, T. A rubberlike stretchable active matrix using elastic conductors. *Science 321*, 5895 (2008), 1468–1472.

[192] Seo, J.-W. T., Green, A. A., Antaris, A. L., and Hersam, M. C. High-concentration aqueous dispersions of graphene using nonionic, biocompatible block copolymers. *The Journal of Physical Chemistry Letters 2*, 9 (2011), 1004–1008.

[193] Shahil, K. M., and Balandin, A. A. Graphene–multilayer graphene nanocomposites as highly efficient thermal interface materials. *Nano letters 12*, 2 (2012), 861–867.

[194] Shahil, K. M., and Balandin, A. A. Thermal properties of graphene and multilayer graphene: Applications in thermal interface materials. *Solid State Communications 152*, 15 (2012), 1331–1340.

[195] Sharma, R., Agarwala, R., and Agarwala, V. Development of copper coatings on ceramic powder by electroless technique. *Applied surface science 252*, 24 (2006), 8487–8493.

[196] Shi, C., Zang, G.-L., Zhang, Z., Sheng, G.-P., Huang, Y.-X., Zhao, G.-X., Wang, X.-K., and Yu, H.-Q. Synthesis of layered mno 2 nanosheets for enhanced oxygen reduction reaction catalytic activity. *Electrochimica Acta 132* (2014), 239–243.

[197] Shi, Y., Wang, D., Zhang, J., Zhang, P., Shi, X., and Hao, Y. Synthesis of multilayer graphene films on copper by modified chemical vapor deposition. *Materials and Manufacturing Processes 30*, 6 (2015), 711–716.

[198] Shih, C.-J., Lin, S., Strano, M. S., and Blankschtein, D. Understanding the stabilization of liquid-phase-exfoliated graphene in polar solvents: molecular dynamics simulations and kinetic theory of colloid aggregation. *Journal of the American Chemical Society 132*, 41 (2010), 14638–14648.

[199] Shin, J.-H., and Hong, S.-H. Microstructure and mechanical properties of single wall carbon nanotube reinforced yttria stabilized zircona ceramics. *Materials Science and Engineering: A 556* (2012), 382–387.

[200] Shin, J.-H., and Hong, S.-H. Fabrication and properties of reduced graphene oxide reinforced yttria-stabilized zirconia composite ceramics. *Journal of the European Ceramic Society 34*, 5 (2014), 1297–1302.

[201] Shioyama, H. Polymerization of isoprene and styrene in the interlayer spacing of graphite. *Carbon 35*, 10-11 (1997), 1664–1665.

[202] Shioyama, H. The interactions of two chemical species in the interlayer spacing of graphite. *Synthetic Metals 114*, 1 (2000), 1–15.

[203] Shtein, M., Nadiv, R., Buzaglo, M., Kahil, K., and Regev, O. Thermally conductive graphene-polymer composites: size, percolation, and synergy effects. *Chemistry of Materials 27*, 6 (2015), 2100–2106.

[204] Sing, S. 2. *Progress in Material Science* (20011).

[205] Singh, V. V., Martin, A., Kaufmann, K., DS de Oliveira, S., and Wang, J. Zirconia/graphene oxide hybrid micromotors for selective capture of nerve agents. *Chemistry of Materials 27*, 23 (2015), 8162–8169.

[206] Smith, R. J., Lotya, M., and Coleman, J. N. The importance of repulsive potential barriers for the dispersion of graphene using surfactants. *New Journal of Physics 12*, 12 (2010), 125008.

[207] Smolyanitsky, A., and Tewary, V. Atomistic simulation of a graphene-nanoribbon–metal interconnect. *Journal of Physics: Condensed Matter 23*, 35 (2011), 355006.

[208] Somani, P. R., Somani, S. P., and Umeno, M. Planer nano-graphenes from camphor by cvd. *Chemical Physics Letters 430*, 1 (2006), 56–59.

[209] Song, H.-Y., and Zha, X.-W. Mechanical properties on ni-coated single graphene sheet and their embedded aluminium matrix composites. *Commun. Theor. Phys 54*, 1 (2010), 143.

[210] Song, Y., Lee, H., Ko, J., Ryu, J., Kim, M., and Sohn, D. Preparation and characterization of surfactant-exfoliated graphene. *Bull. Korean Chem 35*, 7 (2014), 2009–2012.

[211] Song, Y., Lee, H., Ko, J., Ryu, J., Kim, M., and Sohn, D. Preparation and characterization of surfactant-exfoliated graphene. *Bull. Korean Chem 35*, 7 (2014), 2009–2012.

[212] Song, Y., Lee, H., Ko, J., Ryu, J., Kim, M., and Sohn, D. Preparation and characterization of surfactant-exfoliated graphene. *Bull. Korean Chem 35*, 7 (2014), 2009–2012.

[213] Spitsina, N., Lobach, A., and Kaplunov, M. Polymer/nanocarbon composite materials for photonics. *High Energy Chemistry 43*, 7 (2009), 552–556.

[214] Stacy, J., Regmi, Y. N., Leonard, B., and Fan, M. The recent progress and future of oxygen reduction reaction catalysis: A review. *Renewable and Sustainable Energy Reviews 69* (2017), 401–414.

[215] Stankovich, S., Dikin, D. A., Piner, R. D., Kohlhaas, K. A., Kleinhammes, A., Jia, Y., Wu, Y., Nguyen, S. T., and Ruoff, R. S. Synthesis of graphene-based nanosheets via chemical reduction of exfoliated graphite oxide. *carbon 45*, 7 (2007), 1558–1565.

[216] Sun, H., and Yang, X. Molecular simulation of self-assembly structure and interfacial interaction for sdbs adsorption on graphene. *Colloids and Surfaces A: Physicochemical and Engineering Aspects 462* (2014), 82–89.

[217] Sun, W., Hsu, A., and Chen, R. Carbon-supported tetragonal mnooh catalysts for oxygen reduction reaction in alkaline media. *Journal of Power Sources 196*, 2 (2011), 627–635.

[218] Sun, Z., Masa, J., Liu, Z., Schuhmann, W., and Muhler, M. Highly concentrated aqueous dispersions of graphene exfoliated by sodium taurodeoxycholate: dispersion behavior and potential application as a catalyst support for the oxygen-reduction reaction. *Chemistry-A European Journal 18*, 22 (2012), 6972–6978.

[219] Sun, Z., Yan, Z., Yao, J., Beitler, E., Zhu, Y., and Tour, J. M. Growth of graphene from solid carbon sources. *Nature 468*, 7323 (2010), 549–552.

[220] Tang, B., Hu, G., Gao, H., and Hai, L. Application of graphene as filler to improve thermal transport property of epoxy resin for thermal interface materials. *International Journal of Heat and Mass Transfer 85* (2015), 420–429.

[221] Tang, L.-C., Wan, Y.-J., Yan, D., Pei, Y.-B., Zhao, L., Li, Y.-B., Wu, L.-B., Jiang, J.-X., and Lai, G.-Q. The effect of graphene dispersion on the mechanical properties of graphene/epoxy composites. *Carbon 60* (2013), 16–27.

[222] Tang, Y., Yang, X., Wang, R., and Li, M. Enhancement of the mechanical properties of graphene–copper composites with graphene–nickel hybrids. *Materials Science and Engineering: A 599* (2014), 247–254.

[223] Texter, J. Graphene dispersions. *Current Opinion in Colloid & Interface Science 19*, 2 (2014), 163–174.

[224] Texter, J. Graphene dispersions. *Current Opinion in Colloid & Interface Science 19* (2014), 163–174.

[225] Texter, J. Current opinion in colloid & interface science. 305–310.

[226] Texter, J. Editorial overview. *Current opinion in colloid & interface science 20* (2015), 305–310.

[227] Teymourian, H., Salimi, A., Firoozi, S., Korani, A., and Soltanian, S. One-pot hydrothermal synthesis of zirconium dioxide nanoparticles decorated reduced graphene oxide composite as high performance electrochemical sensing and biosensing platform. *Electrochimica Acta 143* (2014), 196–206.

[228] Teymourian, H., Salimi, A., Firoozi, S., Korani, A., and Soltanian, S. One-pot hydrothermal synthesis of zirconium dioxide nanoparticles decorated reduced graphene oxide composite as high performance electrochemical sensing and biosensing platform. *Electrochimica Acta 143* (2014), 196–206.

[229] Thostenson, E. T., and Chou, T.-W. Processing-structure-multi-functional property relationship in carbon nanotube/epoxy composites. *Carbon 44*, 14 (2006), 3022–3029.

[230] Tien, C.-P., and Teng, H. Polymer/graphite oxide composites as high-performance materials for electric double layer capacitors. *Journal of Power Sources 195*, 8 (2010), 2414–2418.

[231] Tölle, F. J., Fabritius, M., and Mülhaupt, R. Emulsifier-free graphene dispersions with high graphene content for printed electronics and freestanding graphene films. *Advanced Functional Materials 22*, 6 (2012), 1136–1144.

[232] Torrisi, F., Hasan, T., Wu, W., Sun, Z., Lombardo, A., Kulmala, T. S., Hsieh, G.-W., Jung, S., Bonaccorso, F., Paul, P. J., et al. Inkjet-printed graphene electronics. *ACS nano 6*, 4 (2012), 2992–3006.

[233] Uddin, M. E., Kuila, T., Nayak, G. C., Kim, N. H., Ku, B.-C., and Lee, J. H. Effects of various surfactants on the dispersion stability and electrical conductivity of surface modified graphene. *Journal of Alloys and Compounds 562* (2013), 134–142.

[234] Umek, P., Korošec, R. C., Gloter, A., and Pirnat, U. The control of the diameter and length of α-mno 2 nanorods by regulation of reaction parameters and their thermogravimetric properties. *Materials Research Bulletin 46*, 2 (2011), 278–284.

[235] Valim, R., Santos, M., Lanza, M. R. d. V., Machado, S. A. S., Lima, F. H. B. d., and Calegaro, M. L. Oxygen reduction reaction catalyzed by -mno 2: influence of the crystalline structure on the reaction mechanism. *Electrochimica Acta 85* (2012), 423–431.

[236] Van Chuc, N., Thanh, C. T., Van Tu, N., Phuong, V. T., Thang, P. V., and Tam, N. T. T. A simple approach to the fabrication of graphene-carbon nanotube hybrid films on copper substrate by chemical vapor deposition. *Journal of Materials Science & Technology 31*, 5 (2015), 479–483.

[237] Van Nang, L., and Kim, E.-T. Low-temperature synthesis of graphene on fe 2 o 3 using inductively coupled plasma chemical vapor deposition. *Materials Letters 92* (2013), 437–439.

[238] Viculis, L. M., Mack, J. J., Mayer, O. M., Hahn, H. T., and Kaner, R. B. Intercalation and exfoliation routes to graphite nanoplatelets. *Journal of Materials Chemistry 15*, 9 (2005), 974–978.

[239] Wan, Y.-J., Tang, L.-C., Gong, L.-X., Yan, D., Li, Y.-B., Wu, L.-B., Jiang, J.-X., and Lai, G.-Q. Grafting of epoxy chains onto graphene oxide for epoxy composites with improved mechanical and thermal properties. *Carbon 69* (2014), 467–480.

[240] Wang, C., Li, H., Zhao, J., Zhu, Y., Yuan, W. Z., and Zhang, Y. Graphene nanoribbons as a novel support material for high performance fuel cell electrocatalysts. *International Journal of Hydrogen Energy 38*, 30 (2013), 13230–13237.

[241] Wang, G., Yang, J., Park, J., Gou, X., Wang, B., Liu, H., and Yao, J. Facile synthesis and characterization of graphene nanosheets. *The Journal of Physical Chemistry C 112*, 22 (2008), 8192–8195.

[242] Wang, H., Robinson, J. T., Li, X., and Dai, H. Solvothermal reduction of chemically exfoliated graphene sheets. *Journal of the American Chemical Society 131*, 29 (2009), 9910–9911.

[243] Wang, L., Ara, M., Wadumesthrige, K., Salley, S., and Ng, K. S. Graphene nanosheet supported bifunctional catalyst for high cycle life li-air batteries. *Journal of Power Sources 234* (2013), 8–15.

[244] Wang, R., Zhuo, D., Weng, Z., Wu, L., Cheng, X., Zhou, Y., Wang, J., and Xuan, B. A novel nanosilica/graphene oxide hybrid and its flame retarding epoxy resin with simultaneously improved mechanical, thermal conductivity, and dielectric properties. *Journal of Materials Chemistry A 3*, 18 (2015), 9826–9836.

[245] Wang, X., Fulvio, P. F., Baker, G. A., Veith, G. M., Unocic, R. R., Mahurin, S. M., Chi, M., and Dai, S. Direct exfoliation of natural graphite into micrometre size few layers graphene sheets using ionic liquids. *Chemical Communications 46*, 25 (2010), 4487–4489.

[246] Wang, X., and Li, Y. Selected-control hydrothermal synthesis of α-and β-mno2 single crystal nanowires. *Journal of the American Chemical Society 124*, 12 (2002), 2880–2881.

[247] Wang, Y., Shi, Z., and Yin, J. Facile synthesis of soluble graphene via a green reduction of graphene oxide in tea solution and its biocomposites. *ACS applied materials & interfaces 3*, 4 (2011), 1127–1133.

[248] Wang J and, L. Z. M matrix composites. *Scripta Materialia 66 (8)*, 594–597.

[249] Wen, Q., Wang, S., Yan, J., Cong, L., Pan, Z., Ren, Y., and Fan, Z. Mno 2–graphene hybrid as an alternative cathodic catalyst to platinum in microbial fuel cells. *Journal of power sources 216* (2012), 187–191.

[250] Whitener, K. E., and Sheehan, P. E. Graphene synthesis. *Diamond and related materials 46* (2014), 25–34.

[251] Wintterlin, J., and Bocquet, M.-L. Graphene on metal surfaces. *Surface Science 603*, 10 (2009), 1841–1852.

[252] Wojtoniszak, M., Chen, X., Kalenczuk, R. J., Wajda, A., Łapczuk, J., Kurzewski, M., Drozdzik, M., Chu, P. K., and Borowiak-Palen, E. Synthesis, dispersion, and cytocompatibility of graphene oxide and reduced graphene oxide. *Colloids and Surfaces B: Biointerfaces 89* (2012), 79–85.

[253] Wu, J., Zhang, D., Wang, Y., and Wan, Y. Manganese oxide–graphene composite as an efficient catalyst for 4-electron reduction of oxygen in alkaline media. *Electrochimica Acta 75* (2012), 305–310.

[254] Xie, H., Liu, B., Yuan, Z., Shen, J., and Cheng, R. Cure kinetics of carbon nanotube/tetrafunctional epoxy nanocomposites by isothermal differential scanning calorimetry. *Journal of Polymer Science Part B: Polymer Physics 42*, 20 (2004), 3701–3712.

[255] Xie, H., Liu, B., Yuan, Z., Shen, J., and Cheng, R. Cure kinetics of carbon nanotube/tetrafunctional epoxy nanocomposites by isothermal differential scanning calorimetry. *Journal of Polymer Science Part B: Polymer Physics 42*, 20 (2004), 3701–3712.

[256] Xiong, Y., Zhou, M., Chen, H., Feng, L., Wang, Z., Yan, X., and Guan, S. Synthesis of honeycomb mno 2 nanospheres/carbon nanoparticles/graphene composites as electrode materials for supercapacitors. *Applied Surface Science 357* (2015), 1024–1030.

[257] Xu, Z., and Buehler, M. J. Interface structure and mechanics between graphene and metal substrates: a first-principles study. *Journal of Physics: Condensed Matter 22*, 48 (2010), 485301.

[258] Y C, Z. Controlled synthesis graphene nanocomposites based on copper species and properties investigation. *Shan Dong University 26*, 11, 28–35.

[259] Yan, C., Kanaththage, Y. W., Short, R., Gibson, C. T., and Zou, L. Graphene/polyaniline nanocomposite as electrode material for membrane capacitive deionization. *Desalination 344* (2014), 274–279.

[260] Yang, J., and Xu, J. J. Nanoporous amorphous manganese oxide as electrocatalyst for oxygen reduction in alkaline solutions. *Electrochemistry communications 5*, 4 (2003), 306–311.

[261] Yang, J., and Zou, L. Graphene films of controllable thickness as binder-free electrodes for high performance supercapacitors. *Electrochimica Acta 130* (2014), 791–799.

[262] Yang, T., Guo, X., Kong, Q., Yang, R., Li, Q., and Jiao, K. Comparative studies on zirconia and graphene composites obtained by one-step and stepwise electrodeposition for deoxyribonucleic acid sensing. *Analytica chimica acta 786* (2013), 29–33.

[263] Yang, Y., Han, C., Jiang, B., Iocozzia, J., He, C., Shi, D., Jiang, T., and Lin, Z. Graphene-based materials with tailored nanostructures for energy conversion and storage. *Materials Science and Engineering: R: Reports 102* (2016), 1–72.

[264] Yao, H., Hawkins, S. A., and Sue, H.-J. Preparation of epoxy nanocomposites containing well-dispersed graphene nanosheets. *Composites Science and Technology* (2017).

[265] Yi, M., Shen, Z., Ma, S., and Zhang, X. A mixed-solvent strategy for facile and green preparation of graphene by liquid-phase exfoliation of graphite. *Journal of Nanoparticle Research 14*, 8 (2012), 1003.

[266] Yi, M., Shen, Z., Ma, S., and Zhang, X. A mixed-solvent strategy for facile and green preparation of graphene by liquid-phase exfoliation of graphite. *Journal of Nanoparticle Research 14*, 8 (2012), 1003.

[267] Young, R. J., Kinloch, I. A., Gong, L., and Novoselov, K. S. The mechanics of graphene nanocomposites: a review. *Composites Science and Technology 72*, 12 (2012), 1459–1476.

[268] Young, R. J., Kinloch, I. A., Gong, L., and Novoselov, K. S. The mechanics of graphene nanocomposites: a review. *Composites Science and Technology 72*, 12 (2012), 1459–1476.

[269] Yuan, B., Bao, C., Song, L., Hong, N., Liew, K. M., and Hu, Y. Preparation of functionalized graphene oxide/polypropylene nanocomposite with significantly improved thermal stability and studies on the crystallization behavior and mechanical properties. *Chemical Engineering Journal 237* (2014), 411–420.

[270] Yun, Y. S., Le, V.-D., Kim, H., Chang, S.-J., Baek, S. J., Park, S., Kim, B. H., Kim, Y.-H., Kang, K., and Jin, H.-J. Effects of sulfur doping on graphene-based nanosheets for use as anode materials in lithium-ion batteries. *Journal of Power Sources 262* (2014), 79–85.

[271] Zang, J., Qian, H., Wei, Z., Cao, Y., Zheng, M., and Dong, Q. Reduced graphene oxide supported mno nanoparticles with excellent lithium storage performance. *Electrochimica Acta 118* (2014), 112–117.

[272] Zhang, D., and Zhan, Z. Preparation of graphene nanoplatelets-copper composites by a modified semi-powder method and their mechanical properties. *Journal of Alloys and Compounds 658* (2016), 663–671.

[273] Zhang, H., Wen, J., Meng, X., Yao, Y., Yin, G., Liao, X., and Huang, Z. An improved method to increase the concentration of graphene in organic solvent. *Chemistry Letters 41*, 7 (2012), 747–749.

[274] Zhang, J., Vukmirovic, M. B., Xu, Y., Mavrikakis, M., and Adzic, R. R. Controlling the catalytic activity of platinum-monolayer electrocatalysts for oxygen reduction with different substrates. *Angewandte Chemie International Edition 44*, 14 (2005), 2132–2135.

[275] Zhang, J., Yang, H., Shen, G., Cheng, P., Zhang, J., and Guo, S. Reduction of graphene oxide via l-ascorbic acid. *Chemical Communications 46*, 7 (2010), 1112–1114.

[276] Zhang, L., Duan, Z., Zhu, H., and Yin, K. Advances in synthesizing copper/-graphene composite material. *Materials and Manufacturing Processes 32*, 5 (2017), 475–479.

[277] Zhang, L., Liu, C., Zhuang, L., Li, W., Zhou, S., and Zhang, J. Manganese dioxide as an alternative cathodic catalyst to platinum in microbial fuel cells. *Biosensors and Bioelectronics 24*, 9 (2009), 2825–2829.

[278] Zhang, P., Li, K., and Liu, X. Carnation-like mno 2 modified activated carbon air cathode improve power generation in microbial fuel cells. *Journal of Power Sources 264* (2014), 248–253.

[279] Zhang, S.-P., Liu, B., Li, C.-Y., Chen, W., Yao, Z.-J., Yao, D.-T., Yu, R.-B., and Song, H.-O. Enhanced dispersibility and thermal stability of β-cyclodextrin functionalized graphene. *Chinese Chemical Letters 25*, 2 (2014), 355–358.

[280] Zhang, Y., Hu, Y., Li, S., Sun, J., and Hou, B. Manganese dioxide-coated carbon nanotubes as an improved cathodic catalyst for oxygen reduction in a microbial fuel cell. *Journal of Power Sources 196*, 22 (2011), 9284–9289.

[281] Zhao, C., and Wang, J. Fabrication and tensile properties of graphene/copper composites prepared by electroless plating for structrual applications. *physica status solidi (a) 211*, 12 (2014), 2878–2885.

[282] Zhu, C., Guo, S., Fang, Y., and Dong, S. Reducing sugar: new functional molecules for the green synthesis of graphene nanosheets. *ACS nano 4*, 4 (2010), 2429–2437.

[283] Zhu, L., Zhao, X., Li, Y., Yu, X., Li, C., and Zhang, Q. High-quality production of graphene by liquid-phase exfoliation of expanded graphite. *Materials Chemistry and Physics 137*, 3 (2013), 984–990.

[284] Zhu, L., Zhao, X., Li, Y., Yu, X., Li, C., and Zhang, Q. High-quality production of graphene by liquid-phase exfoliation of expanded graphite. *Materials Chemistry and Physics 137*, 3 (2013), 984–990.

Appendix A

A1

Datasheets of the employed graphene derivatives

AVANZARE Innovación Tecnológica SL – C/Antonio de Nebrija, 8 – 26006 Logroño (La Rioja). Spain – www.avanzare.es – sales@avanzare.es – Tel +34941587027

avanGRAPHENE-2 (< 2 nm)

Product Description

These products of graphene with lamellar structural morphology, are design for their use as fillers for conductive polymers as an alternative to carbon nanotubes and conductive blackcarbons and graphites due to its exceptional electrical conductivity.

This material is functionalized for their integration in most of the polymers such as PVC, TPU, polyamides, polypropylene or ABS and also for their incorporation in textiles

High conductivity can be obtained due to the easy to achieve percolation limit

avanGRAPHENE-2 can be also use in resins and paints to obtain conductive resins, pains and composites allowing to obtain less than 10 Ohm/cm of surface and volumetric resistance

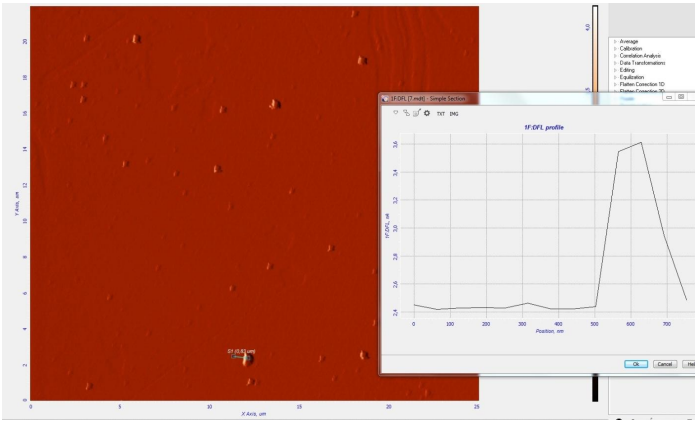

Figure A.1: d

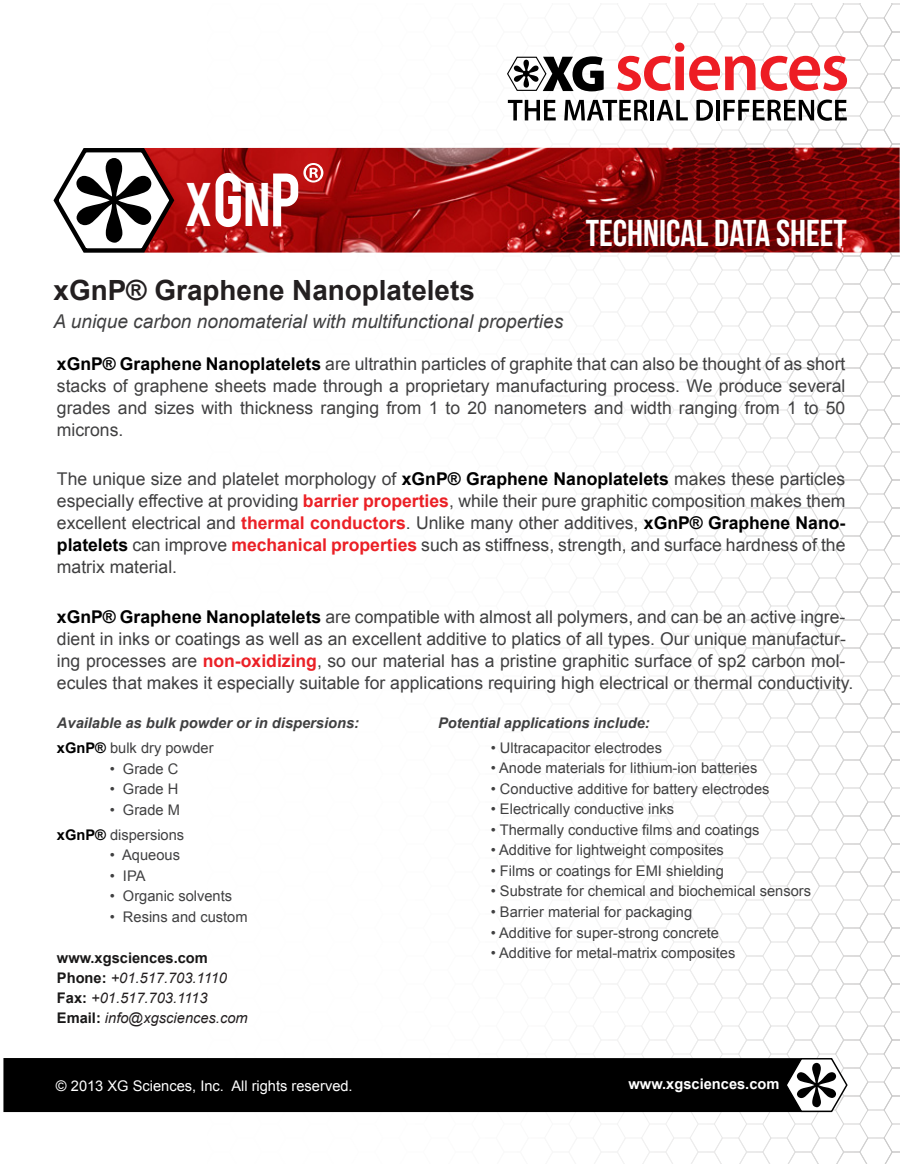

XG sciences
THE MATERIAL DIFFERENCE

xGNP®
TECHNICAL DATA SHEET

xGnP® Graphene Nanoplatelets

A unique carbon nonomaterial with multifunctional properties

xGnP® Graphene Nanoplatelets are ultrathin particles of graphite that can also be thought of as short stacks of graphene sheets made through a proprietary manufacturing process. We produce several grades and sizes with thickness ranging from 1 to 20 nanometers and width ranging from 1 to 50 microns.

The unique size and platelet morphology of **xGnP® Graphene Nanoplatelets** makes these particles especially effective at providing **barrier properties**, while their pure graphitic composition makes them excellent electrical and **thermal conductors**. Unlike many other additives, **xGnP® Graphene Nanoplatelets** can improve **mechanical properties** such as stiffness, strength, and surface hardness of the matrix material.

xGnP® Graphene Nanoplatelets are compatible with almost all polymers, and can be an active ingredient in inks or coatings as well as an excellent additive to platics of all types. Our unique manufacturing processes are **non-oxidizing**, so our material has a pristine graphitic surface of sp2 carbon molecules that makes it especially suitable for applications requiring high electrical or thermal conductivity.

Available as bulk powder or in dispersions:

xGnP® bulk dry powder
- Grade C
- Grade H
- Grade M

xGnP® dispersions
- Aqueous
- IPA
- Organic solvents
- Resins and custom

Potential applications include:
- Ultracapacitor electrodes
- Anode materials for lithium-ion batteries
- Conductive additive for battery electrodes
- Electrically conductive inks
- Thermally conductive films and coatings
- Additive for lightweight composites
- Films or coatings for EMI shielding
- Substrate for chemical and biochemical sensors
- Barrier material for packaging
- Additive for super-strong concrete
- Additive for metal-matrix composites

www.xgsciences.com
Phone: *+01.517.703.1110*
Fax: *+01.517.703.1113*
Email: *info@xgsciences.com*

www.xgsciences.com

Figure A.2: d

Graphenea

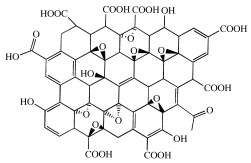

Product Datasheet

Graphenea Graphene Oxide (GO)

Properties

Form	Dispersion of graphene oxide sheets
Sheet dimension	Variable
Color	Yellow-brown
Odor	Odorless
Dispersibility	Polar solvents
Solvents	Water
Concentration	4 mg/mL
pH	2,2-2,5
Monolayer content (measured in 0.5mg/mL)	>95%*

(*) 4mg/ml concentration tends to agglomerate the GO flakes and dilution followed by slight sonication is required in order to obtain a higher percentage of monolayer flakes

Elemental Analysis*

Carbon	49-56%
Hydrogen	0-1%
Nitrogen	0-1%
Sulfur	2-4%
Oxygen	41-50%

* Sample preparation: 2g of 4wt% GO in water were dried under vacuum at 60°C overnight.

SEM image

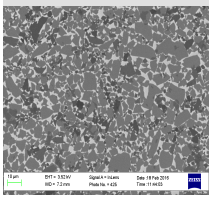

TEM image

XPS

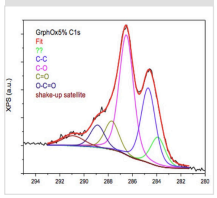

www.graphenea.com

Figure A.3: d

Graphenea

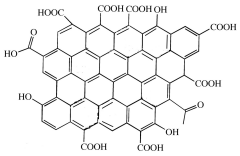

Product Datasheet

Graphenea Reduced Graphene Oxide (rGO)

Properties

Form	Powder
Reduction method	Chemically reduced
Sheet dimension	Variable
Color	Black
Odor	Odorless
Solubility	Insoluble
Dispersability	low concentrations (<0.1mg/mL) in NMP, DMSO, DMF
Humidity (Karl Fisher, TGA)	3.7-4.2%
Electrical conductivity	> 600 S/m
BET surface area	422.69-499.85 m^2/g
Particle size (z-sizer in NMP at 0,1 mg/mm):	260-295nm
Density	1,91 g/cm^3

Elemental Analysis

Carbon	77-87%
Hydrogen	0-1%
Nitrogen	0-1%
Sulfur	0%
Oxygen	13-22%

SEM image

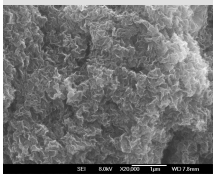

TEM image

XPS

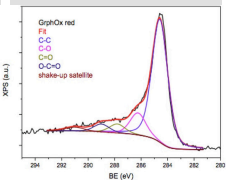

www.graphenea.com

Figure A.4: d

Appendix B

A2

Hysol

ECCOBOND 285
Thermally Conductive, Epoxy Paste Adhesive

Key Feature:	Benefit:
• Thermal conductivity	• Dissipation of heat from bonded components
• Thixotropic paste	• No flow or sag even on vertical surfaces
• Wide variety of catalysts available	• Versatility of resin system
• Low coefficient of thermal expansion	• Low stress on bonded components

Product Description:

ECCOBOND 285 is a highly filled, thermally conductive, thixotropic, non-sag paste epoxy adhesive that can be used with a variety of catalysts. It features low coefficient of thermal expansion and good bond strength. When cured with CATALYST 23 LV, ECCOBOND 285 can be used at cryogenic temperatures and has good thermal cycling properties.

Applications:

ECCOBOND 285 is designed for bonding metals and ceramic substrates in heat sink applications or any application that requires a thermally conductive adhesive for thermal management. It is also useful for any application that requires a thixotropic paste adhesive and low stress bonds.

Instructions For Use:

Thoroughly read the information concerning health and safety contained in this bulletin before using. Observe all precautionary statements that appear on the product label and/or contained in individual Material Safety Data Sheets (MSDS).

To ensure the long term performance of the bonded assembly, complete cleaning of the substrates should be performed to remove contamination such as oxide layers, dust, moisture, salt, and oils which can cause poor adhesion or corrosion in a bonded part. For information on proper substrate preparation, refer to the reprint "Good Adhesive Bonding Starts With Surface Preparation" available from Henkel Corporation.

Some filler settling is common during shipping and storage. For this reason, it is recommended that the contents of the shipping container be thoroughly mixed prior to use. Power mixing is preferred to ensure a homogeneous product.

Accurately weigh resin and hardener into a clean container in the recommended ratio. Weighing apparatus having an accuracy in proportion to the amounts being weighed should be used.

Blend components by hand, using a kneading motion, for 2-3 minutes. Scrape the bottom and sides of the mixing container frequently to produce a uniform mixture. If possible, power mix for an additional 2-3 minutes. Avoid high mixing speeds which could entrap excessive amounts of air or cause overheating of the mixture resulting in reduced working life.

Apply the adhesive to all surfaces to be bonded and join together. In most applications only contact pressure is required.

Properties of Material As Supplied:

Property	Test Method	Unit	Value
Chemical Type			Epoxy
Appearance	Visual		Thixotropic black paste
Density	ASTM-D-792	g/cm^3	2.40

Choice of Curing Agents			
Curing agent	Catalyst 9	Catalyst 11	Catalyst 23 LV
Description	General purpose with good chemical resistance and physical strength.	Long pot life, excellent chemical resistance, good physical and chemical properties at elevated temperatures.	Low color, low viscosity, long pot life. Excellent, thermal shock and impact resistance. Excellent low temperature properties and adhesion to glass.
Type of cure	Room	Heat	Room
Viscosity Pa.s cP	0.080 to 0.105 80 to 105	0.035 to 0.060 @ 65 °C 35 to 60 @ 65 °C	0.020 to 0.030 20 to 30

Properties of Material As Mixed:

Property	Test Method	Unit	Value		
			Catalyst 9	Catalyst 11	Catalyst 23 LV
Mix Ratio - Amount of Catalyst per 100 parts of ECCOBOND 285		By Weight By Volume	3.5 8.5	4.0 9.9	7.3 17.0
Working Life (100 g @ 25°C)	ERF 13-70		45 minutes	4 hours	60 minutes
Density	ASTM-D-792	g/cm^3	2.27	2.27	2.18

Figure B.1: d

Datasheets of the employed epoxy resins

Emerson & Cuming
a National Starch & Chemical Company

ECCOBOND® 55
Unfilled, General Purpose Epoxy Adhesive

Key Feature:	Benefit:
• General purpose	• Bonds well to metal, glass and plastic substrates
• Low viscosity	• Ease of dispensing and use
• Variety of catalysts available	• Versatility of resin system

Product Description:

ECCOBOND 55 is an unfilled, low viscosity, general purpose epoxy adhesive resin that can be cured with a variety of catalysts. It features good wetting of most substrates and offers good chemical, solvent and water resistance. ECCOBOND 55 bonds well to glass, ceramics, metals and plastics.

Applications:

ECCOBOND 55 is designed for electronic component assembly, staking of adjustment and calibration screws, anchoring of inserts, end fills or hermetic sealing.

Instructions For Use:

Thoroughly read the information concerning health and safety contained in this bulletin before using. Observe all precautionary statements that appear on the product label and/or contained in individual Material Safety Data Sheets (MSDS).

To ensure the long term performance of the bonded assembly, complete cleaning of the substrates should be performed to remove contamination such as oxide layers, dust, moisture, salt, and oils which can cause poor adhesion or corrosion in a bonded part. For information on proper substrate preparation, refer to the reprint "Good Adhesive Bonding Starts With Surface Preparation" available from Emerson & Cuming.

Some separation of components is common during shipping and storage. For this reason, it is recommended that the contents of the shipping container be thoroughly mixed prior to use. Power mixing is preferred to ensure a homogeneous product.

Accurately weigh resin and hardener into a clean container in the recommended ratio. Weighing apparatus having an accuracy in proportion to the amounts being weighed should be used.

Blend components by hand, using a kneading motion, for 2-3 minutes. Scrape the bottom and sides of the mixing container frequently to produce a uniform mixture. If possible, power mix for an additional 2-3 minutes. Avoid high mixing speeds which could entrap excessive amounts of air or cause overheating of the mixture resulting in reduced working life.

Apply the adhesive to all surfaces to be bonded and join together. In most applications only contact pressure is required.

Properties of Material As Supplied:

Property	Test Method	Unit	Value
Chemical Type			Epoxy
Appearance	Visual		Milky White Liquid
Density	ASTM-D-792	g/cm^3	1.18
Brookfield Viscosity	ASTM-D-2393	Pa.s cP	16 16,000

Choice of Curing Agents			
Curing agent	Catalyst 9	Catalyst 11	Catalyst 23 LV
Description	General purpose with good chemical resistance and physical strength.	Long pot life, excellent chemical resistance, good physical and chemical properties at elevated temperatures.	Low color, low viscosity, long pot life. Excellent, thermal shock and impact resistance. Excellent low temperature properties and adhesion to glass.
Type of cure	Room	Heat	Room
Viscosity Pa.s cP	0.080 to 0.105 80 to 105	0.035 to 0.060 @ 65 °C 35 to 60 @ 65 °C	0.020 to 0.030 20 to 30

Properties of Material As Mixed:

Property	Test Method	Unit	Value		
			Catalyst 9	Catalyst 11	Catalyst 23 LV
Mix Ratio - Amount of Catalyst per 100 parts of ECCOBOND 55		By Weight By Volume	13.5 15.5	16 17	28 32
Working Life (100 g @ 25°C)	ERF 13-70		45 minutes	>4 hours	60 minutes
Density	ASTM-D-792	g/cm^3	1.14	1.15	1.12
Brookfield Viscosity	ASTM-D-2393	Pa.s cP	8 8,000	7.1 7,100	3.3 3,300

Figure B.2: d

List of Figures

List of Tables

Universidad del País Vasco
Euskal Herriko Unibertsitatea

tecnalia Inspiring Business